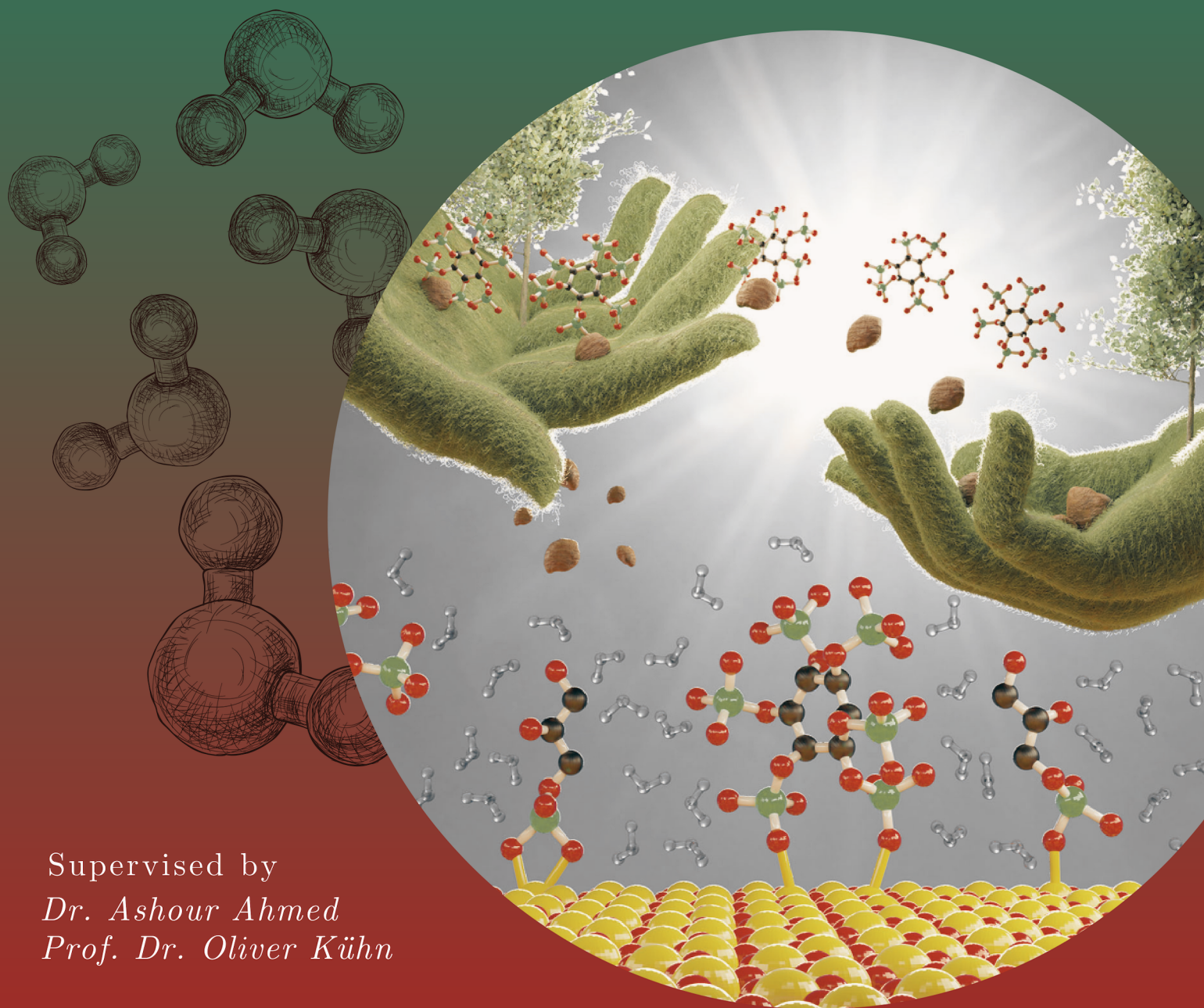


Revealing the Binding Mechanism of Phosphates at the Mineral–Water Interface: Insights from QM/MM Molecular Dynamics Simulations

Kumulative Dissertation zur Erlangung des akademischen Grades
doctor rerum naturalium (Dr. rer. nat.) der Mathematisch–
Naturwissenschaftlichen Fakultät der Universität Rostock



Supervised by
Dr. Ashour Ahmed
Prof. Dr. Oliver Kühn

Submitted by
Prasanth Babu Ganta

SEPTEMBER 2023

Revealing the Binding Mechanism of Phosphates at the Mineral–Water Interface: Insights from QM/MM Molecular Dynamics Simulations

Kumulative Dissertation zur Erlangung
des akademischen Grades
doctor rerum naturalium (Dr. rer. nat.) der
Mathematisch–Naturwissenschaftlichen Fakultät
der Universität Rostock

VORGELEGT VON:
Prasanth Babu Ganta
VON VIJAYAWADA, INDIEN,
MATRIKEL–NR.: 212209057

EINGEREICHT AM:
18.09.2023

BETREUER:
Dr. Ashour Ahmed
Prof. Dr. Oliver Kühn

Abstract

Phosphorus (P) is essential for all life forms and is crucial for global food security. The agricultural industry heavily relies on chemical fertilizers, resulting in inefficient P utilization. With concerns about a potential P peak scenario affecting P importing nations, sustainable P extraction methods are necessary. The effectiveness of P fertilizers relies on P mobilization and fixation, which are strongly connected to the strength of P binding to soil constituents, particularly mineral surfaces. Within this context, this thesis highlights the P binding mechanisms at the mineral–water interface, with a particular emphasis on minerals relevant to the P fixation issue, specifically goethite (α -FeOOH) and its isomorphous diasporite (α -AlOOH). The spotlight is placed on common and abundant phosphates in environmental and biological systems, particularly glycerolphosphate (GP) and inositolhexaphosphate (IHP). The thesis embarks on a scientific journey, employing advanced Computational Chemistry techniques, notably hybrid quantum mechanical/molecular mechanical (QM/MM) methods based on molecular dynamics (MD) simulations. The simulations examine multiple surface planes with distinct properties, specifically (010) and (100) for both goethite and diasporite and the complex interactions with phosphates. For goethite, GP exhibits stable **M** (Fe+O) and **B** (Fe+2O or 2Fe+2O) binding motifs at both (010) and (100) goethite surface planes. IHP exhibits **M** and **2M** (2Fe+2O) motifs on the (100) surface plane and an additional **3M** (3Fe+3O) motif at the (010) surface plane. The prevalence of specific motifs is determined by their abundance, stability throughout the MD trajectory, and corresponding interaction energies. The presence of intermolecular hydrogen bonds (HBs) between phosphates (GP and IHP) and water, as well as intramolecular HBs among phosphate groups within IHP, plays a significant role in influencing the stability of these binding motifs. Notably, the degree of surface saturation and positioning of surface Fe atoms play a critical role in governing the stability of these binding motifs. For example, the (010) surface, characterized by lower saturation, exhibits more robust interactions, thus significantly impacting the formation of motifs. The simulations also capture proton transfer events from phosphates to water and the surface. Similarly, diasporite exhibits stable motifs for phosphates, mirroring the behavior observed in goethite. However, diasporite displays notably higher interaction energies, emphasizing its role in phosphate binding processes. The validity of our molecular modeling approach was confirmed by comparing calculated infrared (IR) spectra to experimental ones, ensuring simulation reliability. Combining simulation results with adsorption experiments provided a comprehensive understanding of the hierarchy of interaction energies, shedding light on the factors that govern phosphate binding. In conclusion, this thesis emphasizes the need to address molecular modeling challenges and bridge scales. This interdisciplinary approach enhances our understanding of phosphate binding and aids sustainable extraction methods, which are crucial for global food security and environmental sustainability.

Zusammenfassung

Phosphor (P) ist für alle Lebensformen und für die weltweite Ernährungssicherheit von entscheidender Bedeutung. Die Landwirtschaft ist stark auf chemische Düngemittel angewiesen, was zu einer ineffizienten P Nutzung führt. Angesichts der Besorgnis über ein mögliches P Peak Szenario, das die P Importländer betrifft, sind nachhaltige P Extraktionsmethoden erforderlich. Die Wirksamkeit von P Düngern hängt von der P Mobilisierung und -Fixierung ab, die eng mit der Stärke der P Bindung an Bodenbestandteile, insbesondere an mineralische Oberflächen, verbunden sind. In diesem Zusammenhang werden in dieser Arbeit die P Bindungsmechanismen an der Mineral Wasser Grenzfläche beleuchtet, wobei der Schwerpunkt auf Mineralen liegt, die für die Frage der P Fixierung relevant sind, insbesondere Goethit (α -FeOOH) und seine isomorphe Diaspore (α -AlOOH). Im Mittelpunkt stehen die in der Umwelt und in biologischen Systemen häufig vorkommenden Phosphate, insbesondere Glycerolphosphat (GP) und Inositolhexaphosphat (IHP). Die Dissertation begibt sich auf eine wissenschaftliche Reise, bei der fortschrittliche Techniken der rechnergestützten Chemie eingesetzt werden, insbesondere hybride quantenmechanische/molekularmechanische (QM/MM) Methoden auf der Grundlage von Molekulardynamiksimulationen (MD). Die Simulationen untersuchen mehrere Oberflächenebenen mit unterschiedlichen Eigenschaften, insbesondere (010) und (100) sowohl für Goethit als auch für Diaspore und die komplexen Wechselwirkungen mit Phosphaten. Bei Goethit zeigt GP stabile **M** (Fe+O) und **B** (Fe+2O oder 2Fe+2O) Bindungsmotive sowohl auf der (010) als auch auf der (100) Goethit Oberflächenebene. IHP weist **M** und **2M** (2Fe+2O) Motive auf der (100) Oberflächenebene und ein zusätzliches **3M** (3Fe+3O) Motiv auf der (010) Oberflächenebene auf. Das Vorherrschen bestimmter Motive wird durch ihre Häufigkeit, ihre Stabilität während der MD Trajektorie und die entsprechenden Wechselwirkungsenergien bestimmt. Das Vorhandensein intermolekularer Wasserstoffbrückenbindungen (HBs) zwischen Phosphaten (GP und IHP) und Wasser sowie intramolekularer HBs zwischen Phosphatgruppen innerhalb von IHP spielt eine wichtige Rolle bei der Beeinflussung der Stabilität dieser Bindungsmotive. Vor allem der Grad der Oberflächensättigung und die Positionierung der Fe Atome an der Oberfläche spielen eine entscheidende Rolle für die Stabilität dieser Bindungsmotive. So weist die (010) Oberfläche, die durch eine geringere Sättigung gekennzeichnet ist, robustere Wechselwirkungen auf, was sich erheblich auf die Bildung von Motiven auswirkt. Die Simulationen erfassen auch den Protonentransfer von Phosphaten auf Wasser und die Oberfläche. In ähnlicher Weise zeigt Diaspore stabile Motive für Phosphate, die das in Goethit beobachtete Verhalten widerspiegeln. Allerdings weist Diaspore deutlich höhere Wechselwirkungsenergien auf, was seine Rolle bei Phosphatbindungsprozessen unterstreicht. Die Gültigkeit unseres Molekülmodellierungsansatzes wurde durch den Vergleich der berechneten Infrarot (IR) Spektren mit den experimentellen Spektren bestätigt, wodurch die Zuverlässigkeit der Simulation sichergestellt wurde. Die Kombination von Simulationsergebnissen mit Adsorptionsexperimenten ermöglichte ein umfassendes Verständnis der Hierarchie der Wechselwirkungsenergien und gab Aufschluss

über die Faktoren, die für die Phosphatbindung entscheidend sind. Zusammenfassend lässt sich sagen, dass diese Arbeit die Notwendigkeit unterstreicht, sich den Herausforderungen der Molekülmodellierung zu stellen und Skalen zu überbrücken. Dieser interdisziplinäre Ansatz verbessert unser Verständnis der Phosphatbindung und unterstützt nachhaltige Extraktionsmethoden, die für die globale Ernährungssicherheit und die ökologische Nachhaltigkeit von entscheidender Bedeutung sind.¹

¹translated using [deepl.com/de/translator](https://www.deepl.com/de/translator)

Betreuer:

Dr. Ashour Ahmed
Institut für Physik, Universität Rostock

Prof. Dr. Oliver Kühn
Institut für Physik, Universität Rostock

Doz. Dr. Daniel Tunega
Institut für Bodenforschung, Universität für Bodenkul-
tur Wien

Tag der Einreichung: 18.09.2023

Tag der Verteidigung: 31.05.2024

Contents

1	Introduction	1
1.1	Motivation – Need for P Study	1
1.2	Basic Overview of P Terrestrial Cycle	2
1.3	Colloidal P in Soil	4
1.4	Molecular Simulations of Geochemical Systems	6
1.5	Thesis Objective	7
2	Theoretical Background	9
2.1	Molecular Simulation Methods Overview	10
2.2	Molecular Mechanics	11
2.2.1	Theoretical Description of Common Force Fields	11
2.3	Quantum Mechanics	15
2.3.1	Schrödinger Equation and Variational Principle	15
2.3.2	Approximations	16
2.3.3	Basis Sets	18
2.3.4	DFT and GPW method	19
2.4	Hybrid Quantum Mechanics/Molecular Mechanics	28
2.5	Molecular Dynamics	32
3	Molecular Systems, Modelling And Analysis	35
3.1	Molecular Systems and Relevant Interactions	35
3.2	Molecular Modelling and Computational Details	41
3.3	Analysis	44
4	Summary of Simulation Results	47
5	Conclusions	59
	Bibliography	61
	Appendices	77
A	Peer Reviewed Publications	79

List of abbreviations

DFT	density functional theory
QM	quantum mechanics
MM	molecular mechanics
QMMM	quantum mechanics and molecular mechanics
MD	molecular dynamics
GPW	Gaussian and plane wave
GTH	Goedecker–Teter–Hutter
PBE	Perdew–Burke–Ernzerhof
GGA	generalized gradient approximation
BSSE	basis set superposition error
FF	force field
SCF	self consistent field
STO	Slater type orbital
GTO	Gaussian type orbital
DZP	double zeta plus polarization
TZP	triple zeta plus polarization
LDA	local density approximation
GGA	generalized gradient approximation
FFT	fast Fourier transform
FTIR	Fourier transform infrared
BSSE	basis set superposition error

- GEEP** Gaussian expansion of the electrostatic potential
- NVT** constant number of atoms, volume and temperature
- CSV** canonical sampling through velocity rescaling
- IHP** inositolhexaphosphate
- GP** glycerolphosphate
- OP** orthophosphate
- M** monodentate
- B** bidentate
- 2M** two monodentate
- 3M** three monodentate
- 4M** four monodentate
- HB** hydrogen bond

List of Figures

1.1	Overview of terrestrial P cycle. Adapted from (Shen et al., 2011; Kruse et al., 2015). The green and red square boxes indicate P inputs and outputs, respectively.	3
2.1	Simulation methods and their corresponding spatiotemporal scales. Note that the ranges mentioned here are approximate values. Adopted from Ozboyaci et al. (2016).	10
2.2	Different scenarios contributing to QM/MM interaction energy. Bond (a), angle (b), torsion (c), vdW interactions like lennard-jones [LJ] (d), link-atoms (e), electrostatic interaction (f). Taken from Groenhof (2013).	27
2.3	Collocation procedure highlighting the MM atom's (green color) collocation radius and its contribution onto QM multigrid setup. MM atom whose collocation radius is greater than its distance from QM grid and another MM atom whose collocation radius lies completely inside QM grid (a), collocation radius partially overlays onto QM grid (b), long-range contribution (RES_{low}) from all the atoms mapped onto the coarsest grid (c). Redrawn from Laino et al. (2006).	30
3.1	Phosphates: Phosphoric acid (fully protonated OP) (a), GP (b) and IHP (c). Red, white, black and green colors correspond to oxygen, hydrogen, carbon and phosphorus atoms, respectively (Ganta et al., 2021b).	36
3.2	Goethite surface: (010) surface plane (a), (100) surface plane (b). Pink, red, yellow and white colors correspond to iron, bridging oxygen, hydroxyl oxygen and hydrogen atoms, respectively. The blue lines show the coordination of surface Fe atoms, four at (010) surface plane and five at (100).	37
3.3	Binding motifs: monodentate M (a), binuclear bidentate BB (b), bidentate B (c), 4M (c). Blue, red, white, black and green colors correspond to iron, oxygen, hydrogen, carbon and phosphorus atoms, respectively (Ganta et al., 2021b).	39
3.4	Goethite-GP-Water complexes: (010) goethite-GP-water complex (a) and (100) goethite-GP-water complex (b). Blue, red, yellow, white, black, and green colors correspond to iron, bridging oxygen, hydroxyl oxygen, hydrogen, carbon, and phosphorus atoms, respectively. The box denotes QM box of the model. (Ganta et al., 2021a,b).	43

3.5	Definition of coordinates q_1 and q_2 in an HB between water's oxygen and IHP's oxygen from a phosphate group (a) (Limbach et al., 2009), intramolecular HB in IHP (b) (Ganta et al., 2019).	45
4.1	Snapshots of GP/IHP at diaspore/goethite–water interface (Ganta et al., 2019, 2020, 2021a,b).	48
4.2	Diaspore-GP B motif along the production trajectory (Ganta et al., 2020). .	51
4.3	Snapshots along the MD trajectory for the 100 diaspore–IHP–water 2M motif (a–c) and the top view of surface atoms showing interatomic Al–Al distances (d). Similarly, the snapshots of 3M motif (e–g) and the top view of surface atoms show interatomic Al–Al distances (h). The circle around the Al atom denotes the site of Al–O _P bonds in 2M and 3M motif, respectively, wherein the red circle denotes the site where Al–O _P bond dissociated. Note that water is ignored in this image for better view (Ganta et al., 2020). Regions R1–R4 are selected regions for understanding Al–O bonds dissociation.	52
4.4	Electrostatic potential (a.u.) at one Å (perpendicular to the surface) for the bare (010) diaspore surface plane (a) as well as for the bare (100) diaspore surface plane (b). These have been calculated for bare surfaces without involving phosphates and water (Ganta et al., 2020).	53
4.5	Comparison of radial distribution functions calculated for (010) and (100) diaspore surface oxygens and hydrogens of water (Ganta et al., 2020).	53
4.6	Comparison of GP and IHP (at goethite) IR spectra with experimental spectra from (Li et al., 2017) and (Yan et al., 2015), respectively. The blue rectangle denotes region within $\pm 15\text{cm}^{-1}$ around frequencies observed in experimental studies (Ganta et al., 2021a).	55
4.7	Sum of Fe–O bond lengths observed in goethite–OP and goethite–GP B motifs (Ganta et al., 2021b).	56

1 Introduction

In the context of extensive industrialization and a growing population, natural resources are depleting with time due to ever-increasing human consumption, which outpaces natural cycling. Even though they are still abundant in nature, they could be emptied as they are limited. Therefore, understanding biogeochemical cycles and corresponding mass and energy transfer between ecosystems is vital for efficiently recycling and reproducing these resources. For instance, carbon (C) in the form of CO₂ from industrial wastes can be converted to methanol (Goeppert et al., 2014) or captured and sequestered to be used in construction applications (Sanna et al., 2014) to reduce global warming and carbon depletion. Likewise, the nitrogen (N) and phosphorus (P) from municipal wastewater can be removed using microalgae, which are then harvested and reused as fertilizer and soil conditioner (Shi et al., 2007). Nevertheless, the biogeochemical cycles are complex systems requiring extensive studies to discover and understand the mass and energy exchange involved. Of the primary biogeochemical cycles C, N and P, the C and N cycles are studied extensively for the past few decades, but the P cycle studies are comparatively limited in number (Bol et al., 2016).

1.1 Motivation – Need for P Study

Phosphorus is an essential element required for both plant and animal growth. However, it is a limiting nutrient as only a small amount of P is present in the soil, which restrains plant growth. While the forests have evolved with efficient strategies to comply with P limitation (Rennenberg and Schmidt, 2010; Hinsinger et al., 2011), in the agriculture setup, fertilizers are added manually to maintain and improve plant and animal production (Daniel et al., 1998). Today's primary P source for fertilizers is mined phosphate rocks, which are expected to be exhausted within the next 100 years (Steen, 1998; Smil, 2000; Vaccari and Strigul, 2011). The US Geological Survey studies show that P rock resources are available only in a few countries, and a P peak scenario might affect regions like northern Europe (no reserves), India (few) and the USA (diminishing) who obtain these resources mainly through imports (Rosmarin, 2004; Elser and Bennett, 2011; Cordell and Neset, 2014; Withers et al., 2019). This projected peak P scenario might evolve into a global environmental challenge that could result in catastrophic food shortages (Cordell et al., 2009; Elser and Bennett, 2011; Cordell and Neset, 2014; van Dijk et al., 2016; Reitzel et al., 2019). As P rock reserves dwindle with time, P importing countries' food security is in question, exposing farmers to exorbitant fertilizer prices.

Only three countries control more than 85% of global P, with Morocco holding the most significant share. A prolonged peak P scenario could flip oil-based economies to P based economies since P has no alternative in agriculture. This scenario emphasizes the need to study the P biogeochemical cycle to discover ways to recycle and reuse P effectively.

The P input to the soil through P fertilizers is not fully available to plants as most of it is bound to soil particulates or colloids (Grant et al., 1996; Hens and Merckx, 2001; Kruse et al., 2015; Jiang et al., 2015) causing P inefficiency. To overcome this, fertilizers are often applied in excess to maintain and increase agricultural production. However, studies showed that excess P fertilizers increased P runoff (Römkens and Nelson, 1974). In the long term, the P bound to colloids accumulate in the off-farm environment causing eutrophication of waterways (Sharpley et al., 1994), lakes and reservoirs (Daniel et al., 1998; Smith, 2003). Eutrophication defines the state of a lake that has excess nutrients, low transparency and dense plant growth. Phosphorus is identified as the main limiting nutrient for algae and aquatic plants' growth in lakes and reservoirs (Schindler, 1977; Caspers, 1984). With an excess supply of P, the algae bloom continues to expand and create dead zones by depleting oxygen in water bodies. Cordell et al. (2009) highlighted that out of 17.5 million tons of mined P, about 14 million tons are used in fertilizers production; however, only three million tons made it to the food table (Elser and Bennett, 2011). P leaching and soil erosion contribute significantly to P losses, which is about 8 million tons. Therefore, in the context of dwindling P rock reservoirs, there is a need for an extensive study of the biogeochemical P cycle for efficient P (re)use. This includes 1) manufacturing fertilizers that improve P efficiency, 2) improving techniques to reduce P leaching and 3) developing recycling methods to extract immobilized and fixed P. The oil crisis in the 1970s emphasized the need for renewable energy sources, but unfortunately, for the peak P crisis, there is no alternative but to extract and reuse P effectively (Rosmarin, 2004; Cordell et al., 2009; Withers et al., 2019; Withers, 2019). In contrast to major biogeochemical elements C, N, oxygen (O) and hydrogen (H), P is not significantly present in gaseous form in the atmosphere. Therefore, terrestrial and marine P cycles are prominent in understanding P's fate, but only the terrestrial P cycle is discussed here in the current work context.

1.2 Basic Overview of P Terrestrial Cycle

When P bearing bedrock minerals (I1, see Fig. 1.1) are uplifted and exposed to *weathering* and *erosion*, the dissolved and particulate P is introduced into the soil system. The most stable and abundant primary P mineral is apatite ($\text{Ca}_5(\text{PO}_4)_3\text{X}$, $\text{X} = \text{F}^{1-}$, OH^{1-} , Cl^{1-}). It accounts for more than 95% of P in Earth's crust ($\text{P} < 10^{-2}\text{gP/kg}$) (Jahnke, 1992; Shen et al., 2011; Kruse et al., 2015). About 90% of the eroded P is bound to mineral lattices of particulate matter and reaches water bodies without involving the biological systems (L1). Another P source is secondary P minerals, which are mainly Ca, Al and

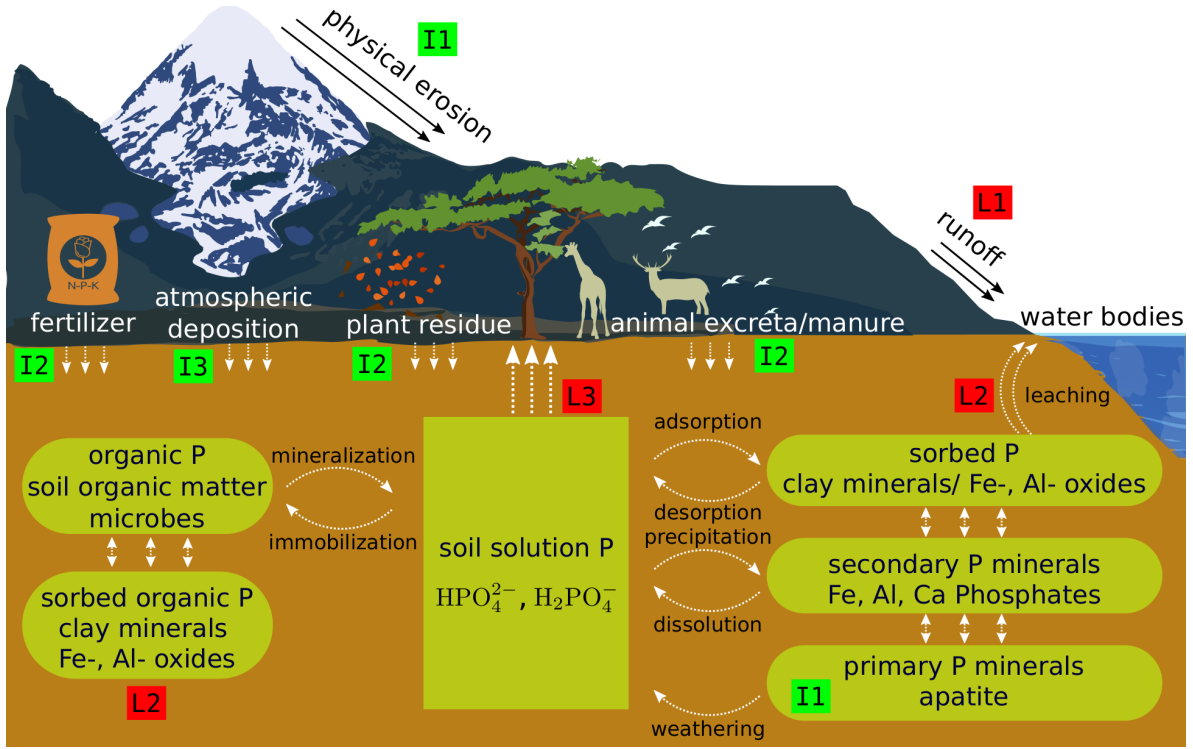


Figure 1.1: Overview of terrestrial P cycle. Adapted from (Shen et al., 2011; Kruse et al., 2015). The green and red square boxes indicate P inputs and outputs, respectively.

Fe phosphates. Monocalcium phosphate [$\text{Ca}(\text{H}_2\text{PO}_4)_2 \cdot \text{H}_2\text{O}$], brushite [$\text{Ca}(\text{H}_2\text{PO}_4)_2 \cdot 2\text{H}_2\text{O}$], monetite [$\text{Ca}(\text{H}_2\text{PO}_4)_2$], fluorapatite [$\text{Ca}_5(\text{PO}_4)_3\text{F}$] and octacalcium phosphate [$\text{Ca}_8\text{H}_2(\text{PO}_4)_6 \cdot 5\text{H}_2\text{O}$] are some of the secondary Ca-phosphate minerals. And variscite [$\text{AlPO}_4 \cdot 2\text{H}_2\text{O}$], wavellite [$\text{Al}_3(\text{PO}_4)_2(\text{OH})_3 \cdot 5\text{H}_2\text{O}$], strengite [$\text{Fe}(\text{PO}_4) \cdot 2\text{H}_2\text{O}$] and vivianite [$\text{Fe}_3(\text{PO}_4)_2 \cdot 8\text{H}_2\text{O}$] are common secondary Al- and Fe-phosphate minerals (Kruse et al., 2015). The secondary minerals are formed through the weathering of primary minerals with time. The P dissolved from these minerals are mainly inorganic P (P_i), i.e., phosphate ions ($\text{H}_2\text{PO}_4^{1-}$, HPO_4^{2-} , PO_4^{3-}) and polyphosphates ($\text{H}_{n+2}\text{P}_n\text{O}_{3n+1}$). Polyphosphates are significantly less abundant than total P in nature and mostly used in industrial and commercial applications. The dissolved P in soil solution is the plant available P form and it is readily available for plant uptake (L3). Even though a small percentage ($\approx 0.1\%$ of total P) is present in soil solution, it is vital as it acts as a reservoir for plant P uptake (Kruse et al., 2015). The P *dissolution* from secondary minerals depends mainly on mineral particle size and soil pH (Shen et al., 2011). The opposite of P *dissolution* is *precipitation* wherein the metal ions Al^{3+} , Fe^{3+} (dominant in acidic soils) and Ca^{2+} (dominant in alkaline soils) interact with P to form corresponding mineral phosphates (Brady, 2017; Penn and Camberato, 2019). Recent studies show that the

soil colloids retain about 50% of the existing P in soil solution (Holzmann et al., 2015; Bol et al., 2016) through the *adsorption* process. Consequently, a significant amount of P in soil solution becomes unavailable to plants. Based on existing soil chemistry, the adsorbed P's *desorption* is also found in nature but with a lower rate than *adsorption* (Jahnke, 1992). Nevertheless, the dissolved P enters the biological systems through plant uptake and plays a crucial role in plant cells' energy storage and formation of nucleic acids (L2). When animals consume plants, P is incorporated into the animal body cells or excreted.

The organic P (P_o) is released into the soil system when soil microorganisms synthesize the plant and animal waste. For instance, dead mass, dried plants, animal excreta/-manure, and bird droppings (I2). For arable soils, the plant accessible P is maintained by adding fertilizers (I2). Often, fertilizers are added in excess to improve production; therefore, the arable soils are usually higher in P than forest soils. The P_i in soil solution is also transformed to P_o by soil microorganisms during the decomposition of organic residues (Condon et al., 2015). This biological transformation of P_i to P_o is called *immobilization*. The process countering this transformation is called *mineralization*, wherein P_i is released from P_o . The contribution of P_o in supplying P nutrient to plants depends on the *immobilization* and *mineralization* rates. Even though P_i is the prime source of P for plants and microorganisms, numerous studies show that P_o contributes significantly to P nutrition of plants (Oehl et al., 2001; Chen et al., 2002). Unfortunately, both P_i and P_o are known to interact with soil colloids in soil solution and get leached to water bodies escaping the terrestrial P cycle (L3). About 90% of P that oceans receive from rivers is in particulate form. The dissolved P participates in biological cycles in oceans while the particulate P accumulates into sediments with time. Due to the confined size of lakes and reservoirs, continuous P input causes P accumulation, which further results in eutrophication. Atmospheric P deposition (I3) with varying quantities based on on-site location, time, rainfall, temperature and season is also observed (Tipping et al., 2014).

This overall picture of the P cycle shows that the P interaction with soil colloids is the main reason that causes P leaching and P inefficiency. Therefore, effective extraction and reuse of P lost through leaching would improve domestic P production, which would improve the global population's food security. For this, one needs to understand the P interaction with soil colloids.

1.3 Colloidal P in Soil

The particles in the soil are divided based on the size as sand (2–0.05 mm), slit (0.05–0.002 mm) and clay (< 0.002 mm). Colloids are part of the fine clay particle phase in soils with sizes ranging from 50 Å to 0.2 μm (Tan, 2011). Most soils contain large amounts

of colloids and the physical and chemical properties of these colloids significantly influence soil chemistry. Many colloids are smaller in size and exhibit higher surface area per mass (specific surface area) than parent sand and slit materials. This could explain why some colloids deviate from the bulk properties of their parent materials. The inorganic colloids include weathered clay minerals (mainly phyllosilicates), Fe- and Al-(oxyhydr)oxides and Ca-oxides, while the organic colloids include mainly SOM (plant solids like humus and cell walls). The aggregates formed from possible combinations of aforelisted constituents are also considered colloids. For instance, SOM interacts with Fe- and Al-(oxyhydr)oxides (Davis, 1982; Gu et al., 1994; Teermann and Jekel, 1999) and other clay minerals (Davis, 1982) primarily through electrostatic interaction, surface complexation and hydrogen bonding to form aggregate colloids (Bolt and van Olphen, 1985). The mineral-SOM colloids show weaker interaction with phosphates than pure mineral colloids because of saturated active sites on the mineral surface. Also, studies show that the SOM interaction with the mineral surface makes mineral-SOM colloid more stable (Kalbitz et al., 2005). Hence, the pure forms of Fe- and Al-(oxyhydr)oxides are comparatively more reactive to adsorb P and contribute significantly to P leaching. Nevertheless, the formation and characteristic of a colloidal P is complicated and mostly depends on the existing soil composition, soil pH, SOM type and many other factors.

Both P_i and P_o phosphates interact with soil colloids to form colloidal P. Naturally, phosphorus is present often in +5 oxidation state as phosphate (PO_4^{3-}) anion and most of the dissolved and particulate form of P in soils are complexed or slightly modified forms of this anion (Jahnke, 1992). While P_i is often present as phosphate ions ($H_2PO_4^{1-}$, HPO_4^{2-} , PO_4^{3-}) (Newman and Tate, 1980), the P_o fractions occur mainly as phosphonates, phosphoanhydrides and orthophosphate monoesters/diesters (Cade-Menun, 2005; Turner, 2008; Missong et al., 2016). Among them, inositol phosphates are the more dominant P_o compounds (Oniani et al., 1973; Turner et al., 2002; Gerke, 2015; Anderson, 2015) which account for an average of 17% (range of 3–52%) of the total P_o (Caldwell and Black, 1958). The phosphates generally exhibit an overall negative charge, especially in acidic to neutral pH and therefore, get adsorbed onto positively charged surfaces. In acidic soils, phosphates often form Fe- and Al-phosphate colloids, whereas in alkaline soils, they form Ca-phosphates (Brady, 2017; Penn and Camberato, 2019). Most soils, especially forest soils are acidic with typical pH in the range of 3–6. Therefore, studying phosphates interaction with Fe- and Al-(oxyhydr)oxides is crucial to control P leaching. Major forces that influence phosphates' interaction with these minerals include 1) physical forces, 2) chemical forces, 3) hydrogen bonding, 4) hydrophobic bonding, 5) electrostatic bonding, 6) coordination reactions and 7) ligand exchange (Tan, 2011). Molecular level analysis would provide a detailed understanding of these interactions and therefore, the mineral-phosphate-water complexes are studied using molecular simulation methods here.

1.4 Molecular Simulations of Geochemical Systems

With increasing computational power and resources, molecular level simulations are becoming essential tools to understand the physical and chemical behavior of complex geochemical systems (Kubicki, 2016). As early as 1973, Tossell et al. studied the electronic structure and bonding in iron oxide minerals with molecular simulations and validated this approach with experimental studies. By the 1980s, computational methods are considered valuable tools for studying Geochemical systems. The review by Mulla (1987) proposes the importance of molecular and theoretical models and highlights the then-popular simulation techniques used to study water–water and surface–water models. Leherste et al. (1991) presented detailed analyses of water’s translational and rotational properties to characterize their behavior inside the ferrierite channels using molecular simulations. Kwon and Kubicki (2004) used molecular simulations to resolve controversies in experimental studies related to phosphate surface complexes on iron hydroxides. They correlated different phosphate motifs with goethite to pH and suggested that binding motifs change with pH.

Analysis of experimental spectra in the light of simulation data provided a more comprehensive picture of the intermolecular interactions. Review by Gaigeot (2010) showed why molecular simulations are mandatory for a precise understanding of experimental spectra. The infrared investigation and theoretical calculations of Guan et al. (2006) to study IHP adsorption onto aluminum hydroxide showed that IHP binds to the surface through two phosphate groups. Kubicki et al. (2012) demonstrated that phosphate interaction with goethite involves various surface complexes in multiple configurations, which explained the difficulties one faces when interpreting, e.g., IR spectra. Huang et al.’s (2014) study on alumina–water interface provided molecular level interpretation of these systems’ structural properties and infrared spectra. Ahmed et al. (2018a) explored the possible binding mechanisms for glyphosate (GLP) with three goethite surface planes (010, 001, and 100) in the presence of water via *ab initio* molecular dynamics simulations. The results showed the prominence of water in controlling the goethite–GLP–water interactions. Further, Ahmed et al. (2019) investigated the molecular level mechanism of phosphate binding at the goethite–water interface referring to the possible phosphate binding motifs formed at the modeled goethite surface planes. Moreover, the latter study’s theoretical IR spectra assignment introduced a benchmark for characterizing experimental IR data for the distribution of adsorbed phosphate species. Kubicki and Watts’s (2019) review present methods to calculate vibrational spectra of materials like clay and silicates using simulation methods. This incomplete list already indicates the vast potential of computational chemistry as a powerful emerging tool for detailed investigations of complex geochemical reactions, especially P species’ reaction mechanisms in soil. In this context, molecular level simulations are selected in this thesis to study mineral–phosphate interactions in the presence of water. An overview of simulation methods and the theoretical background of the simulations used in this thesis is

given in Chapter 2.

1.5 Thesis Objective

This thesis aims to perform molecular level simulations of phosphate interaction at the mineral–water interface and analyze factors that influence these interactions. To achieve this goal, the most common phosphates and mineral surfaces are considered for the study. As discussed in Section 1.3, orthophosphate (OP) and inositol phosphates are the most common P_i and P_o phosphates in nature, respectively. Moreover, among all inositol phosphates, myo-inositol hexaphosphate (IHP) is the most prevalent form in soil (Cosgrove and Irving, 1980; Turner et al., 2002). In addition, glycerolphosphate (GP) is also one of the abundant P in soil (Pant et al., 1999; Doolette et al., 2009; Vincent et al., 2013; Missong et al., 2016). Since OP shows strong interaction with most soil minerals, it was studied extensively (Chitrakar et al., 2006; Torrent et al., 1992; Parfitt and Atkinson, 1976) and hence this study mainly focuses on IHP and GP interaction at the mineral–water interface.

The most common soils are acidic and the pH is in the range of 3–6. In this range, the Fe- and Al-(oxyhydr)oxides are the common and dominant P fixing minerals (Tsao et al., 2011; Tan, 2011; Brady, 2017). Most frequently found iron hydroxide minerals in soils are goethite (α -FeOOH), lepidocrocite (γ -FeOOH), hematite (α -Fe₂O₃), maghemite (γ -Fe₂O₃) and ferrihydrite (Fe₅HO₈.4H₂O) (Tan, 2011). Named after famous German poet *Johann Wolfgang von Goethe*, goethite is one of the most abundant reactive iron oxides with Fe⁺³ oxidation state and has high stability at ambient temperatures. It is also known to exhibit strong interaction with phosphates (Cornell and Schwertmann, 2003). Regarding aluminum hydroxides, the most commonly found oxide is gibbsite (Al(OH)₃), whereas diasporite (α -AlOOH) and boehmite (γ -AlOOH) are less common hydroxides. In addition to pure Fe/Al hydroxides, isomorphous Fe/Al hydroxide mixtures also exist in soil due to frequent isomorphic substitution of Al and Mn with Fe. In this context, the current study focuses on goethite and diasporite mineral's interaction with phosphates IHP and GP. Goethite is selected for its abundance and stability. Diasporite is selected as it is isomorphous with goethite and by analyzing diasporite–P complexes additional insight into P interaction with amorphous Fe/Al hydroxide mixtures could be achieved. Cation substitution is a widespread phenomenon observed for goethite in soil, especially Al atom substitution with Fe (Cornell and Schwertmann, 2003; Bazilevskaya et al., 2011; Li et al., 2016)

In summary, the current study focuses on goethite/diasporite–IHP/GP complexes in the presence of water. This thesis aims to model and simulate goethite/diasporite–IHP/GP complexes at the molecular level using ab initio molecular dynamics (AIMD) simu-

lations. The post-processing analysis scheme involves a systematic understanding of binding motifs, proton transfer events, inter- and intramolecular hydrogen bonds (HB), interaction energies, effects of mineral surface saturation and competition between water and IHP/GP adsorption onto goethite and diaspora mineral surfaces. The current thesis is divided into four chapters. Followed by this introduction, which outlined P in soil, projected peak P scenario and molecular simulations in geochemical systems, the subsequent chapters are:

Chapter 2 outlines the theoretical concepts involved in AIMD simulations and their implementation in CP2K (2017) software.

Chapter 3 discusses the modeling approach behind goethite/diaspora-IHP/GP-water complexes, binding motifs and theoretical concepts to analyze HBs and interaction energies.

Chapter 4 provides overall summary of thesis work.

Chapter 5 focuses on general conclusions based on results.

Appendix A includes accepted and archived manuscripts from this thesis and their summary.

2 Theoretical Background

This chapter provides the theoretical concepts behind molecular level simulations in the present thesis. The phosphate interaction at the mineral–water interface is a dynamic process influenced by multiple physical and chemical factors. These interactions are studied here at the atomic level using molecular dynamics (MD) simulation technique. The MD simulations mimic the atom’s thermal motion and enable us to visualize the sequence of events happening under given conditions. It also provides us options to calculate the time averaged properties that reflect the system’s state. One of the bottlenecks to reaching a higher spatiotemporal scale for an MD simulation is the level of theory adopted, i.e., the method used to describe the forces between the atoms. The most common molecular simulation methods relevant to the current study are quantum mechanical (QM), molecular mechanical (MM) and hybrid quantum mechanical/molecular mechanical (QM/MM) methods. When sorted based on an accurate description of interatomic interactions, the QM level of theory is at the top of the hierarchy, followed by QM/MM and MM. The hybrid QM/MM method combines both QM and MM theories and provides a framework to retain accuracy at a reduced computational cost.

An overview of the simulation methods is provided in Section 2.1, which outlines their hierarchy, advantages and disadvantages, and corresponding spatiotemporal scales. Section 2.2 focuses on MM theoretical concepts involved in calculating the system’s energy and its limitations. In Section 2.3, different *ab initio* methods and their corresponding mathematical formulations for inter– and intramolecular interactions are provided. First, a short overview of the Schrödinger equation and associated bottlenecks to solve it numerically is presented, followed by Hartree and Hartree–Fock approximations. Next, the theory behind Density Functional Theory (DFT) and its implementation using a hybrid basis as in CP2K software (CP2K, 2017; Kühne et al., 2020) is discussed. In Section 2.4 an overview of the hybrid QM/MM methods is given, highlighting the electrostatic embedding method which is used here. In the final Section 2.5, the concepts involved in MD simulations and their corresponding equations of motion are presented briefly. Note that theoretical models are not developed in this study but rather only used to study P interaction with soil minerals. Most of the theoretical concepts presented here could be found in elaborate form in textbooks: Cramer (2004), K I et al. (2008), Marx and Hutter (2009) and Kubicki (2016).

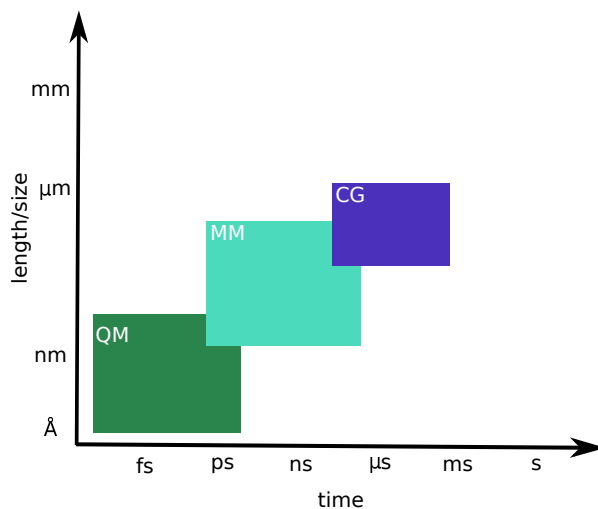


Figure 2.1: Simulation methods and their corresponding spatiotemporal scales. Note that the ranges mentioned here are approximate values. Adopted from Ozboyaci et al. (2016).

2.1 Molecular Simulation Methods Overview

In QM methods, the nuclei and electrons are defined explicitly and the Schrödinger equation is solved to obtain the system’s molecular description. However, solving the Schrödinger equation for a multiatomic and multielectronic system is computationally expensive and time consuming. Therefore, MD simulations performed at the QM level have shorter spatiotemporal ranges than MM methods, as shown in Fig. 2.1. Nevertheless, the main advantage of QM methods is that one could simulate the bond breaking/-formation and the charge transfer events (Marx and Hutter, 2009). Density functional theory (DFT) is a prominent QM method that provides a reasonable trade between accuracy and computational cost. It is used extensively for large systems and often to simulate geochemical models (Kubicki, 2016). The main limitation of DFT is that it is computationally expensive for systems with more than 1000 atoms.

The MM methods, also called force field (FF) methods, are computationally inexpensive compared to QM methods. Here, the system specific atomic parameters are derived based on macroscopic properties obtained experimentally or from QM methods. The atoms are considered as point charges and the bonded and non bonded interactions are defined using simple mathematical functional forms (empirical potentials) (González, M.A., 2011). Comparatively, this method could reach higher spatiotemporal scales than QM methods, see Fig. 2.1. The limitation with most MM methods is that bond breaking/forming and charge transfer events between atoms could not be simulated. Also, the FF parameters must be reparameterized if a new component is added to the simulation model. A more abstract form of the MM method is the coarse grain (CG) method (not

used in the current study). Here, a set of atoms or molecules are grouped into a single interaction functional group (bead), significantly reducing particle numbers and computational cost.

Most geochemical models are complex systems comprising multiple soil components with more than 1000 atoms (Kubicki, 2016). The MM methods could be used to simulate these systems, but if bond breaking/forming is to be observed in the reactive region, the MM methods cannot be adopted. Some FF exists that define bond breaking/forming, but these are computationally expensive, complex to adopt, and available only for limited molecular systems. Unfortunately, considering QM methods would be computationally expensive, given the system size. However, hybrid QM/MM methods allow us to define the reactive region specifically as QM and the remaining part as MM (Senn and Thiel, 2009). Hence, by adopting the QM/MM method, the simulation of large systems is made possible with limited computational resources without compromising the reactive regions' accuracy. This method enables us to reach higher temporal scales for a system compared to pure QM methods. Therefore, the hybrid QM/MM method is employed to perform simulations in the current work.

2.2 Molecular Mechanics

2.2.1 Theoretical Description of Common Force Fields

The FF is a mathematical expression representing the system energy based on the atom's coordinates. The parameters involved in the mathematical expression are derived from QM methods or semi-empirical calculations or experimental studies to reproduce desired system properties. Different variants of FF implementations use different mathematical expressions to define the potential functions (González, M.A., 2011). For instance, polarizable FF (Baker, 2015) and ReaxFF (Senftle et al., 2016) include complex mathematical expressions to define the polarization of atoms and bond making/breaking between atoms, respectively. Nevertheless, developing a complex FF is a rigorous and time consuming process and hence these FF are not commonly available and not often used in studies. A typical expression of a common FF includes components as shown below:

$$E_{\text{system}} = E_{\text{bonded}} + E_{\text{nonbonded}} \quad (2.1)$$

$$E_{\text{bonded}} = E_{\text{bond}} + E_{\text{angle}} + E_{\text{dihedral}} \quad (2.2)$$

$$E_{\text{nonbonded}} = E_{\text{vdW}} + E_{\text{coulomb}} \quad (2.3)$$

The total energy of the system (E_{system}) contains both bonded (E_{bonded}) and nonbonded ($E_{\text{nonbonded}}$) contributions. The bonded part is about intramolecular or local contribu-

tions like bond stretching (E_{bond}), angle bending (E_{angle}) and torsional term (E_{dihedral}) whereas the noncovalent part includes short range van der Waals (vdW) (E_{vdW}) and long range electrostatic interactions (E_{coulomb}).

For instance, in CHARMMFF (Brooks et al., 1983; MacKerell et al., 1998), the bond stretching energy between two bonded atoms i and j is defined as:

$$E_{\text{bond}} = \sum k_b (r_{ij} - r_0)^2 \quad (2.4)$$

where, k_b is the force constant and r_{ij} , r_0 denotes distance between i, j atoms and equilibrium bond length, respectively. The r_0 and k_b values could be estimated from X-ray diffraction experiments and infrared or Raman spectra, respectively (González, M.A., 2011). Similarly, the energy of the angle bend is:

$$E_{\text{angle}} = \sum k_\theta (\theta_{ijk} - \theta_0)^2 \quad (2.5)$$

where, k_θ denotes a force constant, θ_{ijk} is bond angle between i, j and k atoms and θ_0 is equilibrium bond angle. The torsional movements are essential in enforcing the right degree of rigidity in the molecule to reproduce major conformational changes. The dihedral or torsional term is defined as:

$$E_{\text{dihedral}} = \sum k_\phi [1 + \cos(n\phi - \delta)] \quad (2.6)$$

where k_ϕ is the dihedral force constant, ϕ and δ are the torsional angle and phase shift, respectively and n is total maxima or minima in the range of $0-2\pi$. The torsional and angle parameters are mostly obtained from QM methods and then corrected based on experimental data such as molecular geometry or vibrational spectra. The vdW interaction energy between particles i and j separated by distance r_{ij} is given as:

$$E_{\text{vdW}} = \sum_{\substack{i,j \\ i \neq j}} \epsilon_{ij} \left[\left(\frac{\sigma_{ij}}{r_{ij}} \right)^{12} - 2 \left(\frac{\sigma_{ij}}{r_{ij}} \right)^6 \right] \quad (2.7)$$

where, ϵ_{ij} and σ_{ij} are empirical parameters. The terms ϵ_{ij} and σ_{ij} denote the depth of the potential well and the distance at which the inter-particle potential is zero. Most FF provides individual atomic parameters (i.e., ϵ_i and σ_i) and the parameters for the unlike atoms could be obtained as $\sigma_{ij} = \frac{1}{2}(\sigma_i + \sigma_j)$ and $\epsilon_{ij} = \sqrt{\epsilon_i \epsilon_j}$. The long range coulomb interaction energy between atoms is given by:

$$E_{\text{coulomb}} = \sum_{\substack{i,j \\ i \neq j}} e^2 \frac{q_i q_j}{4\pi \epsilon_0 r_{ij}} \quad (2.8)$$

where, q_i, q_j denote partial charges, e denotes electron charge and ϵ_0 is the dielectric

permittivity of vacuum. The parameters involved in vdW and electrostatic interactions are calculated mostly from QM calculations.

To implement these potentials, a fixed topology connection should be predefined for a system, i.e., the bonds, angles and dihedrals between atoms should be predefined in a connection file. These connections are not expected to change with time in simulations. Based on the definitions in the topology file, the nonbonded interactions are set up. Most FF implements nonbonded interactions between atoms that are only separated by more than two or three bonds (i.e., $> 1-3$ or $> 1-4$) and excludes atoms that are 1-2 and 1-3 bonded.

Force fields: Applications in geochemical systems

As discussed in Section. 2.1, molecular mechanics methods are computationally inexpensive, and therefore, employing them would be cost-effective for large geochemical systems. Nevertheless, developing FF for a complex geochemical system is complicated and requires tremendous resources. Despite the complications, molecular mechanics methods have been used significantly for the past two decades to study geochemical systems. For instance, Pavese et al. (1996) studied the effect of temperature on the calcite's elastic constants and structural features. They showed that the simulated thermal coefficients matched well with experimental values. Teppen et al. (1997) derived FF for quartz, gibbsite, kaolinite, and pyrophyllite and the MD simulations of these minerals reproduced structural parameters within 1% of experimentally observed values. In addition to mineral characteristics, mineral-interface interactions are also studied extensively. For instance, Kerisit and Parker (2004) performed MD simulations of calcite-water interface to calculate free energies of water adsorption on the mineral surface to address water ad/desorption rates. Chicot et al.'s (2011) study successfully compared the mechanical properties of pure and complex (corrosion products) iron oxides, magnetite, hematite and goethite computed using molecular dynamics with experiments. Further, complex ReaxFF are also used to study mineral interaction with surface water. Gale et al. (2011) derived ReaxFF for calcium carbonate-water system and reached longer time scales than QM methods. However, the derived FF parameters are often system-specific (Lii and Allinger, 1991; Hwang et al., 2001) and their transferability to other systems is not feasible (Kubicki, 2016). For instance, in the current study where mineral-phosphate-water complexes are of interest, FFs compatible for studying all mutual interactions are not readily available.

Interestingly, FFs for organic and biological molecules have been derived extensively for the past few decades. Popular FFs like CHARMMFF (Vanommeslaeghe et al., 2010), AMBERFF (Wang et al., 2004b) and OPLS (Jorgensen et al., 1996) provide all-atomic general FFs in addition to system-specific ones. This allows one to include new molecules into the system without reparameterizing the FFs. However, an all-atomic general FF is

not available for minerals yet and efforts are in progress to provide a general framework to simulate mineral–organic/biological–water complexes (Kubicki, 2016). CLAYFF (Cygan et al., 2004) and INTERFACEFF (Heinz et al., 2013) FFs are perhaps the only FFs that provide parameters for a wide range of minerals. These FFs are also compatible with the most common water FFs. Hence, they are employed extensively for studies related to mineral–water interfaces. The mutual interactions between atoms are defined using harmonic bond stretching, angle bending, coulombic and Lennard Jones interactions (as discussed in Section. 2.2.1).

For the current study, we adopted CLAYFF, which are developed specifically for clay minerals. These FFs are compatible with flexible and popular single point charge (SPC) (Berendsen et al., 1981) based water FFs. Therefore, they are significantly used to study mineral–water interface interactions. They efficiently simulate different matter phases as most interatomic bonds, like metal–oxygen bonds, are defined only with Lennard Jones and coulombic terms (Cygan et al., 2004). The partial atom charges are assigned based on a combination of Mulliken (Mulliken, 1955) and electrostatic population analysis (Chirlian and Francl, 1987; Breneman and Wiberg, 1990) of DFT results. Further, they are validated extensively by comparing the simulated bulk structures, relaxed surface structures, and intercalation processes to experimental and spectroscopic findings (Cygan et al., 2004). The application of these FFs could also be found extensively in the literature. For instance, Wang et al. (2004a) applied CLAYFF to perform MD simulations of brucite–water interface and found a strong HB network formed with surface atoms acting as HB acceptors and donors. Similarly, Kalinichev et al. (2007) studied the tobermorite–water interface and found strong water structuring above the surface because of the integrated HB network between water and surface active sites. The diffusion coefficients from simulations for the surface–associated water agree with the published experimental results. Vasconcelos et al. (2007) studied the adsorption of various ions onto the basal surface of kaolinite and compared their adsorption behavior. Therefore, the CLAYFF are reliable and efficient FFs to simulate clay minerals containing geochemical systems.

Regarding the goethite surface studied here, the goethite–water interface interactions were also studied successfully using CLAYFF. Boily (2012) studied water structure and hydrogen bonding at different surface planes of goethite. Song and Boily (2013) highlighted the importance of goethite–water vapor interactions and salt effect on these interactions. Criscenti et al. (2018) studied different types of aqueous solutions interacting with different surface planes of goethite. They suggested that a single goethite surface plane adsorption properties cannot be used to represent all goethite interfaces present in soils and sediments. The above list of studies shows successful applications of CLAYFF. An important caution while using the CLAYFF is regarding the topology file generation that contains connection data of atoms in the simulation box. Since the metal–oxygen interactions are defined using the nonbonded formulation, these bonds

should be excluded from the connection file.

2.3 Quantum Mechanics

2.3.1 Schrödinger Equation and Variational Principle

The stationary properties of matter composed of interacting nuclei and electrons are determined by the stationary Schrödinger equation:

$$\hat{H} \Psi(\mathbf{r}, \mathbf{R}) = E \Psi(\mathbf{r}, \mathbf{R}) \quad (2.9)$$

where \hat{H} is the hamiltonian operator, $\Psi(\mathbf{r}, \mathbf{R})$ is the time independent wave function with electron (\mathbf{r}) and nuclei (\mathbf{R}) coordinates as variables and E is the energy of the system. The electrons and nuclei possess kinetic and potential energy depending on the inter- and intra-atomic interactions. The corresponding kinetic (\hat{T}) and potential (\hat{V}) energy operators are defined in the hamiltonian as $\hat{H} = \hat{T} + \hat{V}$. The total hamiltonian is given as:

$$\begin{aligned} \hat{H} = & - \sum_I \frac{\hbar^2}{2M_I} \nabla_{\mathbf{R}_I}^2 - \sum_i \frac{\hbar^2}{2m_i} \nabla_{\mathbf{r}_i}^2 \\ & + \frac{1}{4\pi\epsilon_0} \sum_{\substack{i,j \\ i \neq j}} \frac{e^2}{|\mathbf{r}_i - \mathbf{r}_j|} - \frac{1}{4\pi\epsilon_0} \sum_{I,i} \frac{e^2 Z_I}{|\mathbf{R}_I - \mathbf{r}_i|} + \frac{1}{4\pi\epsilon_0} \sum_{\substack{I,J \\ I \neq J}} \frac{e^2 Z_I Z_J}{|\mathbf{R}_I - \mathbf{R}_J|} \end{aligned} \quad (2.10)$$

The first two terms in the above equation are part of kinetic energy operator \hat{T} and represent nuclei and electronic kinetic energies, respectively. The remaining terms constitute the potential operator \hat{V} and represent electron–electron, electron–nuclei, nuclei–nuclei attraction/repulsion interactions, respectively. The symbols m_i and M_I , $\nabla_{\mathbf{r}_i}^2$ and $\nabla_{\mathbf{R}_I}^2$, \mathbf{r}_i and \mathbf{R}_I are the mass, laplacian operators and coordinates of the i^{th} electron and I^{th} nuclei, respectively. Note that the Schrödinger equation is dependent on both electronic (\mathbf{r}_i) and nuclei (\mathbf{R}_I) degrees of freedom, which consequently increases the computational cost substantially with system size. For instance, consider a system of size $N + n$ (nuclei plus electrons), the computational workload for 1D mesh with 10 points is around $\approx 10^{N+n}$. This increases the storage requirement exponentially and substantially challenges the computational power, which is also called a curse of dimensionality. Therefore, solving the Schrödinger equation numerically for multiatomic and multielectronic systems is a computationally impossible task even with the current state-of-the-art resources.

2.3.2 Approximations

A list of theoretical approximations is adopted to reduce the complexity of solving the Schrödinger equation. One such major approximation is the Born–Oppenheimer approximation, which provides a theoretical framework to decouple electronic and nuclei motion.

Born–Oppenheimer approximation

The proton and neutron’s cumulative mass is ≈ 2000 times larger than that of the electron. Therefore, the electrons can respond instantaneously to the changes in the positions of the nuclei. Numerically, this provides an opportunity to decouple the electron and nuclei motion and consider that the electrons are moving in the field of clamped nuclei. Based on this approximation, the wavefunction could be decoupled into two parts, i.e., a separate wavefunction for electrons (Ψ_{el}) and nuclei (Ψ_{nuc}) as:

$$\Psi(\mathbf{r}, \mathbf{R}) = \Psi_{\text{el}}(\mathbf{r}; \mathbf{R})\Psi_{\text{nuc}}(\mathbf{R}) \quad (2.11)$$

Here the electronic coordinates \mathbf{r} are independent variables while the nuclei coordinates \mathbf{R} are parameters. This decoupling reduces the system’s computational cost as the nuclei coordinates are no longer the variables but parameters of the hamiltonian. The electronic hamiltonian operator ($\hat{H}_{\text{el}}[\mathbf{R}]$) is given as:

$$\hat{H}_{\text{el}} = -\sum_i \frac{\hbar^2}{2m_i} \nabla_i^2 + \frac{1}{4\pi\epsilon_0} \sum_{i<j} \frac{e^2}{|\mathbf{r}_i - \mathbf{r}_j|} - \frac{1}{4\pi\epsilon_0} \sum_{I,i} \frac{e^2 Z_I}{|\mathbf{R}_I - \mathbf{r}_i|} \quad (2.12)$$

and the Schrödinger equation with Born–Oppenheimer approximation is given as:

$$\hat{H}_{\text{el}} \Psi_{\text{el}}(\mathbf{r}; \mathbf{R}) = E_{\text{el}} \Psi_{\text{el}}(\mathbf{r}; \mathbf{R}) \quad (2.13)$$

By applying this approximation, the dynamics between nuclei and electrons are decoupled. Consequently, the computational expense to calculate the nuclear–electron and nuclear–nuclear correlation interactions became relatively cheaper as the nuclei coordinates are fixed. For instance, nuclear–nuclear electrostatic repulsion energy is constant for fixed nuclei and could be calculated analytically. Nevertheless, this approximation reduces the Schrödinger equation’s complexity only slightly as the computationally expensive electron–electron interactions still exist in the electronic hamiltonian.

Hartree and Hartree–Fock methods

In addition to the Born–Oppenheimer approximation, independent particle approximation is another vital approximation in building a practical and numerically solvable wavefunction. Here, the electrons are considered noninteracting independent particles in different orbitals. Hartree was one of the first to introduce the idea of independent

particle approximation in 1927, also called Hartree approximation. In this approximation, the many electron wavefunction is built as the product of individual electron wave functions, also known as the Hartree product:

$$\Psi_{\text{HP}} = \psi_1(\mathbf{r}_1)\psi_2(\mathbf{r}_2)\psi_3(\mathbf{r}_3) \cdots \psi_n(\mathbf{r}_n). \quad (2.14)$$

The Hartree method adopts the many body wavefunction as in Eq. 2.14 to solve the Schrödinger equation for an independent one-electron system. The terms in the one-electron Hamiltonian are electronic kinetic energy, nuclear-electron and electron-electron potential energy, as shown below:

$$\hat{h}_i = -\frac{\hbar^2}{2m_i}\nabla_i^2 - \frac{1}{4\pi\epsilon_0}\sum_{I=1}^N \frac{e^2 Z_I}{|\mathbf{r} - \mathbf{R}_I|} + \frac{1}{4\pi\epsilon_0} \int e \frac{[\rho(\mathbf{r}')] }{|\mathbf{r} - \mathbf{r}'|} d\mathbf{r}' \quad (2.15)$$

The last term in the above equation denotes electron-electron interaction, also known as Hartree potential, where $\rho(\mathbf{r}) = \sum_i |\psi(\mathbf{r})|^2$. Here, the electron-electron interaction is approximated as the interaction potential between the electron at position \mathbf{r} and the mean field from all the electrons. This approximation is called mean field approximation. Even though, Hartree approximation reduced the computational cost of electron-electron interactions, the hamiltonian here does not consider the indistinguishable nature of electrons and the spin and antisymmetric properties (Paulis exclusion principle) of electrons. This is because the Hartree product wavefunction does not incorporate these properties into the wavefunction. The Hartree-Fock method addresses this issue by adopting a wavefunction that defines the missing electronic properties in the Hartree product wavefunction.

The Hartree Fock method is a modification to the Hartree method to include antisymmetric properties into wavefunction, which leads to exchange interaction. The electrons are fermions; therefore, the wavefunction should be antisymmetric and change sign when any pair of coordinates exchange. The electronic wavefunction built using Slater determinants incorporates the above mentioned properties of the electrons into the wavefunction. Therefore, the Hartree product wavefunction in Eq. 2.14 is replaced with Slater determinant wavefunction. The additional exchange term includes the spin properties of the electrons into the hamiltonian and it is non-zero only for the parallel spin electrons and zero otherwise. This also includes correcting the self-interaction between the electrons observed in Hartree potential. One computational bottleneck for the Hartree-Fock method is that it is expensive to calculate the expectation value of the exchange term as it includes sixfold integrals for a pairwise combination of parallel spin electrons. Another limitation of this method is that the instantaneous correlation between the electrons is not included in the wavefunction, which increases the overall electronic energy of the system.

2.3.3 Basis Sets

Basis sets are the building blocks of mathematical functions that describe the system orbitals used for theoretical calculations. A molecular spatial orbital electron wavefunction $[\Psi(\mathbf{r}_i)]$ is expressed in terms of the individual one-electron atomic orbitals (ψ_n) by the concept of a linear combination of atomic orbitals (LCAO) as shown below:

$$\Psi = c_1\psi_1 + c_2\psi_2 + c_3\psi_3 + \cdots + c_n\psi_n \quad (2.16)$$

where c_n denotes molecular orbital coefficient expansion of n^{th} electron which is normally varied during SCF calculations. John. C. Slater is the first to introduce orbital computing using basis sets known as Slater type orbitals (STOs). A typical mathematical expression of an STO as a one-electron orbital is:

$$\psi(\mathbf{r}) = N \mathbf{r}^{n-1} e^{-\alpha \mathbf{r}} \quad (2.17)$$

Here N is the normalization constant and n is an integer in lines with the principal quantum number. Even though the STOs are more accurate, it takes a long time to compute integrals using them as they cannot solve common integrals in quantum calculations analytically. Therefore, another approach is to use a linear combination of Gaussian type functions as basis functions to mimic STOs. The Gaussian type orbitals (GTOs) support calculating common integrals in quantum calculations analytically, which reduces the computational cost. It is essential to use multiple Gaussian functions as a single Gaussian function, i.e., a primitive Gaussian function is not sufficient to accurately describe the electron orbital like STOs, especially the cusps around the nuclei. Therefore, a fixed linear combination of primitive Gaussian functions, called contracted Gaussians, is used to approximate STOs to represent the orbitals better. For instance, STO in terms of a contracted Gaussian with contraction coefficients $c_{i,j}$ and Gaussian function $g_i(\mathbf{r})$ is given as:

$$\psi_j(\mathbf{r}) = \sum_i c_{i,j} g_i(\mathbf{r}) \quad (2.18)$$

A systematic combination of these contracted Gaussian functions would provide the system's wavefunction $\Psi(\mathbf{r})$ for a multiatomic system. There are different types of contracted basis sets, and the basic type is called minimal basis sets and is generally denoted as STO- n G, where n denotes the number of GTOs fitted to mimic one STO. The split-valance basis is an improvement over the minimal basis where the valance orbitals are represented with two basis functions (inner-shell orbitals only one basis) to obtain a more reliable total wavefunction. For instance, in the 6-31G basis set, the inner-shell orbital is defined with six-primitive contracted Gaussians and the valance orbital is described by two orbitals, one made of a contraction of 3 Gaussians and one a single Gaussian function. The splitting of the basis here is to incorporate diffusioness into the valance electron description to obtain a better wavefunction. Nevertheless, the basis is spherical symmetric with atom position and needs to be more flexible to describe complex bond

formations. In the Polarized basis sets, p , d , f type basis functions are added to the s , p and d type orbitals to describe the distortion in the s , p and d type orbitals while forming molecular bonds. For instance, 6-31G(d) denotes that d type functions are added to the basis set of all p orbitals and 6-31G(p,d) denotes p and d functions added to s and p orbitals respectively. The Polarized basis set significantly improves the bond length and bond angles and the corresponding overall energy of a molecule. A basis set that incorporates split valance and polarization description is commonly denoted as DZP (double zeta plus polarization) or TZP (triple zeta plus polarization) and so on, depending on the number of splits adopted for the basis function. To further improve the basis set's reliability, highly diffusive functions are added, generally denoted by a plus "+" sign, for example, 6-31+G(p,d). In general, the diffusive functions are Gaussians with small exponents that would improve the electron's description and flexibility far from the nucleus. These diffuse functions are vital, especially for anions to describe the valance electrons and also for highly electronegative atoms with high electron density, like fluorine, and also for accurate polarizabilities or binding energies of vdW complexes

Both STOs and GTOs are atom centered and localized basis sets. These basis sets are suitable for systems where the electron density is confined to the space centered around the atom. However, the valance electrons roam freely for metallic systems and are not localized. The plane wave basis is suitable for these systems and a single plane wave is defined as:

$$\psi(\mathbf{r}) = e^{i\mathbf{G}\mathbf{r}} \quad (2.19)$$

where \mathbf{G} is a reciprocal lattice vector. A linear combination of plane waves could be used to describe a fairly localized state:

$$\Psi(\mathbf{r}) = \sum_{\mathbf{G}=0}^{\mathbf{G}=\text{cutoff}} e^{i\mathbf{G}\mathbf{r}} \quad (2.20)$$

Nevertheless, describing core electrons requires many plane waves, which increases the computational cost. To overcome this, the core electrons are commonly replaced by Pseudopotentials. The pseudopotentials are often used in quantum calculations to integrate out the highly localized core electrons to reduce computational costs. The core electrons do not contribute much to the physical and chemical properties; hence, only the valance electrons that take part in bond breaking and formation are defined explicitly.

2.3.4 DFT and GPW method

Both Hartree and Hartree-Fock methods do not provide a mathematical framework that describes all electron interactions. Therefore, there is a need to frame an exact method that includes all interactions mathematically while keeping the effective single electron form of the Schrödinger equation. In this context, Hohenberg and Kohn (1964) introduced a landmark paper that states that there is a universal functional of the

electron density, which corresponds to the ground state energy of a system associated with an external potential. This is the basic theoretical idea behind most of the current modern DFT programs. The first Hohenberg–Kohn theorem states that the external potential is a unique functional of the electron density $\rho(\mathbf{r})$. The electron density $\rho(\mathbf{r})$ of n electrons is given as:

$$\rho(\mathbf{r}) = n \int \cdots \int |\Psi(\mathbf{r}_1, \mathbf{r}_2, \cdots, \mathbf{r}_n)|^2 d\mathbf{s}_1 d\mathbf{r}_2 \cdots d\mathbf{r}_n \quad (2.21)$$

where s denotes the spin of the electron. The second Hohenberg–Kohn theorem states that the energy of a system with trial density $\rho_{trial}(\mathbf{r})$ holds:

$$E[\rho_{trial}(\mathbf{r})] \geq E_0 \quad (2.22)$$

where E_0 denotes the ground state energy of the system and the $E[\rho_{trial}(\mathbf{r})]$ denotes energy calculated using trial electron density. This suggests that systematically improving trial electron density would allow us to reach a system's exact ground state density. Therefore, the variational principle approach could be used to fine-tune the electron density to reach the system's ground state. Unfortunately, the Hohenberg–Kohn theorems do not provide any framework to construct the functional $E[\rho_{trial}(\mathbf{r})]$ that could provide the ground state energy. After a year, Kohn and Sham (1965) introduced a framework to build the energy functional, which could also be solved numerically. The Kohn–Sham energy expression is given as:

$$\begin{aligned} E[\rho(\mathbf{r})] &= E^T[\chi(\mathbf{r})] + E^{ne}[\rho(\mathbf{r})] + E^{ee}[\rho(\mathbf{r})] + E^{nn} + \Delta E^T[\rho(\mathbf{r})] + \Delta E^{ee}[\rho(\mathbf{r})] \\ &= -\frac{\hbar^2}{2m_i} \sum_{i=1}^n \int \chi_i(\mathbf{r}) \nabla^2 \chi_i(\mathbf{r}) d\mathbf{r} - \frac{1}{4\pi\epsilon_0} \sum_{I=1}^N \int \frac{e Z_I \rho(\mathbf{r})}{|\mathbf{r} - \mathbf{R}_I|} d\mathbf{r} \\ &\quad + \frac{1}{4\pi\epsilon_0} \int \int \frac{\rho(\mathbf{r})\rho(\mathbf{r}')}{|\mathbf{r} - \mathbf{r}'|} d\mathbf{r} d\mathbf{r}' + \frac{1}{4\pi\epsilon_0} \sum_{\substack{I,J \\ I \neq J}}^N \frac{e^2 Z_I Z_J}{|\mathbf{R}_I - \mathbf{R}_J|} + E^{xc}(\rho(\mathbf{r})) \end{aligned} \quad (2.23)$$

where $E^T[\chi(\mathbf{r})]$ is the kinetic energy of the non-interacting electrons, $E^{ne}[\rho(\mathbf{r})]$ is the nuclear–electron interaction, $E^{ee}[\rho(\mathbf{r})]$ is the electron–electron interaction, E^{nn} is the nucleus–nucleus interaction, $\Delta E^T[\rho(\mathbf{r})]$ is the correction to the electron kinetic energy as the electrons interact in real systems, $\Delta E^{ee}[\rho(\mathbf{r})]$ is the non-classical corrections to the electron–electron interactions. The last two terms are corrections which are collectively referred as $E^{xc}[\rho(\mathbf{r})]$, exchange–correlation energy.

By applying variational principle to energy E in Eq. 2.23 with respect to the spin orbitals χ and the constrain $\langle \chi_i | \chi_j \rangle = \delta_{ij}$, the one-electron Kohn–Sham equation for the orbital

χ_i is given as:

$$\left(-\frac{\hbar^2}{2m_i} \nabla_i^2 - \frac{1}{4\pi\epsilon_0} \sum_{I=1}^N \frac{eZ_I}{|\mathbf{r} - \mathbf{R}_I|} + \frac{1}{4\pi\epsilon_0} \sum_{\substack{j=1 \\ j \neq i}}^n \int \frac{\rho(\mathbf{r}')}{|\mathbf{r} - \mathbf{r}'|} d\mathbf{r}' + V_{XC} \right) \chi_i = \varepsilon_i \chi_i \quad (2.24)$$

Here the ε_i denotes Kohn–Sham energies of the orbitals and V_{XC} is the functional derivative defined as:

$$V_{XC} = \frac{\delta E^{XC}}{\delta \rho} \quad (2.25)$$

A hierarchy of functionals are available to calculate the exchange–correlation energies based on the homogeneous electron gas distribution. At the bottom of the hierarchy is the local density approximation (LDA) where $E_{LDA}^{XC}[\rho(\mathbf{r})]$ depends on the charge density of the electron position. The LDA is suitable for systems whose electron density does not vary much with space. However, since most systems do not have uniform electron density, this approximation does not yield accurate results. The second rung of the ladder is Generalized gradient approximation (GGA). The GGA accounts for the non-uniform electron density by considering the gradients of the electron density in addition to the electron density at that point, i.e., $E_{GGA}^{XC}[\rho(\mathbf{r}), \nabla\rho(\mathbf{r})]$. The GGAs provide more accurate results compared to LDA at a significantly lesser computational cost. Some of the popular GGAs include PBE (Perdew et al., 1996), BLYP (Becke, 1988). In the current work, PBE functional is used to calculate the DFT energies. Even though arranged hierarchically, selecting the functionals based on the system type is advised.

Since the electron–electron correlation is also included in the hamiltonian with exchange term, the DFT method is considered exact, including all required interactions. Note that the computational cost to calculate the kinetic energy, nucleus–electron interaction energy and electron–electron columbic interaction energy here is similar to Hartree–Fock method. However, the computational cost savings in DFT comes mostly from the calculation of the exchange term using approximations in E^{XC} . The exchange term obtained in DFT is not as accurate as the Hartree–Fock method, but choosing an appropriate exchange–correlation functional could still yield good results. However, the E^{XC} is not known accurately, which limits the accuracy of this method.

Dispersion correction

The DFT method does not include the dispersion interaction between the atoms. These interactions are essential, especially for weakly interacting systems and a variety of schemes are available to include them in DFT. In DFT–D, the dispersion correction energy is added as follows:

$$E_{DFT-D} = E_{DFT} + E_{Disp} \quad (2.26)$$

The most popular dispersion correction schemes are Grimmes DFT-D2 (Grimme, 2006) and DFT-D3 (Grimme et al., 2010). In DFT-D2, the dispersion energy ($E_{\text{Disp}}^{\text{D2}}$) includes pairwise sum of interactions between atom i and j as shown below:

$$E_{\text{Disp}}^{\text{D2}} = -S_6 \sum_{\substack{I,J \\ I \neq J}}^N \sum_L \frac{C_6^{\text{IJ}}}{R_{\text{IJ}}^6} f_{\text{dmp}}^{\text{D2}}(R_{\text{IJ}}) \quad (2.27)$$

Here the summation is over a total number of atoms (N) and also includes atoms in the translations of unit cells in x , y , z directions $L = (l_x, l_y, l_z)$. The term C_6^{IJ} is the dispersion coefficient for atoms I and J separated by distance R_{IJ} . The C_6^{IJ} value is in general pair specific and also depends on the oxidation state and hybridization state of atoms. The pairwise dispersion coefficient for atoms I and J is obtained as geometric mean which is common in classical FF:

$$C_6^{\text{IJ}} = \sqrt{C_6^{\text{I}} C_6^{\text{J}}} \quad (2.28)$$

Note that in periodic systems, the distance R_{IJ} could be between atoms from the same unit cell or between an atom in the reference cell and an atom in the translational image of the reference cell. To minimize this correction between bonded atoms or atoms separated by short distances, a damping function:

$$f_{\text{dmp}}^{\text{D2}}(R_{\text{IJ}}) = \frac{S_6}{1 + e^{-d(R_{\text{IJ}}/R_r - 1)}} \quad (2.29)$$

is used. The term R_r is the sum of the vdW radius of the atom pair and d is usually set to 20 or 23. Nevertheless, DFT-D2 does not include the effects of the chemical environment and to overcome this in DFT-D3, the dispersion coefficient is defined as a function of coordination number. The dispersion coefficient varies depending on the neighbors at each step during the simulation. The dispersion correction for DFT-D3 is defined as:

$$E_{\text{Disp}}^{\text{D3}} = E^{(2)} + E^{(3)} \quad (2.30)$$

where the first term refers to the two body contribution and it is given as:

$$E^{(2)} = \sum_{\substack{I,J \\ I \neq J}}^N \sum_{n=6,8,10,\dots} \sum_L S_n \frac{C_n^{\text{IJ}}}{R_{\text{IJ}}^n} f_{\text{dmp},n}^{\text{D3}}(R_{\text{IJ}}) \quad (2.31)$$

with its corresponding damping function is:

$$f_{\text{dmp},n}^{\text{D3}}(R_{\text{IJ}}) = \frac{1}{1 + 6 (R_{\text{IJ}} / (S_{r,n} R_{0\text{IJ}}))^{-\alpha_n}} \quad (2.32)$$

In Eq. 2.31, the term C_n^{IJ} is the averaged n^{th} order dispersion coefficient defined specifically for atoms I and J separated with internuclear distance of R_{IJ} . The scaling factor S_6 is usually set to one while S_8 is functional dependent. For $n > 10$ this approach becomes unstable; hence, the terms after $n = 8$ are usually truncated. In the damping function Eq. 2.32, the term $R_{0IJ} = \sqrt{C_8^{IJ}/C_6^{IJ}}$ with $\alpha_6 = 12$ and $\alpha_8 = 14$. Here the $S_{r,6}$ is functional dependent and $S_{r,8}$ is equal to one.

The second term in Eq. 2.30 is the three body contribution:

$$E^3 = \frac{C_9^{IJK} (3 \cos \theta_a \cos \theta_b \cos \theta_c + 1)}{(R_{IJ} R_{JK} R_{KI})^3} \quad (2.33)$$

Here the angles θ_a , θ_b and θ_c denote the internal angles of the triangle formed between atoms I , J and K , respectively. The term C_9^{IJK} is triple dipole constant defined as $C_9^{IJK} \approx -\sqrt{C_9^{IJ} C_9^{JK} C_9^{KI}}$. The damping function is same as the one in Eq. 2.32 with $\alpha = 16$ and $S_{r,n}=4/3$ (Grimme et al., 2010). The input to the damping function is equal to the geometrically averaged vdW radii of atoms.

DFT implementation in CP2K

This section discusses the hybrid Gaussian Plane Wave (GPW) method and its implementation in Quickstep code (VandeVondele et al., 2005) for DFT in CP2K. The main idea in the GPW method is to consider two representations of the electron density using Gaussian $[\rho(\mathbf{r})]$ and auxiliary plane wave $[\tilde{\rho}(\mathbf{r})]$ basis sets. The advantage of this approach is that with the efficient treatment of electrostatic interactions, one could obtain linear scaling of computational costs in calculating the total energy with system size. The electron density is initially generated on the Gaussian basis and from there, it is transferred to plane waves on a uniform grid using Fast Fourier Transform (FFT). The electron density representation using Gaussian waves is given as:

$$\rho(\mathbf{r}) = \sum_{ij} P^{ij} \chi_i(\mathbf{r}) \chi_j(\mathbf{r}) \quad (2.34)$$

where P^{ij} and $\chi_i(\mathbf{r})$ are the density matrix element and orbital wavefunction, respectively. The second representation on auxiliary plane waves basis is given as:

$$\tilde{\rho}(\mathbf{r}) = \frac{1}{\Omega} \sum_{\mathbf{G}} \tilde{\rho}(\mathbf{G}) \exp(i\mathbf{G} \cdot \mathbf{r}) \quad (2.35)$$

where Ω is the unit cell volume, \mathbf{G} are the reciprocal lattice vectors and $\tilde{\rho}(\mathbf{G})$ are the expansion coefficients which are chosen such that $\rho(\mathbf{r})$ is close to $\tilde{\rho}(\mathbf{r})$. The difference between the $\rho(\mathbf{r})$ and $\tilde{\rho}(\mathbf{r})$ becomes zero for an infinite plane wave cutoff. However, as it is impractical to consider an infinite cutoff, energy based convergence study is performed

before finalizing the plane wave cutoff.

As discussed in Section. 2.3.3, the advantage with Gaussians is that they are localized in the space around the atoms and therefore are efficient in describing the localized atomic characteristics and short range interaction between atoms. The Gaussian product theorem states that the product of two Gaussian functions is also a Gaussian. A typical primitive cartesian Gaussian function centered at atomic coordinate \mathbf{A} is given as:

$$g(\mathbf{r}, \mathbf{A}, \mathbf{l}, \eta) = (x - A_x)^{l_x} (y - A_y)^{l_y} (z - A_z)^{l_z} e^{-\eta(\mathbf{r}-\mathbf{A})^2} \quad (2.36)$$

where \mathbf{r} is electronic coordinate, \mathbf{l} is quantum number that controls angular momentum defined as $\mathbf{l} = l_x + l_y + l_z$ and η is the exponent that describes the diffuseness (small values – broader, large values – localized) of the function. The product of two Gaussian functions with centers \mathbf{A} and \mathbf{B} is also a Gaussian function with center $\mathbf{P} = \frac{\eta_a \mathbf{A} + \eta_b \mathbf{B}}{\eta_a + \eta_b}$. The screening methods take advantage of this property by ignoring the mesh points after a certain cutoff from the product center \mathbf{P} during calculations, which leads to sparse matrices. Also, the wavefunction pairs (i,j) that are far apart from each other could be ignored for integration or mapping. The multigrid meshing approach is used here to speed up the calculations further. Based on the Gaussian product's exponent, this approach maps the Gaussians onto corresponding fine or coarse grids. For instance, a small exponent smooth Gaussian product is mapped onto coarse grids, whereas a large exponent sharp Gaussian is mapped onto fine grids. This reduces the computational cost by avoiding smooth Gaussian mapping onto fine grids, which otherwise would increase the numerical operations. Another advantage of Gaussians is that the analytical expressions are available for density functional calculations involving them. On the other hand, plane waves are originless functions that extend over the complete simulation cell. The main advantage of plane waves basis here is to speed up the calculations with electrostatic interactions more effectively (compared to Gaussian). Also, periodicity comes naturally to the plane wave basis and the GPW method exploits this feature to effectively solve electrostatic interactions for periodic systems.

Calculation of Kohn–Sham DFT energy in Eq. 2.23 using GPW method gives:

$$\begin{aligned} E[\rho(\mathbf{r})] &= E^T[\chi(\mathbf{r})] + E^{\text{ne}}[\rho(\mathbf{r})] + E^{\text{ee}}[\rho(\mathbf{r})] + E^{\text{nn}} + E^{\text{XC}}[\rho(\mathbf{r})] \\ &= \sum_{ij} P^{ij}(\mathbf{r}) \langle \chi_i(\mathbf{r}) | -\frac{\hbar^2}{2m_i} \nabla^2 | \chi_j(\mathbf{r}) \rangle \\ &\quad + \sum_{ij} P^{ij}(\mathbf{r}) \langle \chi_i(\mathbf{r}) | nV_{\text{loc}}^{\text{PP}}(r) | \chi_j(\mathbf{r}) \rangle + \sum_{ij} P^{ij}(\mathbf{r}) \langle \chi_i(\mathbf{r}) | V_{\text{nl}}^{\text{PP}}(\mathbf{r}, \mathbf{r}') | \chi_j(\mathbf{r}) \rangle \quad (2.37) \\ &\quad + 2\pi\Omega \sum_{\mathbf{G}} \frac{\tilde{\rho}^*(\mathbf{G})\tilde{\rho}(\mathbf{G})}{\mathbf{G}^2} + \frac{1}{4\pi\epsilon_0} \sum_{\substack{I,J \\ I \neq J}}^N \frac{e^2 Z_I Z_J}{|\mathbf{R}_I - \mathbf{R}_J|} + E^{\text{XC}}[\rho(\mathbf{r})] \end{aligned}$$

Note that the kinetic energy of the electrons $E^T[\chi(\mathbf{r})]$ is calculated analytically using a Gaussian basis. The labels $V_{\text{loc}}^{\text{PP}}$ and $V_{\text{nl}}^{\text{PP}}$ in the second and third terms are part of norm-conserving Goedecker–Teter–Hutter (GTH) pseudopotentials (VandeVondele and Hutter, 2007) which represent the local part and non-local part, respectively. The formulation of these pseudopotentials is designed to obtain solutions analytically and also through FFTs using plane waves. The pseudopotential’s hardness less influences the GPW method because the electronic kinetic energy and short range pseudopotentials terms are calculated analytically using the Gaussian basis. The electrostatic calculations in terms 2, 4 and 5 of Eq. 2.37 are solved using plane wave basis through the Ewald summation method, which is commonly used in pure plane wave basis codes for cost effective scaling with system size. The long range part of the electrostatic interactions are treated in Fourier space and the short range parts using real space. The potentials calculated using the plane wave basis are transferred back to the Gaussian basis. Hence the GPW method incorporates the best of both Gaussian and plane wave basis sets to calculate DFT energy.

Speedup SCF: Density mixing and Fermi smearing

In the SCF procedure, the electronic charge is redistributed iteratively to reach minimum energy for an external potential of the system. The redistribution is done until a specific SCF criterion is met. Example criteria could be: change in total electronic energy is not more than 10^{-5} Hartree between consecutive SCF iterations. The iterative process fine-tunes the wavefunction to achieve ground state wavefunction until the SCF criterion is met. For tighter SCF criteria, more SCF cycles are required to achieve SCF convergence, which correlates to the overall computational time. Nowadays, system specific cost reduction techniques are available to converge SCF in fewer cycles. Density mixing and Electronic smearing are reliable and commonly applied techniques, especially to metallic systems to attain faster SCF convergence.

Directly using the current iteration output density as the next iteration input density to construct hamiltonian may sometimes result in unstable SCF. This is observed primarily when a slight change in input density results in a significant change in output density followed by strong density fluctuations. In density mixing, the density fractions from previous iterations are added systematically to the current iteration’s input density to damp oscillations in the SCF procedure. A basic mixing technique is called linear mixing, wherein only a fraction of output density ρ_n^{out} is added to the subsequent input density ρ_n^{in} as shown below:

$$\rho_{n+1}^{\text{in}} = (1 - \alpha)\rho_n^{\text{in}} + \alpha\rho_n^{\text{out}} \quad (2.38)$$

The value of α ranges between 0 to 1 and when $\alpha = 1$, it denotes that mixing is not used. Unfortunately, this method is not stable for all atomic systems. Therefore, in the current study, Broyden Mixing (Broyden, 1965; Bendt and Zunger, 1982), based on quasi-Newton–Raphson approach, is used for its reliable convergence for a large class of

DFT problems.

Electronic smearing is another technique that speeds up SCF convergence for metallic systems. The metallic or semiconductor type systems usually consist of multiple free electrons with very close energies. Consequently, during SCF, a significant change in total density or energy in a consecutive iteration is not often observed. Sometimes the magnitude of change might be larger than the SCF criteria, which prevents the SCF convergence indefinitely. Fermi Smearing (Mermin, 1965) is used here wherein some additional higher Kohn–sham orbitals are added during SCF. The states are then smeared out by using fractional occupation numbers obtained from Fermi–Dirac distribution function at a finite temperature. The SCF convergence is achieved faster with smeared out states at the Fermi level.

DFT applications in geochemical systems

Today, nearly all popular DFT codes provide a framework to simulate most atoms in the periodic table. Unlike molecular mechanics, this supports adding new molecules to the simulation environment without reparameterization. Hence, the DFT method usage has risen significantly for almost all chemistry fields, including studies related to geochemical systems (Kruse et al., 2015). For instance, Kwon and Kubicki (2004) employed DFT to provide a detailed understanding of phosphate surface complexes on iron hydroxides. They calculated theoretical IR frequencies through DFT calculations and compared them to experimentally observed frequencies to estimate the most favorable binding motifs at specific pHs. Similarly, Tribe et al. (2006) estimated glyphosate’s most favorable binding motifs on goethite at different pH values. Aquino et al. (2008) computed the effect de/protonation of goethite surface reactive sites and estimated its point of zero charge as 9.1, which matches with the experimental values of 6.4–9.7 (Strauss et al., 1997; Kosmulski, 2009). Tunega et al. (2009) focused on interactions between goethite and a set of mono- and polyaromatic hydrocarbons and found that adsorbates form relatively weak surface complexes with the surface. Kubicki et al. (2012) studied phosphate interactions at different goethite surface planes in the presence of water. Their results highlight that the surface plane type and solution pH are influential for phosphate adsorption onto goethite. Kersten et al. (2014) showed that for the interaction between goethite and 4-chloro-2-methylphenoxyacetic acid herbicide using DFT the outersphere complexes and monodentate innersphere complexes are more stable ones. Ahmed et al.’s (2018a) study of goethite–glyphosate–water complexes for three different goethite surface types of varying saturation (Fe surface atoms coordinated by 3, 4, and 5 $\text{O}^{2-}/\text{OH}^-$ groups) showed the impact of surface saturation on phosphate interaction. The study also highlighted the significance of water in these interactions. Ahmed et al. (2019) showed that an analysis of theoretical spectra for different goethite–phosphate binding motifs could estimate their abundance ratio at the goethite surface. Ahmed et al. (2020) estimated the most abundant binding motifs at extreme pH ranges in light of experimental find-

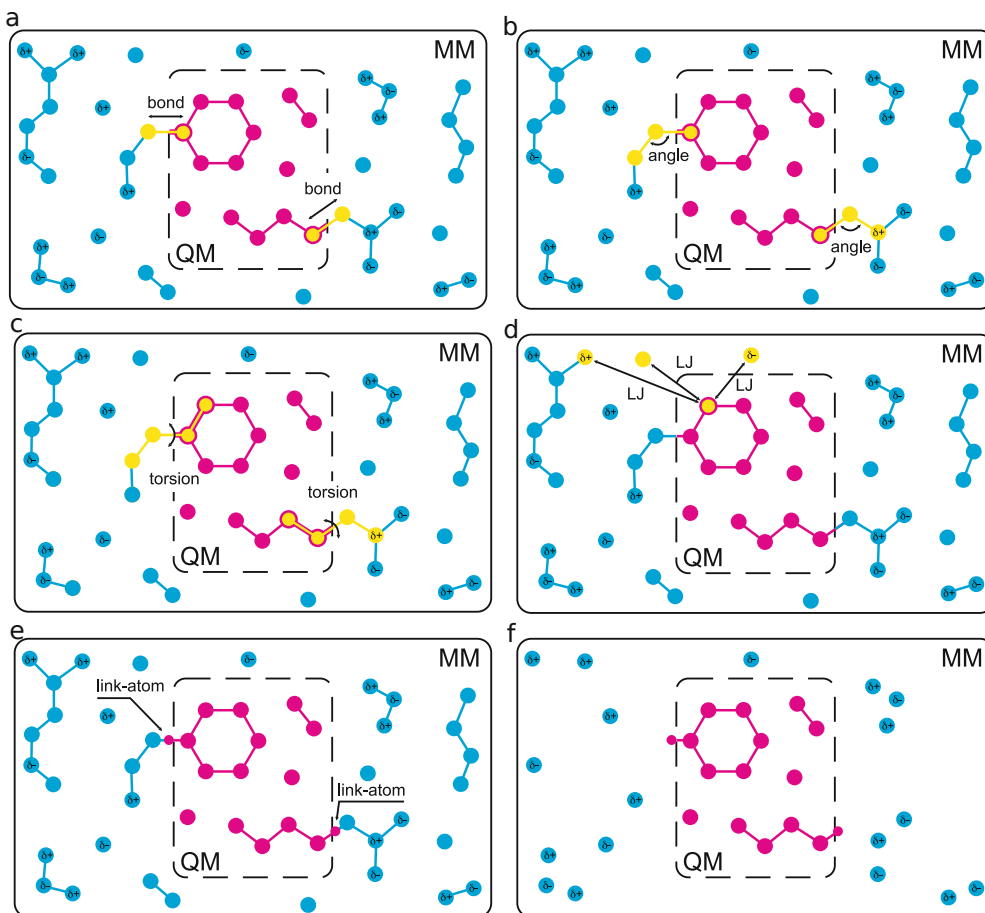


Figure 2.2: Different scenarios contributing to QM/MM interaction energy. Bond (a), angle (b), torsion (c), vdW interactions like lennard-jones [LJ] (d), link-atoms (e), electrostatic interaction (f). Taken from Groenhof (2013).

ings. Kubicki and Ohno (2020) studied complexes of phosphate and salicylate adsorbed onto different goethite surface planes. They predicted the surface complex structures and the vibrational frequencies calculated based on simulations matched well with previous observations. The above literature shows DFT's success in unraveling molecular level insights of geochemical interactions, which is otherwise impossible using only experimental tools. Nevertheless, given the size of the geochemical systems, employing DFT is not always feasible. Therefore, to maintain accuracy at reactive regions and reach higher timescales with reduced computational costs, one might use hybrid QM/MM methods to study geochemical systems.

2.4 Hybrid Quantum Mechanics/Molecular Mechanics

As discussed before, the QM/MM method could reduce the computational cost for atomic systems where a distinct separation could be made between atoms in the reactive center and atoms that do not directly participate in the reaction. This section provides a basic overview of QM/MM methods and a detailed overview of these methods is given in Senn and Thiel (2009) and Groenhof (2013). There are two main schemes by which one could implement the QM/MM method, namely subtractive and additive schemes. The system's total energy in the subtractive scheme is evaluated in three steps, 1) calculate the energy of the total system at the MM level, 2) calculate the energy of the QM system at QM level, 3) calculate the energy of the QM system at MM level and subtract. The steps above are formulated as shown below:

$$E = E^{\text{MM}}(\mathbf{r}_i, \mathbf{R}_I) + E^{\text{QM}}(\mathbf{R}_I) - E^{\text{MM}}(\mathbf{R}_I) \quad (2.39)$$

where \mathbf{r}_i and \mathbf{R}_I are MM and QM atoms, respectively. This method's main advantage is that there is no interaction between the QM and MM subsystems, making the implementation straightforward. The disadvantage with this method is that the FF parameters are required for both QM and MM subsystems to calculate $E^{\text{MM}}(\mathbf{r}_i, \mathbf{R}_I)$ and $E^{\text{MM}}(\mathbf{R}_I)$ terms. Also, the FF should be flexible to adapt to the changes happening in the reactive QM region. The additive scheme overcomes this problem by treating the interaction between the QM and MM systems explicitly, as shown below:

$$E(\mathbf{R}_I, \mathbf{r}_i) = E^{\text{QM}}(\mathbf{R}_I) + E^{\text{MM}}(\mathbf{r}_i) + E^{\text{QM/MM}}(\mathbf{R}_I, \mathbf{r}_i) \quad (2.40)$$

The interaction between QM and MM subsystems decides on the nature of the additive QM/MM method. For instance, in the mechanical embedding QM/MM method, the interaction between QM and MM systems is handled at the MM level of theory. That is, the bonded interactions like bonds, angles, dihedrals and nonbonded interactions between QM and MM atoms are defined at the MM level, see Fig. 2.2a–d,f. To handle the nonbonded electrostatic interactions, partial MM charges are assigned to QM atoms and pairwise coulomb interactions are computed classically. Since handling interactions at the MM level is computationally inexpensive, this method is generally faster but compromises accuracy than other methods below. This method's main disadvantage is that the MM section could not influence the QM region's reactions. This is addressed in the electrostatic embedding method (used in the current study), wherein the MM atoms polarize the QM atoms and bonds across QM and MM subsystems could be handled at QM level, see Fig. 2.2d–f. However, note that the QM subsystem cannot polarize the MM subsystem. The total interaction energy between QM and MM subsystems is given as:

$$E^{\text{QM/MM}} = E_{\text{bond}}^{\text{QM/MM}} + E_{\text{elec.}}^{\text{QM/MM}} + E_{\text{vdW}}^{\text{QM/MM}} \quad (2.41)$$

The first term in the above equation is the QM/MM interaction energy due to bonds that

are formed across QM and MM subsystems (see Fig. 2.2e), the second and third term are nonbonded interaction energies ($E_{\text{NB}}^{\text{QM/MM}}$) due to electrostatic and vdW interactions (see Fig. 2.2d,f). The nonbonded interaction energy between QM and MM subsections is given as:

$$E_{\text{NB}}^{\text{QM/MM}}(\mathbf{r}_i, \mathbf{R}_I) = \frac{1}{4\pi\epsilon_0} \sum_{a \in \text{MM}} q_a \int \frac{\rho(\mathbf{r}, \mathbf{R}_I)}{|\mathbf{r} - \mathbf{r}_i|} d\mathbf{r} + \sum_{\substack{a \in \text{MM} \\ \alpha \in \text{QM}}} \nu_{\text{vdW}}(\mathbf{r}_i, \mathbf{R}_I) \quad (2.42)$$

Here $\rho(\mathbf{R}_I, \mathbf{r})$ is the total (electronic plus nuclear) charge density of the quantum system and $\nu_{\text{vdW}}(\mathbf{r}_i, \mathbf{R}_I)$ is the vdW interaction between QM and MM atoms. The QM subsystem's polarization is achieved by including MM charges as one electron operator into QM hamiltonian, as shown in the above equation. This improves the accuracy of the reactive region simulation but raises the computational cost. Nevertheless, this method is more accurate than the mechanical embedding method as the latter method does not polarize the QM subsystem. An important issue with this approach is that the point charge MM atoms in short-range interaction with QM atoms may attract or repel the QM charge distribution strongly, leading to electron spilling. This artefact is more profound if the adopted basis set includes polarization and diffuse functions or plane wave basis. To avoid this, the MM atoms are defined as smeared-out charges instead of point charges using Gaussian functions centered at the MM atom position. The Gaussian function's initial guess width is expected to be the covalent radius of the MM atom.

Gaussian expansion of the QM/MM electrostatic potential (GEEP) (Laino et al., 2005) is a module in CP2K package that defines MM charges as smeared out Gaussians and adopts efficient screening techniques to reduce the computational cost in calculating $E_{\text{NB}}^{\text{QM/MM}}$. In this method, the charge distribution of an MM atom “ a ” using Gaussian function is defined as:

$$\rho(\mathbf{r}, \mathbf{r}_i) = \frac{1}{(\sqrt{\pi} r_{c,a})^3} \exp\left(-\left(\frac{|\mathbf{r} - \mathbf{r}_i|}{r_{c,a}}\right)^2\right) \quad (2.43)$$

and its corresponding classical potential is:

$$\nu_a(\mathbf{r}, \mathbf{r}_i) = \frac{\text{erf}\left(\frac{|\mathbf{r} - \mathbf{r}_i|}{r_{c,a}}\right)}{|\mathbf{r} - \mathbf{r}_i|} \quad (2.44)$$

where $r_{c,a}$ is the atomic parameter that often has a value close to the atom's covalent radius. The key feature of the GEEP method is to breakdown the electrostatic potential of a MM atom in Eq. 2.44 into Gaussians of different cutoffs and a residual function

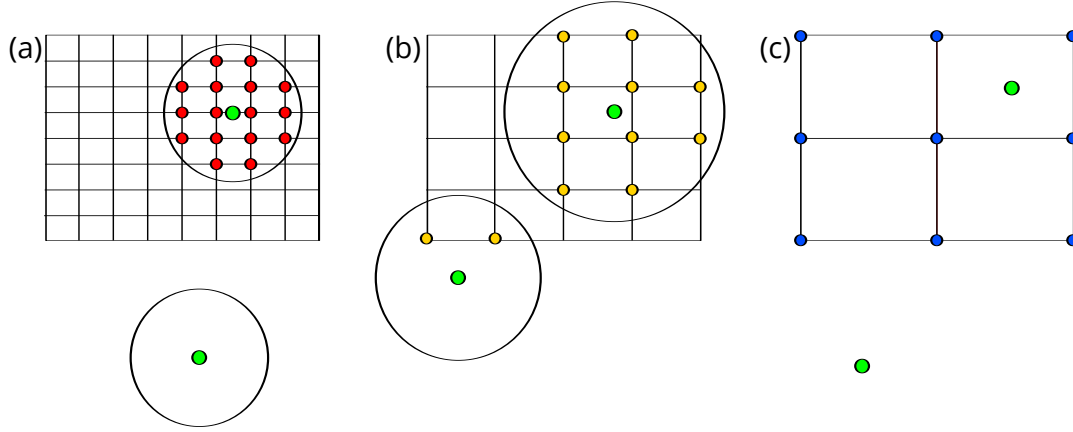


Figure 2.3: Collocation procedure highlighting the MM atom's (green color) collocation radius and its contribution onto QM multigrid setup. MM atom whose collocation radius is greater than its distance from QM grid and another MM atom whose collocation radius lies completely inside QM grid (a), collocation radius partially overlays onto QM grid (b), long-range contribution (RES_{low}) from all the atoms mapped onto the coarsest grid (c). Redrawn from Laino et al. (2006).

RES_{low} as shown below:

$$\nu_a(\mathbf{r}, \mathbf{r}_i) = \sum_{N_g} A_g \exp \left(- \left(\frac{|\mathbf{r} - \mathbf{r}_i|}{G_g} \right)^2 \right) + \text{RES}_{\text{low}}(|\mathbf{r} - \mathbf{r}_i|) \quad (2.45)$$

where N_g is the number of Gaussian functions expressed as the sum of the potential and RES_{low} is the residual function. By appropriately choosing the amplitude A_g and width G_g of the Gaussian functions a smooth residual function RES_{low} could be obtained. The main idea behind decomposing the potential to Gaussian and residual functions is to provide a framework to reduce computational cost and use the multigrid setup discussed in Section. 2.3.4. The sharp Gaussians are mapped onto the fine grids and the smooth Gaussians are mapped onto the coarse grids while the residual function is mapped onto the coarsest grid. The Gaussians are truncated after a certain threshold radius called collocation radius, beyond which the Gaussian function values are set to zero. This reduces the computational cost by avoiding MM atoms in calculations whose collocation radius does not overlap with the QM box. The framework for collocation of Gaussians onto the QM grid is as follows: 1) MM atom inside QM box or close to it whose collocation radius is less than or equal to its distance to QM box contributes to the finer grids 2) MM atom whose collocation radius is shorter than its distance from QM box does not contribute to finer grids, 3) all atoms contribute to the coarsest grid through the residual function RES_{low} , see Fig. 2.3. The grids are commensurate, i.e., all

the points on the coarse grid are also present on the fine grid. The potential contribution from all the grids is then interpolated onto the finest grid and the QM/MM electrostatic energy is calculated as shown below:

$$E_{\text{elec.}}^{\text{QM/MM}}(\mathbf{R}_I, \mathbf{r}_i) = \int \rho(\mathbf{r}, \mathbf{R}_I) V^{\text{QM/MM}}(\mathbf{r}, \mathbf{r}_i) d\mathbf{r} \quad (2.46)$$

where $V^{\text{QM/MM}}(\mathbf{r}, \mathbf{r}_i)$ is the electrostatic potential due to MM atoms onto the finest grid and $\rho(\mathbf{r}, \mathbf{R}_I)$ is the total density (electron plus nucleus) evaluated on the same finest grid.

As mentioned before, in the electrostatic embedding method, the MM subsystem is not polarized by the QM subsystem. The mutual polarization of QM and MM systems i.e., QM subsystem polarized by MM subsystem and vice versa, is implemented in the polarization embedding method. However, this method is computationally expensive compared to the methods mentioned above due to the implementation of mutual polarization. The MM parameters should also be compatible with polarization, which is hard to find for a specific system since polarizable force fields are not often used in simulation studies. Therefore, the polarization embedding method is not commonly used for geochemical systems.

For cases where QM and MM systems are connected with covalent bonds, the bonded interaction energy should also be calculated. In the subtractive QM/MM scheme and Mechanical embedding (additive QM/MM scheme), the bonds and angles across subsystems are handled at MM level. In electrostatic embedding and polarization embedding methods, the covalent bonds are handled at the QM level by adopting the “link atom” scheme, see Fig. 2.2e. In this scheme, a monovalent link atom is added along the bond vector between QM and MM atoms. This monovalent atom is visible only to the QM subsystem during the calculation of energies but remains invisible to the MM subsystem. Another approach is the “localized orbitals” scheme, where a doubly occupied molecular orbital replaces the covalent bond.

QM/MM simulations in geochemical systems

Even though the QM/MM method allows one to simulate longer trajectories at lower simulation costs, setting the simulation environment that describes precisely the QM and MM subsystems’ mutual interaction is not straightforward. Also, the limitations with readily available force fields discourage one from adopting QM/MM methods. Therefore, the hybrid QM/MM methods are not used extensively as pure QM and MM methods to study geochemical systems (Kubicki, 2016). Nevertheless, successful QM/MM studies for geochemical systems highlight the benefits of QM/MM methods. Ivanova Shor et al. (2005) studied the aluminum content effect on acidic zeolites’ properties at reduced computational costs than pure QM methods. However, they had to develop custom force fields for aluminum containing zeolites since the required force fields are

not readily available, which is time-consuming. Stoyanov et al. (2008) performed both pure DFT calculations and QM/MM calculations to investigate zeolite nanoparticles' surface acidity. Both methods' observed molecular orbital spatial distributions are quite close, suggesting a good correlation between QM/MM and pure DFT methods and again at reduced computational costs with the former. Recently, Ha et al. (2018) investigation of arsenate-goethite clusters adsorption onto carbon nanotubes showed that a broader diameter carbon nanotube improved the chemisorption capability of carbon nanotubes. Thus, there are only a few QM/MM applications to geochemical systems. This holds the same, especially for mineral-phosphate-water interactions and the current study contributes towards initial steps in this region.

2.5 Molecular Dynamics

MD simulations provide a theoretical framework to simulate the evolution of reaction in a thermal ensemble. The typical steps in an MD algorithm are to calculate the attractive/repulsive force acting on every atom due to interatomic interaction in a simulation box, followed by updating the position and velocity of atoms by Newton's law of motion. The atoms in the system have potential energy based on the charge and its position. The overall potential energy $E(\mathbf{R}_1, \mathbf{R}_2, \dots, \mathbf{R}_N)$ of a system is a function of its atom positions in the system. The forces acting on the atoms could be calculated numerically as the gradient of the system potential energy. From Newton's second law of motion, the MM atom's equation of motion is given as:

$$\begin{aligned} M_I \frac{d^2 \mathbf{R}_I}{dt^2} &= -\nabla_I E(\mathbf{R}_1, \mathbf{R}_2, \dots, \mathbf{R}_N) \\ &= -\nabla_I \min_{\rho(\mathbf{r})} E(\{\mathbf{R}_1, \mathbf{R}_2, \dots, \mathbf{R}_N, \rho(\mathbf{r})\}) \end{aligned} \quad (2.47)$$

where M_I and \mathbf{R}_I are the atomic mass and the cartesian coordinates of QM atom "I". The dynamics of the QM atoms is simulated here using the Born–Oppenheimer MD (BOMD) scheme. As discussed in Section. 2.3.1, the electron and nuclei wavefunction are decoupled after applying the Born–Oppenheimer approximation. In the BOMD scheme, the decoupled nuclei are considered classical particles and these particles are then propagated in time using the Newton equations of motion. In both MM and QM atom cases, the time propagation of the atoms is performed using the velocity Verlet algorithm:

$$\mathbf{R}(t + \Delta t) = \mathbf{R}(t) + \mathbf{V}(t)\Delta t + \frac{1}{2}\mathbf{a}(t)\Delta t^2 \quad (2.48)$$

$$\mathbf{V}(t + \Delta t) = \mathbf{V}(t) + \frac{\mathbf{a}(t) + \mathbf{a}(t + \Delta t)}{2}\Delta t \quad (2.49)$$

where $\mathbf{V}(t)$ and $\mathbf{a}(t)$ are the instantaneous velocity and acceleration of the atom, which are updated at each time step of Δt . The time step is dependent only on the frequency spectrum of the system. For molecular systems with flexible and light atoms like hydrogen, one needs shorter intervals (around 0.25–0.5 fs). One of the bottlenecks to reach higher timescales with the QM/MM method is that the Kohn–Sham equations are to be solved self-consistently at each time step. The time required to reach full self-consistency is usually high since many iterations are required to achieve it. Nevertheless, since only a fraction of system atoms is considered QM in QM/MM methods, this reduces the overall computational cost and time compared to the pure QM case. It is common to consider relaxed SCF criteria in MD simulations with shorter time intervals as the system changes are insignificant. Even with relaxed SCF criteria, the MD simulations using QM/MM methods do not reach the time scales that one achieves with pure MM.

Thermostat and NVT ensemble

Many experiments and natural phenomena are related to the canonical ensemble (NVT). In the canonical ensemble, the total number of particles (N), system volume (V) and the overall system temperature (T) are to be maintained constant theoretically. Maintaining a constant number of particles and volume in a system during the simulation is straightforward. However, to maintain a constant average temperature system must be coupled with a thermostat (heat bath). From classical statistical mechanics, the average temperature of the system with N particles and kinetic energy (E_{kin}) is:

$$\langle T \rangle = \frac{2 \langle E_{\text{kin}} \rangle}{3N k_B} \quad (2.50)$$

where k_B is the Boltzmann constant. One could use the instantaneous kinetic energy to find the system’s instantaneous temperature from the above equation. Also, for a fixed number of particles, the probability of kinetic energy of particles follows the Maxwell–Boltzmann distribution based on the temperature as:

$$P(E_{\text{kin}}) \propto \exp\left(-\frac{E_{\text{kin}}}{k_B T}\right) \quad (2.51)$$

The basic idea for implementing a thermostat from the above equations is to rescale and redistribute particles’ velocities in a system to maintain the overall temperature at the desired temperature. In the Berendsen thermostat (Berendsen et al., 1984), all particles’ velocities are rescaled by a factor that includes a ratio of target and instant velocity. This method does not sample canonical ensemble and causes unusual atoms dynamics during simulations. The Andersen thermostat (Andersen, 1980) adopts a stochastic approach wherein at each n^{th} time step, the particles’ velocities are randomly

distributed based on the velocities drawn from the Maxwell–Boltzmann distribution at the target temperature. Unfortunately, this method is inefficient for canonical ensemble cases and is very sensitive to relaxation time. A combination of these approaches is the thermostat by Bussi et al. (2007) called canonical sampling through velocity rescaling (CSVR) thermostat. This combines both velocity rescaling and stochastic approach. This thermostat (used in the current study) is very efficient with canonical ensemble cases and exhibits weak dependence on relaxation time.

3 Molecular Systems, Modelling And Analysis

This chapter provides a basic overview of soil minerals and phosphates' characteristics relevant to the current study. Section 3.1 focuses on the characteristics of abundant phosphates: orthophosphate (OP) (Newman and Tate, 1980; Missong et al., 2016), glycerolphosphate (GP) (Pant et al., 1999; Doolette et al., 2011; Vincent et al., 2013; Missong et al., 2016) and inositol hexaphosphate (IHP) (Turner et al., 2002; Gerke, 2015; Missong et al., 2016; Missong, 2018) and common P-fixing minerals: diaspore and goethite (Cornell and Schwertmann, 2003; Tsao et al., 2011). The critical properties of minerals and phosphates that influence mineral-phosphate interactions are detailed. Next, Section 3.2 presents an overview of molecular modeling for mineral-phosphate-water complexes. Section 3.3 discusses the calculation of interaction energies between a combination of mineral, phosphate and water complexes. The last Section 3.3 presents the importance of HBs and a theoretical approach from the literature to quantify their strengths. For more details related to the present discussions, refer to textbooks: Dixon et al. (2002), Cornell and Schwertmann (2003), Tan (2011) and Kubicki (2016).

3.1 Molecular Systems and Relevant Interactions

Phosphates: OP, GP and IHP

The phosphorus atom has five valance electrons ($1s^2$, $2s^2$, $2p^6$, $3s^2$, $3p^3$), three electrons short of completing the third shell. Therefore, it is less electronegative than fluorine and oxygen atoms and often forms covalent bonds. It is commonly found in nature as phosphate or also known as OP anion $[\text{PO}_4^{3-}]$ (Jahnke, 1992). In OP, the P atom is tetrahedrally coordinated with four oxygens, see Fig. 3.1a and as the O atom is more electronegative than P, the electron density is spatially distributed around the tetrahedron. In solution, these oxygens further interact with hydrogens to form protonated anions (H_2PO_4^- , HPO_4^{2-}). The protonation state of phosphate anion depends mostly on the solution pH and increases with a decrease in pH. Also, given the asymmetry of the charge distribution, the unprotonated oxygens of phosphate anions interact strongly with mineral cations. The strong interaction of phosphate anion with the mineral surface sometimes results in displacement and substitution of ligands like OH^- or water (Beek and van Riemsdijk, 1979). This substitution is a ligand exchange reaction and the phos-

phate bound to the surface becomes part of the mineral's surface metal atoms coordinate sphere. Furthermore, the adsorbed phosphate influences the surface charge and alters the mineral interaction with molecules of the environment.

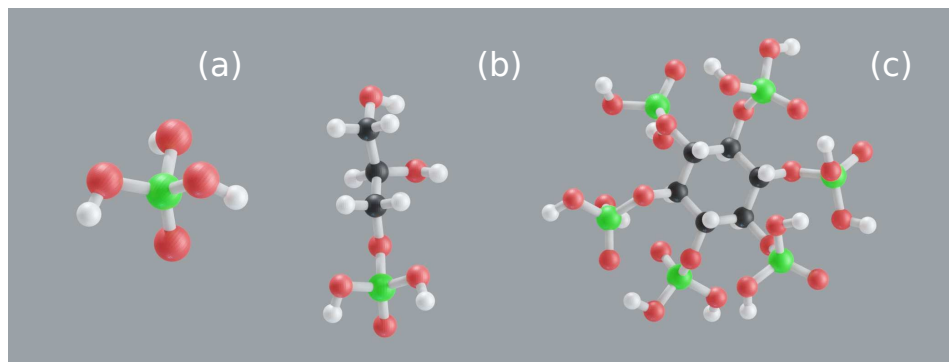


Figure 3.1: Phosphates: Phosphoric acid (fully protonated OP) (a), GP (b) and IHP (c). Red, white, black and green colors correspond to oxygen, hydrogen, carbon and phosphorus atoms, respectively (Ganta et al., 2021b).

GP and IHP are organic phosphates P_o , also called organophosphates, are esters of phosphoric acid. At least one OH group of phosphoric acid ($O-P[OH]_3$) is replaced by an O-R group, where R is an organic species. For instance, in the formation of GP, glycerolphosphate ($H_2PO_3-C_3H_7O_3$), the glycerol group replaces the hydroxyl group of phosphoric acid. Note that forming a polyphosphate compound is also possible where phosphate ions are linked together by sharing oxygen atoms. The organic part is known to alter the characteristics of phosphate ions and influence P_o interaction with the mineral surfaces. In the case of GP, only three out of four phosphate oxygens are free to bind with the soil minerals; see Fig. 3.1b. Hori et al. (1985) suggest that the tendency of GP to adsorb onto a surface might be weaker than OP because all the oxygens of OP are free to bind. Studies show that ligands characteristics influence the phosphate interaction with soil minerals and the attraction/adsorption of incoming phosphates. The mechanism of GP interaction with minerals is similar to that of OP, where GP replaces hydroxyl groups or water molecules at the mineral surface, i.e., ligand exchange to form innersphere complexes (Li et al., 2017).

Inositol phosphates ($IP_x = 1, 2, \dots, 6$) are a family of phosphoric esters found widely in nature. Among these esters, IHP is the most prevalent form, which interacts strongly with cations and positively charged surfaces (Turner et al., 2002). IHP has six phosphate groups (see Fig. 3.1c) and acts as a strong ligand because of its high anionic charge and ability to interact with multiple phosphate groups. The interaction of individual phosphate groups with minerals is similar to that of OP. However, intramolecular hydrogen bonds (HBs) between adjacent phosphate groups and interaction of additional

phosphate groups with environmental molecules differentiate IHP interaction with minerals compared to other phosphates (Johnson et al., 2012). The study by Anderson and Arlidge (1962) proposed that phosphate molecules with multiple phosphate groups like IHP could form a more stable mineral–phosphate complex compared to a single phosphate group like OP and GP.

Minerals: Goethite and diaspore

Goethite (α -FeOOH) is one of the most common and highly reactive soil minerals that bind phosphates. The overall positive surface charge of the goethite surface allows it to attract and bind the phosphate anions under common soil conditions. The (un)saturation of surface Fe atoms is a key factor controlling goethite's interaction strength. The Fe atoms inside the bulk of goethite are surrounded by three O^{2-} and three OH^- forming an octahedron with orthorhombic unit cell. However, the Fe atoms are undercoordinated at the surface, exhibiting an overall positive charge. The common surface planes of goethite are (010), (100), (110), (021), according to $Pbnm$ space group (Cornell and Schwertmann, 2003). Depending on the bare surface plane, the surface iron atoms are coordinated by 3, 4 or 5 oxygens. For instance, the surface Fe atoms of (010) surface plane are coordinated by four atoms whereas the ones at (100) surface plane are coordinated by five oxygen atoms, see Fig. 3.2. The highly undercoordinated surface iron atoms can attract and bind phosphates more. Ahmed et al.'s (2018a) study of glyphosate adsorption at goethite surface with three different degrees of saturation (Fe surface atoms are coordinated by 3, 4, and 5 $\text{O}^{2-}/\text{OH}^-$ groups) highlighted the effect of goethite surface saturation on phosphate binding stability.

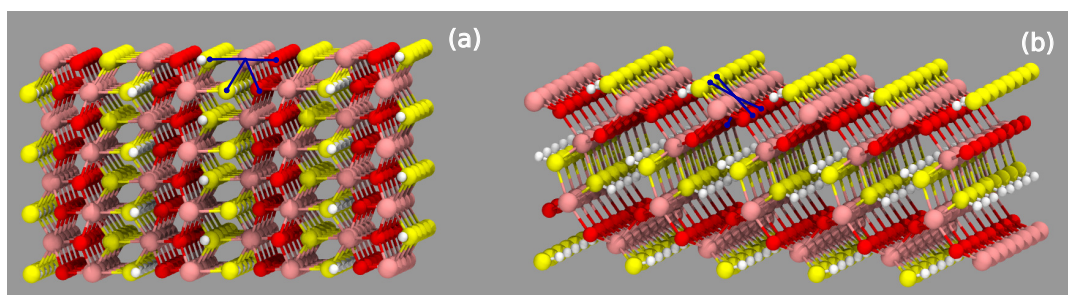


Figure 3.2: Goethite surface: (010) surface plane (a), (100) surface plane (b). Pink, red, yellow and white colors correspond to iron, bridging oxygen, hydroxyl oxygen and hydrogen atoms, respectively. The blue lines show the coordination of surface Fe atoms, four at (010) surface plane and five at (100).

In addition to the surface plane type, the pH of the environment and the purity and crystallinity of goethite are other main factors that control the phosphate adsorption

process. In general, the overall surface charge of a mineral is a function of pH (Tan, 2011) where for $\text{pH} < \text{point of zero charge (PZC)}$, the mineral surface is unsaturated with positive surface charges, which attract anions. For $\text{pH} > \text{PZC}$, it is saturated with a negative surface charge which attracts cations. As phosphates often exist as negatively charged anions, their adsorption is more favorable at $\text{pH} < \text{PZC}$. OP adsorption onto goethite was more favorable (Tejedor-Tejedor and Anderson, 1990; Strauss et al., 1997) below pH values of 6–10, which is the PZC range of goethite (Cornell and Schwertmann, 2003; Kosmulski, 2009).

The cation substitution (Al, Co, Cr, Ga could substitute Fe) in goethite and several other iron oxides and hydroxides is common in nature (Cornell and Schwertmann, 2003). Given the abundance of Al in nature, it is more commonly found to substitute Fe even though it has a smaller atomic size than Fe. This substitution often does not completely modify the structure of the goethite unit cell but affects the unit cell size. However, the adsorption properties of goethite are affected; for instance, the Fe:Al ratio in amorphous Fe/Al hydroxide mixtures influenced the phosphate adsorption/desorption rates (Gypser et al., 2018). In this context, analyzing the phosphate binding to diaspore ($\alpha\text{-AlOOH}$) surface could provide additional insight into the P interaction with these amorphous mixtures. Diaspore is isomorphous with goethite with Al^{+3} oxidation state instead of Fe^{+3} . Interestingly, diaspore exhibits higher surface energy compared to goethite (Guo and Barnard, 2011). Surfaces with higher surface energy interact stronger with the adsorbents than those with lower surface energy. This implies that diaspore would adsorb phosphates stronger than goethite. Diaspore PZC value is around pH 6 (Kosmulski, 2009) and therefore, one might expect significant adsorption at $\text{pH} < 6$.

Mineral–Phosphate interactions

Newman and Tate's (1980) characterized Newzeland soils by ^{31}P nuclear magnetic resonance (NMR) and showed that OP is abundant phosphate and it dominates other phosphates adsorption onto minerals. A similar study using ^{31}P NMR of forest soils by Missong et al. (2016), showed that OP is the most abundant phosphate in forest soils. The abundance of OP in common soils is because of its strong interaction with soil minerals and soluble metal ions (Beek and van Riemsdijk, 1979). Regarding OP interaction with ions, Rose et al. (1997) established that it interacts strongly with Fe^{3+} metal ion and one OP could be bound with two to three free metal ions. Focusing on mineral–OP interactions, OP interacts with soil minerals through unprotonated oxygens, often forming one or two P–O–Fe/Al covalent bonds with surface mineral atoms. Parfitt and Atkinson (1976) studied the OP interaction with goethite and other iron oxides using infrared (IR) spectroscopy. They showed that OP often forms a bridging binuclear **BB** ($2\text{Fe} + 2\text{O}$, see Fig. 3.3b) complex and forms innersphere complexes. Innersphere complex adsorption proceeds by a coordination reaction where the ligand, here OP, interacts directly with a surface metal atom. In contrast, the outersphere complex reaction

denotes the bonding of OP to water in the hydration shell of the metal (Tan, 2011). Hori et al. (1985) investigated the OP adsorption experiment as a function of pH and showed that it adsorbs onto hydrated iron (Fe^{+3}) oxides precipitates mostly between pH 4.0–8.0. Tejedor-Tejedor and Anderson (1990) provided a detailed overview of binding motifs between OP and goethite and the change of OP's protonation with pH. They suggested that OP forms three different complexes, a protonated and nonprotonated **BB** motif and a non protonated monodentate (**M** motif ($\text{Fe} + \text{O}$), see Fig. 3.3a). Predominantly, OP forms **BB** motif at the goethite surface. Further, OP is singly protonated in the pH range of 3.6–6, but above pH 6 it often exists in a completely deprotonated state. In contrast, Persson et al.'s (1996) Fourier-transform infrared spectroscopy (FTIR) interpretation suggests that at the mineral–water interface, OP forms only **M** motifs with different protonation states. The study focuses on OP interaction with goethite and hematite in the presence of water. In another study focusing on binding as a function of pH and phosphate concentrations, Kim et al. (2011) found that OP formed **BB** motif. In contrast, Abdala et al. (2015) investigated surface loading effects of OP adsorption onto goethite and demonstrated that at low ($1.25 \mu\text{molm}^{-2}$) surface loading **B** motif ($2\text{Fe} + \text{O}$ see Fig. 3.3c) and **BB** motifs are dominant, at medium loading ($2.5 \mu\text{molm}^{-2}$) **B** motif is dominant, and at high loading ($10 \mu\text{molm}^{-2}$) **M** motif is dominant.

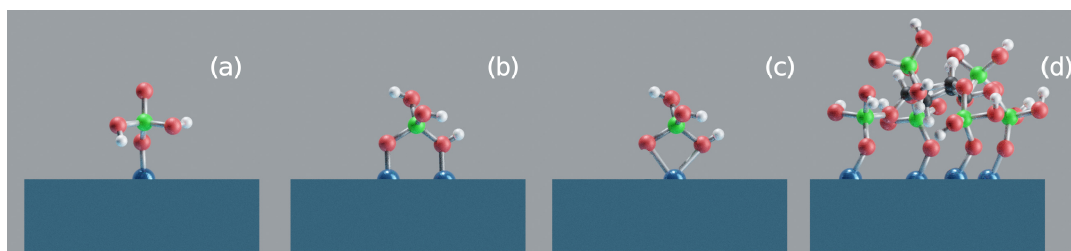


Figure 3.3: Binding motifs: monodentate **M** (a), binuclear bidentate **BB** (b), bidentate **B** (c), **4M** (c). Blue, red, white, black and green colors correspond to iron, oxygen, hydrogen, carbon and phosphorus atoms, respectively (Ganta et al., 2021b).

In addition to existing experimental efforts, theoretical investigations of the OP interaction with minerals are also available in the literature. Kwon and Kubicki (2004) using DFT simulations resolved controversies in experimental studies about phosphate surface complexes on iron hydroxides and suggested how the interactions change with pH. They proposed that OP forms both **M** and **BB** motifs, but the latter one is dominant in the range of pH 4–6. Kubicki et al. (2012) in a joint experiment and theoretical approach explored goethite–phosphate binding motifs and their corresponding stability at different surface planes to find dominant motifs that contribute significantly to IR spectra. They highlighted the influence of surface plane and solution pH on the formation of binding motifs. Depending on the surface plane, they proposed three complex types for OP:

OP forming innersphere complexes via **M**, **B** motifs and OP forming an outersphere complex. Ahmed et al. (2019) showed that both **M**, **B** motifs are possible. However, based on analysis of theoretical spectra for different motifs compared to experiments, it was concluded that **B** motif is dominant at (010) goethite surface and **M** motif at (100) goethite surface. A combined experimental and theoretical work focusing on the OP adsorption concerning pH concluded that OP forms both **M** and **B** motifs, but depending on pH, their abundance changes (Ahmed et al., 2020). The **M** motif is dominant at both extremely low and high pH values, while the **B** motif is dominant at the intermediate pH range. Summarizing the OP interaction with minerals, both experimental and theoretical results point out that depending on surface type, surface loading and pH, OP forms **M** and **B** motifs. It interacts with mineral surface via ligand exchange and could replace water.

GP interaction with soil minerals was not studied extensively; therefore, the information about factors influencing its interaction is limited. However, as GP interaction with minerals is only through the phosphate group, one could imply that the same factors that influence OP interaction with minerals could be present here as well. Li et al. (2017) showed that GP forms innersphere complexes with goethite by replacing water and hydroxyl groups from surface active sites. The study also proposes that GP might only form **M** motif as the formation of **BB** motif is sterically hindered by the organic moiety. Yan et al. (2014) studied sorption of different phosphates involving OP and GP on aluminum (oxyhydr)oxides and found that for identical conditions, the amount of GP adsorbed onto minerals is less than OP. Xu et al.'s (2017) study of GP on hematite showed that GP adsorbed onto the surface through ligand exchange and remained as twice deprotonated at high pH. The adsorption of GP onto the hematite surface resulted in a more negatively charged hematite surface than OP adsorbed hematite surface. The recent study by Amadou et al. (2022) shows that GP is retained in lower proportions at goethite than OP. Focusing on the literature of other monoester phosphates, Persson et al. (2012) suggested monomethyl phosphate ($\text{CH}_3\text{-H}_2\text{PO}_4$) forms a dominant **M** motif for its adsorption onto goethite. In addition, Lü et al. (2017) suggested that molecules with a similar binding mechanism like GP, such as glucose 6-phosphate and adenosine mono/triphosphates, form nonprotonated bidentate complexes within the first ten minutes after mixing. Further, adsorption isotherms and FTIR spectra by Sheals et al. (2002) proposed that glyphosate (GLP, $\text{H}_2\text{PO}_3\text{-CH}_2\text{-NH}_2\text{-CH}_2\text{-COO}$) binds predominantly through an **M** motif but **B** motifs might be formed at low P concentration and neutral pH. Ahmed et al. (2018b) using periodic DFT based MD simulations proposed that the glyphosate dominant binding motif depends on surface plane type. Summarizing, GP could form both **M** motif and **B** motifs by replacing water at the mineral surface and the organic moiety could influence its interaction with the mineral surface.

A review by Turner et al. (2002) pointed out that IHP exists abundantly in nature and its interaction with soil minerals needs significant focus. Ognalaga et al. (1994) showed

that IHP was adsorbed onto goethite through their phosphate groups. It formed inner-sphere complexes with goethite and the adsorption mechanism involved ligand exchange with surface hydroxyl groups. Also, tentative configurations for goethite–IHP complexes are proposed, which show that IHP interacts with four phosphate groups (probably forms **4M** motif, $4\text{Fe} + 4\text{O}$ see Fig. 3.3d), while two remain free. Supporting the same conclusion, Celi et al. (1999) proposed that IHP forms inner-sphere complexes with goethite and interacts through its multiple phosphate groups. They also proposed that phosphate groups of IHP interact with goethite with the same mechanism as OP. Guan et al.’s (2006) ATR–FTIR study showed that IHP formed inner-sphere complex with aluminum hydroxide and the adsorption facilitated deprotonation of its phosphate groups. In addition, molecular simulations by the same authors showed that IHP formed stable **3M** motif ($3\text{Al} + 3\text{O}$) while the remaining three phosphates remained free. In contrast, Johnson et al.’s (2012) study suggested that IHP forms outer-sphere complexes with goethite. Intramolecular HBs are observed between adjacent phosphate groups and intermolecular HBs are observed between IHP and water. In literature, there is no consensus on the number of IHP’s phosphates that interact with minerals, for instance: four (Ognalaga et al., 1994), three (Guan et al., 2006; Xu et al., 2017), two and one (Celi et al., 2003) and 0 (Johnson et al., 2012). Numerous studies show that IHP can compete with OP for the same binding sites and could release and replace OP on goethite (Turner et al., 2002). Interestingly, De Groot and Golterman (1993) showed that IHP adsorption on goethite had an inhibitory effect on OP adsorption. Also, their results showed that IHP replaced OP and inhibited its adsorption. Anderson and Arlidge (1962) investigation of IHP and GP interaction on clay minerals show that IHP is adsorbed more in quantity than GP. Xu et al.’s (2017) comparative study of OP, GP and IHP on hematite showed that IHP was adsorbed almost twice of OP and GP. In contrast, OP and GP adsorption values were close. A similar pattern of phosphate adsorption on goethite is observed in a recent study by Amadou et al. (2022). Summarizing IHP interaction with minerals, IHP interacts with minerals through multiple phosphate groups and therefore, strongly adsorbs at the surface compared to phosphates with a single phosphate group. A consensus on IHP’s dominant motif is not achieved in the literature.

3.2 Molecular Modelling and Computational Details

Goethite is an orthorhombic crystal containing ferric iron coordinated by six oxygen atoms with the unit cell lattice constants: $a = 9.95$, $b = 3.01$, $c = 4.62$ Å. Its unit cell contains 16 atoms, i.e., four $\text{FeO}(\text{OH})$ units. To understand the goethite–OP/GP/IHP–water complex interactions, two common surface planes, (010) and (100), of goethite are considered here. The (010) goethite surface is known for its high stability (Xiu et al., 2016; Guo and Barnard, 2011), whereas the (100) goethite surface plane is one of the most abundant ones (Cornell and Schwertmann, 2003; Rakovan et al., 1999). The goethite surface planes, (010) and (100) are modeled by repetition of the goethite unit

cell as: $2a \times 4b \times 5c$ and $1a \times 8b \times 5c$, respectively, see Fig. 3.4. Each model comprises 640 atoms (160 Fe, 160 H, and 320 O atoms). Both surface planes exhibit unsaturation at the surface with active surface sites and are modeled as undercoordinated surfaces, as shown in Fig. 3.2. This aligns with experimental findings that phosphates adsorption occurs mainly at $\text{pH} < \text{PZC}$, where the surface has unsaturated active sites with overall positive charge (Celi et al., 2001; Li et al., 2017). This also mimics common acidic soil conditions, which have a pH range of 3–6. In this pH range, the adsorbed phosphates are deprotonated (Tejedor-Tejedor and Anderson, 1990; Persson et al., 1996; Ahmed et al., 2020) and the water is adsorbed to remaining active surface sites. The initial models, see Fig. 3.4, are modeled with neutral phosphate molecules. During the first few pico-seconds (ps) of equilibration, the phosphates are deprotonated and the unsaturated surface sites are occupied by water molecules, reflecting the experimental findings under acidic soil conditions.

Regarding binding motifs, three main motifs: **M**, **B** and **BB** found in literature (Abdala et al., 2015) are considered here for OP at the goethite surface. As GP interacts with the surface via the phosphate group, the same motifs are also considered for goethite–GP complexes. At both surface planes, (010) and (100), **M** motif is considered for goethite–OP/GP complexes, the **B** motif is considered only at (010) surface plane as the interatomic distance between surface Fe atoms is not feasible for OP/GP to form **BB** motif. The **BB** is considered only at the (100) surface plane as it is more favorable to form than the **B** motif. For IHP, additional **3M** ($3\text{Fe} + 3\text{O}$) and **4M** ($4\text{Fe} + 4\text{O}$) are considered at (010) and (100) surfaces, respectively. These motifs are chosen based on the individual phosphate group’s feasibility of bonding with surface iron atoms. Modeling different initial configurations for each binding motif could give more information about the mineral–phosphate interactions. However, as high-level molecular simulations are computationally expensive, only binding motifs observed in the literature are considered. First, a vacuum layer of about 18 Å is added in the perpendicular direction (along the z axis) between goethite periodic slabs to model these motifs. Then the phosphates are added to the goethite surface, forming the desired motif in the vacuum region. To simulate the soil solution and its prominent role in influencing the interactions of the phosphates with the mineral surfaces, the goethite–phosphate complexes are solvated with water. The density of water is chosen to be $\approx 1 \text{ g cm}^{-3}$, and water molecules are added perpendicular to the surface plane with a height of $\approx 18 \text{ Å}$ by using the solvate plugin of visual molecular dynamics (VMD) package (Humphrey et al., 1996). The bottom layer of goethite is kept fixed during the simulation to mimic the underlying extended goethite bulk characteristics. This also avoids artefacts due to the water interaction in the next box image.

Even though ab initio methods provide better accuracy, the computational costs restrict their applicability to large systems. One could simulate a reduced system size to avoid this, but this might incorporate unnecessary artefacts due to a finite simulation box that

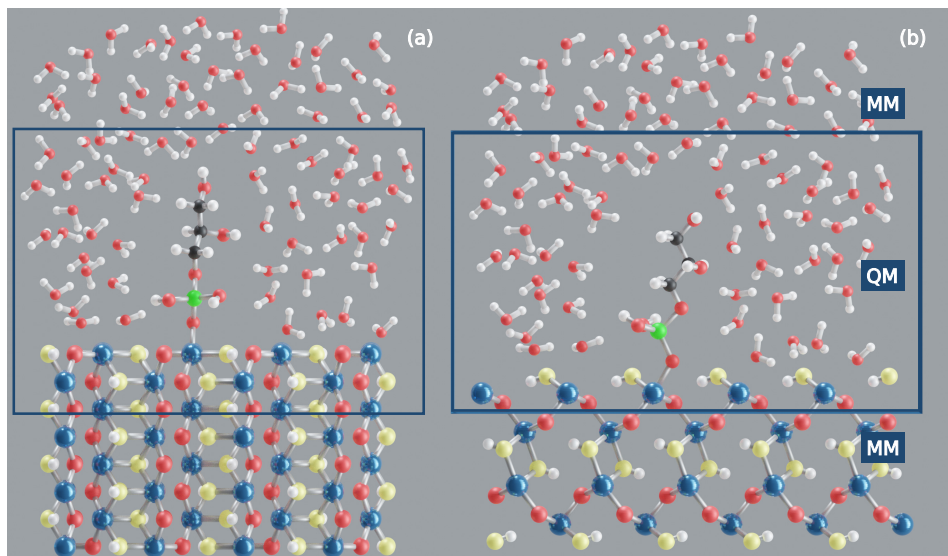


Figure 3.4: Goethite–GP–Water complexes: (010) goethite–GP–water complex (a) and (100) goethite–GP–water complex (b). Blue, red, yellow, white, black, and green colors correspond to iron, bridging oxygen, hydroxyl oxygen, hydrogen, carbon, and phosphorus atoms, respectively. The box denotes QM box of the model. (Ganta et al., 2021a,b).

alters the goethite–phosphate interactions. Therefore, the quantum mechanics/molecular mechanics (QM/MM) (Senn and Thiel, 2009) method is adopted here because of the large number of atoms (≈ 1200) in each complex. In QM/MM methods, the reactive part of the system where the targeted reaction happens is modeled using the QM method, while the rest of the system is treated with MM. For instance, our focus is on goethite–phosphate interaction which is local at goethite–water interface and therefore, the top two layers of goethite surface, phosphate and solvating water within a layer of ≈ 10 Å perpendicular to the surface are chosen as QM part and the rest of the system as MM. The QM box dimension is chosen the same as the total simulation box dimension in x and y directions, but it is confined only to cover the reactive region along the z direction.

The simulations have been performed using the CP2K (CP2K, 2017) package with electrostatic embedding QM/MM method. The electrostatic embedding QM/MM method allows the MM atoms to polarize the QM atoms, which provides a more accurate picture of goethite–phosphate interactions. The QM region is defined with density functional theory (DFT) as implemented in the quickstep code (VandeVondele et al., 2005) and MM by the FIST package (Mundy et al., 2017). In quickstep code, a hybrid Gaussian and plane wave (GPW) dual basis method is used with ionic cores described by Goedecker-Teter-Hutter (GTH) pseudopotentials (Krack, 2005) in combination with the Perdew-Burke-Ernzerhof (PBE) (Perdew et al., 1996) exchange–correlation functional

and the Grimme D3 empirical dispersion correction (Grimme et al., 2010). The valence electrons of all atoms are defined with the double- ζ valence polarized MOLOPT (DZVP-MOLOPT-SR-GTH) basis set except water for which the single- ζ valence (SZV-MOLOPT-SR-GTH) basis set is used to reduce computational cost (VandeVondele and Hutter, 2007). The SCF convergence threshold was chosen to be 10^{-5} Hartree. The MM part is described by classical force fields (FF). The goethite surface is modeled with the CLAYFF (Cygan et al., 2004) while water is modeled with the single point charge (SPC) water model (Berendsen et al., 1987) and OP/GP/IHP with CHARMMFF using the SwissParm tool (Zoete et al., 2011). Both CLAYFF and CHARMMFF are compatible with the SPC water model. The interaction between the QM and MM parts in CP2K is implemented using the Gaussian expansion of the electrostatic potential method (GEEP) (Laino et al., 2006), wherein the MM charge is distributed by defining it using Gaussians instead of point charges to avoid electron spilling. QM/MM-based canonical (NVT, i.e., constant number of atoms N , volume V and temperature T) MD simulations are performed with a 0.5 fs time step while the temperature was maintained at 300 K using velocity rescaling thermostat (CSVR) (Bussi et al., 2007). The first ten ps of each trajectory are assigned for the equilibration, and the remaining trajectory (production trajectory) is used for analysis.

Regarding the diaspore–phosphate–water simulations, an identical procedure as mentioned above is followed to perform the simulations, as diaspore is isomorphous with goethite. More detailed information regarding diaspore and goethite simulations are presented in Appendix. A and also at corresponding publications: (010) diaspore–GP/IHP–water (Ganta et al., 2019), (100) diaspore–GP/IHP–water (Ganta et al., 2020), (010) goethite–GP/IHP–water (Ganta et al., 2021a), (100) goethite–OP/GP/IHP–water (Ganta et al., 2021b).

3.3 Analysis

Interaction Energies

The modeled goethite–phosphate–water complexes comprise three sub-systems or fragments. Often one wants to find the interaction energy between the combination of two sub-systems along the production trajectory. The pair interaction between two sub-systems is calculated using the CP2K software, which separates the influence of the third sub-system from the selected ones. The interaction energy between the goethite and phosphate is given as:

$$E_{\text{interaction}} = E_{\text{goethite-phosphate}} - (E_{\text{goethite}} + E_{\text{phosphate}}) \quad (3.1)$$

Even though water influences the phosphate geometry, it is not included in the above equation. However, the calculated binding energies are overestimated if basis set super-

position error (BSSE) is not considered. This error arises as the energies of individual sub-systems are usually higher if only the basis functions of individual sub-systems are used. This error can be corrected if the energies of individual sub-systems are calculated in the presence of basis functions of both sub-systems. This allows the sub-system wavefunction to relax further and provide better energy values without overestimating. Similarly, the interaction energies between goethite–water:

$$E_{\text{interaction}} = E_{\text{goethite-water}} - (E_{\text{goethite}} + E_{\text{water}}) \quad (3.2)$$

and phosphate–water is given as:

$$E_{\text{interaction}} = E_{\text{phosphate-water}} - (E_{\text{phosphate}} + E_{\text{water}}) \quad (3.3)$$

The interaction energies involving water are divided by the number of water molecules in the simulation box to calculate interaction energies per water molecule.

HB Analysis

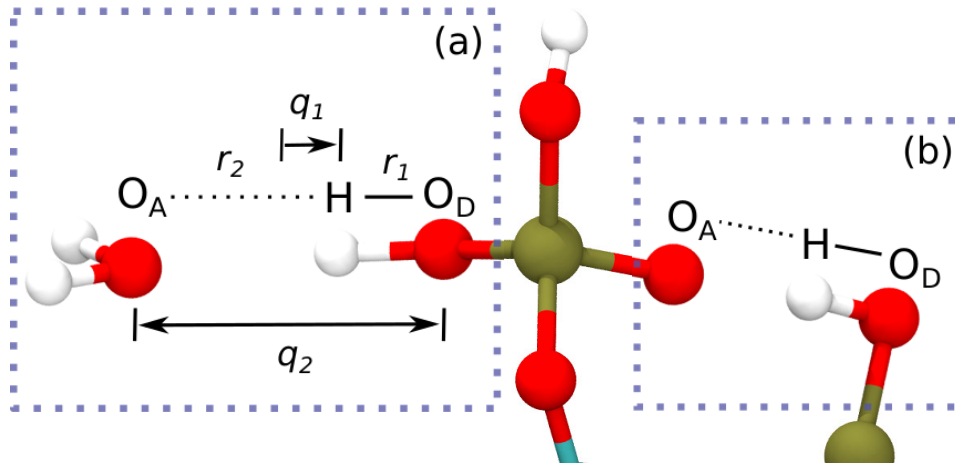


Figure 3.5: Definition of coordinates q_1 and q_2 in an HB between water's oxygen and IHP's oxygen from a phosphate group (a) (Limbach et al., 2009), intramolecular HB in IHP (b) (Ganta et al., 2019).

HBs play an important role in influencing mineral–phosphate interactions (Parfitt and Atkinson, 1976; Persson et al., 1996; Johnson et al., 2012). Intermolecular HBs are observed mainly between phosphates and water as well as between mineral surface and water. Interestingly, intramolecular HBs are observed between adjacent phosphate groups of IHP (Johnson et al., 2012). Therefore, there is a need to understand the strength of these hydrogen bonds theoretically.

Here, the HB strengths are analyzed using their geometrical correlations expressed in terms of the coordinates q_1 and q_2 (Strassner, 2006; Limbach et al., 2009; Zentel and Kühn, 2017) where $q_1 = \frac{1}{2}(r_1 - r_2)$ Å and $q_2 = (r_1 + r_2)$ Å. Here r_1 and r_2 denote the distance between donor oxygen and hydrogen (O_D-H) and distance between hydrogen and acceptor oxygen ($H \cdots O_A$), respectively, see Fig. 3.5a. The same holds for intramolecular HBs between phosphate groups for the IHP case, see Fig. 3.5b. Thus, q_1 denotes the hydrogen deviation from the HB's center and q_2 denotes the total HB length. In addition, $q_1 < 0$ indicates that the hydrogen stays with the donor oxygen, whereas $q_1 > 0$ denotes a proton transfer to the acceptor. A HB will be called strong if r_2 is about 1.2–1.5 Å and thus q_2 ($O_D-H \cdots O_A$) about 2.2–2.5 Å. When $r_1 \approx r_2$, i.e., q_1 tends to zero. Similarly, moderate and weak HBs have r_2 distances ranging from 1.5–2.2 Å (q_2 from 2.5–3.2 Å and $r_1 < r_2$) and 2.2–3.2 Å (q_2 from 3.2–4 Å and $r_1 \ll r_2$), respectively. In this study, HB analysis is performed only for the QM part of the system because we are mainly interested in the interface region. This region is our reactive system which includes all reactions concerning and affecting the surface binding/adsorption process.

4 Summary of Simulation Results

This chapter summarizes the current thesis results and outlines the highlights of the corresponding publications. The focus is on common phosphates like glycerolphosphate (GP) and inositol hexaphosphate (IHP) interacting with abundant soil minerals, i.e., goethite (α -FeOOH) and diaspore (α -AlOOH). In forest soils, phosphates generally have an overall negative charge and interact with positively charged surfaces like soil minerals. Goethite is one of the most abundant and reactive soil minerals having an Fe^{+3} oxidation state, whereas diaspore is isomorphous with goethite with Al^{+3} oxidation state. These minerals often exhibit an overall positive surface charge that attracts phosphates to their surface, which leads to the binding of phosphates on reactive sites on minerals. In addition to pure minerals, amorphous Fe/Al hydroxides also exist in nature, emphasizing the need to study these minerals. The current thesis provides a molecular level picture of interactions in mineral–phosphate–water complexes and analyzes the factors that influence them. Molecular dynamics (MD) simulations provide a framework to simulate interatomic interactions. However, a detailed description of these interactions with Quantum Mechanics (QM) methods is expensive; therefore, the current simulations are performed using hybrid electrostatic embedding quantum mechanics/molecular mechanics (QM/MM) based MD simulations to investigate interactions in mineral–phosphate–water complexes. In the hybrid QM/MM approach, the reactive region is described with QM and others with MM to reduce computational cost and time; see Section. 2.1 for an overview of the methods.

Previous studies showed that the mineral–phosphate interaction in diaspore/goethite–IHP/GP–water complexes is mainly through covalent bonds and proton transfer events. Furthermore, the binding energy of the mineral–phosphate complex depends on the total number of covalent bonds. However, factors that lead to the stable binding motifs for diaspore/goethite–IHP/GP complexes were not explored thoroughly. Hence, the typical surface planes of diaspore and goethite are investigated here to understand the effect of surface termination and its saturation on phosphate’s adsorption (more details in Chapter. 3). The initial mineral–phosphate binding motifs at the beginning of the simulations are modeled to match the stable motifs found in experiments. The mineral and phosphate binding strength is calculated by averaging the binding energies of diaspore/goethite and IHP/GP at multiple timesteps along the production trajectory. In literature, the water interaction with minerals is found mainly through the formation of covalent bonds at the mineral surface. Its interaction with phosphates is mainly through hydrogen bonds (HBs). Therefore, water’s influence on the mineral–phosphate binding

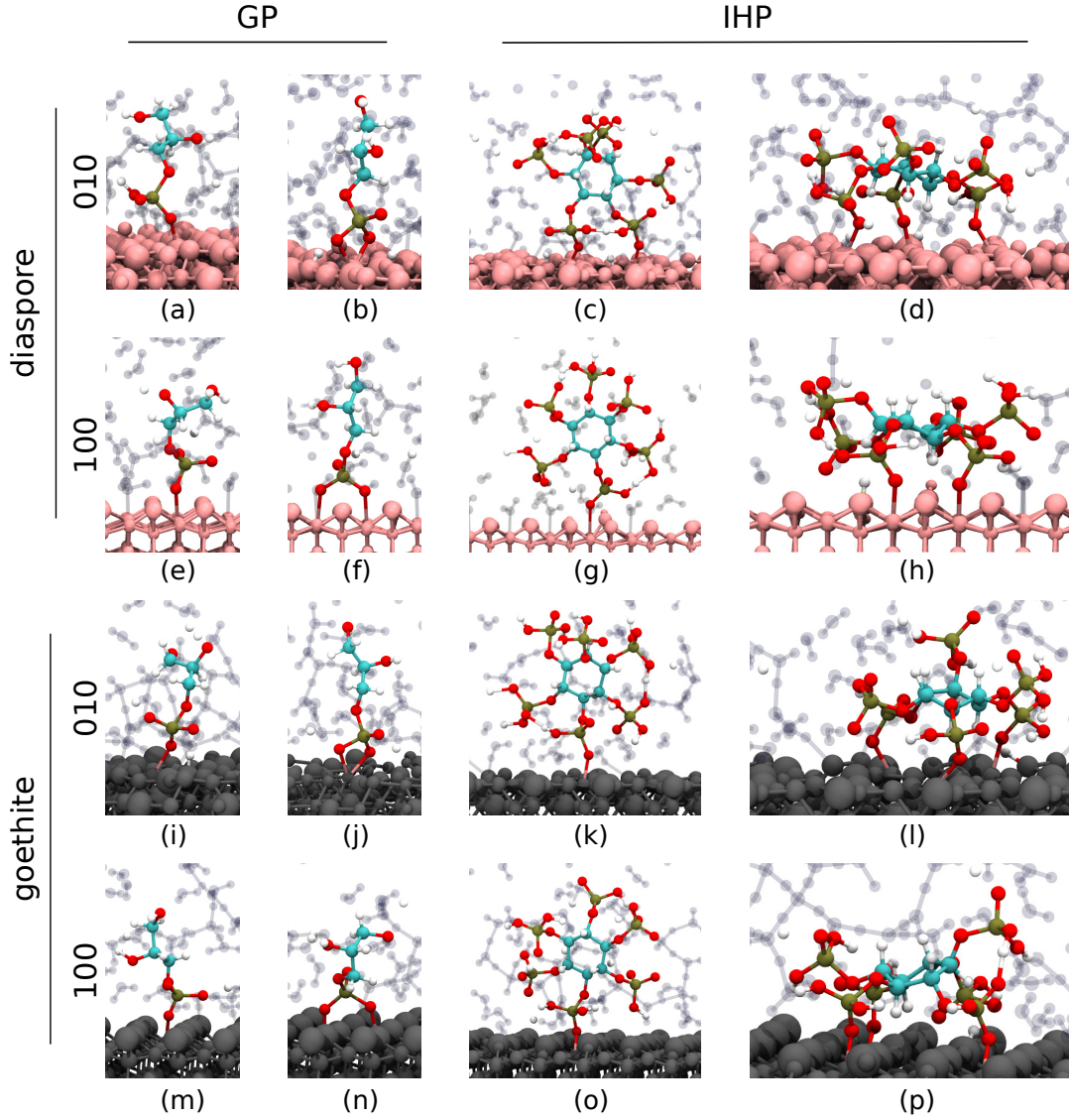


Figure 4.1: Snapshots of GP/IHP at diaspore/goethite–water interface (Ganta et al., 2019, 2020, 2021a,b).

motifs is studied by calculating the phosphate–water and mineral–water binding energies and analyzing the strength of HBs between them. Further, the phosphate–water interactions that restrict the mineral–phosphate binding motifs are highlighted through trajectory snapshots. The following sections outline diaspore and goethite’s (010) and (100) surface planes and phosphates, IHP and GP’s interaction with them in the presence of water. For the goethite (100) surface, orthophosphate (OP) is also included in our study to correlate with experiments.

Diaspore (010)

Diaspore (010) surface interaction with glycerolphosphate (GP) and inositol hexaphosphate (IHP) (Ganta et al., 2019) leads to the formation of monodentate (**M**, $1\text{Al} + \text{O}$) and bidentate (**B**, $\text{Al} + 2\text{O}$ or $2\text{Al} + 2\text{O}$) motifs for GP and two (**2M**, $2\text{Al} + 2\text{O}$), three (**3M**, $3\text{Al} + 3\text{O}$) monodentate motifs for IHP, see Fig. 4.1(a–d). Examining diaspore–GP complexes, GP **B** motif remained stable throughout the production trajectory and exhibited higher interaction energies than the **M** motif. The interaction energies discussed here are time averages of production trajectories, which quantitatively measure the interaction strength. The interaction energy per bond of the **B** motif is 2.4 times higher than of **M**. The higher overall interaction energy in the former case is due to additional bond and proton transfer to the surface. Both motifs formed around seven HBs with water. The strength of these HBs is often strong to moderately strong (see Section. 3.3 for details about calculating HB strength).

For diaspore–IHP complexes (see Fig. 4.1c–d), IHP formed stable **2M** and **3M** motifs. The IHP **3M** motif has higher overall interaction energy than the **2M** motif. However, it has 1.2 times weaker interaction energy per bond due to a mismatch between the phosphate group’s position in IHP and the surface Al sites. This mismatch also introduces strain into the **3M** motif and restricts the formation of additional P–O–Al bonds. The IHP **B** motif transformed to **2M** motif due to intramolecular HBs between adjacent phosphate groups and its interaction with nearby water molecules. The IHP–water interaction caused considerable fluctuation of IHP concerning the diaspore surface, leading to the dissociation of the covalent bond in the **B** motif. Intramolecular HBs are found to be strong to moderately strong. The binding motif interaction energies comparison shows that IHP binds stronger than GP. The results agree with experiments that the number of phosphate groups in phosphate is an important factor in deciding the P–binding strength. The phosphate’s interaction with minerals does not affect the organic moiety.

Water played an essential role in these interactions through multiple HBs and proton transfer events (see Fig. 4.1a–d) with phosphates and diaspore. Both GP motifs formed around 7 HBs with water, whereas IHP ones formed more than 15 HBs each, mostly strong to moderately strong HBs. The IHP–water interaction energy per water molecule is more than thrice that of GP, suggesting that IHP interacts more strongly with water. The reason is that IHP has a higher water–accessible surface area compared to GP. The interfacial water molecules interacted strongly with the diaspore surface by forming **M** motifs and strong HBs at the diaspore–water interface. Almost all surface Al atoms have formed a **M** motif with water oxygens. Some water molecules dissociate into protons and hydroxyl groups, leading to proton transfer processes at the interface. The diaspore–water interaction energy per water molecule in all motifs here is higher than that of IHP/GP–water suggesting that water interacts more strongly with dias-

Table 4.1: Time-averaged interaction energies divided by the number of bonds of selected stable binding motifs, bond lengths and distances for phosphates at diaspore/goethite-water interface.

P _o	motif	E _{int} /bond(kcal/mol)	Al-O _P (Å)	Al-P (Å)
Diaspore (010) surface (Ganta et al., 2019)				
GP	M	-63	1.90	3.3
	B	-148	2.03 & 2.05	2.65
IHP	M	-170	1.84 & 1.87	3.15 & 3.25
	3M	-145	1.90 & 1.88 & 1.86	3.25 & 3.17 & 3.18
Diaspore (100) surface (Ganta et al., 2020)				
GP	M	-23	2.3	3.4
	B	-15	2.3 & 2.4	3.3
IHP	M	-33	2.4	3.5
	2M	-109	2.1 & 2.2	3.3 & 3.4
Goethite (010) surface (Ganta et al., 2021a)				
GP	M	-112	2.0	3.2
	B	-61	2.2 & 2.3	2.6
IHP	M	-190	1.95	3.2
	3M	-86	2.07 & 1.9 & 1.91	3.3 & 3.4
Goethite (100) surface (Ganta et al., 2021b)				
OP	M	-35	2.1	3.5
	B	-41	2.01 & 1.97	3.19 & 3.2
GP	M	-48	1.99	3.19
	B	-38	2.01 & 2.03	3.19 & 3.1
IHP	M	-85	2.0	3.1
	3M	-72	2.01 & 1.98 & 1.94	3.1 & 3.2 & 3.4

pore than IHP/GP. The diaspore–IHP/GP interaction energies are dominant compared to diaspore–water interaction energies per water molecule, suggesting phosphate could replace water bound to the diaspore surface.

Diaspore (100)

At diaspore (100) surface, the GP formed stable **M** and **B** motifs as shown in Fig. 4.1e–f. In contrast to GP **B** motif in diaspore (010), the dynamics of the GP **B** motif here show elongated and compressed Al–O covalent bonds in an alternating see–saw fashion suggesting a strain in covalent bonds, see Fig. 4.2. Therefore, the interaction energy per bond for GP **B** motif case is 1.5 times less than for the **M** motif. However, the overall interaction energy of the **B** motif dominates the **M** motif suggesting that the former motif is more likely to form.

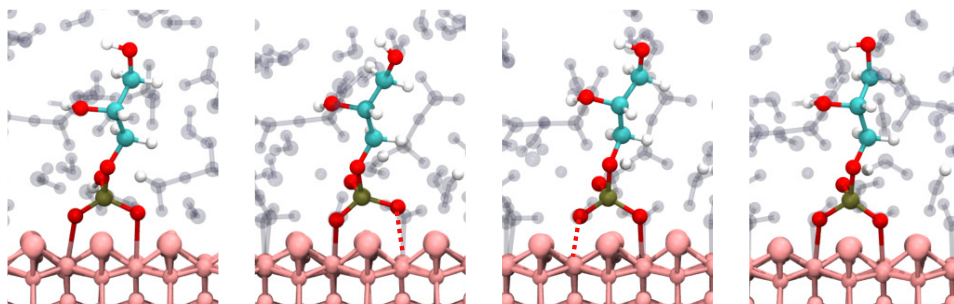


Figure 4.2: Diaspore-GP **B** motif along the production trajectory (Ganta et al., 2020).

For diaspore–IHP complexes, IHP formed stable **M** and **2M** motifs with diaspore (100) surface, see Fig. 4.1g,h. The initial **B** and **4M** motifs transformed to form **M** and **2M** motifs, respectively. The reason for the transformation of **B** motif is the same as discussed in the diaspore (010) surface case. Whereas the **4M** transformation to **2M** motif is due to the diaspore (100) surface termination. As shown in Fig. 4.3, the Al–O bonds are inclined due to repulsion between IHP oxygens and surface hydroxyl oxygens. During equilibration, some oxygens in Al–O bonds dissociate from the surface Al atoms as they are restricted to the region (see regions R1–R2 in Fig. 4.3) between surface hydroxyl groups. Consequently, IHP **4M** motif transforms to **2M** motif. The diaspore–IHP **2M** motif has more than three times higher interaction energy per bond than **M** motif and is hence more likely to form with a diaspore (100) surface. IHP formed intramolecular HBs between adjacent phosphate groups, see Fig. 4.1g.

The water interaction with GP showed multiple proton transfers from GP to water (see Fig. 4.1e–f) with few strong to moderately strong HBs. The see–saw motion of GP in **B** motif is also influenced by GPs interaction with surrounding flexible water molecules. IHP also showed proton transfer events to water in addition to multiple strong HBs.

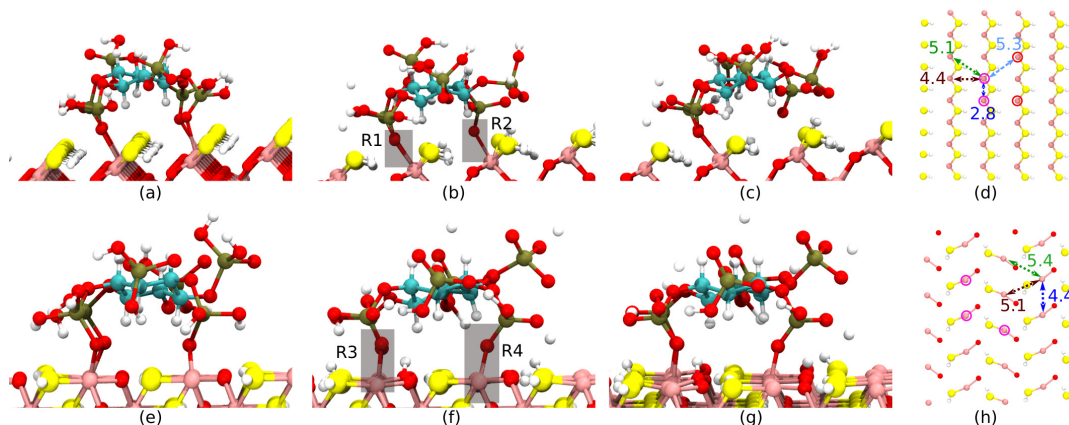


Figure 4.3: Snapshots along the MD trajectory for the 100 diaspore-IHP-water **2M** motif (a–c) and the top view of surface atoms showing interatomic Al–Al distances (d). Similarly, the snapshots of **3M** motif (e–g) and the top view of surface atoms show interatomic Al–Al distances (h). The circle around the Al atom denotes the site of Al–O_P bonds in **2M** and **3M** motif, respectively, wherein the red circle denotes the site where Al–O_P bond dissociated. Note that water is ignored in this image for better view (Ganta et al., 2020). Regions R1–R4 are selected regions for understanding Al–O bonds dissociation.

The IHP–water interaction energy is about 2.3 times higher than GP–water interaction energies. At the diaspore–water interface, an average of 17 out of 40 surface Al atoms formed **M** motif with water. Some water molecules also formed moderately strong HBs with surface Al atoms. However, the diaspore–IHP/GP interaction energies are higher than the diaspore–water interaction energy.

The effect of surface saturation and its termination is evident with the interaction energy differences observed for IHP/GP at diaspore (010) and (100) surfaces, see Table. 4.1. A highly saturated (100) surface with five oxygens (O^{−2}/OH[−] groups) coordinating the surface Al atoms showed weak interaction with surrounding molecules compared to a (010) surface with only four oxygens coordinating the surface Al atoms. The electrostatic potential of these surfaces in Fig. 4.4 shows that the (010) surface could interact more strongly with negatively charged molecules than the (100) surface. The GP **B** motif dominates **M** at both surface planes, with the GP **B** motif at the diaspore (010) surface interacting ten times stronger than at the diaspore (100) surface. In GP **B** motif at the diaspore (010) surface, two oxygens from the phosphate group are coordinated to the same surface Al atom. In contrast, on the diaspore (100) surface, the oxygens from phosphate are coordinated with two adjacent surface Al atoms resulting in unfavorable large O–Al–O angles for strong binding. This resulted in a weaker **B** motif in the latter surface plane. Similarly, IHP could only form **2M** motif at the diaspore (100) surface,

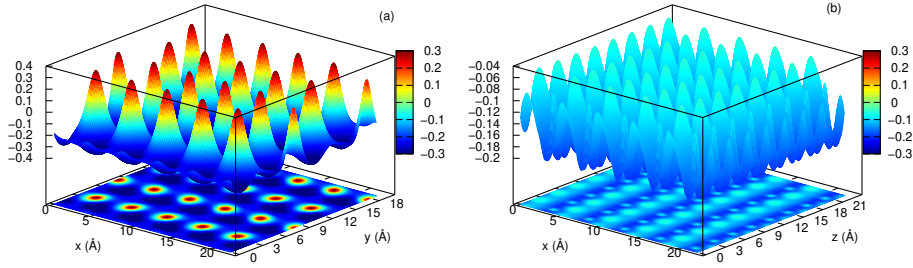


Figure 4.4: Electrostatic potential (a.u.) at one Å (perpendicular to the surface) for the bare (010) diaspore surface plane (a) as well as for the bare (100) diaspore surface plane (b). These have been calculated for bare surfaces without involving phosphates and water (Ganta et al., 2020).

but at (010) surface, it formed **3M** motif with about twice the overall interaction energy. In addition to IHP/GP, the water showed weaker interaction at the diaspore (100) surface. The diaspore–water interaction energy in the case of the diaspore (100) surface is 3.4 times smaller than that of (010) case. The number of water **M** motifs with surface Al atoms is half at the diaspore (100) surface compared to (010). Further, the IHP/GP–water interactions are also affected because the water accumulated more around the (010) surface than (100), see Fig. 4.5. For both surfaces, the diaspore–water interaction energy per water molecule is lower than diaspore–IHP/GP, suggesting phosphates could replace water bound to the diaspore.

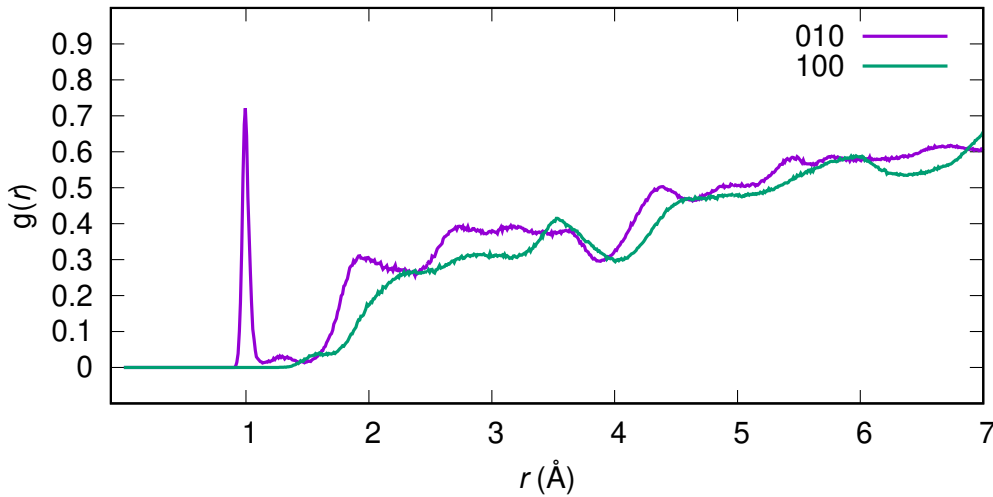


Figure 4.5: Comparison of radial distribution functions calculated for (010) and (100) diaspore surface oxygens and hydrogens of water (Ganta et al., 2020).

Goethite (010)

Goethite (010) surface interaction with GP (Ganta et al., 2021a) shows that it forms similar motifs as for diaspore (010) surface, see Fig. 4.1i–j. The interaction energy per bond of the GP **M** motif is higher than the **B** motif, but the overall interaction energy for the latter motif is twice that of the former. This suggests that **B** motif is more likely to form. However, Li et al. (2017) suggested that GP might only form **M** motifs due to steric hindrance of organic moiety in GP molecule. Along these lines, other literature suggests that GP or similar molecules with a single phosphate group dominantly form **M** motifs. The study by Abdala et al. (2015) related to surfacing loading of orthophosphate (OP) on goethite showed that at low surface loading, OP forms **B** motif and at high surface loading, the **M** motif dominates. The current simulation setup corresponds to a low surface loading situation; therefore, the **B** motif is more dominant than **M**. GP formed around eight HBs with water and multiple protons transfer events in both motifs.

IHP interaction at goethite (010) surface formed stable **M** and **3M** motifs, see Fig. 4.1k,l. Similar to diaspore surfaces, it interacted through multiple phosphate groups. Unlike at the diaspore (010) surface, the IHP initial **M** motif did not transform to **2M** motif. However, the initial **B** motif transformed to **M**. The interaction energy per bond of **3M** motif is smaller than that of **M** motif, but its overall interaction energy is higher than the latter. The IHP binding motifs at goethite from literature range from **4M**, **3M**, **2M**, **M** and zero. In current results and from diaspore–IHP motifs (Ganta et al., 2019, 2020), IHP formed three different types of stable motifs, namely **M**, **2M** and **3M**. Therefore, one can conclude that based on interface interaction, IHP could form different types of binding motifs. Here, IHP formed more than 20 HBs with water, often strong to moderately strong ones and donated multiple protons to water in both motifs. Compared to GP, IHP exhibited strong interaction with both goethite and water.

Water interacts strongly with both IHP and GP and also with the goethite surface. It forms multiple **M** motifs with surface iron atoms, proton transfer events and HBs with goethite surface. The goethite–water interaction energy for the GP **M** motif is 1.2 times larger than that of IHP **M** motif, supporting the finding by Celi et al. (2001) that IHP adsorption on goethite makes the surface more negative.

To further characterize the binding motifs, the IR spectra originating from the stable binding motifs of the goethite–IHP/GP–water complexes were investigated. For the GP, the IR spectra calculated for **M** and **B** motifs matched well with spectra of GP and phosphates with a single phosphate group from experimental and theoretical studies in the literature. Similarly, the calculated IR spectra for IHP match well with experimental spectra from literature, see Fig. 4.6. The match of calculated spectra with experiments suggests that the current modeling approach is valid for simulating mineral–phosphate–water interactions.

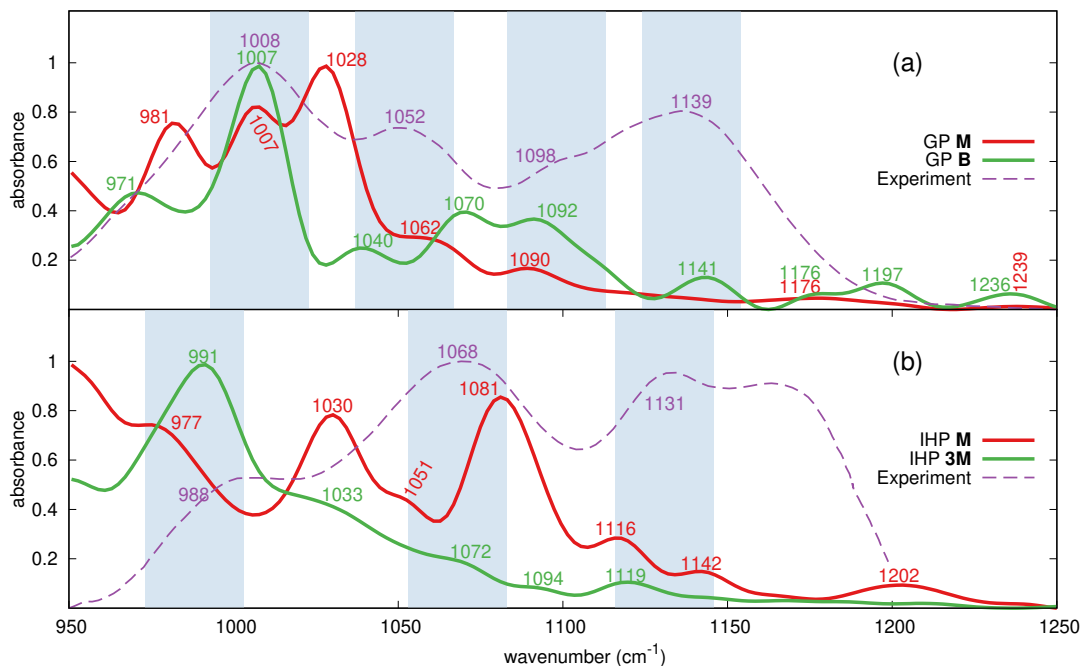


Figure 4.6: Comparison of GP and IHP (at goethite) IR spectra with experimental spectra from (Li et al., 2017) and (Yan et al., 2015), respectively. The blue rectangle denotes region within $\pm 15 \text{cm}^{-1}$ around frequencies observed in experimental studies (Ganta et al., 2021a).

Goethite (100)

In addition to GP and IHP, orthophosphate (OP) has been studied to understand its adsorption onto the goethite (100) surface plane in the light of adsorption experiments (Ganta et al., 2021b). As goethite is isomorphous with diasporite, the diasporite (100) surface, as seen in Fig. 4.2, is similar to goethite (100) surface but surface metal atoms as Fe. OP is one of the most abundant inorganic phosphates, which often exists in the deprotonated state with an overall negative charge and hence attracts to the overall positively charged surface. Goethite–OP complexes show that OP **B** motif has higher interaction energy per bond than **M** motif, suggesting that the additional bond in **B** motif is favorable. OP **B** motif’s overall interaction energy is 2.3 times higher than of **M** motif. In both motifs, two proton transfer events are observed from OP to water forming an average of five HBs each.

Goethite–GP complexes show that GP formed stable **M** and **B** motifs. In contrast to OP, the **B** motif interaction energy per bond is less than the **M** motif, suggesting the

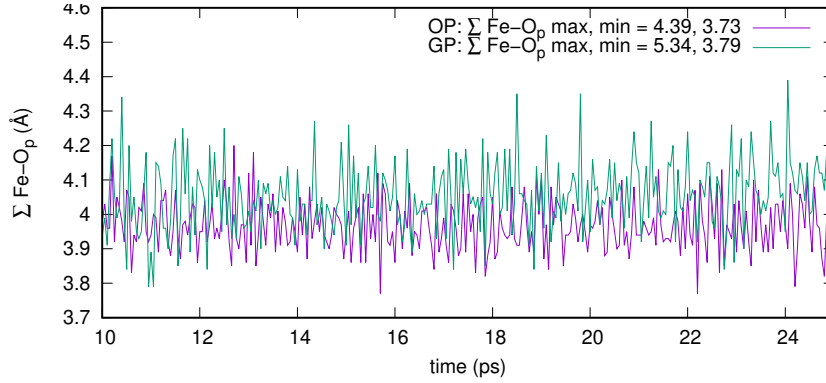


Figure 4.7: Sum of Fe–O bond lengths observed in goethite–OP and goethite–GP **B** motifs (Ganta et al., 2021b).

additional covalent bond is unfavorable. Even though both OP and GP interact with goethite through a single phosphate group, the interaction energy pattern is not the same. The glycerol group present in GP increases the water-accessible surface area for GP and hence its interaction with water compared to OP. This interaction strains the Fe–O covalent bonds of the GP **B** motif. Therefore, the GP molecule, similar to GP interaction at the diaspore (100) surface discussed above, performs see-saw like motion. The time averaged Fe–O bond lengths of OP and GP **B** motifs show that the latter bonds are elongated, see Fig. 4.7. Therefore, the OP **B** motif’s interaction energy is 1.1 times greater than that of the GP **B** motif. Both GP motifs showed that GP formed around seven HBs with water with more than two proton transfers. GP showed stronger interaction with water than OP because of its higher water-accessible surface area.

IHP formed stable **M** and **3M** motifs at goethite (100) surface. The initial **B** motif is unstable and transformed to **M** as seen in diaspore–IHP and goethite–IHP studies above. Interestingly, the initial **4M** motif transformed to **3M**, for the same reason as to why IHP transformed from initial **4M** to **2M** motif at diaspore (100) surface, see Fig. 4.3. The **3M** motif showed higher overall interaction energy, but the interaction energy per bond is less than **M** motif. This suggests that the alignment of IHP over goethite in **3M** motif weakens the overall strength of individual Fe–O covalent bonds. IHP has multiple proton transfers to water with more than 20 HBs with surrounding water molecules. Comparing the phosphate’s interaction energies, the order of interaction strength with the goethite surface is IHP > OP > GP and water is IHP > GP > OP.

The adsorption data from collaboration with the experiment provided new insight into the binding interaction energies from modeling. The adsorption isotherms based on Freundlich model (Freundlich, 1907) are mainly used to correlate the simulation findings. The Freundlich equation reads:

$$Q_{ads} = K_f C_e^{m_f} \quad (4.1)$$

Q_{ads} denotes the adsorbate quantity adsorbed per unit mass of adsorbent, C_e is adsorbate equilibrium concentration in solution, K_f is Freundlich adsorption constant or Freundlich unit adsorption capacity, and n_f is the Freundlich exponent. Correlating to modeling, the term K_f relates to the phosphate binding energies, whereas n_f denotes the extent of surface saturation that affects the interaction of the next incoming P molecules to the surface. The order of K_f values are in line with interaction energy strength order GP **B** < OP **B** < IHP **3M** (Ganta et al., 2021b). However, OP K_f values are more than twice the GP value, but the interaction energies obtained through simulations do not hold the same relation, see Table. 4.1. This suggests that GP might predominantly form **M** motif instead of **B**. Also, the IHP K_f value is 1.58 times of OP, meaning that IHP might form both **M** and **3M** motifs. The order of n_f values, IHP < GP < OP, shows that IHP saturates the surface faster than GP and OP and avoids subsequent incoming phosphates interaction with goethite. This is because multiple unbounded phosphate groups, often unprotonated, induce a negative charge to the surface compared to GP or OP. The n_f order could be related to the total number of proton transfer events from phosphates at goethite–water interface. IHP showed more proton transfer events than GP and OP, whereas GP dominates OP.

5 Conclusions

Phosphorus (P) is a vital element for life on Earth, playing a crucial role in the growth of plants and animals. A potential future scenario involving a peak in P availability could disrupt global food production. Given the continuously growing global population, exploring ways to recycle phosphorus efficiently is essential. In addition to numerous experimental studies, molecular modeling methods can provide a comprehensive molecular level understanding of how P binds to soil minerals. In this thesis, we demonstrate this approach by investigating the impact of various important factors on the process and strength of P binding. These factors include the type of P-containing compound, the mineral surfaces and their planes, the degree of surface saturation, binding patterns, and the presence of water. Specifically, we conduct a molecular modeling study to examine the binding of common phosphates like glycerolphosphate (GP), inositol hexaphosphate (IHP), and orthophosphate (OP) to soil minerals such as goethite (α -FeOOH) and diaspore (α -AlOOH).

Based on both the modeling results and existing literature, we can make the following general observations and predictions:

- The adsorption of phosphates onto a mineral surface is significantly influenced by the degree of surface saturation and the surface's structure. A highly saturated surface tends to have weaker interactions with phosphates. Additionally, the positions of surface atoms play a crucial role in determining the binding patterns and their strength. If surface metal atoms are in an unfavorable position relative to phosphate oxygens, it can strain the covalent bonds between the mineral and phosphate or, in some cases, lead to temporary dissociation.
- Phosphates with a single phosphate group, such as OP and GP, typically form stable **M** and **B** motifs when binding to mineral surfaces. However, the dominant motif may change depending on the surface loading of phosphates. The organic part of organic phosphates can also affect their interaction with the mineral surface and the resulting binding motif.
- Phosphates with multiple phosphate groups, like IHP, can bind to the mineral surface through multiple phosphate groups. In this case, the alignment of phosphate groups with surface metal atoms significantly impacts their interaction with minerals. Unlike phosphates with a single phosphate group, IHP exhibits intramolecular HBs between adjacent phosphate groups. These HBs can be strong enough

to strain the covalent bonds between the mineral and IHP, occasionally causing dissociation. However, IHP can form stable **M**, **2M**, and **3M** motifs, with the dominant motif depending on the mineral–water interface interactions.

- The number of phosphate groups in a phosphate increases its binding strength with minerals. IHP exhibited stronger interaction than GP and OP. The order of binding strength at the goethite/diaspore–water interface can be estimated as IHP > OP > GP. Furthermore, phosphates induce a negative charge on goethite/diaspore, with IHP inducing the highest charge, followed by GP and OP.
- Water plays a significant role in goethite/diaspore–phosphate interactions. HBs between phosphate and water molecules can strain the covalent bonds between minerals and phosphates, depending on the water–accessible surface area of the phosphate. This also affects the stability of binding motifs. Multiple proton transfers from phosphates to water can result in negatively charged phosphates interacting with mineral surfaces. Water forms multiple **M** motifs with diaspore/goethite and strong hydrogen bonds, saturating the surface.
- The binding strength order of phosphates and water with goethite/diaspore can be projected as IHP > OP > GP > water. This suggests that IHP, GP, or OP can replace water at the diaspore/goethite surface, with IHP being capable of replacing OP and GP. This finding helps explain why IHP is more commonly found in forest colloid samples than other phosphates.
- Comparing goethite and diaspore surfaces, the binding energies of water and phosphates with diaspore are significantly higher compared to goethite. This indicates that the phosphates have a strong interaction with diaspore mineral. Therefore, one can suggest that the isomorphic substitution of Al with Fe in nature might further increase the phosphate binding capabilities of the goethite.

In the future, more comprehensive studies should encompass a wider range of soil minerals, various surface orientations for each mineral, an expanded array of phosphates and other related compounds, different levels of phosphate loading, consideration of organic matter and metal ions, and exploration across a range of pH values. These studies should aim to provide a more detailed and nuanced understanding of how phosphates are adsorbed onto soil minerals. This can be achieved through the application of diverse multi-scale molecular modeling techniques.

Bibliography

- Abdala, D. B., Northrup, P. A., Arai, Y., and Sparks, D. L. (2015). Surface loading effects on orthophosphate surface complexation at the goethite/water interface as examined by extended X-ray Absorption Fine Structure (EXAFS) spectroscopy. *J. Colloid Interface Sci.* 437, 297–303. doi:10.1016/j.jcis.2014.09.057
- Ahmed, A. A., Gros, P., Kühn, O., and Leinweber, P. (2018a). Molecular level investigation of the role of peptide interactions in the glyphosate analytics. *Chemosphere* 196, 129–134. doi:10.1016/j.chemosphere.2017.12.162
- Ahmed, A. A., Gypser, S., Freese, D., Leinweber, P., and Kuehn, O. (2020). Molecular level picture of the interplay between pH and phosphate binding at the goethite–water interface. *Phys. Chem. Chem. Phys.* doi:10.1039/D0CP04698A
- Ahmed, A. A., Gypser, S., Leinweber, P., Freese, D., and Kühn, O. (2019). Infrared spectroscopic characterization of phosphate binding at the goethite-water interface. *Phys. Chem. Chem. Phys.* 21, 4421–4434. doi:10.1039/C8CP07168C
- Ahmed, A. A., Leinweber, P., and Kühn, O. (2018b). Unravelling the nature of glyphosate binding to goethite surfaces by ab initio molecular dynamics simulations. *Phys. Chem. Chem. Phys.* 20, 1531–1539. doi:10.1039/C7CP06245A
- Amadou, I., Faucon, M.-P., and Houben, D. (2022). New insights into sorption and desorption of organic phosphorus on goethite, gibbsite, kaolinite and montmorillonite. *Applied Geochemistry* 143, 105378. doi:10.1016/j.apgeochem.2022.105378
- Andersen, H. C. (1980). Molecular dynamics simulations at constant pressure and/or temperature. *J. Chem. Phys.* 72, 2384–2393. doi:10.1063/1.439486
- Anderson, G. (2015). Assessing organic phosphorus in soils. In *The Role of Phosphorus in Agriculture* (John Wiley & Sons, Ltd), chap. 15. 411–431. doi:10.2134/1980.roleofphosphorus.c16
- Anderson, G. and Arlidge, E. Z. (1962). The adsorption of inositol phosphates and glycerophosphate by soil clays, clay minerals, and hydrated sesquioxides in acid media. *J. Soil Sci.* 13, 216–224. doi:10.1111/j.1365-2389.1962.tb00699.x
- Aquino, A. J., Tunega, D., Haberhauer, G., Gerzabek, M. H., and Lischka, H. (2008). Acid–base properties of a goethite surface model: A theoretical view. *Geochim. Cosmochim. Acta* 72, 3587–3602. doi:10.1016/j.gca.2008.04.037

- Baker, C. M. (2015). Polarizable force fields for molecular dynamics simulations of biomolecules. *Wiley Interdiscip. Rev. Comput. Mol. Sci.* 5, 241–254. doi:10.1002/wcms.1215
- Bazilevskaya, E., Archibald, D. D., Aryanpour, M., Kubicki, J. D., and Martínez, C. E. (2011). Aluminum coprecipitates with Fe (hydr)oxides: Does isomorphous substitution of Al³⁺ for Fe³⁺ in goethite occur? *Geochimica et Cosmochimica Acta* 75, 4667–4683. doi:10.1016/j.gca.2011.05.041
- Becke, A. D. (1988). Density-functional exchange-energy approximation with correct asymptotic behavior. *Phys. Rev. A* 38, 3098–3100. doi:10.1103/PhysRevA.38.3098
- Beek, J. and van Riemsdijk, W. (1979). Chapter 8: Interaction of orthophosphate ions with soil. In *Soil Chemistry: B. Physico-chemical Models*, ed. G. Bolt (Elsevier), vol. 5 of *Developments in Soil Science*. 259–284. doi:10.1016/S0166-2481(08)70663-9
- Bendt, P. and Zunger, A. (1982). New approach for solving the density-functional self-consistent-field problem. *Phys. Rev. B* 26, 3114–3137. doi:10.1103/PhysRevB.26.3114
- Berendsen, H. J. C., Grigera, J. R., and Straatsma, T. P. (1987). The missing term in effective pair potentials. *J. Phys. Chem.* 91, 6269–6271. doi:10.1021/j100308a038
- Berendsen, H. J. C., Postma, J. P. M., van Gunsteren, W. F., DiNola, A., and Haak, J. R. (1984). Molecular dynamics with coupling to an external bath. *J. Chem. Phys.* 81, 3684–3690. doi:10.1063/1.448118
- Berendsen, H. J. C., Postma, J. P. M., van Gunsteren, W. F., and Hermans, J. (1981). Interaction Models for Water in Relation to Protein Hydration. In *Intermolecular Forces: Proceedings of the Fourteenth Jerusalem Symposium on Quantum Chemistry and Biochemistry Held in Jerusalem, Israel, April 13–16, 1981*, ed. B. Pullman (Dordrecht: Springer Netherlands). 331–342. doi:10.1007/978-94-015-7658-1_21
- Boily, J.-F. (2012). Water Structure and Hydrogen Bonding at Goethite/Water Interfaces: Implications for Proton Affinities. *J. Phys. Chem. C* 116, 4714–4724. doi:10.1021/jp2110456
- Bol, R., Julich, D., Brödlin, D., Siemens, J., Kaiser, K., Dippold, M. A., et al. (2016). Dissolved and colloidal phosphorus fluxes in forest ecosystems—an almost blind spot in ecosystem research. *J. Soil Sci. Plant Nutr.* 179, 425–438. doi:10.1002/jpln.201600079
- Bolt, G. H. and van Olphen, H. (1985). The Surface Chemistry of Soils. *Clays and Clay Minerals* 33, 367–367. doi:10.1346/CCMN.1985.0330415
- Brady, N. (2017). *The Nature and Properties of Soils. 15th Edition*

- Breneman, C. M. and Wiberg, K. B. (1990). Determining atom-centered monopoles from molecular electrostatic potentials. The need for high sampling density in formamide conformational analysis. *Journal of Computational Chemistry* 11, 361–373. doi:10.1002/jcc.540110311
- Brooks, B. R., Bruccoleri, R. E., Olafson, B. D., States, D. J., Swaminathan, S., and Karplus, M. (1983). CHARMM: A program for macromolecular energy, minimization, and dynamics calculations. *Journal of Computational Chemistry* 4, 187–217. doi:10.1002/jcc.540040211
- Broyden, C. G. (1965). A class of methods for solving nonlinear simultaneous equations. *Math. Comput.* 19, 577–593. doi:doi.org/10.2307/2003941
- Bussi, G., Donadio, D., and Parrinello, M. (2007). Canonical sampling through velocity rescaling. *J. Chem. Phys.* 126, 014101:1–014101:6. doi:10.1063/1.2408420
- Cade-Menun, B. J. (2005). Characterizing phosphorus in environmental and agricultural samples by ³¹P nuclear magnetic resonance spectroscopy. *Talanta* 66, 359–371. doi:10.1016/j.talanta.2004.12.024
- Caldwell, A. G. and Black, C. A. (1958). Inositol hexaphosphate: III. Content in soils. *Soil Sci. Soc. Am. J.* 22, 296–298. doi:10.2136/sssaj1958.03615995002200040008x
- Caspers, H. (1984). OECD: Eutrophication of waters. Monitoring, assessment and control. — 154 pp. Paris: Organisation for economic co-operation and development 1982. *Int. Rev. Gesamten Hydrobiol. Hydrogr.* 69, 200–200. doi:10.1002/iroh.19840690206
- Celi, L., De Luca, G., and Barberis, E. (2003). Effects of interaction of organic and inorganic p with ferrihydrite and kaolinite-iron oxide systems on iron release. *Soil Sci.* 168, 479–488. doi:10.1097/01.ss.0000080333.10341.a4
- Celi, L., Lamacchia, S., Marsan, F. A., and Barberis, E. (1999). Interaction of Inositol hexaphosphate on clays: Adsorption and charging phenomena. *Soil Sci.* 164, 574–585. doi:10.1097/00010694-199908000-00005
- Celi, L., M, P., Marsan, F. A., and Barberis, E. (2001). Effects of pH and Electrolytes on Inositol Hexaphosphate Interaction with Goethite. *Soil Sci. Soc. Am. J.* 65, 753–760. doi:10.2136/sssaj2001.653753x
- Chen, C., Condron, L., Davis, M., and Sherlock, R. (2002). Phosphorus dynamics in the rhizosphere of perennial ryegrass (*Lolium perenne* L.) and radiata pine (*Pinus radiata* D. Don.). *Soil Biol. Biochem.* 34, 487–499. doi:10.1016/S0038-0717(01)00207-3

- Chicot, D., Mendoza, J., Zaoui, A., Louis, G., Lepingle, V., Roudet, F., et al. (2011). Mechanical properties of magnetite (Fe_3O_4), hematite ($\alpha\text{-Fe}_2\text{O}_3$) and goethite ($\alpha\text{-FeO}\cdot\text{OH}$) by instrumented indentation and molecular dynamics analysis. *Materials Chemistry and Physics* 129, 862–870. doi:10.1016/j.matchemphys.2011.05.056
- Chirlian, L. E. and Francel, M. M. (1987). Atomic charges derived from electrostatic potentials: A detailed study. *Journal of Computational Chemistry* 8, 894–905. doi:10.1002/jcc.540080616
- Chitrakar, R., Tezuka, S., Sonoda, A., Sakane, K., Ooi, K., and Hirotsu, T. (2006). Phosphate adsorption on synthetic goethite and akaganeite. *J. Colloid Interface Sci.* 298, 602–608. doi:10.1016/j.jcis.2005.12.054
- Condrón, L. M., Turner, B. L., and Cade-Menun, B. J. (2015). Chemistry and dynamics of soil organic phosphorus. In *Phosphorus: Agriculture and the Environment* (John Wiley & Sons, Ltd), chap. 4. 87–121. doi:10.2134/agronmonogr46.c4
- Cordell, D., Drangert, J.-O., and White, S. (2009). The story of phosphorus: Global food security and food for thought. *Glob. Env. Chang* 19, 292–305. doi:10.1016/j.gloenvcha.2008.10.009
- Cordell, D. and Neset, T.-S. S. (2014). Phosphorus vulnerability: A qualitative framework for assessing the vulnerability of national and regional food systems to the multi-dimensional stressors of phosphorus scarcity. *Glob. Env. Chang* 24, 108–122. doi:10.1016/j.gloenvcha.2013.11.005
- Cornell, R. M. and Schwertmann, U. (2003). *The Iron Oxides: Structure, Properties Reactions Occurrence and Uses* (Wiley-VCH Verlag GmbH and Co. KGaA). doi:10.1002/3527602097
- Cosgrove, D. and Irving, G. (1980). *Inositol Phosphates: Their Chemistry, Biochemistry, and Physiology*. Studies in Organic Chemistry (Elsevier Scientific Pub. Co.)
- [Software] CP2K (2017). Open source molecular dynamics code. CP2K
- Cramer, C. (2004). *Essentials of Computational Chemistry: Theories and Models* (Wiley)
- Criscenti, L. J., Ho, T. A., and Hart, D. (2018). Structural Properties of Aqueous Solutions at the (100) and (101) Goethite Surfaces by Molecular Dynamics Simulation. *Langmuir* 34, 14498–14510. doi:10.1021/acs.langmuir.8b02612
- Cygan, R. T., Liang, J. J., and Kalinichev, A. G. (2004). Molecular Models of Hydroxide, Oxyhydroxide, and Clay Phases and the Development of a General Force Field. *J. Phys. Chem. B* 108, 1255–1266. doi:10.1021/jp0363287

- Daniel, T. C., Sharpley, A. N., and Lemunyon, J. L. (1998). Agricultural Phosphorus and Eutrophication: A Symposium Overview. *J. Environ. Qual.* 27, 251–257. doi:10.2134/jeq1998.00472425002700020002x
- Davis, J. A. (1982). Adsorption of natural dissolved organic matter at the oxide/water interface. *Geochimica et Cosmochimica Acta* 46, 2381–2393. doi:10.1016/0016-7037(82)90209-5
- De Groot, C. J. and Golterman, H. L. (1993). On the presence of organic phosphate in some Camargue sediments: Evidence for the importance of phytate. *Hydrobiologia* 252, 117–126. doi:10.1007/BF00000133
- Dixon, J., Schulze, D., Amonette, J., and of America, S. S. S. (2002). *Soil Mineralogy with Environmental Applications*. SSSA Special Publication (Soil Science Society of America)
- Doolette, A., Smernik, R., and Dougherty, W. (2009). Spiking Improved Solution Phosphorus³¹ Nuclear Magnetic Resonance Identification of Soil Phosphorus Compounds. *Soil Sci. Soc. Am. J.* 73. doi:10.2136/sssaj2008.0192
- Doolette, A. L., Smernik, R. J., and Dougherty, W. J. (2011). A quantitative assessment of phosphorus forms in some Australian soils. *Soil Res.* 49, 152. doi:10.1071/SR10092
- Elser, J. and Bennett, E. (2011). A broken biogeochemical cycle. *Nature* 478, 29–31. doi:10.1038/478029a
- Freundlich, H. (1907). über Die Adsorption in Lösungen. *Z. Für Phys. Chem.* 57U. doi:10.1515/zpch-1907-5723
- Gaigeot, M.-P. (2010). Theoretical spectroscopy of floppy peptides at room temperature. A DFTMD perspective: Gas and aqueous phase. *Phys. Chem. Chem. Phys.* 12, 3336–3359. doi:10.1039/B924048A
- Gale, J. D., Raiteri, P., and van Duin, A. C. T. (2011). A reactive force field for aqueous-calcium carbonate systems. *Phys. Chem. Chem. Phys.* 13, 16666–16679. doi:10.1039/C1CP21034C
- Ganta, P. B., Kühn, O., and Ahmed, A. A. (2019). QM/MM simulations of organic phosphorus adsorption at the diaspore–water interface. *Phys. Chem. Chem. Phys.* 21, 24316–24325. doi:10.1039/C9CP04032C
- Ganta, P. B., Kühn, O., and Ahmed, A. A. (2020). QM/MM molecular dynamics investigation of the binding of organic phosphates to the 100 diaspore surface. *Front Glob Change* 3, 71. doi:10.3389/ffgc.2020.00071

- Ganta, P. B., Kühn, O., and Ahmed, A. A. (2021a). Ab initio molecular dynamics simulations of the interaction between organic phosphates and goethite. *Molecules* 26. doi:10.3390/molecules26010160
- Ganta, P. B., Morshedizad, M., Kühn, O., Leinweber, P., and Ahmed, A. A. (2021b). The binding of phosphorus species at goethite: A joint experimental and theoretical study. *Minerals* 11. doi:10.3390/min11030323
- Gerke, J. (2015). Phytate (Inositol Hexakisphosphate) in Soil and Phosphate Acquisition from Inositol Phosphates by Higher Plants: A Review. *Plants* 4, 253–266. doi:10.3390/plants4020253
- Goeppert, A., Czaun, M., Jones, J.-P., Surya Prakash, G. K., and Olah, G. A. (2014). Recycling of carbon dioxide to methanol and derived products – closing the loop. *Chem. Soc. Rev.* 43, 7995–8048. doi:10.1039/C4CS00122B
- González, M.A. (2011). Force fields and molecular dynamics simulations. *Collect. SFN* 2011 12, 169–200. doi:10.1051/sfn/201112009
- Grant, R., Laubel, A., Kronvang, B., Andersen, H., Svendsen, L., and Fuglsang, A. (1996). Loss of dissolved and particulate phosphorus from arable catchments by sub-surface drainage. *Water Res.* 30, 2633–2642. doi:10.1016/S0043-1354(96)00164-9
- Grimme, S. (2006). Semiempirical GGA-type density functional constructed with a long-range dispersion correction. *Journal of Computational Chemistry* 27, 1787–1799. doi:10.1002/jcc.20495
- Grimme, S., Antony, J., Ehrlich, S., and Krieg, H. (2010). A consistent and accurate ab initio parametrization of density functional dispersion correction (DFT-D) for the 94 elements H-Pu. *J. Phys. Chem.* 132, 154104:1–154104:15. doi:10.1063/1.3382344
- Groenhof, G. (2013). Introduction to QM/MM Simulations. In *Biomolecular Simulations: Methods and Protocols*, eds. L. Monticelli and E. Salonen (Totowa, NJ: Humana Press). 43–66. doi:10.1007/978-1-62703-017-5_3
- Gu, B., Schmitt, J., Chen, Z., Liang, L., and McCarthy, J. F. (1994). Adsorption and desorption of natural organic matter on iron oxide: Mechanisms and models. *Environ Sci Technol* 28, 38–46. doi:10.1021/es00050a007
- Guan, X.-H., Shang, C., Zhu, J., and Chen, G.-H. (2006). ATR-FTIR investigation on the complexation of myo-inositol hexaphosphate with aluminum hydroxide. *J. Colloid Interface Sci.* 293, 296–302. doi:10.1016/j.jcis.2005.06.070
- Guo, H. and Barnard, A. S. (2011). Thermodynamic modelling of nanomorphologies of hematite and goethite. *J. Mater. Chem.* 21, 11566–11577. doi:10.1039/C1JM10381D

- Gypser, S., Hirsch, F., Schleicher, A. M., and Freese, D. (2018). Impact of crystalline and amorphous iron- and aluminum hydroxides on mechanisms of phosphate adsorption and desorption. *J. Env. Sci. China* 70, 175–189. doi:10.1016/j.jes.2017.12.001
- Ha, N. N., Cam, L. M., Thi Thu Ha, N., Jiang, Z.-T., El-Harbawi, M., and Yin, C.-Y. (2018). Integrated QMMM and Monte Carlo methods for analysis of adsorptive interactions between goethite cluster, carbon nanotubes, and arsenate. *International Journal of Quantum Chemistry* 118, e25653. doi:10.1002/qua.25653
- Heinz, H., Lin, T.-J., Kishore Mishra, R., and Emami, F. S. (2013). Thermodynamically Consistent Force Fields for the Assembly of Inorganic, Organic, and Biological Nanostructures: The INTERFACE Force Field. *Langmuir* 29, 1754–1765. doi:10.1021/la3038846
- Hens, M. and Merckx, R. (2001). Functional Characterization of Colloidal Phosphorus Species in the Soil Solution of Sandy Soils. *Env. Sci. Technol* 35, 493–500. doi:10.1021/es0013576
- Hinsinger, P., Brauman, A., Devau, N., Gérard, F., Jourdan, C., Laclau, J.-P., et al. (2011). Acquisition of phosphorus and other poorly mobile nutrients by roots. Where do plant nutrition models fail? *Plant and Soil* 348, 29. doi:10.1007/s11104-011-0903-y
- Hohenberg, P. and Kohn, W. (1964). Inhomogeneous electron gas. *Phys. Rev.* 136, B864–B871. doi:10.1103/PhysRev.136.B864
- Holzmann, S., Missong, A., Puhlmann, H., Siemens, J., Bol, R., Klumpp, E., et al. (2015). Impact of anthropogenic induced nitrogen input and liming on phosphorus leaching in forest soils. *J. Soil Sci. Plant Nutr.* 179, 443–453. doi:10.1002/jpln.201500552
- Hori, T., Moriguchi, M., Sasaki, M., Kitagawa, S., and Munakata, M. (1985). Preconcentration of some phosphorus-containing anions by adsorption on hydrated iron(III) oxide. *Anal. Chim. Acta* 173, 299–303. doi:10.1016/S0003-2670(00)84967-3
- Huang, P., Pham, T. A., Galli, G., and Schwegler, E. (2014). Alumina(0001)/Water Interface: Structural Properties and Infrared Spectra from First-Principles Molecular Dynamics Simulations. *J. Phys. Chem. C* 118, 8944–8951. doi:10.1021/jp4123002
- Humphrey, W., Dalke, A., and Schulten, K. (1996). VMD – Visual Molecular Dynamics. *J. Mol. Graph.* 14, 33–38
- Hwang, S., Blanco, M., Demiralp, E., Cagin, T., and Goddard, W. A. (2001). The MS-Q Force Field for Clay Minerals: Application to Oil Production. *J. Phys. Chem. B* 105, 4122–4127. doi:10.1021/jp002570r

- Ivanova Shor, E. A., Shor, A. M., Nasluzov, V. A., Vayssilov, G. N., and Rösch, N. (2005). Effects of the Aluminum Content of a Zeolite Framework: A DFT/MM Hybrid Approach Based on Cluster Models Embedded in an Elastic Polarizable Environment. *J. Chem. Theory Comput.* 1, 459–471. doi:10.1021/ct049910n
- Jahnke, R. A. (1992). 14 The Phosphorus Cycle. In *International Geophysics* (Elsevier), vol. 50. 301–315. doi:10.1016/S0074-6142(08)62697-2
- Jiang, X., Bol, R., Nischwitz, V., Siebers, N., Willbold, S., Vereecken, H., et al. (2015). Phosphorus Containing Water Dispersible Nanoparticles in Arable Soil. *J. Env. Qual.* 44, 1772–1781. doi:10.2134/jeq2015.02.0085
- Johnson, B. B., Quill, E., and Angove, M. J. (2012). An investigation of the mode of sorption of inositol hexaphosphate to goethite. *J. Colloid Interface Sci.* 367, 436–442. doi:10.1016/j.jcis.2011.09.066
- Jorgensen, W., Maxwell, D., and Tirado-Rives, J. (1996). Development and testing of the OPLS all-atom force field on conformational energetics and properties of organic liquids. *J. Am. Chem. Soc.* 118, 11225–11236. doi:doi.org/10.1021/ja9621760
- K I, R., Deepa, G., and Namboori, D. K. (2008). *Computational Chemistry and Molecular Modeling: Principles and Applications*. doi:10.1007/978-3-540-77304-7
- Kalbitz, K., Schwesig, D., Rethemeyer, J., and Matzner, E. (2005). Stabilization of dissolved organic matter by sorption to the mineral soil. *Soil Biology and Biochemistry* 37, 1319–1331. doi:10.1016/j.soilbio.2004.11.028
- Kalinichev, A. G., Wang, J., and Kirkpatrick, R. J. (2007). Molecular dynamics modeling of the structure, dynamics and energetics of mineral–water interfaces: Application to cement materials. *Cem. Concr. Res.* 37, 337–347. doi:10.1016/j.cemconres.2006.07.004
- Kerisit, S. and Parker, S. C. (2004). Free energy of adsorption of water and calcium on the {10 1 4} calcite surface. *Chem. Commun.* , 52–53. doi:10.1039/B311928A
- Kersten, M., Tunega, D., Georgieva, I., Vlasova, N., and Branscheid, R. (2014). Adsorption of the Herbicide 4-Chloro-2-methylphenoxyacetic Acid (MCPA) by Goethite. *Environ. Sci. Technol.* 48, 11803–11810. doi:10.1021/es502444c
- Kim, J., Li, W., Philips, B. L., and Grey, C. P. (2011). Phosphate adsorption on the iron oxyhydroxides goethite (α -FeOOH), akaganeite (β -FeOOH), and lepidocrocite (γ -FeOOH): A ^{31}P NMR Study. *Energy Environ. Sci.* 4, 4298. doi:10.1039/c1ee02093e
- Kohn, W. and Sham, L. J. (1965). Self-consistent equations including exchange and correlation effects. *Phys. Rev.* 140, A1133–A1138. doi:10.1103/PhysRev.140.A1133

- Kosmulski, M. (2009). pH-dependent surface charging and points of zero charge. IV. Update and new approach. *J. Colloid Interface Sci.* 337, 439–448. doi:10.1016/j.jcis.2009.04.072
- Krack, M. (2005). Pseudopotentials for H to Kr optimized for gradient-corrected exchange-correlation functionals. *Theor. Chem. Acc.* 114, 145–152. doi:10.1007/s00214-005-0655-y
- Kruse, J., Abraham, M., Amelung, W., Baum, C., Bol, R., Kühn, O., et al. (2015). Innovative methods in soil phosphorus research: A review. *J. Soil Sci. Plant Nutr.* 178, 43–88. doi:10.1002/jpln.201400327
- Kubicki, J. D. (ed.) (2016). *Molecular Modeling of Geochemical Reactions* (Chichester: Wiley and Sons)
- Kubicki, J. D. and Ohno, T. (2020). Integrating Density Functional Theory Modeling with Experimental Data to Understand and Predict Sorption Reactions: Exchange of Salicylate for Phosphate on Goethite. *Soil Syst.* 4. doi:10.3390/soilsystems4020027
- Kubicki, J. D., Paul, K. W., Kabalan, L., Zhu, Q., Mrozik, M. K., Aryanpour, M., et al. (2012). ATR-FTIR and Density Functional Theory Study of the Structures, Energetics, and Vibrational Spectra of Phosphate Adsorbed onto Goethite. *Langmuir* 28, 14573–14587. doi:10.1021/la303111a
- Kubicki, J. D. and Watts, H. D. (2019). Quantum Mechanical Modeling of the Vibrational Spectra of Minerals with a Focus on Clays. *Minerals* 9, 141. doi:10.3390/min9030141
- Kühne, T. D., Iannuzzi, M., Del Ben, M., Rybkin, V. V., Seewald, P., Stein, F., et al. (2020). CP2K: An electronic structure and molecular dynamics software package - Quickstep: Efficient and accurate electronic structure calculations. *J. Chem. Phys.* 152, 194103. doi:10.1063/5.0007045
- Kwon, K. D. and Kubicki, J. D. (2004). Molecular Orbital Theory Study on Surface Complex Structures of Phosphates to Iron Hydroxides: Calculation of Vibrational Frequencies and Adsorption Energies. *Langmuir* 20, 9249–9254. doi:10.1021/la0487444
- Laino, T., Mohamed, F., Laio, A., and Parrinello, M. (2005). An Efficient Real Space Multigrid QM/MM Electrostatic Coupling. *J. Chem. Theory Comput.* 1, 1176–1184. doi:10.1021/ct050123f
- Laino, T., Mohamed, F., Laio, A., and Parrinello, M. (2006). An Efficient Linear-Scaling Electrostatic Coupling for Treating Periodic Boundary Conditions in QM/MM Simulations. *J. Chem. Theory Comput.* 2, 1370–1378. doi:10.1021/ct6001169

- Leherte, L., Andre, J.-M., Derouane, E., and Vercauteren, D. (1991). Molecular dynamics studies of sorbates in zeolites: Water in ferrierite. *Catalysis Today* 10, 177–200. doi:10.1016/0920-5861(91)80064-G
- Li, H., Wan, B., Yan, Y., Zhang, Y., Cheng, W., and Feng, X. (2017). Adsorption of glycerophosphate on goethite: A macroscopic and infrared spectroscopic study. *J. Soil Sci. Plant Nutr.* 181, 557–565. doi:10.1002/jpln.201700517
- Li, W., Wang, L., Liu, F., Liang, X., Feng, X., Tan, W., et al. (2016). Effects of Al³⁺ doping on the structure and properties of goethite and its adsorption behavior towards phosphate. *Int J Env. Sci* 45, 18–27. doi:10.1016/j.jes.2015.12.013
- Lii, J.-H. and Allinger, N. L. (1991). The MM3 force field for amides, polypeptides and proteins. *Journal of Computational Chemistry* 12, 186–199. doi:10.1002/jcc.540120208
- Limbach, H.-H., Tolstoy, P. M., Pérez-Hernández, N., Guo, J., Shenderovich, I. G., and Denisov, G. S. (2009). OHO Hydrogen Bond Geometries and NMR Chemical Shifts: From Equilibrium Structures to Geometric H/D Isotope Effects, with Applications for Water, Protonated Water, and Compressed Ice. *Isr. J. Chem.* 49, 199–216. doi:10.1560/IJC.49.2.199
- Lü, C., Yan, D., He, J., Zhou, B., Li, L., and Zheng, Q. (2017). Environmental geochemistry significance of organic phosphorus: An insight from its adsorption on iron oxides. *Applied Geochemistry* 84, 52–60. doi:10.1016/j.apgeochem.2017.05.026
- MacKerell, A. D., Bashford, D., Bellott, M., Dunbrack, R. L., Evanseck, J. D., Field, M. J., et al. (1998). All-atom empirical potential for molecular modeling and dynamics studies of proteins. *J Phys Chem B* 102, 3586–3616. doi:10.1021/jp973084f
- Marx, D. and Hutter, J. (2009). *Ab Initio Molecular Dynamics: Basic Theory and Advanced Methods* (Cambridge University Press). doi:10.1017/CBO9780511609633
- Mermin, N. D. (1965). Thermal properties of the inhomogeneous electron gas. *Phys. Rev.* 137, A1441–A1443. doi:10.1103/PhysRev.137.A1441
- Misong, A. (2018). *Phosphorus Associated to Forest Soil Colloids*. Ph.D. thesis, RWTH Aachen University. doi:10.18154/RWTH-2018-226800
- Misong, A., Bol, R., Willbold, S., Siemens, J., and Klumpp, E. (2016). Phosphorous forms in forest soil colloids as revealed by liquid-state P-NMR. *J. Soil Sci. Plant Nutr.* 179, 159–167. doi:doi.org/10.1002/jpln.201500119

- Mulla, D. J. (1987). Simulating Liquid Water near Mineral Surfaces: Current Methods and Limitations. In *Geochemical Processes at Mineral Surfaces* (American Chemical Society), vol. 323 of *ACS Symposium Series*, chap. 2. 20–36. doi:10.1021/bk-1987-0323.ch002
- Mulliken, R. S. (1955). Electronic Population Analysis on LCAO–MO Molecular Wave Functions. I. *J. Chem. Phys.* 23, 1833–1840. doi:10.1063/1.1740588
- [Software] Mundy, C. J., Balasubramanian, S., Bagchi, K., Hutter, J., Kuo, A. S. I., Laino, T., et al. (2017). Frontiers in Simulation Technology (FIST). www.cp2k.org
- Newman, R. H. and Tate, K. R. (1980). Soil phosphorus characterisation by ^{31}P Nuclear Magnetic Resonance. *Commun. Soil Sci. Plant Anal.* 11, 835–842. doi:10.1080/00103628009367083
- Oehl, F., Oberson, A., Sinaj, S., and Frossard, E. (2001). Organic phosphorus mineralization studies using isotopic dilution techniques. *Soil Sci. Soc. Am. J.* 65, 780–787. doi:10.2136/sssaj2001.653780x
- Ognalaga, M., Frossard, E., and Thomas, F. (1994). Glucose-1-phosphate and Myo-inositol Hexaphosphate Adsorption Mechanisms on Goethite. *Soil Sci. Soc. Am. J.* , 332–337doi:10.2136/sssaj1994.03615995005800020011x
- Oniani, O. G., Chater, M., and Mattingly, G. E. G. (1973). Some effects of fertilizers and farmyard manure on the organic phosphorus in soils. *Journal of Soil Science* 24, 1–9. doi:10.1111/j.1365-2389.1973.tb00736.x
- Ozboyaci, M., Kokh, D. B., Corni, S., and Wade, R. C. (2016). Modeling and simulation of protein–surface interactions: Achievements and challenges. *Q. Rev. Biophys.* 49, e4. doi:10.1017/S0033583515000256
- Pant, H. K., Warman, P. R., and Nowak, J. (1999). Identification of soil organic phosphorus by ^{31}P Nuclear Magnetic Resonance spectroscopy. *Commun. Soil. Sci. Plant Anal.* 30, 757–772. doi:10.1080/00103629909370244
- Parfitt, R. L. and Atkinson, R. J. (1976). Phosphate adsorption on goethite ($\alpha\text{-FeOOH}$). *Nature* 264, 740–742. doi:10.1038/264740a0
- Pavese, A., Catti, M., Parker, S. C., and Wall, A. (1996). Modelling of the thermal dependence of structural and elastic properties of calcite, CaCO_3 . *Physics and Chemistry of Minerals* 23, 89–93. doi:10.1007/BF00202303
- Penn, C. and Camberato, J. (2019). A critical review on soil chemical processes that control how soil pH affects phosphorus availability to plants. *Agriculture* 9, 120. doi:10.3390/agriculture9060120

- Perdew, J. P., Burke, K., and Ernzerhof, M. (1996). Generalized Gradient Approximation Made Simple. *Phys. Rev. Lett.* 77, 3865–3868. doi:10.1103/PhysRevLett.77.3865
- Persson, P., Andersson, T., Nelson, H., Sjöberg, S., Giesler, R., and Lövgren, L. (2012). Surface complexes of monomethyl phosphate stabilized by hydrogen bonding on goethite (α -FeOOH) nanoparticles. *J. Colloid Interface Sci.* 386, 350–358. doi:10.1016/j.jcis.2012.07.042
- Persson, P., Nilsson, N., and Sjöberg, S. (1996). Structure and Bonding of Orthophosphate Ions at the Iron Oxide–Aqueous Interface. *Journal of Colloid and Interface Science* 177, 263–275. doi:10.1006/jcis.1996.0030
- Rakovan, J., Becker, U., and Hochella, M. F. (1999). Aspects of goethite surface microtopography, structure, chemistry, and reactivity. *Am. Mineral.* 84, 884–894. doi:10.2138/am-1999-5-624
- Reitzel, K., Bennett, W. W., Berger, N., Brownlie, W. J., Bruun, S., Christensen, M. L., et al. (2019). New Training to Meet the Global Phosphorus Challenge. *Env. Sci Technol* 53, 8479–8481. doi:10.1021/acs.est.9b03519
- Rennenberg, H. and Schmidt, S. (2010). Perennial lifestyle—an adaptation to nutrient limitation? *Tree Physiol.* 30, 1047–1049. doi:10.1093/treephys/tpq076
- Römken, M. J. M. and Nelson, D. W. (1974). Phosphorus Relationships in Runoff from Fertilized Soils. *J. Environ. Qual.* 3, 10–13. doi:10.2134/jeq1974.00472425000300010003x
- Rose, J., Flank, A.-M., Masion, A., Bottero, J.-Y., and Elmerich, P. (1997). Nucleation and Growth Mechanisms of Fe Oxyhydroxide in the Presence of PO₄ Ions. 2. P K-Edge EXAFS Study. *Langmuir* 13, 1827–1834. doi:10.1021/la961039d
- Rosmarin, A. (2004). The Precarious Geopolitics of Phosphorous. *Earth Sci Env. Fortn*, 27–31
- Sanna, A., Uibu, M., Caramanna, G., Kuusik, R., and Maroto-Valer, M. M. (2014). A review of mineral carbonation technologies to sequester CO₂. *Chem. Soc. Rev.* 43, 8049–8080. doi:10.1039/C4CS00035H
- Schindler, D. W. (1977). Evolution of phosphorus limitation in lakes. *Science* 195, 260–262. doi:10.1126/science.195.4275.260
- Senftle, T. P., Hong, S., Islam, M. M., Kylasa, S. B., Zheng, Y., Shin, Y. K., et al. (2016). The ReaxFF reactive force-field: Development, applications and future directions. *Npj Comput. Mater.* 2, 15011. doi:10.1038/npjcompumats.2015.11

- Senn, H. M. and Thiel, W. (2009). QM/MM Methods for Biomolecular Systems. *Angew. Chem.* 48, 1198–1229. doi:10.1002/anie.200802019
- Sharpley, A. N., Chapra, S. C., Wedepohl, R., Sims, J. T., Daniel, T. C., and Reddy, K. R. (1994). Managing agricultural phosphorus for protection of surface waters: Issues and options. *J. Env. Qual* 23, 437–451. doi:10.2134/jeq1994.00472425002300030006x
- Sheals, J., Sjöberg, S., and Persson, P. (2002). Adsorption of glyphosate on goethite: Molecular characterization of surface complexes. *Env. Sci. Technol* 36, 3090–3095. doi:10.1021/es010295w
- Shen, J., Yuan, L., Zhang, J., Li, H., Bai, Z., Chen, X., et al. (2011). Phosphorus dynamics: From soil to plant. *Plant Physiol* 156, 997–1005. doi:10.1104/pp.111.175232
- Shi, J., Podola, B., and Melkonian, M. (2007). Removal of nitrogen and phosphorus from wastewater using microalgae immobilized on twin layers: An experimental study. *J. Appl. Phycol.* 19, 417–423. doi:10.1007/s10811-006-9148-1
- Smil, V. (2000). Phosphorus in the Environment: Natural Flows and Human Interferences. *Annu Rev Env. Resour* 25, 53–88. doi:10.1146/annurev.energy.25.1.53
- Smith, V. H. (2003). Eutrophication of freshwater and coastal marine ecosystems a global problem. *Environ. Sci. Pollut.* 10, 126–139. doi:10.1065/espr2002.12.142
- Song, X. and Boily, J.-F. (2013). Water Vapor Adsorption on Goethite. *Environ. Sci. Technol.* 47, 7171–7177. doi:10.1021/es400147a
- Steen, I. (1998). Phosphorus availability in the 21st century : Management of a non-renewable resource. *Phosphorus Potassium* 217, 25–31
- Stoyanov, S. R., Gusarov, S., Kuznicki, S. M., and Kovalenko, A. (2008). Theoretical Modeling of Zeolite Nanoparticle Surface Acidity for Heavy Oil Upgrading. *J. Phys. Chem. C* 112, 6794–6810. doi:10.1021/jp075688h
- Strassner, T. (2006). Isotope Effects in Chemistry and Biology. Edited by Amnon Kohen and Hans-Heinrich Limbach. *Angew. Chem.* 45, 6420–6421. doi:10.1002/anie.200585384
- Strauss, R., Brümmer, G., and Barrow, N. (1997). Effects of crystallinity of goethite: II. Rates of sorption and desorption of phosphate. *Eur. J. Soil Sci.* 48, 101–114. doi:10.1111/j.1365-2389.1997.tb00189.x
- Tan, K. (2011). *Principles of Soil Chemistry, Fourth Edition*. Books in Soils, Plants, and the Environment (Taylor & Francis)

- Teermann, I. and Jekel, M. (1999). Adsorption of humic substances onto beta-FeOOH and its chemical regeneration. *Water Sci. Technol.* 40, 199–206. doi:10.1016/S0273-1223(99)00657-5
- Tejedor-Tejedor, M. I. and Anderson, M. A. (1990). The protonation of phosphate on the surface of goethite as studied by CIR-FTIR and electrophoretic mobility. *Langmuir* 6, 602–611. doi:10.1021/la00093a015
- Teppen, B. J., Rasmussen, K., Bertsch, P. M., Miller, D. M., and Schäfer, L. (1997). Molecular Dynamics Modeling of Clay Minerals. 1. Gibbsite, Kaolinite, Pyrophyllite, and Beidellite. *J. Phys. Chem. B* 101, 1579–1587. doi:10.1021/jp961577z
- Tipping, E., Benham, S., Boyle, J. F., Crow, P., Davies, J., Fischer, U., et al. (2014). Atmospheric deposition of phosphorus to land and freshwater. *Environ. Sci.: Processes Impacts* 16, 1608–1617. doi:10.1039/C3EM00641G
- Torrent, J., Schwertmann, U., and Barron, V. (1992). Fast and Slow Phosphate Sorption by Goethite-Rich Natural Materials. *Clays Clay Min.* 40, 14–21. doi:10.1346/CCMN.1992.0400103
- Tossell, J. A., Vaughan, D. J., and Johnson, K. H. (1973). Electronic Structure of Ferric Iron Octahedrally Coordinated to Oxygen. *Nat. Phys. Sci.* 244, 42–45. doi:10.1038/physci244042a0
- Tribe, L., Kwon, K. D., Trout, C. C., and Kubicki, J. D. (2006). Molecular Orbital Theory Study on Surface Complex Structures of Glyphosate on Goethite: Calculation of Vibrational Frequencies. *Environ. Sci. Technol.* 40, 3836–3841. doi:10.1021/es052363a
- Tsao, T. M., Chen, Y. M., and Wang, M. K. (2011). Origin, separation and identification of environmental nanoparticles: A review. *J. Env. Monit* 13, 1156–1163. doi:10.1039/C1EM10013K
- Tunega, D., Gerzabek, M. H., Haberhauer, G., Totsche, K. U., and Lischka, H. (2009). Model study on sorption of polycyclic aromatic hydrocarbons to goethite. *Journal of Colloid and Interface Science* 330, 244–249. doi:10.1016/j.jcis.2008.10.056
- Turner, B. L. (2008). Soil organic phosphorus in tropical forests: An assessment of the NaOH–EDTA extraction procedure for quantitative analysis by solution ³¹P NMR spectroscopy. *European Journal of Soil Science* 59, 453–466. doi:10.1111/j.1365-2389.2007.00994.x
- Turner, B. L., Papházy, M. J., Haygarth, P. M., and Mckelvie, I. D. (2002). Inositol phosphates in the environment. *Philos Trans R. Soc B* 357, 449–469. doi:10.1098/rstb.2001.0837

- Vaccari, D. A. and Strigul, N. (2011). Extrapolating phosphorus production to estimate resource reserves. *Chemosphere* 84, 792–797. doi:10.1016/j.chemosphere.2011.01.052
- van Dijk, K. C., Lesschen, J. P., and Oenema, O. (2016). Phosphorus flows and balances of the european union member states. *Sci. Total Environ.* 542, 1078–1093. doi:10.1016/j.scitotenv.2015.08.048
- VandeVondele, J. and Hutter, J. (2007). Gaussian basis sets for accurate calculations on molecular systems in gas and condensed phases. *J. Chem. Phys.* 127, 114105:1–114105:8. doi:10.1063/1.2770708
- VandeVondele, J., Krack, M., Mohamed, F., Parrinello, M., Chassaing, T., and Hutter, J. (2005). Quickstep: Fast and accurate density functional calculations using a mixed Gaussian and plane waves approach. *Comput. Phys. Commun.* 167, 103–128. doi:10.1016/j.cpc.2004.12.014
- Vanommeslaeghe, K., Hatcher, E., Acharya, C., Kundu, S., Zhong, S., Shim, J., et al. (2010). CHARMM general force field: A force field for drug-like molecules compatible with the CHARMM all-atom additive biological force fields. *Journal of Computational Chemistry* 31, 671–690. doi:10.1002/jcc.21367
- Vasconcelos, I. F., Bunker, B. A., and Cygan, R. T. (2007). Molecular Dynamics Modeling of Ion Adsorption to the Basal Surfaces of Kaolinite. *J. Phys. Chem. C* 111, 6753–6762. doi:10.1021/jp065687+
- Vincent, A. G., Vestergren, J., Gröbner, G., Persson, P., Schleucher, J., and Giesler, R. (2013). Soil organic phosphorus transformations in a boreal forest chronosequence. *Plant Soil* 367, 149–162. doi:10.1007/s11104-013-1731-z
- Wang, J., Kalinichev, A. G., and Kirkpatrick, R. (2004a). Molecular modeling of water structure in nano-pores between brucite (001) surfaces1 1Associate editor: U. Becker. *Geochimica et Cosmochimica Acta* 68, 3351–3365. doi:10.1016/j.gca.2004.02.016
- Wang, J., Wolf, R. M., Caldwell, J. W., Kollman, P. A., and Case, D. A. (2004b). Development and testing of a general amber force field. *J. Comput. Chem.* 25, 1157–1174. doi:10.1002/jcc.20035
- Withers, P. (2019). Closing the phosphorus cycle. *Nat. Sustain* , 1001–1002doi:10.1038/s41893-019-0428-6
- Withers, PJA., Forber, K., Lyon, C., Rothwell, S., Doody, D., Jarvie, H., et al. (2019). Towards resolving the phosphorus chaos created by food systems. *Ambio J. Hum. Environ.* doi:10.1007/s13280-019-01255-1

- Xiu, F., Zhou, L., Xia, S., and Yu, L. (2016). Adsorption mechanism of water molecule on goethite (010) surface. *J. Ocean Univ. China* 15, 1021–1026. doi:10.1007/s11802-016-3171-x
- Xu, C.-y., Li, J.-y., Xu, R.-k., and Hong, Z.-n. (2017). Sorption of organic phosphates and its effects on aggregation of hematite nanoparticles in monovalent and bivalent solutions. *Environmental Science and Pollution Research* 24, 7197–7207. doi:10.1007/s11356-017-8382-1
- Yan, Y., Koopal, L. K., Liu, F., Huang, Q., and Feng, X. (2015). Desorption of myo-inositol hexakisphosphate and phosphate from goethite by different reagents. *J. Plant. Nutr. Soil Sci.* 178, 878–887. doi:10.1002/jpln.201500254
- Yan, Y. P., Liu, F., Li, W., Liu, F., Feng, X. H., and Sparks, D. L. (2014). Sorption and desorption characteristics of organic phosphates of different structures on aluminium (oxyhydr)oxides. *Eur. J. Soil Sci.* 65, 308–317. doi:10.1111/ejss.12119
- Zentel, T. and Kühn, O. (2017). Properties of hydrogen bonds in the protic ionic liquid ethylammonium nitrate. *Theor. Chem. Acc.* 136, 87. doi:10.1007/s00214-017-2119-6
- Zoete, V., Cuendet, M. A., Grosdidier, A., and Michielin, O. (2011). SwissParam: A fast force field generation tool for small organic molecules. *J. Comput. Chem.* 32, 2359–2368. doi:10.1002/jcc.21816

Appendices

A Peer Reviewed Publications

1. QM/MM simulations of organic phosphorus adsorption at the diaspore–water interface. DOI:10.1039/C9CP04032C

My contribution: I have contributed to the project by conducting modelling, corresponding simulations, and post-processing of simulation data. The work was suggested, designed, and supervised by my co-authors. Additionally, I participated in analyzing and interpreting results with my co-authors. I have written the initial draft of the article and collaborated with my co-authors on subsequent revisions. This article was chosen to be featured on the back cover of the journal. I modeled, designed, and rendered the cover while my co-authors were instrumental in the initial design and subsequent revisions.

2. QM/MM molecular dynamics investigation of the binding of organic phosphates to the 100 diaspore surface. DOI:10.3389/ffgc.2020.00071

My contribution: I have contributed to the project by conducting modelling, corresponding simulations, and post-processing of simulation data. The work was suggested, designed, and supervised by my co-authors. Additionally, I participated in analyzing and interpreting results with my co-authors. I have written the initial draft of the article and collaborated with my co-authors on subsequent revisions.

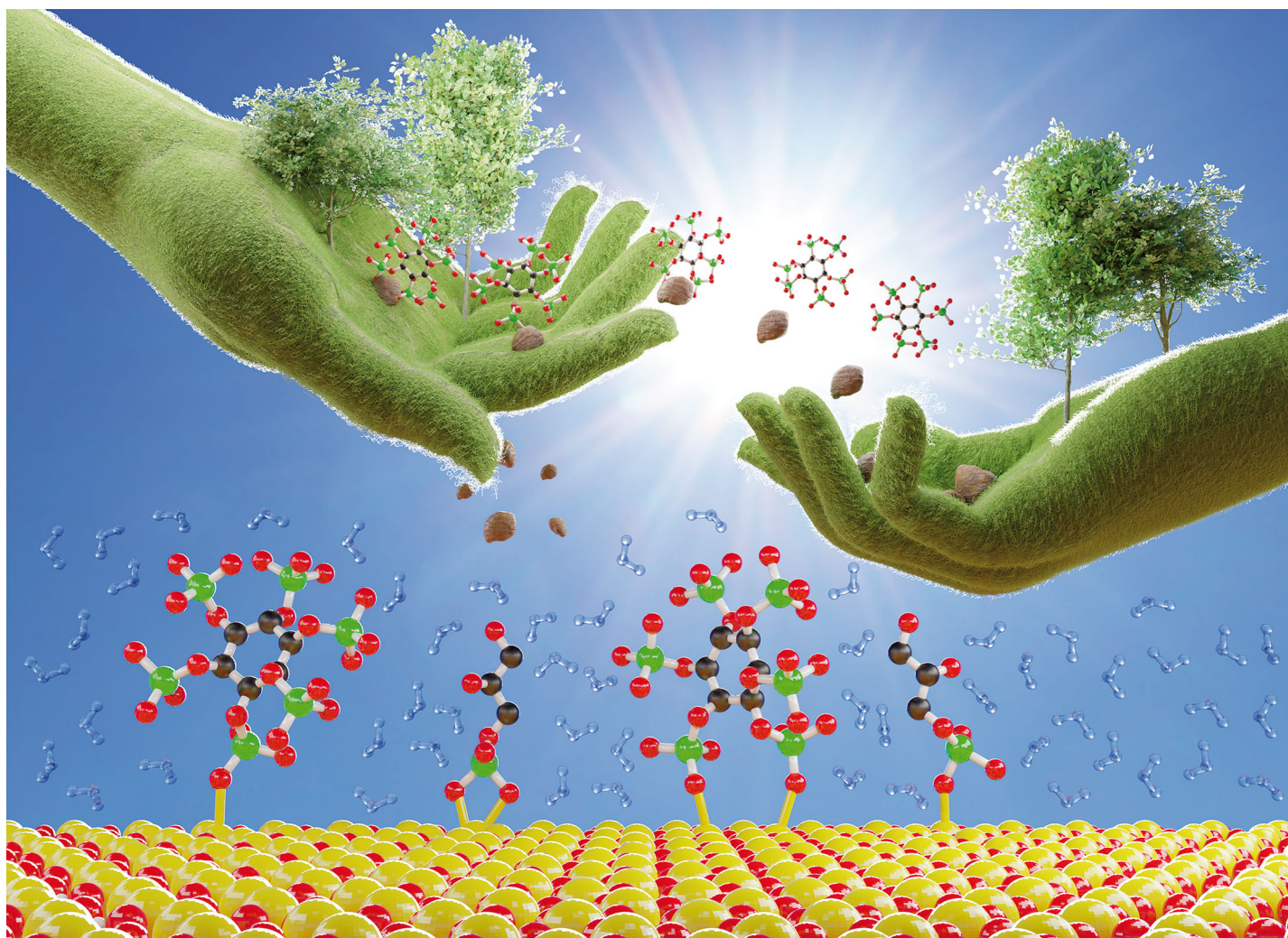
3. Ab Initio Molecular Dynamics Simulations of the Interaction between Organic Phosphates and Goethite. DOI:10.3390/molecules26010160

My contribution: I have contributed to the project by conducting modelling, corresponding simulations, and post-processing of simulation data. The work was suggested, designed, and supervised by my co-authors. Additionally, I participated in analyzing and interpreting results with my co-authors. I have written the initial draft of the article and collaborated with my co-authors on subsequent revisions.

4. The Binding of Phosphorus Species at Goethite: A Joint Experimental and Theoretical Study. DOI:10.3390/min11030323

My contribution: I have contributed to the project by conducting modelling, corresponding simulations, and post-processing of simulation data. My co-authors Ashour

A. Ahmed and Oliver Kühn suggested, designed, and supervised the work. Mohsen Morshedizad performed the experiments and related data post-processing. Additionally, I participated in analyzing and interpreting results with my co-authors. I have written the initial draft of the simulations-related sections of the article and collaborated with my co-authors on subsequent revisions.

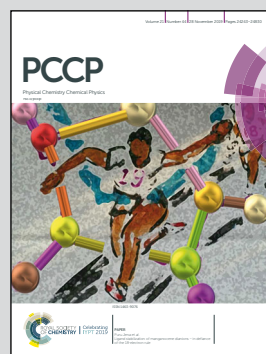


**Showcasing research from the Group of Prof. Oliver Kühn
at the University of Rostock, Germany**

**QM/MM simulations of organic phosphorus adsorption at the
diaspore–water interface**

The focus of the junior group led by Dr Ashour Ahmed is on the establishment of atomistic simulation techniques into the field of environmental chemistry and physics. A major target is phosphorous, its transport and immobilization in the soil. The present work highlights the nature and strength of the binding of the most abundant organic phosphates in forest eco-systems to the diaspore surface. For the diaspore–water interface, different binding motifs are explored. Further, the role of water in controlling binding strengths via formation of H-bonds and proton transfers, adsorption and dissociation at the surface is demonstrated.

As featured in:



See Ashour A. Ahmed *et al.*,
Phys. Chem. Chem. Phys.,
2019, **21**, 24316.



Cite this: *Phys. Chem. Chem. Phys.*,
2019, 21, 24316

QM/MM simulations of organic phosphorus adsorption at the diaspore–water interface†

Prasanth B. Ganta, ^a Oliver Kühn ^{ab} and Ashour A. Ahmed ^{*ab}

Phosphorus (P) immobilization and thus its availability for plants are mainly affected by the strong interaction of phosphates with soil components especially soil mineral surfaces. The related reactions have been studied extensively *via* sorption experiments especially by carrying out adsorption of *ortho*-phosphates onto Fe-oxide surfaces. But a molecular-level understanding of the P-binding mechanisms at the mineral–water interface is still lacking, especially for forest eco-systems. Therefore, the current contribution provides an investigation of the molecular binding mechanisms for two abundant phosphates in forest soils, inositol hexaphosphate (IHP) and glycerolphosphate (GP), at the diaspore mineral surface. Here a hybrid electrostatic embedding quantum mechanics/molecular mechanics (QM/MM) based molecular dynamics simulation has been applied to explore the diaspore–IHP/GP–water interactions. The results provide evidence for the formation of different P-diaspore binding motifs involving monodentate (**M**) and bidentate (**B**) for GP and two (**2M**) as well as three (**3M**) monodentates for IHP. The interaction energy results indicated the abundance of the GP **B** motif compared to the **M** one. The IHP **3M** motif has a higher total interaction energy compared to its **2M** motif, but exhibits a lower interaction energy per bond. Compared to GP, IHP exhibited stronger interaction with the surface as well as with water. Water was found to play an important role in controlling these diaspore–IHP/GP–water interactions. The interfacial water molecules form moderately strong H-bonds (HBs) with GP and IHP as well as with the diaspore surface. For all the diaspore–IHP/GP–water complexes, the interaction of water with the diaspore exceeds that with the studied phosphates. Furthermore, some water molecules form covalent bonds with diaspore Al atoms while others dissociate at the surface to protons and hydroxyl groups leading to proton transfer processes. Finally, the current results confirm the previous experimental conclusions indicating the importance of the number of phosphate groups, HBs, and proton transfers in controlling the P-binding at soil mineral surfaces.

Received 18th July 2019,
Accepted 27th August 2019

DOI: 10.1039/c9cp04032c

rsc.li/pccp

1 Introduction

Phosphorus (P) is a vital element supporting global food systems by enhancing soil fertility, plant growth and consequently the nutritional security of the world population. A P peak scenario has been predicted to arise this century¹ and thus P scarcity could become one of the most important global food security challenges. Knowledge about substantial P leaching as well as about a more efficient and sustainable use of P resources is still limited and needs to be enhanced.^{2–4} For instance, P leaching accompanies heavy rains through the dispersion of rain water with soluble and adsorbed P.⁵ In rain water, minerals retain about 50% of the existing P in the soil solution.^{4,6} A major factor in the context of P efficiency is the interaction between P-containing compounds and soil components.⁷ Specifically, phosphates bind strongly to soil

mineral surfaces and especially to Fe- and Al-(oxyhydr)oxides.^{8–10} This strong binding will reduce the availability of P to the plants and consequently reduce the P efficiency. Molecular level insight into this interaction could trigger a deeper understanding of the fate of P in the environment and eventually lead to smarter fertilisers with increased P efficiency.^{4,8,11}

Organic and inorganic P (P_o and P_i) containing compounds play a substantial role in controlling the P environmental cycle. The most abundant P compounds in soils and especially forest ecosystems are orthophosphates,¹² inositolhexaphosphates (IHPs)^{13–15} and glycerolphosphates (GPs).^{16–18} In addition, Fe- and Al-(oxyhydr)oxides are among the most common P-fixing minerals found in forest soils.¹⁹ The colloids of these minerals can adsorb P at their surfaces forming colloidal P complexes. Goethite (α -FeOOH) is one of the most abundant reactive soil minerals having a ferric ion (Fe^{3+}) in an iron oxyhydroxide chemical formula within the orthorhombic crystal system. In general, phosphates and especially orthophosphates show strong interactions with goethite and thus, these interactions are thoroughly studied.^{20–23} Here, it was found that the

^a Institute of Physics, University of Rostock, Albert-Einstein-Str. 23-24, D-18059 Rostock, Germany. E-mail: ashour.ahmed@uni-rostock.de

^b Department of Life, Light, and Matter (LLM), University of Rostock, Albert-Einstein-Str. 25, D-18059 Rostock, Germany

† Electronic supplementary information (ESI) available. See DOI: 10.1039/c9cp04032c

number of phosphate groups in a certain P_o compound determines the stability of its complex with the mineral surface.²⁴ For instance, IHP with its six phosphate groups generally exhibits a strong binding and high stability compared with other P_o compounds with a smaller number of phosphate groups. Ognalaga *et al.*²⁵ showed that IHP interacts with goethite *via* the formation of inner-sphere complexes between the IHP phosphate groups and the goethite surface Fe atoms. It was suggested that IHP binds to the goethite surface by up to four phosphate groups. The remaining non-interacting phosphate groups induce a modification of the electro-chemical properties, for instance, IHP adsorption causes particle dispersion and a net increase of the negative charge of the surface. The IHP organic moiety affects only the conformational flexibility of the binding motif. In addition, very little dissolution of the goethite surface has been observed during the adsorption process. Adsorption experiments and FTIR results by Celi *et al.*²⁶ confirmed the above conclusions by Ognalaga *et al.*²⁵ In contrast, FTIR and adsorption experiments by Guan *et al.*²⁷ showed that only three phosphate groups in IHP were bound to the amorphous aluminium hydroxide while others remained free.

The binding capabilities of IHP can be compared with those of GP which has a single phosphate group only. Li *et al.*²⁸ suggested that GP adsorbs onto the goethite surface by forming inner-sphere complexes through the phosphate group. Moriguchi *et al.*²⁹ showed that GP adsorbs onto hydrated iron (Fe^{3+}) oxide precipitates. In addition, GP exhibits strong interaction with boehmite, $\alpha-Al_2O_3$ and $Al(OH)_3$,³⁰ and also with ferric oxide.³¹

Despite the presence of quite a few studies reporting on the binding of IHP and GP to the goethite surface, almost nothing is known about the interaction of these P_o compounds with the diaspore surface. Diaspore ($\alpha-AlOOH$) is isomorphous with goethite having an Al^{3+} oxidation state instead of Fe^{3+} . Compared with goethite it exhibits a higher surface energy.³² In soil minerals amorphous Fe/Al hydroxide mixtures are present, thus having a more detailed knowledge about the P interaction with diaspore will provide a better understanding of the P interaction with these soil mineral components.

Accompanying experimental studies, molecular level simulations are emerging as an important tool in soil sciences.³³ For instance, Kubicki *et al.*^{34,35} analysed different phosphate-goethite complexes in terms of their fingerprints in infrared vibrational spectra. Recently, Ahmed *et al.*²³ performed *ab initio* simulations of infrared spectra and the associated binding motifs for the phosphate at the goethite-water interface. A comparison with experiments emphasised the importance of combining the results from different binding motifs and surface planes in order to account for the heterogeneous nature of the samples. A similar statistical approach has been proven useful also for the description of the interactions of pollutants with soil organic matter.^{36,37} Taking into account solvating water molecules in the simulations is essential for a realistic description of the P-mineral surface interaction, which has also been concluded from a study of glyphosate at the goethite-water interface.³⁸

A similar molecular level analysis of the IHP and GP interaction with the diaspore surface is missing so far, which provides motivation for the present study. The main objective of this work is to characterise the adsorption of IHP and GP at the

diaspore-water interface on the basis of periodic boundary quantum mechanics/molecular mechanics (QM/MM)³⁹ molecular dynamics simulations. To this end, a systematic analysis of the binding motifs, proton transfers, intramolecular and intermolecular hydrogen bonds (HB), interaction energies and the competition between water and IHP/GP adsorption onto the diaspore surface will be presented.

2 Computational details

2.1 Model systems

The interaction of IHP and GP with diaspore will be investigated by considering the 010 diaspore surface plane (according to the $Pnma$ space group) which corresponds to the 001 diaspore surface plane within the $Pbnm$ space group. The orthorhombic diaspore unit cell has 16 atoms, *i.e.*, four $AlO(OH)$ formula units with lattice constants $a = 4.4007$, $b = 9.4253$, and $c = 2.8452$ Å (according to the $Pbnm$ space group), see Fig. 1a. The surface plane slab was generated by repetition of the diaspore unit cell as $5a \times 2b \times 4c$, Fig. 1b and c. This slab model consists of 640 atoms (160 Al, 160 H, and 320 O atoms). Each top surface Al atom of the slab is coordinated by four O atoms, see Fig. 1c. This means that in the present contribution the diaspore has been simulated as an unsaturated surface. The main reason for that is the diaspore has point of zero charge (PZC) around 6.⁴⁰ Consequently, at pH below 6, the diaspore surface will be partially unsaturated and exhibit a positive charge. Thus it has the ability to attract/adsorb anions such as phosphates and/or hydroxyl groups. More details about modeling of the diaspore surface is given in the ESI.† It is important to mention that here we are simulating common and normal acidic soil conditions, *i.e.* in the pH range of 3–6.

The initial binding motifs are modelled to have phosphate group(s) of GP and IHP interacting with the Al atoms of the diaspore surface. GP has one phosphate group, see Fig. 2a, and IHP has six phosphate groups, see Fig. 2b. To differentiate between phosphate groups in the IHP, each phosphorus is color-coded and denoted as P_x , where $x = 1, 2, \dots, 6$ and the corresponding oxygens are denoted as O_{x1} (non-protonated oxygen), O_{x2} and O_{x3} (OH functional group oxygens), and O_{x4} (oxygen bonded with carbon) with the same color as the

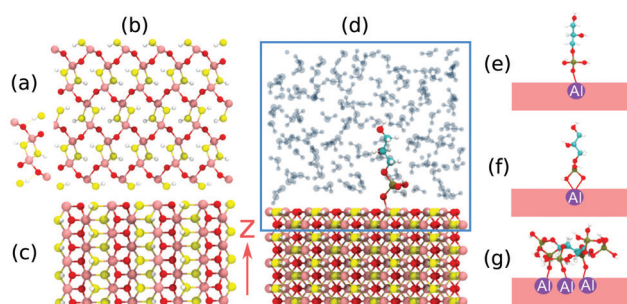


Fig. 1 Diaspore unit cell (a), top view (b) and side view of the modelled diaspore surface (c), the diaspore-GP-water complex (d), the **M** motif (e), the **B** motif (f), and the **3M** motif (g). Pink, red, yellow, white and lime colors correspond to Al, bridging oxygen, hydroxyl oxygen, hydrogen and phosphorus respectively.

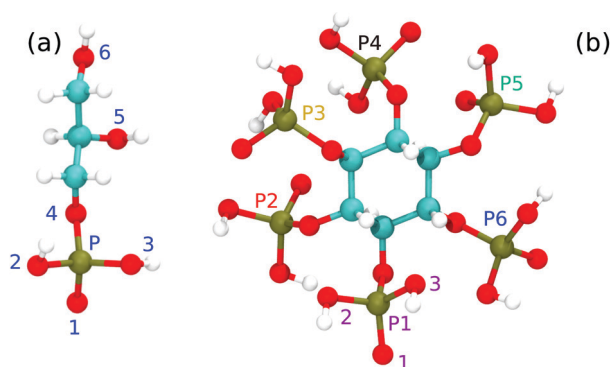


Fig. 2 Molecular structure of glycerolphosphate ($\text{C}_3\text{H}_9\text{O}_6\text{P}$, GP) (a) and inositol hexaphosphate ($\text{C}_6\text{H}_{18}\text{O}_{24}\text{P}_6$, IHP) (b). In general all the phosphate groups are equivalent. The oxygen and phosphorus atoms are labelled to ease the discussion of diaspor–IHP/GP–water interactions.

corresponding phosphate, see Fig. 2b. More details about modelling of IHP and GP are given in the ESI.†

A vacuum layer of about 18 Å was added between the periodic slabs perpendicular (along the z axis) to the studied surface plane. Then, GP was added into the vacuum region with its long axis perpendicular to the surface and solvated, see Fig. 1d. Here, the GP's phosphate group was aligned to bind to the surface Al atoms *via* two different binding motifs. These motifs involved the formation of diaspor–GP complexes with monodentate (**M**, 1 covalent bond between 1 phosphate O atom and 1 surface Al atom), see Fig. 1e and bidentate (**B**, 2 covalent bonds between 2 phosphate O atoms and 1 surface Al atom), see Fig. 1f bonds. The same binding motifs have been considered for the diaspor–IHP complex. In addition, another binding motif (**3M**, 3 phosphate O atoms with 3 Al atoms) Fig. 1g was modelled for the IHP interaction with the diaspor surface. The choice of the latter motif is mainly based on the experimental studies in ref. 25 and 27 which concluded a higher number of IHP–surface bonds. It is important to mention that having different starting configurations for each binding motif could give more insight into understanding the diaspor–IHP/GP interactions. However, this was not possible within a reasonable time due to the size of the modeled systems and the used computationally expensive QM/MM level of theory. To simulate the soil solution and its vital role in controlling the interaction of the P containing compounds with the mineral surfaces,³⁸ the modelled diaspor–IHP/GP complexes are solvated with water at a density of about 1 g cm^{-3} using the solvate plugin provided by the VMD package,⁴¹ see Fig. 1d. For each model, the slab bottom layer atoms were kept fixed to approximate the properties of the underlying extended diaspor bulk and to diminish artefacts due to the interaction with water of the next box image. Except for these fixed atoms, all other MM atoms including the MM water molecules are left fully flexible during the MD simulations.

2.2 QM/MM setup

The accuracy provided by the *ab initio* methods comes at high computational costs which restricts the applicability to systems

with a few hundred atoms at best. The modelled diaspor–IHP/GP–water complexes include about 1200 atoms and therefore cannot reasonably be treated by pure *ab initio* methods. Reducing the system size, however, always bears the danger of artefacts due to the finite simulation box in combination with periodic boundary conditions. Setting the focus on the adsorption of the P-compounds, *i.e.* a process which is local at the mineral–water surface, a full *ab initio* treatment is not necessary and a hybrid QM/MM approach is the method of choice.³⁹ In the present case, the QM (reactive) part is chosen to include the top two layers of the diaspor surface (160 atoms), IHP (54 atoms)/GP (19 atoms), and solvating water within a layer of ≈ 10 Å perpendicular to the surface (≈ 114 atoms). The size of the QM box is $5a \times 2b \times 22 \text{ Å}$ *i.e.* $22.0035 \times 18.8506 \times 22 \text{ Å}$, where a and b are the diaspor lattice constants. The remaining part of the system is treated at the MM level. Thereby electrostatic embedding is used, including the polarization of the QM atoms by the MM atoms. The QM/MM implementation is performed employing the CP2K⁴² package, where QM is treated by the quickstep code⁴³ and MM by the FIST package.⁴⁴ For the QM method, density functional theory (DFT) was adopted with the hybrid Gaussian and plane wave (GPW) dual basis method, wherein the atom centered Gaussian basis describes the wave function and the auxiliary plane waves describe the electron density. The core electrons are replaced by Goedecker–Teter–Hutter (GTH) pseudopotentials⁴⁵ and the Perdew–Burke–Ernzerhof (PBE)⁴⁶ version of generalized gradient approximation (GGA) was used as an exchange–correlation functional. To account for the van der Waals forces, the D3 empirical dispersion correction⁴⁷ was adopted. The electronic density cut-off of the auxiliary plane wave basis is set to 500 Ry. The double- ζ valence polarized (DZVP-MOLOPT-SR-GTH), MOLOPT⁴⁸ basis sets that reduce the computational cost for condensed phase systems and minimize the basis set superposition error (BSSE) are used except for water atoms. The single- ζ valence basis set was selected for the water atoms to further reduce the computational costs. An SCF energy convergence study was performed for various configurations and a convergence threshold of 10^{-5} was chosen. In the MM part, water is modeled using a SPC⁴⁹ based water model and the surface is modelled with CLAYFF force fields,⁵⁰ see Tables S1 and S2 in the ESI.† These force fields are suitable to simulate mineral surfaces and their corresponding water interfaces. CHARMM force fields for IHP and GP are obtained *via* the SwissParm force field generation tool,⁵¹ see Table S3 and Fig. S1 in the ESI.† The QM/MM driver in CP2K is the Gaussian expansion of the electrostatic potential method (GEEP),⁵² wherein the MM atom charges are described using Gaussians to prevent electron spill out and to accelerate QM/MM electrostatic calculations. More details about the current implementation of the QM/MM approach are given in the ESI.† The parameters used in the current QM/MM approach are validated by comparing pair correlation functions and P–O–Al bond formations observed in pure QM and QM/MM trajectories as shown in Fig. S2 and S3 in the ESI.† Periodic boundary conditions (PBC) are applied in all the three spatial directions to the whole molecular system involving the diaspor surface, phosphate species (IHP/GP), and all water molecules. A total of 25 ps NVT–MD simulations are performed with a time step of 0.5 fs. To maintain the average

temperature of the system around 300 K, the canonical sampling through velocity rescaling thermostat (CSVR)⁵³ approach is used with 100 fs time constant. The first 10 ps are considered as equilibration (see Fig. S4 in the ESI†) of the system and the production trajectory (remaining 15 ps) was used for analysis of the diaspore–IHP/GP–water interactions.

To characterize the complexation reaction between the modeled phosphate species (IHP/GP) and the diaspore surface, the interaction energy (E_{int}) between each phosphate species and the diaspore surface is calculated at every 100 fs along the production trajectory. For example, for the complexation reaction diaspore + GP \rightarrow diaspore–GP–complex, E_{int} between GP and the diaspore surface is calculated as follows:

$$E_{\text{int}} = E_{\text{diaspore-GP-complex}} - (E_{\text{diaspore}} + E_{\text{GP}}) \quad (1)$$

where, $E_{\text{diaspore-GP-complex}}$, E_{GP} , and E_{diaspore} are the total electronic energies of the diaspore–GP–complex, GP, and the diaspore surface, respectively. Here, the BSSE is corrected using the counterpoise scheme.⁵⁴ Similarly, the interaction energies between IHP and diaspore, water and diaspore, GP and water, and IHP and water are calculated. For each model, the interaction energy between each of the two subsystems is calculated for 150 snapshots along the production trajectory and the time-averaged value is presented here. For more details regarding the

calculation of interaction energies, see the ESI†. Energies related to the interaction with water will also be given as per the water molecule, *i.e.* by dividing the total energy by the total number of water molecules in the box.

3 Results and discussion

3.1 Diaspore–GP–water interactions

3.1.1 GP M motif. In this model, initially the long side of GP was placed perpendicular to the diaspore surface in forming an **M** binding motif between the GP's non-protonated oxygen atom (O1) and the central surface Al atom, see Fig. 3a. The MD simulation results show that a stable monodentate complex is formed between GP and the diaspore with an Al–O1 average bond length of 1.90 Å. P–Ox and Al–Ox interatomic distances are given in the ESI† (Fig. S5b and S6a). Two proton transfer events are observed from O3 and O5 of GP to water, see Fig. 3c and d. It is to be noted that the proton transfer events are not entirely a consequence of diaspore–GP binding, but they are also observed in the simulations carried out in the bulk, see Fig. S7 and S8 (ESI†). The average geometry of the PO₄ moiety is rather close to that of a free tetrahedral PO₄^{3−} with a RMSD of 0.06 Å (see Table 1 and Fig. S5a, b and S6a in the ESI†).

On average 7 HBs are observed between GP and water in the production trajectory. In the following, HB strengths are analysed using their geometrical correlations expressed in terms of the coordinates q_1 and q_2 ,^{55–57} where $q_1 = \frac{1}{2}(r_1 - r_2)$ Å and $q_2 = (r_1 + r_2)$ Å. Here r_1 and r_2 denote the distance between donor oxygen and hydrogen (O_D–H) and the distance between hydrogen and acceptor oxygen (H···O_A), respectively, see Fig. 4. Thus, for a linear HB q_1 and q_2 denote the deviation of the hydrogen from the center of the HB and the total HB length, respectively. In addition $q_1 < 0$ indicates that the hydrogen stays with the donor oxygen, whereas $q_1 > 0$ denotes a proton transfer to the acceptor. A HB will be called strong if r_2 is about 1.2–1.5 Å and thus q_2 is about 2.2–2.5 Å. In addition $r_1 \approx r_2$ *i.e.* q_1 is close to zero. Similarly, moderate and weak HBs

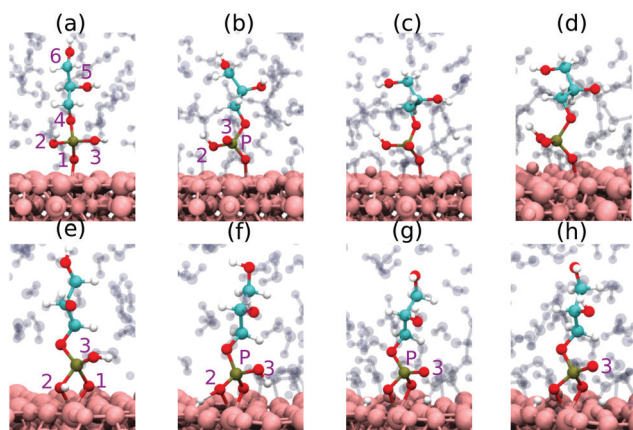


Fig. 3 Snapshots along the trajectories of diaspore–GP–water models. Initial **M** (O + Al) motif (a), proton transfer from O3 to water (b), at 20 ps (c), a stable **M** motif at 25 ps (d), the initial **B** (2O + Al) motif (e), proton transfer from O2 to diaspore (f), proton transfer from O3 to diaspore (g), a stable **B** motif at 25 ps (h).

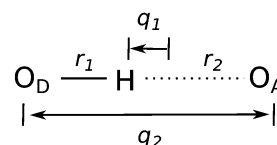


Fig. 4 Definition of HB coordinates q_1 and q_2 .⁵⁶

Table 1 Time-averaged interaction energies (E_{int} according to eqn (1) divided by the number of bonds in the motif) of diaspore–IHP/GP, selected bond lengths and distances as well as the RMSD of the average phosphate geometry from that of the isolated PO₄^{3−} one (*cf.* Fig. S5 and S6 in the ESI). Here, 'motif' denotes the final motif adopted in the production trajectory, Al and O_p denote covalent bonded Al and IHP/GP O atoms. The P denotes the phosphorus atom of the phosphate group bonded to Al and **2M(1)** and **2M(2)** denote the two different **2M** motifs of IHP

P _o	Motif	$E_{\text{int}}/\text{bond}$ (kcal mol ^{−1})	Al–OP (Å)	Al–P (Å)	RMSD(PO ₄ ^{3−}) (Å)
GP	M	−63	1.90	3.3	0.06
	B	−148	2.03 & 2.05	2.65	0.10
IHP	2M(1)	−170	1.84 & 1.87	3.15 & 3.25	0.06 & 0.10
	2M(2)	−115	1.91 & 2.07	2.92 & 3.19	0.10 & 0.19
	3M	−145	1.90 & 1.88 & 1.86	3.25 & 3.17 & 3.18	0.07 & 0.08 & 0.10

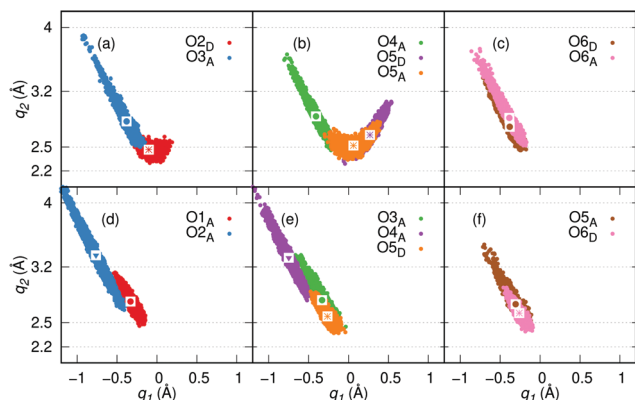


Fig. 5 HB correlation q_2 vs. q_1 of the GP **M** motif (a–c) and the GP **B** motif (d–f), respectively, along the production trajectory. The points in white square boxes denote the average values of q_1 and q_2 . Here, the symbols *, ● and ▼ denote strong to moderately strong HB, moderately strong HB and moderately strong to weak HB respectively.

have r_2 distances in the range of 1.5–2.2 (q_2 from 2.5–3.2 Å and $r_1 < r_2$) and 2.2–3.2 Å (q_2 from 3.2–4 Å and $r_1 \ll r_2$), respectively.⁵⁸

The trajectory data will be analysed by taking snapshot geometries for all the observed HBs. In addition the averaged q_2 and q_1 lengths will be given. The results for the GP **M** motif are shown in Fig. 5. Panel (a) considers the O2 atom which forms a moderate to strong HB and O3 being involved in a weak to moderately strong HB. According to Fig. 5b O4 forms a weak to moderately strong HB, whereas from O5 a proton is transferred to a water oxygen ($r_2 < r_1$). The transferred proton forms a moderate to strong HB with the donating O5. In addition, O5 is an acceptor for a HB with a water H atom. From Fig. 5c we notice that O6 acts as both, donor and acceptor for moderately strong HBs. From the overall analysis of HB strengths, 3 (O2, O5_D, and O5_A) strong to moderately strong HBs and 4 (O3, O4, O6_D, and O6_A) moderately strong HBs are observed. In this study H-bond analysis is performed only for the QM part of the system because we are mainly interested in the interface region. This region is our reactive system which includes all reactions concerning and affecting the surface binding/adsorption process.

Regarding the diasporo–water interaction, an average of 19 water molecules (out of 20 possible) formed **M** binding motifs (Al–O_{H₂O}) with the diasporo surface. The oxygen atoms of water, O_{H₂O} are bound to the surface Al atoms of the diasporo with average bond lengths in the range of 1.8 to 2.0 Å. Around five protons transferred to the diasporo surface after dissociation of a few water molecules near the surface. In addition to the proton transfers and covalent bonds, moderate to strong HBs are also observed between water and diasporo, see Fig. S9a and b in the ESI†

The analysis of the time averaged interaction energies of the production trajectory provides a quantitative measure for the significance of the bonds and proton transfers discussed above. The average interaction energy between diasporo and GP is around –63 kcal mol^{–1}, see Table 1. The average interaction energy values per water molecule with diasporo and GP are –9.8 and –2.2 kcal mol^{–1} respectively. This indicates that water

has a stronger interaction with diasporo than with GP due to several **M** motifs (1Al–1O_{H₂O}), proton transfers and HBs formed between water and the diasporo surface. This appears to be a general observation valid for all the studied diasporo–IHP/GP–water models (see below).

3.1.2 GP **B motif.** The starting configuration the phosphate group is placed in a **B** (2O + 1Al) motif with a surface Al atom and the long side of GP perpendicular to the diasporo surface, see Fig. 3e. A stable **B** motif complex is observed throughout the trajectory, see Fig. S10 in the ESI†. The average covalent bond length of Al–O1 and Al–O2 is 2.03 and 2.05 Å, respectively. Note that these bond lengths are larger than those of the **M** motif, see Table 1. The distance between the P atom and the bonded Al atom has an average value of around 2.65 Å, which is shorter than the one observed in the **M** motif, see Table 1. Hence, establishing a cyclic closed-membered ring structure at the Al site in the **B** motif requires the O1–P–O2 angle to widen, while P moves closer to the surface. As a consequence the average geometry of the PO₄ moiety has a RMSD value of 0.10 Å with respect to the free tetrahedral PO₄^{3–} (see Table 1 and Fig. S5c and S6b in the ESI†).

The proton bonded to oxygen O2 is transferred to the surface in the first 5 ps of the trajectory, see Fig. 3f and thus both oxygens bonded to the Al atom are non-protonated in the production trajectory. This could be the reason for similar covalent bond lengths for the Al–O1 and Al–O2 bonds. The P–Ox and Al–Ox interatomic distances are given in the ESI† (Fig. S5c and S6b). Observe that O3 is closer to Al compared to the **M** motif, see Fig. S6a and b in the ESI†. In contrast to the **M** motif, two protons are transferred from O2 and O3 to the surface, see Fig. 3h. Moderately strong HBs are formed between oxygens O1, O2 and protons transferred to the surface, see Fig. S5c in the ESI†.

Similar to the **M** motif, GP forms an average of 7 HBs with water. Geometrical correlations and HB strengths can be taken from Fig. 5. Observe that 2 (O5 and O6) strong to moderately strong HBs, 3 (O1, O3, and O5) moderately strong HBs and 2 (O2 and O4) moderately strong to weak HBs are formed, see Fig. 5d–f. Altogether, GP often forms moderately strong HBs with water see Fig. S11a and b in the ESI†. The interaction of water with the diasporo surface in the **B** motif is similar to the interaction of water with the diasporo in the **M** motif.

The average interaction energy between GP and diasporo for the **B** motif is –295 kcal mol^{–1}, i.e. –148 kcal mol^{–1} per bond, see Table 1. This interaction energy is more than twice of the interaction energy calculated per bond in the **M** motif case. The increased interaction energy is due to the two proton transfer processes from GP to the diasporo surface. Therefore, the formation of the **B** motif is more favourable compared to the formation of the **M** motif. The average interaction energy per water molecule with GP is –0.78 kcal mol^{–1}. A weaker GP–water interaction energy is observed compared to the **M** motif case since in the latter two proton transfers to the water solvation shell are found.

3.2 Diasporo–IHP–water interactions

3.2.1 IHP 2M motifs. Here, two different initial configurations of the diasporo–IHP–water model have been modelled and both

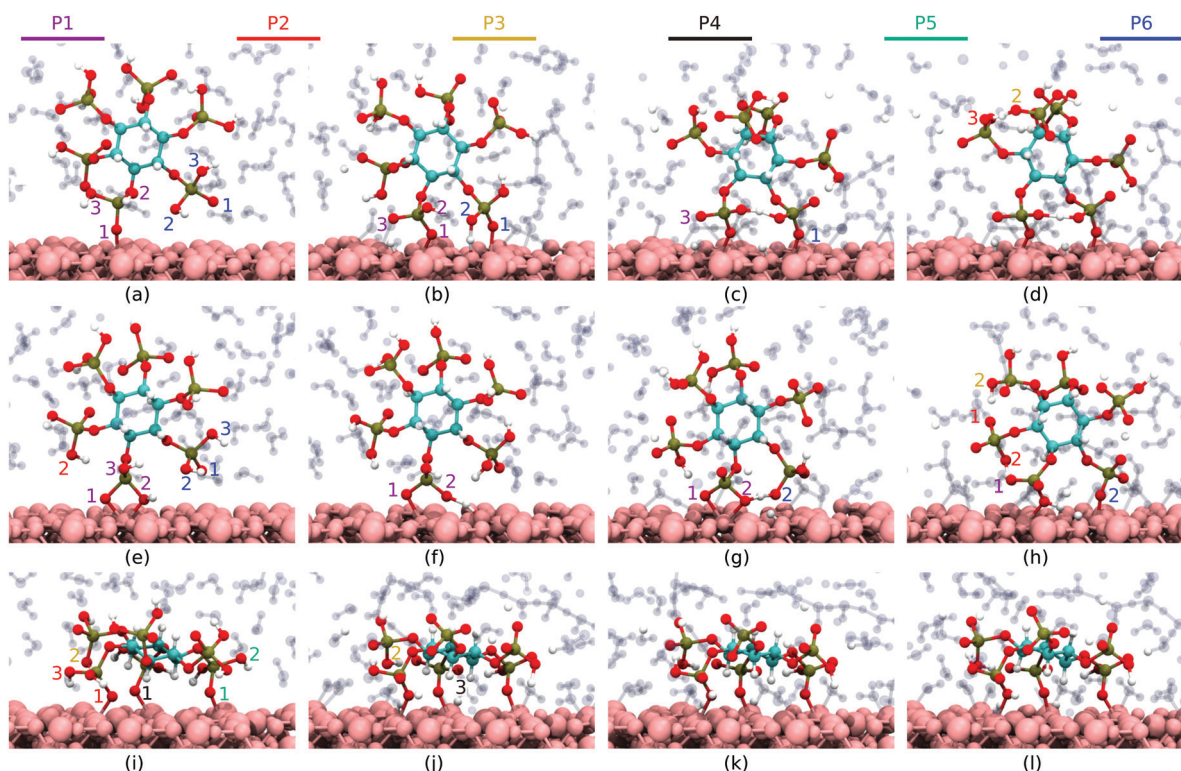


Fig. 6 Snapshots along the trajectories of diaspore-IHP-water models. Here, the phosphate groups are color-coded and the oxygen label color denotes the phosphate group it belongs to. Initial **1M** (O + Al) motif (a), proton transfer from O13 and O62 to the surface and formation of the Al2–O61 covalent bond (b), proton sharing between P1 and P6 phosphate groups (c), a stable **2M** motif (d), the initial **B** (2O + Al) motif (e), proton transfer from O12 to the surface (f), proton sharing and HB between P1 and P6 phosphate groups (g), HB between P1 and P2 phosphate groups and a broken Al2–O62 covalent bond (h), the initial **3M** motif (i), proton transfer from O43 to the surface and protonation of O32 (j), and a stable **3M** motif (k) and (l).

cases finally transformed to **2M** motifs (2 covalent bonds between 2 phosphate's 2 O atoms and 2 surface Al atoms). In the first case, **2M(1)**, a non-protonated IHP phosphate oxygen atom (O11) is aligned to form a **M** motif with a surface Al atom (Al1) and the remaining part of IHP is aligned perpendicular to the diaspore surface, see Fig. 6a. The MD results show that within 2 ps, O61 forms a covalent bond with another surface Al atom (Al2), adjacent to Al1. A stable **2M** binding motif is observed between IHP and diaspore with Al1–O11 and Al2–O61 average covalent bond lengths of 1.84 and 1.87 Å, see Fig. S12b in the ESI† and Fig. 6d, respectively. Further, the average geometries of the PO_4 moieties deviate from that of a free tetrahedral PO_4^{3-} with RMSD values of 0.06 and 0.10 Å (see Table 1 and Fig. S5d and S6c in the ESI†).

The series of events which culminated to form the stable **2M(1)** motif starting from Fig. 6a is as follows: from O13 a proton is transferred to the surface, followed by HB formation between the transferred proton and the donating oxygen O13. After a few fs a HB to the surface from O62 oxygen of the P6 phosphate group is formed, see Fig. 6b. After the formation of this HB, the P6 phosphate group is now close to the surface and the non-protonated oxygen atom (O61) of the P6 phosphate makes a covalent bond with Al2. The formation of HBs between IHP's phosphate group and the surface supported the formation of the Al2–O61 covalent bond. For P–O1 x , P–O6 x , Al1–O1 x and Al2–O6 x interatomic distances, where $x = 1, 2, 3$, and 4, see Fig. S5d and S6c in the ESI†. Notice that the bond lengths,

P–O–Al angle and distances observed between Al1 and the P1 phosphate group are shorter than those between Al2 and the P6 phosphate group, *i.e.* the two binding sites are not equivalent. The distance between Al1 and all P atoms along the course of the trajectory is shown in Fig. S12a in the ESI†.

A total of two proton transfer processes is observed from IHP to the surface, one proton transfers from O13 and it forms a moderately strong HB with the donating oxygen atom O13. Another proton transfers from O62 to form a moderately strong to weak HB with O62, see Fig. 7a ($r_2 < r_1$). In addition to the intermolecular HBs, strong to moderately strong intramolecular

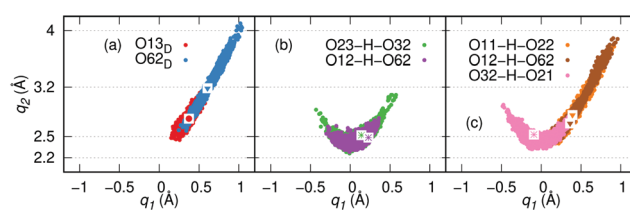


Fig. 7 HB correlation q_2 vs. q_1 of O13, O62 and protons transferred to the surface in IHP **2M(1)** motif (a), intramolecular HBs in IHP observed in the IHP **2M(1)** motif (b) and the IHP **2M(2)** motif (c). The points in white square boxes denote the average value of q_1 and q_2 along the course of the corresponding production trajectory. Here, the symbols *, ● and ▼ denote strong to moderately strong HB, moderately strong HB and moderately strong to weak HB respectively.

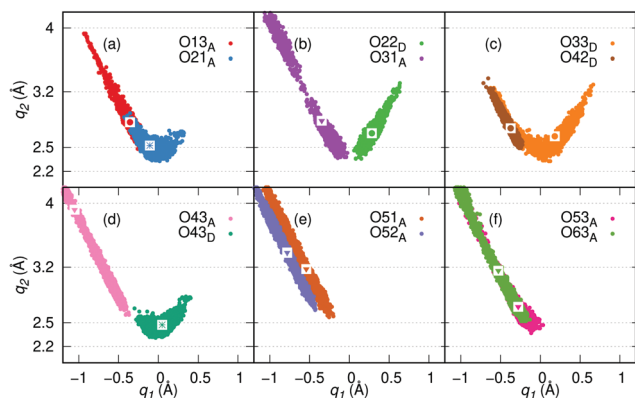


Fig. 8 HB correlation q_2 vs. q_1 of IHP and water in the IHP **2M(1)** motif (a–f). The points in white square boxes denote the average value of q_1 and q_2 along the course of the corresponding production trajectory. Here, the symbols *, ● and ▼ denote strong to moderately strong HB, moderately strong HB and moderately strong to weak HB, respectively.

HBs are observed in IHP, namely O12–H–O62 and O23–H–O32 (see Fig. 7b). Regarding the IHP interaction with water, a total of 5 proton transfers are observed from IHP to water with an average of 19 HBs between IHP and water. Upon analyzing HB strengths between IHP and water using the q_2 vs. q_1 correlation, 2 (O21 and O43) strong to moderately strong HBs, 4 (O13, O22, O33, and O42) moderately strong HBs and 6 (O31, O43A, O51, O52, O53, and O63) moderately strong to weak HBs are formed, see Fig. 8. Note that in Fig. 8b O22 exhibits a proton transfer ($r_2 < r_1$). In addition, it is also observed that the water molecules tend to move closer to the diaspore surface during the course of the simulation, see Fig. S12c and d in the ESI†.

The time-averaged interaction energy between IHP and the diaspore surface is $-340 \text{ kcal mol}^{-1}$, *i.e.* $-170 \text{ kcal mol}^{-1}$ per bond, see Table 1. The interaction energy of IHP with diaspore is higher than that of the GP **B** motif. The average interaction energy per water molecule with IHP is $-6.9 \text{ kcal mol}^{-1}$. Observe that the interaction of water with IHP is stronger than that with GP.

Given the size and flexibility of IHP a number of different configurations can be expected for a given motif. Exemplarily, we discuss a second **2M** motif, in the following called **2M(2)**. It has been obtained starting with a **B** motif, where the phosphate group is placed such that the surface Al atom forms a **B** motif with O11 and O12 oxygens and the remaining part is aligned perpendicular to the diaspore surface, see Fig. 6e. The stable **2M(2)** motif which is obtained is shown in panel (h). The P6 phosphate group forms an additional covalent bond with another surface Al atom (Al2), which is adjacent to the P1 phosphate group bonded surface Al atom (Al1). The average covalent bond length of Al1–O12 and Al2–O62 is 1.91 and 2.07 Å, respectively. Further, the average geometries of the PO_4 moieties deviate from that of a free tetrahedral PO_4^{3-} with RMSD values of 0.10 and 0.19 Å (see Table 1 and Fig. S5e and S6d in the ESI†).

One proton transfer occurs from IHP to diaspore which forms a HB with the bonded oxygens O12 and O62. The series of events that led to the formation of **2M(2)** is as follows: a

proton is transferred from O12 to the diaspore surface followed by intramolecular HB formation between O12 and O62 (O12–H–O62), see Fig. 6f. The HB pulls O62 close to the surface, see Fig. 6g and supports the formation of the Al2–O62 covalent bond. After a few ps, the covalent bond between the non-protonated oxygen O11 and Al1 (see Fig. S13 in the ESI†) is distorted by a moderately strong to weak intramolecular HB formed between O11 and O22 (O11–H–O22). In addition two moderately strong to weak intramolecular HBs (O11–H–O22 and O12–H–O62) are present (see Fig. 6h and 7c).

In addition to the O11–H–O22 intramolecular HB, another reason for dissociation of the Al1–O11 covalent bond in the initial **B** motif could be that IHP has a strong interaction with water. The phosphate groups of IHP often form moderately strong HBs with the surrounding water molecules. A total of three proton transfers and 17 HBs are observed between IHP and water molecules. These interactions lead to a considerable fluctuation of IHP with respect to the diaspore surface, causing dissociation of the covalent bond in the **B** motif.

The average interaction energy between IHP and the diaspore surface is $-230 \text{ kcal mol}^{-1}$ *i.e.* $-115 \text{ kcal mol}^{-1}$ per bond, see Table 1. The average interaction energy per water molecule with IHP is -6 kcal mol^{-1} . The interaction energy per bond is smaller than that for **2M(1)**, implying that eventually **2M(2)** could transform into **2M(1)** on a longer time scale. Observe that the P1–O12 average bond length (1.64 Å) is larger than the average bond length observed between phosphorus and the corresponding Al-bonded oxygen in the IHP **2M(1)** motif, see Fig. S5d and e in the ESI†. Also, the P1–O12–Al1 angle is smaller than the angle observed between P, corresponding Al-bonded oxygen and Al in the IHP **2M(1)** motif, see Fig. S5d and e in the ESI†.

There are several reasons for the higher stability of **2M(1)** as compared to **2M(2)**. Most importantly there is a difference in the deprotonation state, *i.e.* in the case of **2M(1)** a total of seven proton transfers are observed, whereas only four are found for **2M(2)**. In addition, the intramolecular HB O12–H–O62, which is close to the binding sites, could have a stabilizing function. It is much stronger for **2M(1)** as compared to **2M(2)**.

Analyzing the binding mechanisms in the IHP **2M** motif cases, one can conclude that intermolecular HBs, proton transfer processes and intramolecular HBs play a prominent role in deciding the stability of the IHP binding motifs with the diaspore surface.

3.2.2 IHP 3M motif. Initially, IHP has been aligned parallel to the surface with non-protonated oxygens of three phosphate groups forming the **3M** motif with the surface, see Fig. 6i. A stable **3M** motif is observed along the whole trajectory. The average Al1–O21, Al2–O41 and Al3–O51 covalent bond length is 1.90, 1.88 and 1.86 Å, respectively (P2–O2x, P4–O4x, P5–O5x, Al1–O2x, Al2–O4x and Al3–O5x interatomic distances, where $x = 1, 2, 3$, and 4 are given in Fig. S5e and S6f in the ESI†). Further, the average geometries of the PO_4 moieties deviate from that of a free tetrahedral PO_4^{3-} with RMSD values of 0.07, 0.08, and 0.10 Å (see Table 1 and Fig. S5e and S6f in the ESI†). Two protons transferred from O32 and O43 to the diaspore surface. The proton transferred from O43 was kept within a HB close to O43.

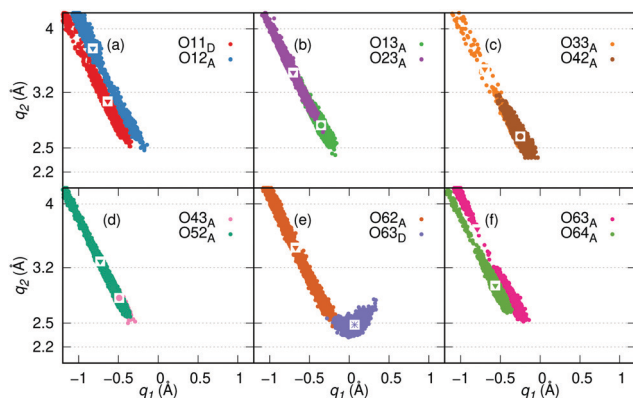


Fig. 9 HB correlation q_2 vs. q_1 of IHP and water in the IHP **3M** motif (a–f). The points in white square boxes denote the average value of q_1 and q_2 along the course of the corresponding production trajectory. Here, the symbols *, ● and ▼ denote strong to moderately strong HB, moderately strong HB and moderately strong to weak HB respectively.

A total of 4 proton transfers are observed from IHP to water with an average of 17 HBs between them. Upon analyzing a few HBs, in Fig. 9, 8 (O11, O12, O23, O33, O52, O62, O63, and O64) moderately strong to weak HBs, 3 (O13, O42, and O43) moderately strong HBs, and 1 (O63) strong to moderately strong HB are observed over the course of the trajectory. Thus, similar to the **2M** motifs, IHP and water form predominantly moderately strong HBs (cf. Fig. S11c and d in the ESI†).

The interaction energy between IHP and diaspore is $-436 \text{ kcal mol}^{-1}$, i.e. $-145 \text{ kcal mol}^{-1}$ per bond, see Table 1. Thus the additional bond in the **3M** motif does not yield an increase in the stability per bond compared to the stable **2M** motif. This may be caused by steric and strain effects due to the fact that the positions of the phosphate groups in IHP do not fit the positions of the possible Al binding sites at the surface. The average interaction energy per water molecule with IHP is $-6.8 \text{ kcal mol}^{-1}$, similar to the interaction energies observed in the **2M** motif cases.

4 Summary and conclusions

The interaction between the reactive hydroxide surface of the mineral diaspore with organic phosphates has been investigated for the exemplary cases of IHP and GP. To this end, periodic boundary QM/MM simulations of GP and IHP at the diaspore–water interface have been performed. The analysis of the individual interactions, i.e. diaspore–IHP/GP, IHP/GP–water, and diaspore–water, provided information about the factors that control the binding mechanisms and the stability of different motifs. Besides the actual covalent P–O–Al bonds, HBs and proton transfers were found to be vital for understanding the relative stability of the binding motifs. In fact the proper description of the various deprotonation steps has been one of the main motivations for using the computationally expensive QM/MM approach.

Upon analyzing the diaspore–GP–water complexes, the interaction energy per bond of the **B** motif is found to exceed the one of the **M** motif by a factor of 2.4. The higher interaction energy

of the **B** motif is to some extent due to the larger number of deprotonation steps, i.e. two more protons transfer from GP to the surface in the case of **B**.

Regarding the diaspore–IHP–water complexes, the IHP **3M** motif is found to have a higher interaction energy compared to the most stable **2M(1)** motif, but exhibits a 1.2 times weaker interaction energy per bond. A possible reason could be the mismatch between the positions of the phosphate groups in IHP and the surface Al sites, which introduces some strain into the **3M** motif. This mismatch makes the formation of a fourth P–O–Al bond rather unlikely. We have also shown that the **B** motif is not stable and if chosen initially it transforms into a **2M** motif.

The HBs between GP/IHP and water as well as diaspore have been characterized using correlations between their geometries along the trajectory. Most of the HBs can be classified as being of moderate strength. In the case of GP, compared to **B** the **M** motif exhibits a stronger interaction with water and has two more proton transfers to the water. For IHP the interaction with the solvating water is of similar strength for **2M** and **3M**. In all cases the interaction of water with diaspore exceeds that with phosphate.

GP and IHP are abundant species in forest soils. Based on the present investigation of their interaction with the diaspore–water interface it becomes clear that once the two species compete for the same active sites of the respective mineral particle, binding of IHP will dominate. Although the interaction energy per bond of the GP **B** and the IHP **3M** motifs is similar, IHP's larger number of phosphate groups allows for more covalent bonds to the surface and more HBs to the solvating water. Note that this should hold true under low concentration conditions, i.e. not regarding surface coverage effects.

Correlating the current analysis with experiments, our simulations confirm the general observation that the number of phosphate groups is the most important parameter controlling the P-binding strength.³¹ As far as the suggestion by Ognalaga *et al.*,²⁵ that IHP binds to the goethite surface by up to four phosphate groups, is concerned, our findings provide evidence that the **4M** motif is not stable at the studied diaspore surface that is structurally isomorphous to goethite. Further, our results are in accordance with the observation that stable binding motifs include only IHP/GP's phosphate groups and do not affect the organic moiety, i.e. no dissociation of C–H, C–O, and C–O–P bonds occurs.^{26,28} In addition, our simulations confirm the general notion regarding the importance of HBs and proton transfers in deciding on the stable binding motif.⁵⁹

Conflicts of interest

There are no conflicts to declare.

Acknowledgements

We gratefully acknowledge the financial support from the German Research Foundation (DFG) as a part of the SPP 1685

Priority program “Ecosystem Nutrition: Forest strategies for limited phosphorus resources” (PBG, OK, AA) and the InnoSoilPhos-project (AA), funded by the German Federal Ministry of Education and Research (BMBF) in the frame of the BonaRes-program (No. 031A558). This research was performed within the scope of the Leibniz Science Campus “Phosphorus Research Rostock”. The authors thank the North German Super computing Alliance for providing HPC resources (project mvp00016). The authors would like to thank Prof. Peter Leinweber (Chair of Soil Science, Rostock University) for helpful discussions.

References

- 1 D. Cordell and T.-S. Neset, *Global Environ. Change*, 2014, **24**, 108–122.
- 2 R. Bol, G. Gruau, P.-E. Mellander, R. Dupas, M. Bechmann, E. Skarbøvik, M. Bieroza, F. Djodjic, M. Glendell, P. Jordan, B. Van der Grift, M. Rode, E. Smolders, M. Verbeeck, S. Gu, E. Klumpp, I. Pohle, M. Fresne and C. Gascuel-Oudou, *Front. Mater. Sci.*, 2018, **5**, 276:1–276:16.
- 3 A. Missong, S. Holzmann, R. Bol, V. Nischwitz, H. Puhlmann, K. v. Wilpert, J. Siemens and E. Klumpp, *Sci. Total Environ.*, 2018, **634**, 305–315.
- 4 R. Bol, D. Julich, D. Brödlin, J. Siemens, K. Kaiser, M. A. Dippold, S. Spielvogel, T. Zilla, D. Mewes, F. von Blanckenburg, H. Puhlmann, S. Holzmann, M. Weiler, W. Amelung, F. Lang, Y. Kuzyakov, K.-H. Feger, N. Gottselig, E. Klumpp, A. Missong, C. Winkelmann, D. Uhlig, J. Sohr, K. von Wilpert, B. Wu and F. Hagedorn, *J. Soil Sci. Plant Nutr.*, 2016, **179**, 425–438.
- 5 J. Boy, C. Valarezo and W. Wilcke, *Eur. J. Soil Sci.*, 2008, **59**, 1209–1227.
- 6 S. Holzmann, A. Missong, H. Puhlmann, J. Siemens, R. Bol, E. Klumpp and K. v. Wilpert, *J. Soil Sci. Plant Nutr.*, 2015, **179**, 443–453.
- 7 P. Gros, A. Ahmed, O. Kühn and P. Leinweber, *Sci. Total Environ.*, 2017, **586**, 527–535.
- 8 J. Kruse, M. Abraham, W. Amelung, C. Baum, R. Bol, O. Kühn, H. Lewandowski, J. Niederberger, Y. Oelmann, C. Rüger, J. Santner, M. Siebers, N. Siebers, M. Spohn, J. Vestergren, A. Vogts and P. Leinweber, *J. Soil Sci. Plant Nutr.*, 2015, **178**, 43–88.
- 9 M. Hens and R. Merckx, *Environ. Sci. Technol.*, 2001, **35**, 493–500.
- 10 X. Jiang, R. Bol, V. Nischwitz, N. Siebers, S. Willbold, H. Vereecken, W. Amelung and E. Klumpp, *J. Environ. Qual.*, 2015, **44**, 1772–1781.
- 11 J. Peñuelas, J. Sardans, A. Rivas-ubach and I. A. Janssens, *Global Change Biol.*, 2011, **18**, 3–6.
- 12 R. H. Newman and K. R. Tate, *Commun. Soil Sci. Plant Anal.*, 1980, **11**, 835–842.
- 13 B. L. Turner, M. J. Papházy, P. M. Haygarth and I. D. Mckelvie, *Philos. Trans. R. Soc., B*, 2002, **357**, 449–469.
- 14 J. Gerke, *Plants*, 2015, **4**, 253–266.
- 15 A. Doolette, R. Smernik and W. Dougherty, *Soil Sci. Soc. Am. J.*, 2009, **73**, 919–927.
- 16 A. Missong, R. Bol, S. Willbold, J. Siemens and E. Klumpp, *J. Soil Sci. Plant Nutr.*, 2016, **179**, 159–167.
- 17 A. G. Vincent, J. Vestergren, G. Gröbner, P. Persson, J. Schleucher and R. Giesler, *Plant Soil*, 2013, **367**, 149–162.
- 18 H. K. Pant, P. R. Warman and J. Nowak, *Commun. Soil Sci. Plant Anal.*, 1999, **30**, 757–772.
- 19 T. M. Tsao, Y. M. Chen and M. K. Wang, *J. Environ. Monit.*, 2011, **13**, 1156–1163.
- 20 R. Chitrakar, S. Tezuka, A. Sonoda, K. Sakane, K. Ooi and T. Hirotsu, *J. Colloid Interface Sci.*, 2006, **298**, 602–608.
- 21 J. Torrent, U. Schwertmann and V. Barron, *Clays Clay Miner.*, 1992, **40**, 14–21.
- 22 R. L. Parfitt and R. J. Atkinson, *Nature*, 1976, **264**, 740–742.
- 23 A. A. Ahmed, S. Gypser, P. Leinweber, D. Freese and O. Kühn, *Phys. Chem. Chem. Phys.*, 2019, **21**, 4421–4434.
- 24 G. Anderson and E. Z. Arlidge, *J. Soil Sci.*, 1962, **13**, 216–224.
- 25 M. Ognalaga, E. Frossard and F. Thomas, *Soil Sci. Soc. Am. J.*, 1994, 332–337.
- 26 L. Celi, S. Lamacchia, F. A. Marsan and E. Barberis, *Soil Sci.*, 1999, **164**, 574–585.
- 27 X.-H. Guan, C. Shang, J. Zhu and G.-H. Chen, *J. Colloid Interface Sci.*, 2006, **293**, 296–302.
- 28 H. Li, B. Wan, Y. Yan, Y. Zhang, W. Cheng and X. Feng, *J. Soil Sci. Plant Nutr.*, 2017, **181**, 557–565.
- 29 T. Hori, M. Moriguchi, M. Sasaki, S. Kitagawa and M. Munakata, *Anal. Chim. Acta*, 1985, **173**, 299–303.
- 30 Y. P. Yan, F. Liu, W. Li, F. Liu, X. H. Feng and D. L. Sparks, *Eur. J. Soil Sci.*, 2014, **65**, 308–317.
- 31 G. Anderson and E. Z. Arlidge, *Eur. J. Soil Sci.*, 1962, **13**, 216–224.
- 32 H. Guo and A. S. Barnard, *J. Mater. Chem.*, 2011, **21**, 11566–11577.
- 33 *Molecular Modeling of Geochemical Reactions*, ed. J. D. Kubicki, Wiley and Sons, Chichester, 2016.
- 34 J. D. Kubicki and H. D. Watts, *Minerals*, 2019, **9**, 141.
- 35 J. D. Kubicki, K. W. Paul, L. Kaban, Q. Zhu, M. K. Mrozik, M. Aryanpour, A.-M. Pierre-Louis and D. R. Strongin, *Langmuir*, 2012, **28**, 14573–14587.
- 36 A. A. Ahmed, O. Kühn, S. G. Aziz, R. H. Hilal and P. Leinweber, *Sci. Total Environ.*, 2014, **476–477C**, 98–106.
- 37 A. A. Ahmed, P. Leinweber and O. Kühn, *J. Theor. Comput. Chem.*, 2014, **13**, 1450009.
- 38 A. A. Ahmed, P. Leinweber and O. Kühn, *Phys. Chem. Chem. Phys.*, 2018, **20**, 1531–1539.
- 39 H. M. Senn and W. Thiel, *Angew. Chem., Int. Ed.*, 2009, **48**, 1198–1229.
- 40 M. Kosmulski, *J. Colloid Interface Sci.*, 2009, **337**, 439–448.
- 41 W. Humphrey, A. Dalke and K. Schulten, *J. Mol. Graphics*, 1996, **14**, 33–38.
- 42 CP2K, Open source molecular dynamics code., www.cp2k.org.
- 43 J. VandeVondele, M. Krack, F. Mohamed, M. Parrinello, T. Chassaing and J. Hutter, *Comput. Phys. Commun.*, 2005, **167**, 103–128.
- 44 C. Mundy, S. Balasubramanian, K. Bagchi, J. Hutter, A. S. I. Kuo, T. Laino and J. VandeVondele, *Frontiers in Simulation Technology (FIST)*.

- 45 M. Krack, *Theor. Chem. Acc.*, 2005, **114**, 145–152.
- 46 J. P. Perdew, K. Burke and M. Ernzerhof, *Phys. Rev. Lett.*, 1996, **77**, 3865–3868.
- 47 S. Grimme, J. Antony, S. Ehrlich and H. Krieg, *J. Phys. Chem.*, 2010, **132**, 154104.
- 48 J. VandeVondele and J. Hutter, *J. Chem. Phys.*, 2007, **127**, 114105.
- 49 H. J. C. Berendsen, J. R. Grigera and T. P. Straatsma, *J. Phys. Chem.*, 1987, **91**, 6269–6271.
- 50 R. T. Cygan, J. J. Liang and A. G. Kalinichev, *J. Phys. Chem. B*, 2004, **108**, 1255–1266.
- 51 V. Zoete, M. A. Cuendet, A. Grosdidier and O. Michielin, *J. Comput. Chem.*, 2011, **32**, 2359–2368.
- 52 T. Laino, F. Mohamed, A. Laio and M. Parrinello, *J. Chem. Theory Comput.*, 2006, **2**, 1370–1378.
- 53 G. Bussi, D. Donadio and M. Parrinello, *J. Chem. Phys.*, 2007, **126**, 014101.
- 54 S. Boys and F. Bernardi, *Mol. Phys.*, 1970, **19**, 553–566.
- 55 T. Strassner, *Angew. Chem.*, 2006, **45**, 6420–6421.
- 56 H.-H. Limbach, P. M. Tolstoy, N. Pérez-Hernández, J. Guo, I. G. Shenderovich and G. S. Denisov, *Isr. J. Chem.*, 2009, **49**, 199–216.
- 57 T. Zentel and O. Kühn, *Theor. Chem. Acc.*, 2017, **136**, 87.
- 58 M. J. Minch, *J. Chem. Educ.*, 1999, **76**, 759.
- 59 B. B. Johnson, E. Quill and M. J. Angove, *J. Colloid Interface Sci.*, 2012, **367**, 436–442.

Supplementary Information:

QM/MM simulations of organic phosphorus adsorption at the diaspore-water interface

Prasanth B. Ganta,^a Oliver Kühn,^{a,b} and Ashour A. Ahmed,^{a,b†}

^aUniversity of Rostock, Institute of Physics, Albert-Einstein-Str. 23-24, D-18059 Rostock, Germany

^bUniversity of Rostock, Department of Life, Light, and Matter (LLM), Albert-Einstein-Str. 25, D-18059 Rostock, Germany

prasanth.ganta@uni-rostock.de

oliver.kuehn@uni-rostock.de

ashour.ahmed@uni-rostock.de

CONTENTS

1. Force fields used in the current simulations
2. Description and validation of the present QM/MM approach
3. Modeling of diaspore surface with unsaturated active sites
4. Model conditions (soil pH and pKa for phosphates)
5. Proton transfer in the bulk and at the interface
6. Description of the interaction energy calculations

1. Force fields used in the current simulations

The MM level interaction between the diaspore (α -AlOOH) surface and water is defined based on the CLAYFF force fields [S1]. It is to be noted that the CLAYFF force fields are compatible with SPC water model. The total energy of the MM system using CLAYFF is given by:

$$E_{\text{sys}} = E_{\text{bond}} + E_{\text{angle}} + E_{\text{vdW}} + E_{\text{coulomb}}$$

where, E_{bond} and E_{angle} are energies due to bond stretching and angle bending. E_{vdW} and E_{coulomb} denote energies due to van der Waals (vdW) and electrostatic interactions. The total energy is sum of bonded interactions (bond/angle) and nonbonded interactions (vdW and electrostatic). The bond stretching energy is defined as:

$$E_{\text{bond}} = k_b(r_{ij} - r_0)^2$$

where, k_b denotes force constant, r_{ij} denotes distance between i,j atoms, and r_0 denotes equilibrium bond length. Similarly the energy of the angle bend is given by:

$$E_{\text{angle}} = k_\theta(\theta_{ijk} - \theta_0)^2$$

where, k_θ denotes a force constant, θ_{ijk} is bond angle between i, j and k atoms and θ_0 is equilibrium bond angle.

Table S1: Bond and angle parameters for diaspore and water

bond stretch				
species i	species j		k_b (kcal/mol \AA^2)	r_0 (\AA)
water hydrogen	water oxygen		554.1349	1.0
hydroxyl hydrogen	hydroxyl oxygen		554.1349	1.0
angle bend				
species i	species j	species k	k_θ (kcal/mol rad ²)	θ_0 (deg)
water hydrogen	water oxygen	water hydrogen	45.7696	109.47
aluminium	hydroxyl oxygen	hydroxyl hydrogen	30.0	109.47

The short range vdW interaction energy is represented as:

$$E_{\text{vdW}} = \sum_{\text{vdW}}^{i < j} D_{o,ij} \left[\left(\frac{R_{o,ij}}{r_{ij}} \right)^{12} - 2 \left(\frac{R_{o,ij}}{r_{ij}} \right)^6 \right]$$

where, $D_{o,ij}$ and $R_{o,ij}$ are empirical parameters. For unlike atoms, the parameters can be calculated using:

$$R_{o,ij} = \frac{1}{2}(R_{o,i} + R_{o,j})$$

$$D_{o,ij} = \sqrt{D_{o,i}D_{o,j}}$$

The long range coulomb interaction energy is given by:

$$E_{\text{coulomb}} = \sum_{\text{coulomb}}^{i < j} e^2 \frac{q_i q_j}{4\pi\epsilon_0 r_{ij}}$$

Table S2: Nonbonded parameters for diaspoire and water

species	charge (e)	$D_0(\text{kcal mol}^{-1})$	$R_0(\text{\AA})$
water hydrogen	0.41		
water oxygen	-0.82	0.1554	3.5532
bridging oxygen	-1.05	0.1554	3.5532
aluminium	1.575	1.3298e-6	4.7943
hydroxyl hydrogen	0.425		
hydroxyl oxygen	-0.95	0.1554	3.5532

where, q_i, q_j denote partial charges, e denotes electron charge and ϵ_0 is the dielectric permittivity of vacuum.

The MM level interaction between IHP/GP and water is defined with the CHARMM force field parameters obtained from SwissParm, a force field generation tool [S2]. Here also, the water is defined based on the SPC water model.

Table S3: Nonbonded parameters for IHP, GP

species	charge (e)	$D_0(\text{kcal mol}^{-1})$	$R_0(\text{\AA})$
CR	0.2800	0.0550	3.8754
O2CM	-0.7000	0.1200	3.0290
ORC2P	-0.5512	0.1520	3.1537
ORPOH	-0.7712	0.1520	3.1537
ORCOH	-0.6800	0.1520	3.1537
PO4	1.5136	0.5850	3.8308
HCMM	0.0000	0.0220	2.3519
HOCO	0.5000	0.0460	0.4000
HORCOH	0.4000	0.0460	0.4000

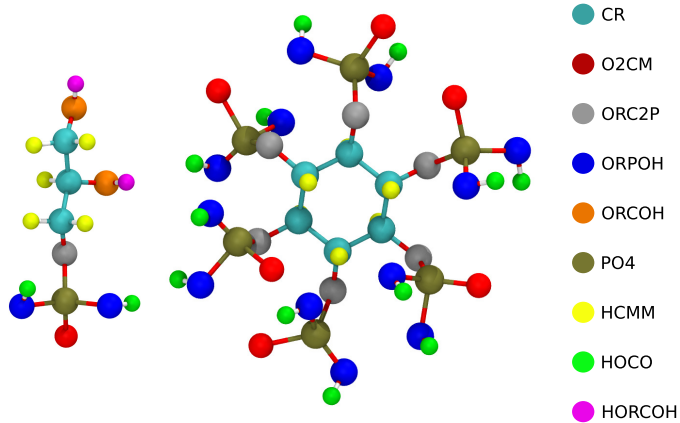


Figure S1: IHP and GP color-coded to denote atoms listed in Table S3.

2. Description and validation of the present QM/MM approach

For the current applied electrostatic embedding QMMM approach, the MM parameters are used for calculating

- interaction between the MM subsystems
- coupling interaction between the QM and MM subsystems

The whole MM subsystem consists of two subsystems, 1- bottom six layers of diaspore surface (480 atoms) and 2- about 175 water molecules in the simulation box. Here, the CLAYFF parameters for the diaspore surface and the SPC model parameters for water molecules (which are completely compatible with the CLAYFF parameters) are sufficient to simulate the diaspore-water interactions.

Regarding QM and MM coupling the following approach is implemented:

- QM(water+diaspore+IHP/GP) interaction with MM(diaspore): Here, $\text{water}_{\text{QM}} - \text{diaspore}_{\text{MM}}$ and $\text{diaspore}_{\text{QM}} - \text{diaspore}_{\text{MM}}$ interactions are defined with respect to two compatible force fields CLAYFF and SPC based water model. Regarding $\text{IHP/GP}_{\text{QM}} - \text{diaspore}_{\text{MM}}$ interactions, the long range interactions are ignored, since the corresponding parameters are not available.
- QM(water+diaspore+IHP/GP) interaction with MM(water): Here, MM water is defined based on SPC water model which is compatible with both CLAYFF (diaspore) and CHARMM (IHP/GP) force fields.

To validate our approach, pure QM(DFT) NVT-MD simulation using IHP **2M(1)** model is performed for 5 ps. The trajectory analysis showed similar pair correlation functions between the corresponding QM and QMMM trajectories, please refer Fig. S2. In addition, the trajectories obtained using pure QM and QMMM have similar Al-O-P bond formations, please ref Fig. S3.

3. Modeling of diaspore surface with unsaturated active sites

- Diaspore has a point of zero charge (PZC) around 6 [S3, S4]. This means that below pH 6 the surrounding water molecules will dissociate and donate more protons than hydroxyl groups to the diaspore surface leading to a positively charged surface. This explains that the diaspore surface at pH below 6 will be partially unsaturated and has the ability to attract/adsorb anions such as phosphate and/or hydroxyl groups at its surface. Hence, this adsorption process (or binding reaction) could happen mainly by direct reaction to the unsaturated surface centers (active sites) without need for a ligand-exchange mechanism. Conversely, above pH 6 the surface will be negatively charged and more saturated by hydroxyl groups from water. Here the surface saturation will increase upon increasing the solution pH and the surface will have the ability to attract cations and repel anions. Under these conditions, the chemisorption process of anions at surfaces (i.e. inner-sphere complexes) should take place via a ligand-exchange mechanism. Considering the fact that most soils and especially forest soils are acidic [S5, S6], gives the motivation to model the diaspore surface as a partially unsaturated one.
- In addition to the poor knowledge of the molecular reaction mechanisms of the phosphate binding at the diaspore surface, diaspore has been modeled in the current contribution for two main reasons. The first one is that diaspore

is isomorphous with goethite (α -FeOOH) which is most abundant and common mineral containing iron atom in the form of ferric (Fe^{+3}). Hence, by investigating the adsorption process at both diasporite and goethite surfaces with same degree of unsaturation the effect of central metal ion (Fe/Al) on adsorption process could be understood in more detail. The second reason is arising from the fact that Fe/Al hydroxide mixtures are highly abundant in soils thus affecting P fixation and release. It is to be noted that goethite has PZC around 9 [S3]. Therefore, goethite surface will be unsaturated below pH 9 and thus can adsorb phosphate and form inner-sphere complexes via a direct interaction mechanism and not a ligand-exchange one. Keeping in mind the PZC of diasporite and goethite one may expect the amorphous Fe/Al hydroxide mixtures should have PZC values in the range of pH 6-9. So according to reported PZC values, which are in that range, a more realistic model for both diasporite and goethite should be partially unsaturated and not saturated completely. This holds true unless one is studying a high pH range which, however, is not in the focus of the present investigation.

- It is well-known from sorption experiments that the phosphate adsorption decreases with increasing the soil solution pH [S7, S8]. This means that in the presence of OH^- at high pH, OH^- groups can replace the adsorbed phosphate indicating a stronger adsorption for OH^- than for phosphate at mineral surfaces. This behaviour has been observed and explained in more details at a molecular level by our group [S9, S10]. The modelling results indicated that phosphate can replace the competing water molecules at the goethite surface, but phosphate could be replaced by OH^- groups. This shows that the reverse reaction, i.e. replacement of OH^- groups by phosphate, is mainly a non-spontaneous reaction and unlikely to take place. This indicates that formation of inner-sphere complexes of phosphate with goethite/diasporite surfaces could happen mainly due to direct reaction of phosphate with the surface unsaturated centers and not with a ligand-exchange mechanism. Consequently, this points to the necessity of the presence of some unsaturated centers at the mineral surface to form inner-sphere complexes with phosphates.

4. Model conditions (soil pH and pKa for phosphates)

As mentioned in the previous section and according to the diasporite's PZC value, we are simulating common and normal acidic soil conditions, i.e. at pH in the range of 3-6. Consequently, the diasporite surface was modeled with active unsaturated centers. According to the best of our knowledge, there are some differences and conflicts between the available pKa values for IHP and GP. For example, the estimated pKa values by the "ChemAxon" software are 0.14 for IHP and 1.5 for GP. Experimentally, it was mentioned that IHP is a relatively reactive phosphate compound having 12 dissociable protons with pKa values in the range of about 1.5 to 10 [S11]. In view of these conflicts, we have started our simulation with the neutral forms for both IHP and GP. However, we have observed deprotonation of the phosphates (IHP and GP) in the first few pico-seconds (ps) of the simulation trajectories (see Figs. S7 and S8), according to the acidic character of these phosphates which is thus properly taking into account by our modelling approach.

5. Proton transfer in the bulk and at the interface

The proton transfer events have been triggered by the surface. But in general, these processes could take place either in the presence or absence of the surface (i.e. for simulations carried out in the bulk). To investigate such goal practically,

two additional MD simulations have been performed with the same applied approach. One simulation was carried out with GP in the presence of the diaspore surface with a separation distance of about 5 Å between them. The second simulation involved GP in a pure water without diaspore. Both simulations showed proton transfer processes during the simulation trajectory (see Figs. S7 and S8).

6. Description of the interaction energy calculations

In general, the effect of water on the calculated diaspore-phosphate interaction has been considered during the MD trajectory due to the diaspore-phosphate-water interactions based on the electronic and Van der Waals interactions. Here phosphate refers to GP and IHP. However, this effect has not been considered explicitly for computing the interaction energy in Eq. 1. In practice, each diaspore-phosphate-water model could be considered as three sub-systems (fragments). These fragments are diaspore (fragment1), IHP/GP (fragment2) and water (fragment3). Within CP2K it is possible to calculate the pair interaction energy between two fragments. According to Eq. 1 of the main paper

$$E_{\text{int}} = E_{\text{diaspore-phosphate-complex}} - (E_{\text{diaspore}} + E_{\text{phosphate}}),$$

we have defined diaspore as the first fragment and phosphate as the second fragment. Water enters only insofar as it determines the actual geometry of the interacting fragments. The interaction energy is calculated within the BSSE counterpoise correction philosophy, i.e. by performing five energy calculations as follows: diaspore including only the diaspore basis functions ($E_{\text{diaspore}}^{\text{diaspore}}$), total electronic energy of phosphate including only the phosphate basis functions ($E_{\text{phosphate}}^{\text{phosphate}}$), diaspore including the basis functions of phosphate and diaspore ($E_{\text{diaspore}}^{\text{diaspore+phosphate}}$), phosphate including the basis functions of phosphate and diaspore ($E_{\text{phosphate}}^{\text{diaspore+phosphate}}$) and finally diaspore-phosphate complex including the basis functions of diaspore and phosphate ($E_{\text{diaspore-phosphate-complex}}^{\text{diaspore+phosphate}}$). From these numbers one gets the interaction energy between diaspore and phosphate as $E_{\text{int}} = E_{\text{diaspore-phosphate-complex}}^{\text{diaspore+phosphate}} - (E_{\text{diaspore}}^{\text{diaspore+phosphate}} + E_{\text{phosphate}}^{\text{diaspore+phosphate}})$. Similarly, the interaction energies between phosphate and water ($E_{\text{int}} = E_{\text{phosphate-water-complex}}^{\text{phosphate+water}} - (E_{\text{phosphate}}^{\text{phosphate+water}} + E_{\text{water}}^{\text{phosphate+water}})$) and between diaspore and water ($E_{\text{int}} = E_{\text{diaspore-water-complex}}^{\text{diaspore+water}} - (E_{\text{diaspore}}^{\text{diaspore+water}} + E_{\text{water}}^{\text{diaspore+water}})$) could be calculated.

References

- [S1] R. T. Cygan, J. J. Liang, A. G. Kalinichev, Molecular models of hydroxide, oxyhydroxide, and clay phases and the development of a general force field, *J. Phys. Chem. B* 108 (2004) 1255–1266.
- [S2] V. Zoete, M. A. Cuendet, A. Grosdidier, O. Michielin, Swissparam: A fast force field generation tool for small organic molecules, *J. Comput. Chem.* 32 (2011) 2359–2368.
- [S3] M. Kosmulski, pH-dependent surface charging and points of zero charge. IV. Update and new approach, *J. Colloid Interface Sci.* 337 (2009) 439 – 448.
- [S4] C.-b. Huang, L. Zhang, Y.-h. Wang, Y. Lan, Separation of aluminosilicates and diaspore from diasporic-bauxite by selective flocculation, *J. Cent. South Univ. Technol.* 15 (2008) 520–525.
- [S5] E. Slessarev, Y. Lin, N. Bingham, J. E Johnson, Y. Dai, J. Schimel, O. Chadwick, Water balance creates a threshold in soil pH at the global scale, *Nature* 540 (2016) 567–569.

- [S6] Breemen, C. Driscoll, J. Mulder, Acidic deposition and internal proton in acidification of soils and waters, *Nature* 307 (1984) 599-604 307 (1984) 599–604.
- [S7] B. Barja, M. Dos Santos AFONSO, Aminomethylphosphonic acid and glyphosate adsorption onto goethite: A comparative study, *Environ. Sci. Technol.* 39 (2005) 585–92.
- [S8] J. Sheals, S. Sjöberg, P. Persson, Adsorption of glyphosate on goethite: Molecular characterization of surface complexes, *Environ. Sci. Technol.* 36 (2002) 3090–3095.
- [S9] A. A. Ahmed, P. Leinweber, O. Kühn, Unravelling the nature of glyphosate binding to goethite surfaces by ab initio molecular dynamics simulations, *Phys. Chem. Chem. Phys.* 20 (2018) 1531–1539.
- [S10] A. A. Ahmed, S. Gypser, P. Leinweber, D. Freese, O. Kühn, Infrared spectroscopic characterization of phosphate binding at the goethite-water interface, *Phys. Chem. Chem. Phys.* 21 (2019) 4421–4434.
- [S11] A. J. Costello, T. Glonek, T. C. Myers, ^{31}P Nuclear magnetic resonance pH titrations of myo-inositol hexaphosphatex, *Carbohydr. Res.* 46 (1976) 159 – 171.

FIGURES

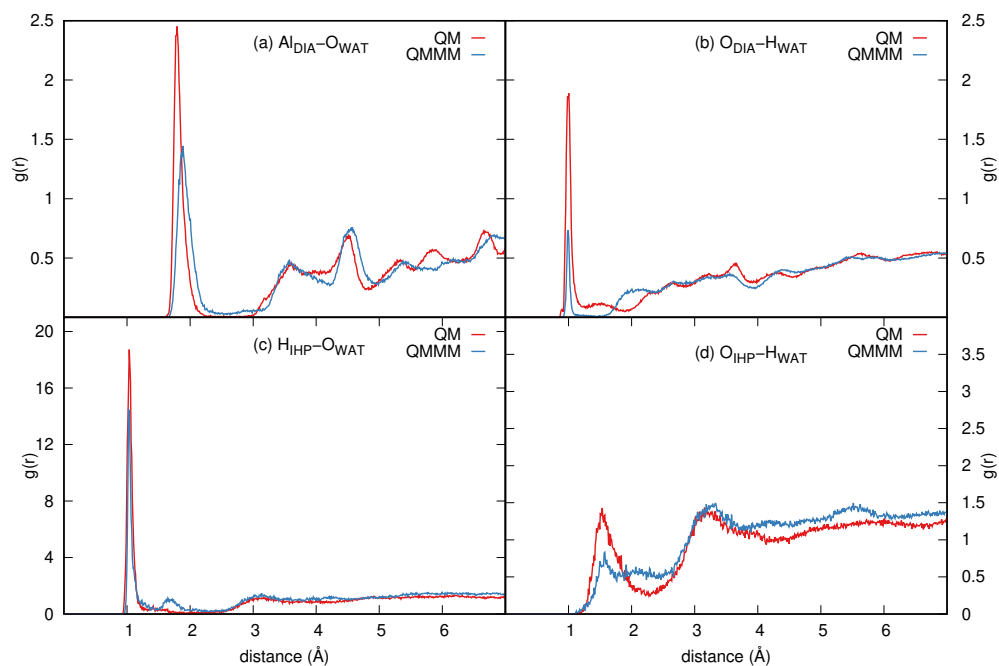


Figure S2: Comparison of pair correlation functions calculated using QM and QMMM methods. Al of diaspore and oxygens of water (a), oxygens of diaspore and hydrogens of water (b), hydrogens of IHP and oxygens of water (c), oxygens of IHP and hydrogens of water (d). The red and black lines denote correlation function obtained using QM method and QMMM method respectively.

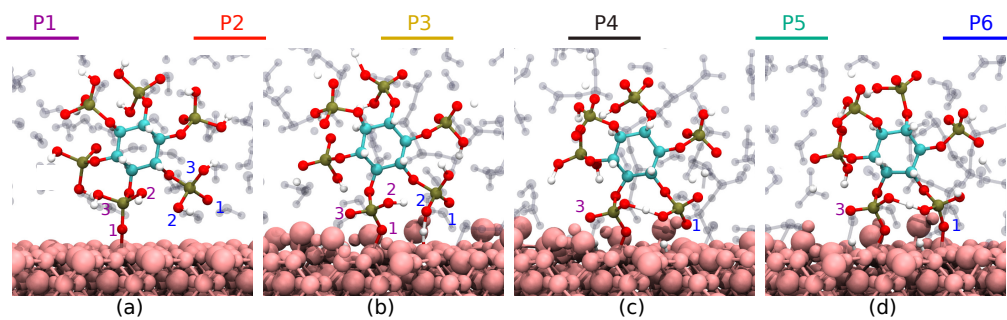


Figure S3: Snapshots along the trajectory of IHP **2M(1)** model simulated using QM (DFT) only. Initial M(O + Al) motif (a), proton transfer from O13 and O62 to surface (b), proton sharing between P1 and P6 phosphate groups (c), and formation of Al2-O61 covalent bond (d). Similar events are observed in IHP **2M(1)** model trajectory simulated using QM/MM.

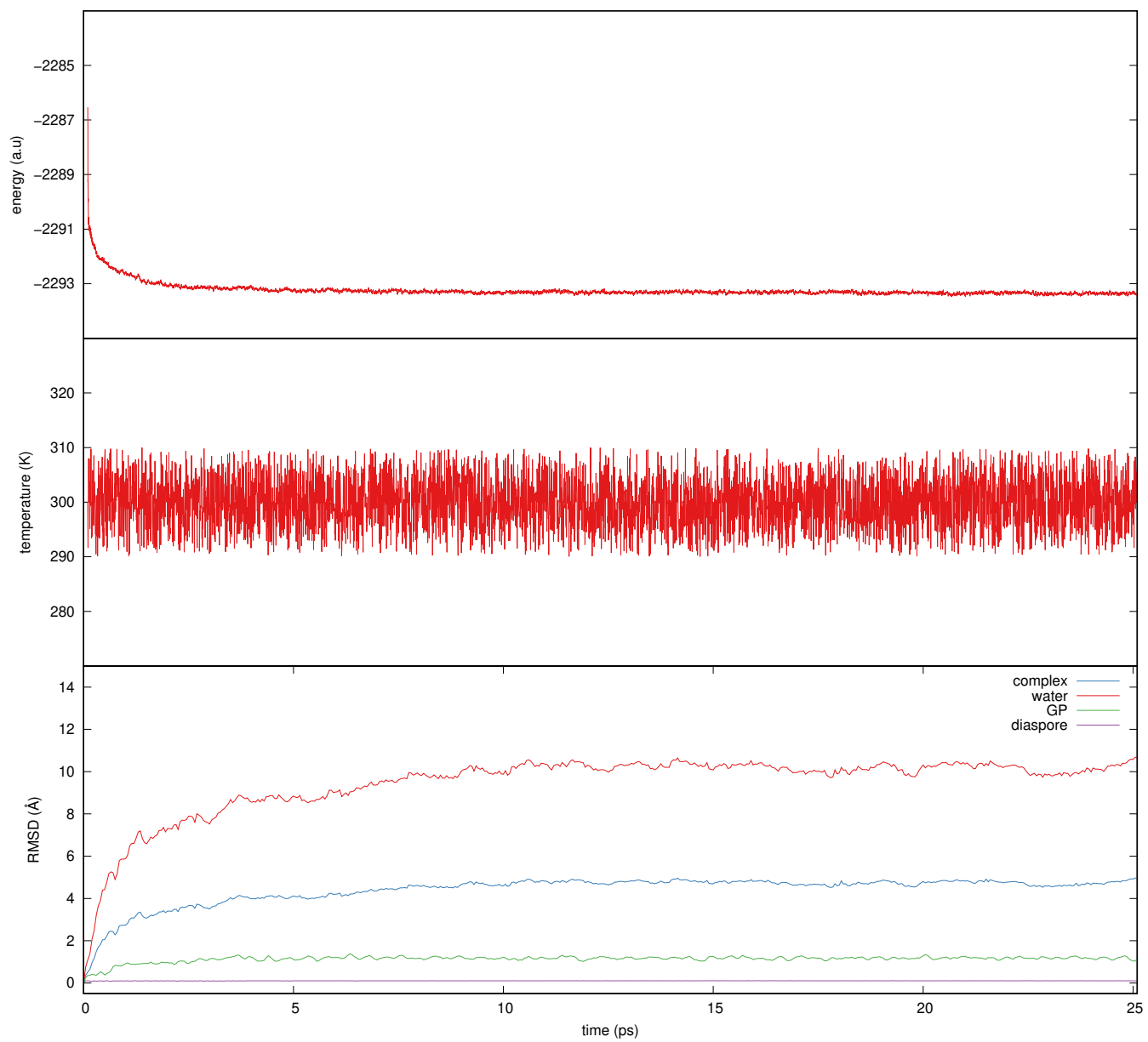


Figure S4: GP **M** motif potential energy (top), temperature (middle), root mean square deviation (RMSD, bottom) along MD trajectory. This figure suggests that the GP **M** motif diaspore-GP-water complex is equilibrated within the first 10 ps of the whole trajectory.

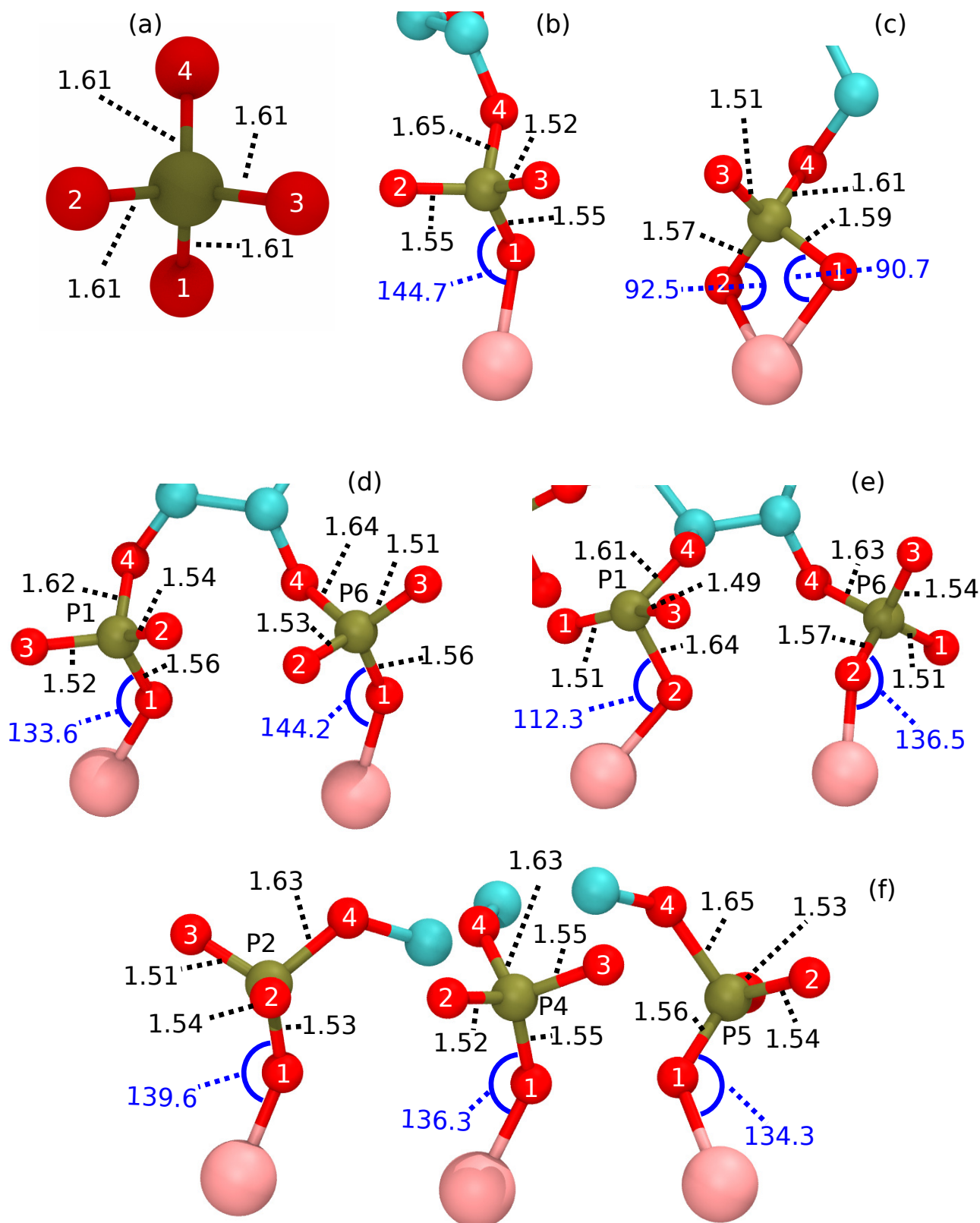


Figure S5: Interatomic distances between phosphorus and corresponding oxygens of orthophosphate (a), GP M motif (b), GP B motif (c), IHP 2M(1) motif (d), IHP 2M(2) motif (e), IHP 3M motif (f). Note that P-O-Al angle is also provided for relevant cases, where O and Al are covalently bonded. Only Al bonded phosphate groups and Al are shown in all motifs for better visualisation.

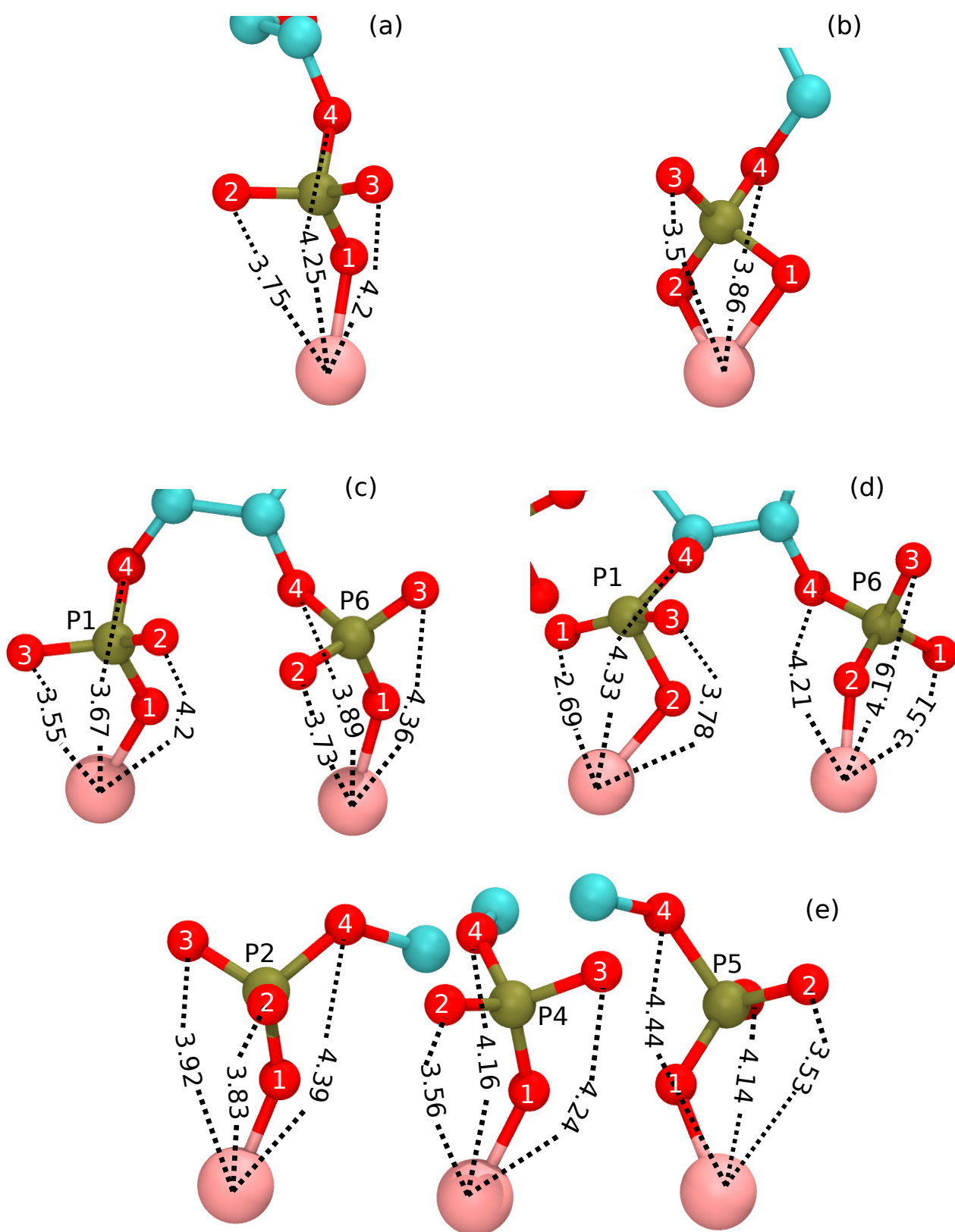


Figure S6: Interatomic distances between Al-nonbonded oxygens in phosphate group and Al. GP **M** motif (a), GP **B** motif (b), IHP **2M(1)** motif (c), IHP **2M(2)** motif (d), IHP **3M** motif (e).

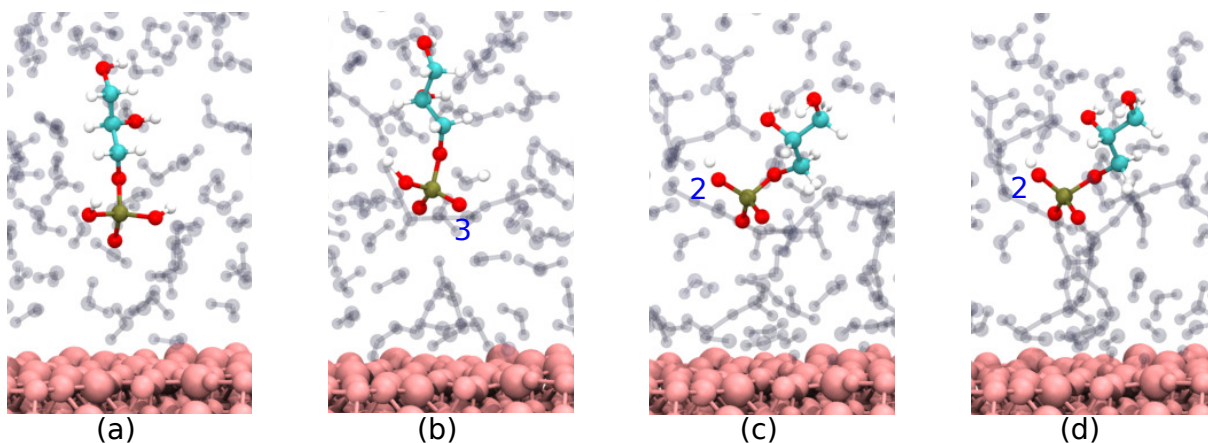


Figure S7: Snapshots along 10 ps trajectory of diaspore-GP-water model with GP above 5 Å from diaspore surface. Initial configuration (a), proton transfer from O3 to water (b), proton transfer from O2 to water (c) and (d).

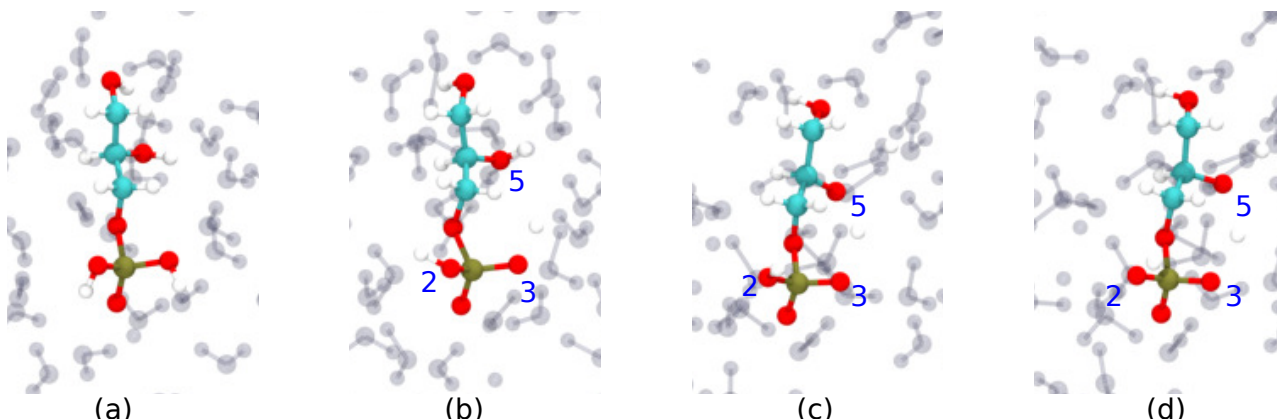


Figure S8: Snapshots along 10 ps trajectory of GP-water model. Initial configuration (a), proton transfer from O3 to water (b), proton transfer from O5 to water (c) and proton transfer from O2 to water (d).

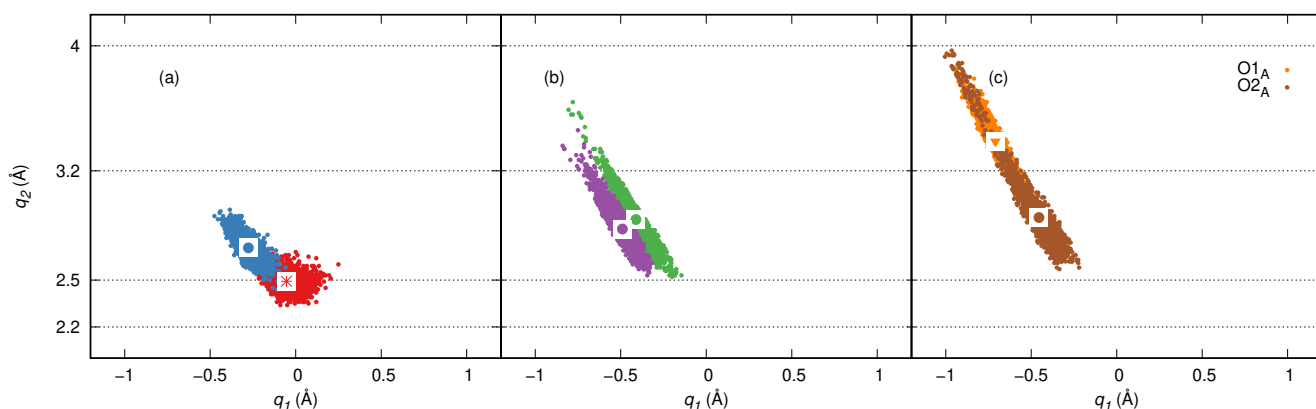


Figure S9: HB correlation q_2 vs. q_1 of a few diaspore oxygens and water molecules in GP M motif (a), (b) and HBs strength between O1, O2 and protons transferred to diaspore in GP B motif (c). Here, the symbols *, • and ▼ denote strong to moderately strong HB, moderately strong HB and moderately strong to weak HB respectively.

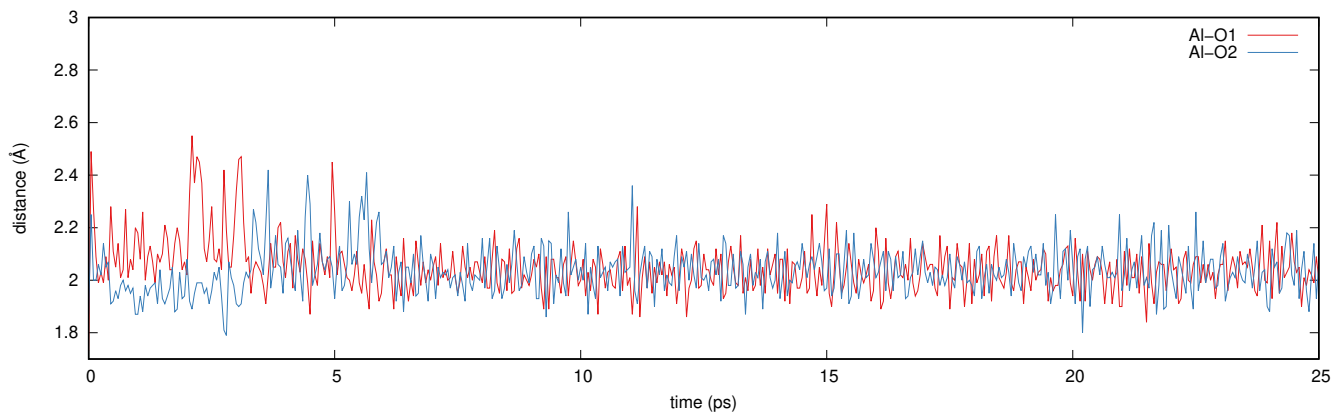


Figure S10: Al-O bond lengths in GP **B** motif with **B** motif along MD trajectory. Observe that a stable **B** motif is maintained until the end of the trajectory.

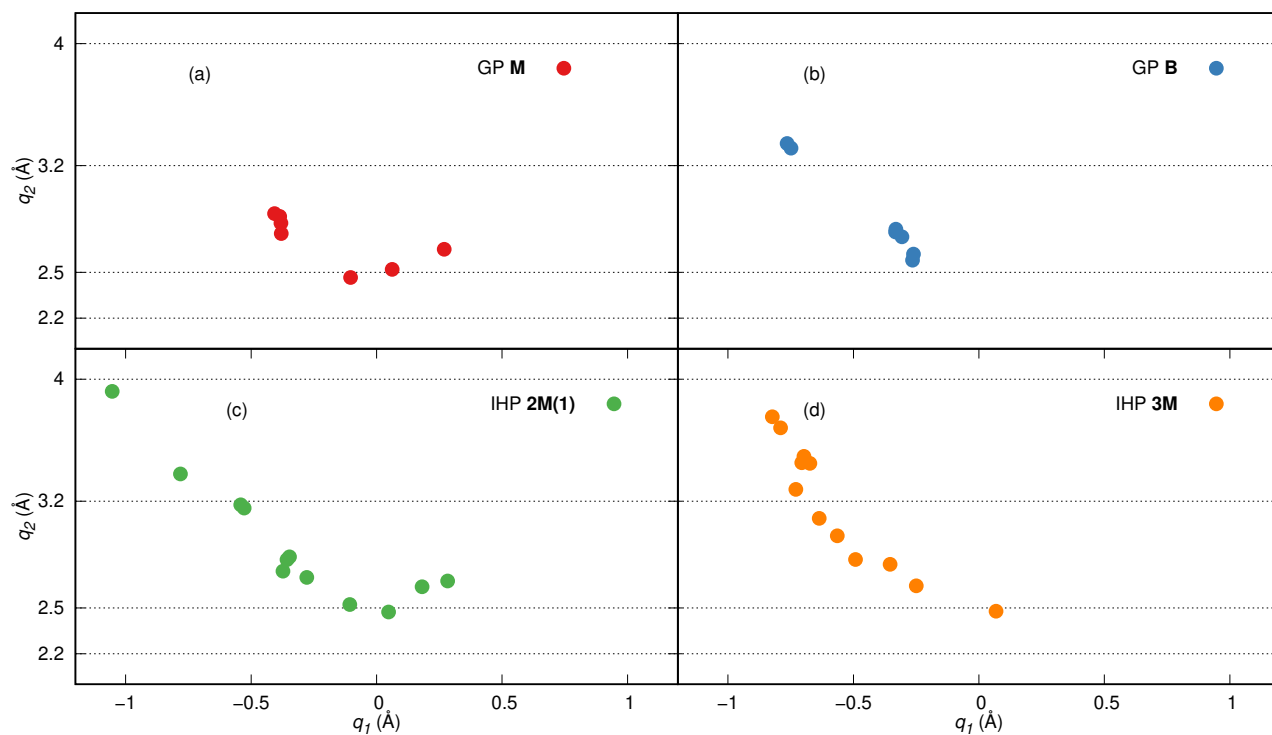


Figure S11: HB correlation q_2 vs. q_1 of selected HBs observed in IHP/GP with water. Observe that IHP and GP often formed moderately strong HBs with water.

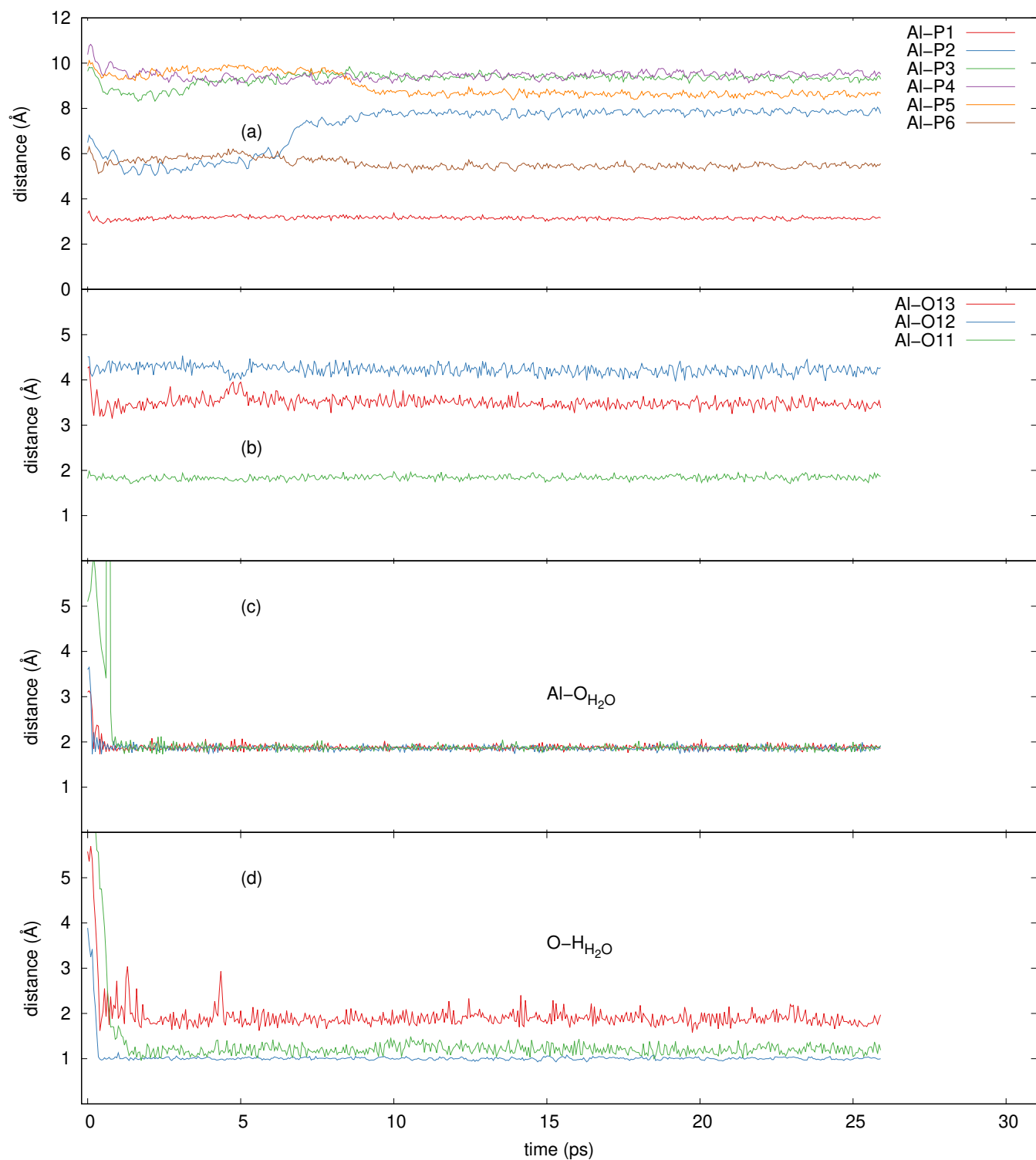


Figure S12: In IHP **2M(1)** motif, distance between surface Al1 contributed to **M** motif and all phosphorus atoms in IHP (a), distance between surface Al1 contributed to **M** motif and bonded phosphate oxygens (b), distance between a few different surface Al and water oxygens (c), distance between a few different diaspore oxygens and water hydrogens (d).

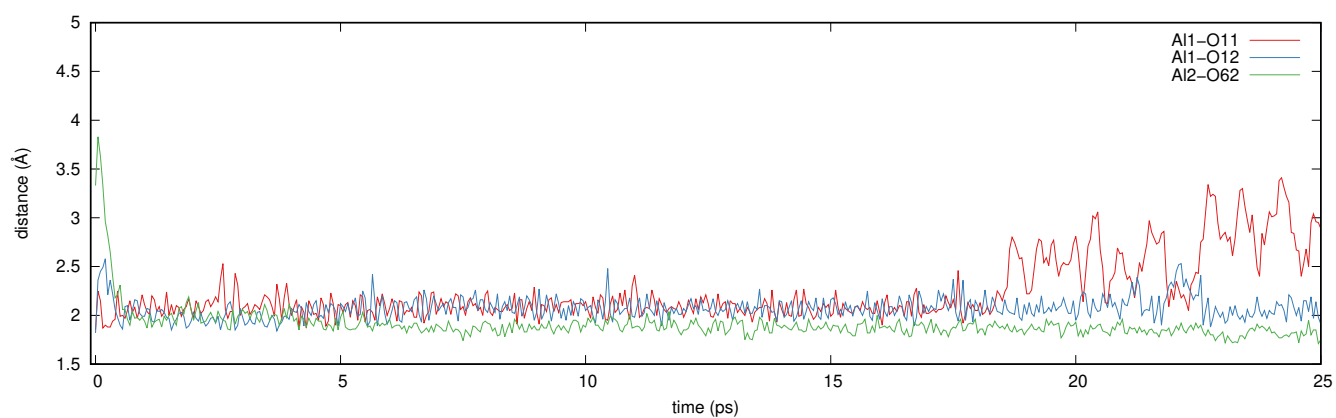


Figure S13: Al-O bond lengths in IHP **2M(2)** motif along MD trajectory. Observe disassociation of Al1-O11 and formation of Al2-O62 resulting in **2M** motif until the end of the trajectory.



QM/MM Molecular Dynamics Investigation of the Binding of Organic Phosphates to the 100 Diaspore Surface

Prasanth B. Ganta¹, Oliver Kühn^{1,2} and Ashour A. Ahmed^{1,2*}

¹ Institute of Physics, University of Rostock, Rostock, Germany, ² Department of Life, Light, and Matter (LLM), University of Rostock, Rostock, Germany

OPEN ACCESS

Edited by:

Friederike Lang,
University of Freiburg, Germany

Reviewed by:

Zachary E. Kayler,
University of Idaho, United States
Daniel Tunega,
University of Natural Resources and
Life Sciences Vienna, Austria

*Correspondence:

Ashour A. Ahmed
ashour.ahmed@uni-rostock.de

Specialty section:

This article was submitted to
Forest Soils,
a section of the journal
Frontiers in Forests and Global
Change

Received: 12 December 2019

Accepted: 20 May 2020

Published: 17 June 2020

Citation:

Ganta PB, Kühn O and Ahmed AA
(2020) QM/MM Molecular Dynamics
Investigation of the Binding of Organic
Phosphates to the 100 Diaspore
Surface.

Front. For. Glob. Change 3:71.
doi: 10.3389/ffgc.2020.00071

The fate of phosphorus (P) in the eco-system is strongly affected by the interaction of phosphates with soil components and especially reactive soil mineral surfaces. As a consequence, P immobilization occurs which eventually leads to P inefficiency and thus unavailability to plants with strong implications on the global food system. A molecular level understanding of the mechanisms of the P binding to soil mineral surfaces could be a key for the development of novel strategies for more efficient P application. Much experimental work has been done to understand P binding to several reactive and abundant minerals especially goethite (α -FeOOH). Complementary, atomistic modeling of the P-mineral molecular systems using molecular dynamics (MD) simulations is emerging as a new tool in environmental science, which provides more detailed information regarding the mechanisms, nature, and strength of these binding processes. The present study characterizes the binding of the most abundant organic phosphates in forest soils, inositol hexaphosphate (IHP), and glycerolphosphate (GP), to the 100 diaspore (α -AlOOH) surface plane. Here, different molecular models have been introduced to simulate typical situations for the P-binding at the diaspore/water interface. For all models, quantum mechanics/molecular mechanics (QM/MM) based MD simulations have been performed to explore the diaspore–IHP/GP–water interactions. The results provide evidence for the formation of monodentate (**M**) and bidentate (**B**) motifs for GP and **M** and as well as two monodentate (**2M**) motifs for IHP with the surface. The calculated interaction energies suggest that GP and IHP prefer to form the **B** and **2M** motif, respectively. Moreover, IHP exhibited stronger binding than GP with diaspore and water. Further, the role of water in controlling binding strengths via promoting of specific binding motifs, formation of H-bonds, adsorption and dissociation at the surface, as well as proton transfer processes is demonstrated. Finally, the P-binding at the 100 diaspore surface plane is weaker than that at the 010 plane, studied previously (Ganta et al., 2019), highlighting the influential role of the coordination number of Al atoms at the top surface of diaspore.

Keywords: P-efficiency, P-adsorption, inositolhexaphosphate (IHP), glycerolphosphate (GP), diaspore (AlOOH), QM/MM simulations

1. INTRODUCTION

Phosphorus (P) is essential for plant growth and plays an important role in photosynthesis, energy storage, cell growth, and many other plant processes. It has been pointed out that P scarcity could arise in near future (Cordell and Neset, 2014) and to cope with this situation there is a need to understand the P cycle in forest and agro-ecosystems (Bol et al., 2016, 2018; Missong et al., 2018). In general, phosphates bind to soil components like soil organic matter (Gros et al., 2017, 2019; Ahmed et al., 2018a) and to soil minerals like Fe/Al(oxyhydr)oxides (Hens and Merckx, 2001; Jiang et al., 2015; Kruse et al., 2015; Ahmed et al., 2019) and amorphous Fe/Al hydroxide mixtures (Gypser et al., 2018). The P bound to soil minerals forms colloidal P complexes and consequently becomes unavailable to plants causing P inefficiency (Holzmann et al., 2015; Bol et al., 2016). These colloidal P complexes disperse during heavy rains and accumulate in specific regions resulting in P leaching which further reduces P availability to plants (Boy et al., 2008). Molecular level understanding of P adsorption onto these soil minerals could support efforts to improve P availability to plants (Bol et al., 2016).

Goethite (α -FeOOH) is one of the most common and abundant soil minerals that interacts strongly with phosphates (Parfitt and Atkinson, 1976; Torrent et al., 1992; Chitrakar et al., 2006; Kubicki et al., 2012; Ahmed et al., 2019). It is a highly reactive soil mineral containing ferric ions (Fe^{+3}) with common surface planes as 010, 100, 110, 021 (according to *Pnma* space group) (Cornell and Schwertmann, 2003). The surface iron atoms are coordinated by 3, 4, 5, or more atoms depending on the surface plane as well as the pH of the environment. Consequently, goethite exhibits different levels of saturation according to the interaction with its environment. The same holds true for most minerals, i.e., minerals exhibit a net positive or negative surface charge based on surface (un)saturation and pH (Cornell and Schwertmann, 2003). Hence, the type of surface plane, its termination and saturation are important factors that influence the adsorption of phosphates onto soil minerals. For instance, Ahmed et al. (2018b) studied glyphosate adsorption at goethite surface with three different degrees of (un)saturation (Fe surface atoms coordinated by 3, 4, and 5 $\text{O}^{2-}/\text{OH}^-$ groups) and showed the effect of the surface's (un)saturation on phosphate binding stability.

In addition to surface saturation and pH, the Fe and Al ratio in amorphous Fe/Al hydroxides is also vital for understanding the phosphates' interaction with soil minerals. Gypser et al. (2018) showed the influence of the Fe:Al ratio in amorphous Fe/Al hydroxide mixtures on phosphate adsorption/desorption rates. The omnipresent Al in weathering environment results in most of Fe oxides in soils being substituted by Al and goethite is no exception (Cornell and Schwertmann, 2003). Diaspore (α -AlOOH) is isomorphous with goethite with Al^{+3} oxidation state exhibiting a higher surface energy compared to goethite (Guo and Barnard, 2011). Since amorphous Fe/Al hydroxide mixtures exist in soils, analyzing phosphate binding to diasporite provides additional insight into the P interaction with these amorphous mixtures.

Orthophosphates (Newman and Tate, 1980), inositolhexaphosphate (IHP) (Turner et al., 2002; Doolette et al., 2009; Gerke, 2015), and glycerolphosphate (GP) (Pant et al., 1999; Vincent et al., 2013; Missong et al., 2016) are the most abundant phosphates in soils. Orthophosphate interaction with goethite has been studied extensively (Parfitt and Atkinson, 1976; Torrent et al., 1992; Chitrakar et al., 2006; Ahmed et al., 2019). Yan et al. (2014) studied sorption of different phosphates involving GP and IHP on aluminum (oxyhydr)oxides. They found that the maximum adsorbed phosphate normalized to the mass of adsorbent increases with decreasing crystallinity of the minerals: $\alpha\text{-Al}_2\text{O}_3 < \text{boehmite} < \text{amorphous Al(OH)}_3$. Moreover, they concluded that the phosphate adsorption, interfacial reactions, and phosphate fate in the environment are strongly affected by molecular structure and size of phosphates, and degree of crystallinity and crystal structure of mineral surfaces. Li et al. (2017) suggested that GP adsorbs onto the goethite surface through its phosphate group forming inner-sphere complexes. IHP has six phosphate groups, and in general it exhibits strong binding with P-fixing minerals compared to other phosphates with fewer phosphate groups. Anderson and Arlidge (1962) suggested that the total number of phosphate groups in a compound determines the stability of its interaction with minerals. Ognalaga et al. (1994) showed that IHP forms inner-sphere complexes with goethite through its phosphate groups and suggested that up to four phosphate groups could be involved in binding with the mineral surface; the remaining non-interacting phosphate groups could alter the electrochemical properties of the surroundings. However, Guan et al. (2006) revealed that only three phosphate groups were bound to aluminum hydroxide while the other three groups remained free. This was based on adsorption experiments of IHP on amorphous aluminum hydroxide, FTIR characterization, and quantum chemical calculations.

Quantum chemical calculations become increasingly important when it comes to develop a mechanistic understanding of chemical processes in general. Although not yet widely used, computational chemistry approaches to environmentally relevant questions are recognized as tools to complement experimental investigations. Interestingly, as early as 1973 Tossell et al. (1973) studied electronic structure and bonding in iron oxide minerals with molecular simulations and validated this approach with experimental studies. Kwon and Kubicki (2004) used molecular simulations to resolve controversies in experimental studies related to phosphate surface complexes on iron hydroxides. In another study, Kubicki et al. (2012) demonstrated that phosphate interaction with goethite involves a variety of surface complexes in multiple configurations, which explained the difficulties one faces when interpreting, e.g., IR spectra. Moreover, Ahmed et al. (2018b) explored the possible binding mechanisms for glyphosate (GLP) with three goethite surface planes (010, 001, and 100) in the presence of water via ab initio molecular dynamics simulations. The results showed the prominence of water in controlling the GLP-goethite-water interactions. Further (Ahmed et al., 2019) investigated the molecular level mechanism of phosphate binding at the goethite-water interface referring to the possible phosphate

binding motifs formed at the modeled goethite surface planes. Moreover, the theoretical assignment of IR spectra in the latter study introduced a benchmark for characterizing experimental IR data for a distribution of adsorbed phosphate species. This incomplete list already indicates the huge potential of computational chemistry as an emerging powerful tool for detailed investigations of complex geochemical reactions and especially reaction mechanisms of P-species in soil (for a more complete overview, see also Kubicki, 2016).

Which computational methods are available today? Thinking of it in terms of a hierarchy (Kubicki, 2016; Ozboyaci et al., 2016), quantum mechanics (QM) methods are at the top because they provide, at least in principle, an unbiased *ab initio* description in terms of the molecular Schrödinger equation. In practice, such a treatment is not feasible except for the simplest cases. Density Functional Theory (DFT) has emerged as a low-cost alternative, which despite of the involved approximations often provides reliable results even for systems with hundreds of atoms (Kubicki, 2016). At the bottom of the hierarchy there are molecular mechanics (MM) methods, which are based on parameterized empirical functions (force fields) describing bonded and non-bonded interactions. This allows to treat millions of atoms, but unless special purpose force fields are used chemical reactions, i.e., bond making and breaking, cannot be simulated (González, M.A., 2011). Here, the hybrid QM/MM approach comes into play, combining the accuracy of QM methods with the efficiency of MM methods. In this approach, the reactive region of the molecular system is treated at the QM level while the remaining part of the system enters at the MM level (Senn and Thiel, 2009). By this, the bond changes, proton transfer events and hydrogen bonds (HBs), e.g., at water-mineral interfaces can be properly described. Besides providing energies in dependence on nuclear positions, forces on the nuclei can be calculated as well. This is prerequisite for molecular dynamics simulations which gives statistical information including thermally accessible configurations (Marx and Hutter, 2009).

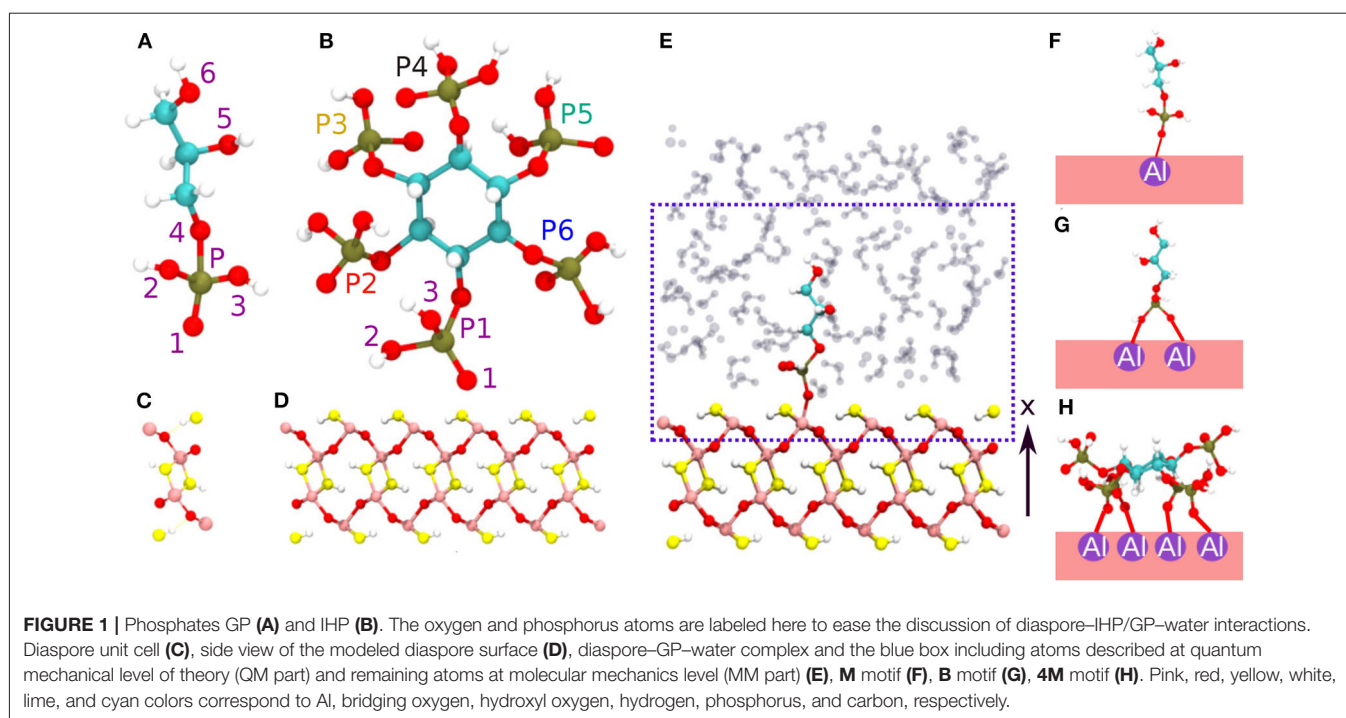
In an earlier hybrid QM/MM study of IHP and GP binding to the 010 diaspore surface plane we have demonstrated a strong interaction of IHP/GP with the diaspore surface (Ganta et al., 2019). Here, IHP forms multiple intramolecular HBs with three of its phosphate groups bound to the surface, while GP is bound through its single phosphate group only. Overall, it has been found that proton transfers from phosphate to water or surface have a stabilizing effect, most likely due to the interaction of the HBs dipole with surface charges. Moreover, in case of IHP intramolecular HBs can be formed, which lead to a steric constraint that could weaken the binding to the surface. Since the interaction of IHP and GP with diaspore is not yet fully explored, in the present work we extend our previous study in two directions, i.e., we consider a chemically different surface plane and incorporate the effect of saturation of the diaspore surface on phosphates adsorption. In our previous work (Ganta et al., 2019), IHP/GP and water showed strong and spontaneous interactions with an unsaturated diaspore surface (010 in *pnma*) where the surface Al atoms are coordinated by four oxygens ($\text{O}^{2-}/\text{OH}^-$ groups). Here, a more saturated diaspore surface (100 in *pnma*) is selected where the surface Al atoms

are coordinated by five oxygens i.e., $\text{O}^{2-}/\text{OH}^-$ groups. The main objective of current work is to characterize the binding mechanism of IHP and GP at this diaspore–water interface and also to understand the effect of (un)saturation of the diaspore surface on this binding mechanism.

2. MOLECULAR MODELING APPROACH

In general, the surface charge of a certain mineral can be determined as a function of pH via its point of zero charge (PZC) (Tan, 2011). For $\text{pH} > \text{PZC}$, the mineral surface is saturated with negative surface charges which attract cations. In contrast, for $\text{pH} < \text{PZC}$, the mineral surface is unsaturated with positive surface charges which attract anions. The phosphates in general exhibit overall negative charge and hence can be adsorbed at the partially unsaturated 100 diaspore surface (according to the *Pnma* space group) (Tan, 2011). The diaspore unit cell has four $\text{AlO}(\text{OH})$ units i.e., total of 16 atoms with lattice constants $a = 9.4253$, $b = 2.8452$, $c = 4.4007$ Å (see Figure 1C). The 100 surface plane model is generated by repetition of the diaspore unit cell as $1a \times 8b \times 5c$ along x , y , z axes, respectively (see Figure 1D). In total, the used diaspore slab consists of 640 atoms (160 Al, 160 H, and 320 O atoms). Observe that the surface Al atoms are coordinated by five oxygen atoms (see Figure S3B). The phosphates IHP and GP (see Figures 1A,B) are modeled to have their phosphate group(s) interacting via inner-sphere complexes with surface Al atoms of diaspore (see Figures 1F–H, Figures S2A–C). The diaspore-IHP/GP complexes are then solvated using the *solvate* plugin from the VMD package (Humphrey et al., 1996) with a water layer of about 18 Å perpendicular to the surface along the x axis and with a density of $\approx 1 \text{ g cm}^{-3}$ (see Figure 1E). Since we are interested in IHP/GP interaction at diaspore–water interface, the QM part of the system (see dashed box in Figure 1E) includes the top layer of diaspore (160 atoms), IHP (54 atoms)/GP (19 atoms), and a few water molecules (≈ 53 molecules depending on the setup) surrounding IHP/GP within layer of ≈ 10 Å perpendicular to the diaspore surface. The enclosing QM box has a size of $22 \times 8b \times 5c$ Å i.e., $22 \times 22.7616 \times 22.0035$ Å, where b , c are diaspore lattice constants (see Figure 1E). The remaining part of the system is treated at the MM level.

The initial motifs of diaspore–GP complexes include the monodentate motif **M** (1Al + 1O) (see Figure 1F) and bidentate motif **B** (2Al + 2O, here both oxygens are from same phosphate group) (see Figure 1G). Note that in contrast to this setup, in the 010 case the two oxygens bind to the same Al atom. In addition to these two, the diaspore–IHP complexes include the four monodentate motif **4M** (4Al + 4O) as experimental studies suggest that IHP forms multiple bonds with the goethite surface (Ognalaga et al., 1994; Guan et al., 2006) (see Figure 1H, Figure S2C). Note that in principle even more initial conditions/motifs could be sampled. But considering the size of the modeled systems here and the used computationally expensive QM/MM level of theory the initial configurations for the MD simulations are limited to the most common and experimentally observed binding motifs. More technical details



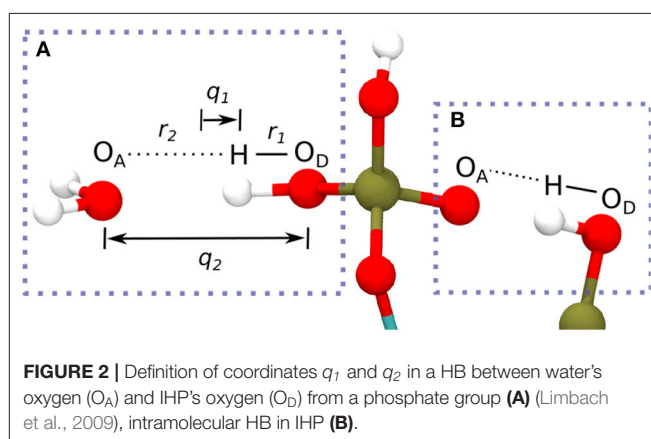
about QM and MM methods and their mutual interaction adopted here is given in **Supplementary Material**. The QM/MM based MD simulations are performed for 25 ps with 0.5 fs time step and with an average temperature of 300 K maintained using canonical sampling through the velocity rescaling thermostat (CSVR) (Bussi et al., 2007). Here, for each molecular model the first 10 ps of the MD trajectory is assigned for equilibration. The last 15 ps of the trajectory is considered as the production trajectory which is used for analysis of interactions at diaspore-water interface with IHP/GP.

To analyze the interaction energies of the complexes, snapshots are taken at every 100 fs of the production trajectory and interaction energies between diaspore and IHP/GP ($E_{\text{diaspore-IHP/GP}}$), IHP/GP and water ($E_{\text{IHP/GP-water}}$), and diaspore and water ($E_{\text{diaspore-water}}$) are calculated. For example, the interaction energy E_{int} between diaspore and GP for a certain diaspore-GP-water snapshot is calculated as follows:

$$E_{\text{int}} = E_{\text{diaspore-GP}} - (E_{\text{diaspore}} + E_{\text{GP}}) \quad (1)$$

where $E_{\text{diaspore-GP}}$, E_{GP} , and E_{diaspore} denote electronic energies of the diaspore-GP complex, GP and diaspore surface, respectively. Likewise, the interaction energies for each pair of diaspore, IHP/GP and water are calculated at every 100 fs during the corresponding production trajectory. The interaction energies with water are divided by the total number of water molecules involved in the simulation box for better comparison. More details regarding the calculation of interaction energies are given in Ganta et al. (2019).

The HBs strength between IHP/GP and water as well as for the intramolecular HBs of one IHP motif are analyzed using geometrical correlations of distances between atoms in HB as



discussed in Strassner (2006), Limbach et al. (2009), Yan and Kühn (2010), and Zentel and Kühn (2017). The quantities q_1 and q_2 in **Figures 4, 6** below are defined as the deviation of the hydrogen from HB center assuming a linear HB (q_1) and the total HB length (q_2) (see **Figure 2A**). Geometrically q_1 and q_2 are defined as $q_1 = \frac{1}{2}(r_1 - r_2)$ Å and $q_2 = (r_1 + r_2)$ Å where r_1 , r_2 denote the distance between donor oxygen and hydrogen (O_D-H) and distance between hydrogen and acceptor oxygen ($H \cdots O_A$), respectively (see **Figure 2A**). The same holds true for intramolecular HBs between phosphate groups for the IHP case (see **Figure 2B**).

A HB will be called strong if $q_1 \approx 0$ and q_2 is in the range 2.2–2.5 Å. Similarly, moderate and weak HBs have q_2 distances ranging from 2.5 to 3.2 and 3.2 to 4 Å, respectively. Also if $q_1 < 0$ the hydrogen atom stays with the donor oxygen and if $q_1 > 0$

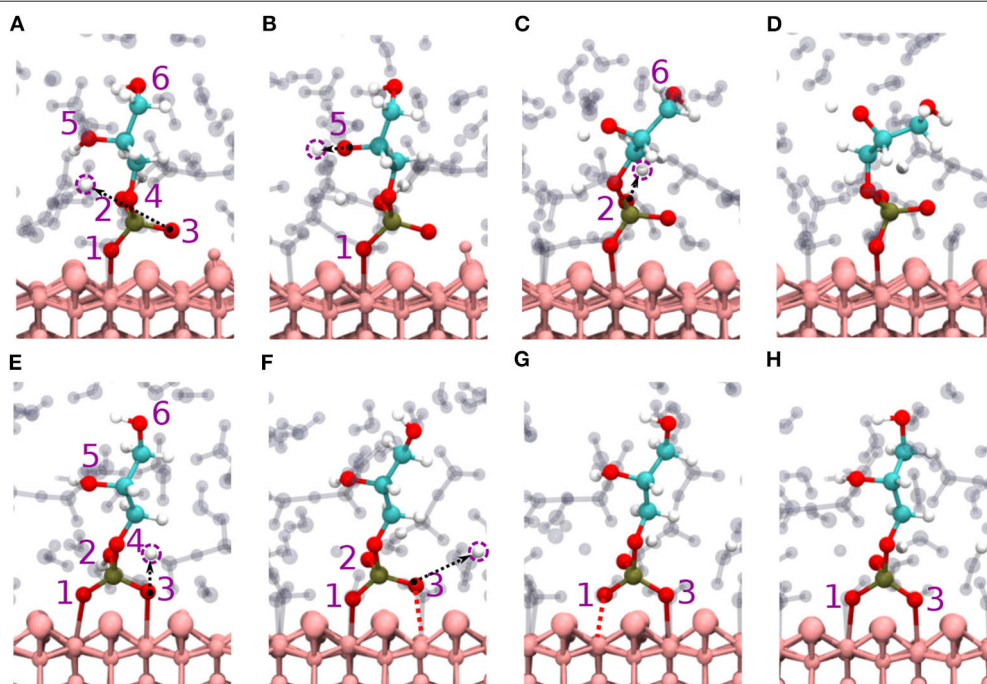


FIGURE 3 | Diaspore–GP–water snapshots displaying proton transfer events and GP dynamics along trajectories. Proton transfers observed during production trajectory of **M** motif from O3 to water (**A**) from O5 to water (**B**), and from O2 to water (**C**), GP **M** motif at 25 ps (**D**). Proton transfer events in **B** (2Al+2O) motif from O3 to water (**E**), from O2 to water and momentary dissociation of Al1–O1 bond (**F**), momentary dissociation of Al2–O3 bond (**G**), GP **B** motif at 25 ps (**H**).

the hydrogen atom (proton) transferred to the acceptor oxygen. In the following a HB analysis is performed for the QM part of the system only as the emphasis of this study is on the interface region where the binding/adsorption process takes place.

3. RESULTS AND DISCUSSION

3.1. Diaspore–GP–Water Interactions

3.1.1. GP **M** Motif

For the GP–**M** initial condition a stable monodentate (1Al+1O) motif is observed between GP and the diaspore surface over the course of the production trajectory with the Al–O1 average bond length of 2.3 Å (see **Figures 3A–D**). The average geometry of the PO₄ moiety here has root mean square deviation (RMSD) value of 0.17 Å with respect to free tetrahedral PO₄^{3−} (see **Figure S2D**).

Proton transfer events from GP to the diaspore surface are not observed, instead three proton transfer events are found from O3, O5, and O2 oxygens of GP to water (see **Figures 3A–C**), respectively. On average, eight HBs are observed between GP and water in the production trajectory. Here, the GPs oxygen atoms act as HB donors (O_{xD}) as well as acceptors (O_{xA}). Exemplary analysis of six of the above eight HBs shows that four (O2_A, O3_A, O5_A, O5_D) are strong to moderately strong HBs and two (O1_A, O6_A) moderately strong to weak HBs (see **Figures 4A–C**).

Regarding the diaspore–water interaction, an average of 17 water molecules (out of 40 surface Al atoms) formed **M** binding motifs (Al–O_{H₂O}) with the diaspore surface and have average bond length of 1.9–2.3 Å. Also moderately strong HBs are

observed between water and diaspore (see **Figure S1A**). This scheme of diaspore–water interactions is also observed for the other diaspore–IHP/GP–water models studied below. For the average diaspore–water interaction energy per water molecule one obtains about −3 kcal/mol for all considered models.

The time averaged interaction energy per surface bond between diaspore and GP is around −23 kcal/mol (see **Table 1**). The average GP–water interaction energy per water molecule is −2.6 kcal/mol.

3.1.2. GP **B** Motif

The **B** motif (2Al+2O i.e., Al1–O1 and Al2–O3) is observed over the course of the production trajectory with Al1–O1 and Al2–O3 covalent bond length ranging from 2–2.7 and 1.9–2.7 Å with an average value of 2.4 and 2.3 Å, respectively (see **Figures 3E–H**). Most notably the Al2–O3 and Al1–O1 bonds are elongated and compressed in an alternating see-saw fashion as seen in **Figures 3E,G**. The **B** motif's average geometry of the PO₄ moiety has a RMSD value of 0.17 Å with respect to the free tetrahedral PO₄^{3−}.

Proton transfer events are observed from O3 and O2 oxygens to water (see **Figures 3E,F**), respectively. The **B** motif features on average a total of seven HBs between GP and water. According to **Figures 4D–F**, four (O1_A, O2_A, O2_D, O5_D) strong to moderately strong HBs and two (O1_A, O6_D) moderately strong to weak HBs are formed between GP and water.

The average interaction energy per surface bond between diaspore and GP for the **B** motif is around −15 kcal/mol. The

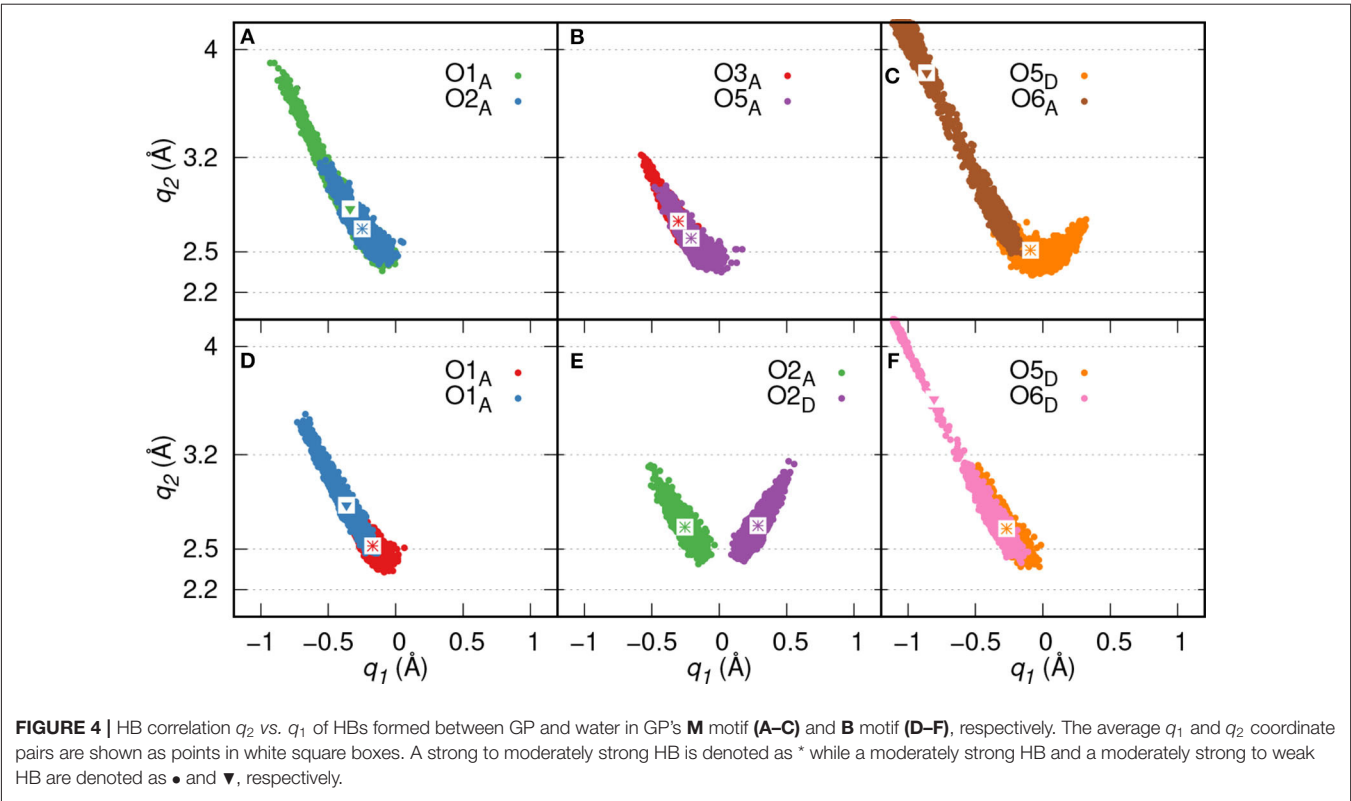


TABLE 1 | The per bond time averaged interaction energies (calculated with Equation 1) of diaspore–IHP/GP complexes and some selected bond lengths and distances.

100 diaspore surface					
P _o	Motif	E _{int} /bond (kcal/mol)	Al–O _P (Å)	Al–P (Å)	RMSD(PO ₄ ^{3–}) (Å)
GP	M	–23	2.3	3.4	0.17
	B	–15	2.3 and 2.4	3.3	0.17
IHP	M(1)	–33	2.4	3.5	0.16
	M(2)	–18	2.7	3.6	0.19
	2M	–109	2.1 and 2.2	3.3 and 3.4	0.18 and 0.17
010 diaspore surface (Ganta et al., 2019)					
GP	B	–148	2.03 and 2.05	2.65	0.1
IHP	3M	–145	1.90 and 1.88 and 1.86	3.25 and 3.17 and 3.18	0.07 and 0.08 and 0.1

The RMSD difference between average phosphate geometry and isolated tetrahedral PO₄^{3–} (see Figure S2D) is also provided. Here, P_o denotes phosphate and motif denotes average motif observed during production trajectory. Further, Al–O_P denotes bond distance between covalent bonded Al and O_P oxygen of IHP/GP.

per surface bond interaction energy here is smaller than for the **M** motif due to GP’s see-saw type of motion over the surface. Nevertheless, the total interaction energy observed here is larger than for the **M** motif and hence the **B** motif is more likely to form. Note that due to the formation of a strong to moderately strong HB with water, the O3 oxygen in **M** cannot easily

transform into the **B** motif, i.e., the barrier is too high to be sampled in the present trajectory (see Figure 4B). The average GP–water interaction energy per water molecule is around –2.3 kcal/mol. The smaller value as compared with **M** could be due to the additional proton transfer event observed in that case.

3.2. Diaspore–IHP–Water Interactions

3.2.1. IHP M Motifs

Here, two initial configurations (**M**, **B** motifs) of the diaspore–IHP–water model resulted in two different **M** final motifs. In the first case, **M(1)**, the initial configuration was an **M** motif, wherein O11 oxygen is aligned to form a **M** motif with a surface Al atom (see Figure S2A). A stable **M** motif is observed throughout the production trajectory with average Al–O11 bond length of 2.4 Å (see Figures 5A–D). The series of events that are observed during the formation of the **M(1)** motif are: a proton transfer from O12 to water (see Figure 5A), followed by intramolecular proton transfer from O62 to O12 and formation of O13–H–O61 intramolecular HB (see Figure 5B). After a few femtoseconds, the O12–H–O62 HB is formed and a proton transfer is observed from O32 to water (see Figure 5C) to reach the final **M** motif in Figure 5D. The events in Figures 5A–C occurred within 2 ps of the simulation trajectory. Overall, a total of three protons transfer events are observed from IHP to water from O12, O53, and O32 (see Figures 5A–C), respectively. On average IHP has formed 19 HBs with water over the course of the production trajectory. Analyzing for illustration 12 out of these 19 HBs, IHP has formed nine (O12_A, O21_A, O22_A, O23_A, O31_A, O43_A, O51_A, O53_A,

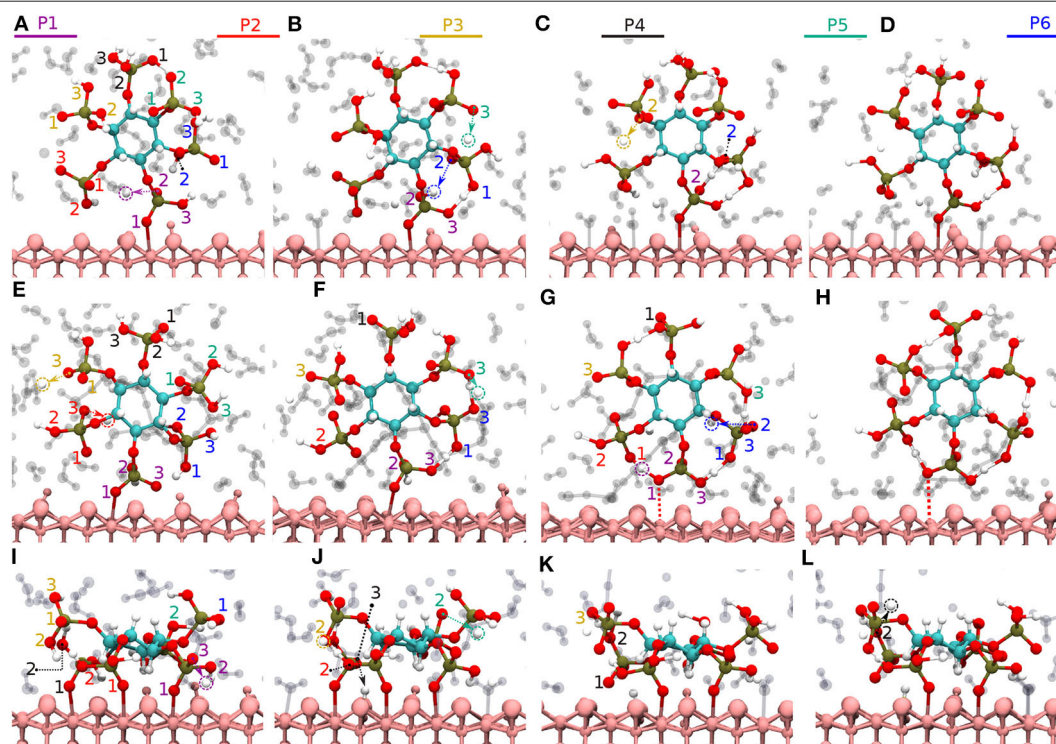


FIGURE 5 | Diaspore-IHP-water snapshots displaying proton transfer events and IHP dynamics along trajectories. The phosphate groups are color-coded and the oxygen atom label color denotes to the phosphate group it belongs to. In **M(1)** motif, proton transfer from O12 to water (**A**), proton transfer from O53 to water and intramolecular proton transfer from O62 to O12 (**B**), moderately strong O12-H-O62 HB and proton sharing between O12 to O62 oxygens and proton transfer from O32 to water (**C**), **M(1)** motif at 25 ps (**D**). In **M(2)** motif, dissociation of Al2-O13 covalent bond due to O13-H-O61 HB and proton transfers from O23 and O33 to water (**E**), proton transfer from O53 to water and formation of O53-H-O63 HB (**F**), dissociation of Al1-O11 bond due to formation of O11-H-O21 HB (**G**), **M(2)** motif at 25 ps (**H**). In **2M** motif, dissociation of Al4-O51 bond and proton transfer from O13 to water (**I**), proton transfer from O43 to diaspore and from O32 to water, also proton sharing and HB between O22 and O32 (**J**), and between O33 and O42 followed by dissociation of Al3-O41 bond (**K**), proton transfer from O42 to water and **2M** motif at 25 ps (**L**).

O63_D) strong to moderately strong HBs, two (O33_D, O41_A) moderately strong HBs and one (O31_A) moderately strong to weak HB with water (see **Figures 6A–E**). Interestingly, IHP also forms multiple intramolecular HBs, for instance, O13-H-O61, O41-H-O52, and O12-H-O62 (see **Figures 5A–C**). Analyzing the strength of the intramolecular HBs between P1 and P6 phosphate groups, one finds two (O13-H-O61, O12-H-O62) moderately strong HBs (see **Figure 6F**). The average geometry of PO₄ moiety has a RMSD value of 0.16 Å with respect to the free tetrahedral PO₄^{3−}.

The time averaged interaction energy per surface bond between diaspore and IHP is around −33 kcal/mol (see **Table 1**) and between IHP and water is around −5.5 kcal/mol per water molecule. Notice that IHP exhibits a larger interaction energy with water as well with the diaspore surface compared to GP.

For the **M(2)** motif, the initial configuration had the O11 and O13 oxygens aligned such as to form a **B** motif with adjacent surface Al atoms (see **Figure S2B**). The Al2-O13 covalent bond is dissociated during the trajectory and the **B** motif is transformed into the **M(2)** motif (see **Figures 5E,F**). Over the course of the production trajectory the Al1-O11 bond length ranges from 2.4 to 3.2 Å with an average of 2.7 Å. In more detail, the series

of events that unfold in this case are as follows: From the O23 and O33 oxygens, two protons are transferred to water and the Al2-O13 covalent bond is dissociated (see **Figure 5E**). After a few femtoseconds, a proton transfer is observed from O53 to water followed by formation of an intramolecular HB between O53 and O63 oxygens (see **Figure 5F**). Also formation of the intramolecular O13-H-O61 HB is observed. With progressing simulation time an intramolecular proton transfer event is observed from O12 to O21, followed by formation of O11-H-O21 HB. Afterwards, the Al1-O11 covalent bond weakens at around 6 ps and its bond length ranges from 2.4 to 3.2 Å further on (see **Figure 5G**, **Figure S1B**). In addition, a proton transfer is observed from O62 to water (see **Figure 5G**). The snapshot at 25 ps shows that multiple inter- and intramolecular HBs are observed for IHP (see **Figure 5H**). Their characterization in terms of HB geometries leads to a similar distribution of HB strengths as for **M(1)**. Overall the average geometry of PO₄ moiety has RMSD value of 0.19 Å with respect to the free tetrahedral PO₄^{3−}.

The average interaction energy per surface bond between the diaspore surface and IHP in this case is around −18 kcal/mol. The interaction energy observed here is smaller than for the **M(1)**

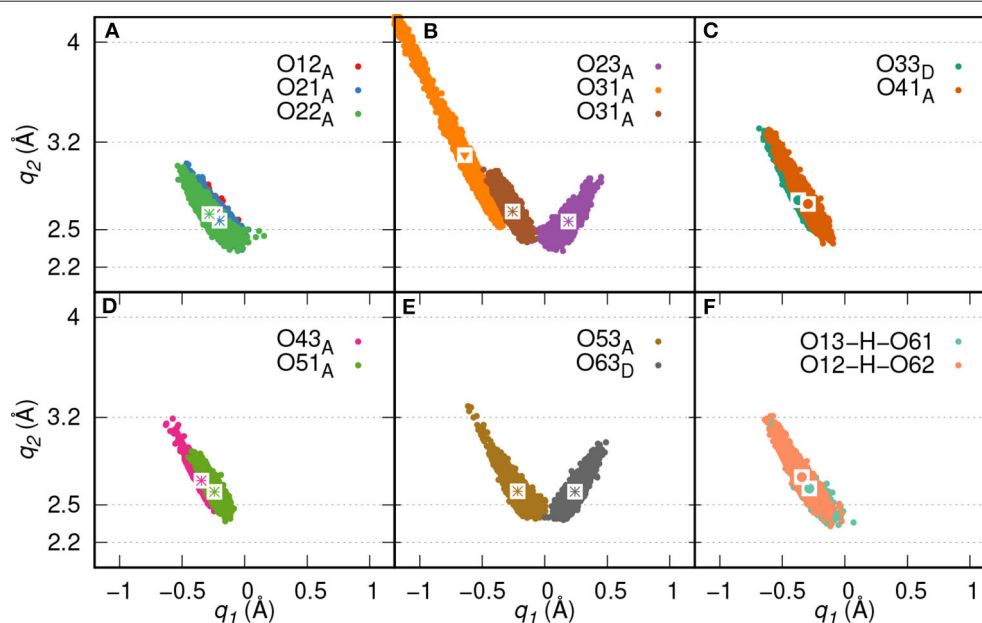


FIGURE 6 | HB correlation q_2 vs. q_1 of HBs formed between IHP and water (A–E) and between P1 and P6 phosphate groups (F) along trajectory of IHP's **M(1)** motif. The average q_1 and q_2 coordinate pairs are shown as points in white square boxes. A strong to moderately strong HB is denoted as * while a moderately strong HB and a moderately strong to weak HB are denoted as • and ▼, respectively.

case as the Al1-O11 bond length is longer due to formation of O13-H-O61 and O12-H-O21 intramolecular HBs. The observed interaction energy between IHP and water here is -5.7 kcal/mol per water molecule which is slightly higher than for the **M(1)** case, probably due to additional proton transfer from IHP to water.

3.2.2. IHP 2M Motif

Here, IHP is initially aligned parallel to surface with the non-protonated oxygens of the four phosphate groups forming a **4M** motif, i.e., Al1-O11, Al2-O21, Al3-O41, Al4-O51 covalent bonds with the surface (see **Figure S2C**). However, only a stable **2M** motif is observed along the production trajectory with average bond lengths of Al1-O11, Al2-O21 as 2.13 and 2.22 Å, respectively. The events observed during simulation that led to the formation of **2M** motif are as follows: within a few picoseconds, the Al-O51 bond is dissociated transforming **4M** into a **3M** motif. A proton transfer is observed from O13 oxygen to water and from O43 oxygen to diaspore (see **Figures 5I,J**). Further, an intramolecular HB is observed between O22 and O32 oxygens and two proton transfer events from O32 and O52 to water (see **Figure 5J**). The Al3-O41 covalent bond is dissociated due to intramolecular HB formed between O33 and O42 oxygens (see **Figure 5K**), followed by a proton transfer event from O42 to water (see **Figure 5L**). Totally four proton transfer events are observed from IHP to water and an average of 19 HBs are formed between IHP and water. The inter- and intramolecular HBs have a similar distribution of strengths as for **M(1)** and **M(2)**. The average geometry of the PO_4 moieties deviate

from that of free tetrahedral PO_4^{3-} with RMSD values of 0.18 and 0.17 Å.

The interaction energy between IHP and diaspore in the **2M** motif is -109 kcal/mol per bond (see **Table 1**). The interaction energy is larger here compared to **M(1)** and **M(2)** motifs due to the additional covalent bond and a proton transfer from IHP to the diaspore surface. Hence, the **2M** motif is more likely to form compared to both the **M(1)** and **M(2)** motifs. The average interaction energy per water molecule with IHP is -5.9 kcal/mol which is slightly larger than the IHP-water interaction energy observed in **M(1)** motif case due to additional proton transfer from IHP to water here.

3.3. Effect of Surface Saturation

In the following we will compare the present results with those of our previous work for the 010 surface plane (Ganta et al., 2019). The 010 diaspore surface plane is relatively unsaturated, i.e. the surface Al atoms are coordinated by only four oxygen atoms (see **Figure S3A**). In contrast, for the present more saturated 100 plane, surface Al atoms are coordinated by five oxygens (see **Figure S3B**). Also the 010 diaspore surface plane exhibits higher electrostatic potential compared to the 100 surface plane as shown in **Figure S6**.

For the 010 plane the largest total interaction energy was observed for the **B** and **3M** motif in case of GP and IHP, respectively (see **Table 1**). In case of 100 plane, the **B** and **2M** motifs dominate the total interaction energies. Comparing the two **B** motifs for GP one finds that the binding to 010 being 10 times stronger than to 100 surface plane. The reason for the weaker interaction energy in case of 100 is due to see-saw type

of motion of GP yielding a weakening/strengthening of Al1-O1 and Al2-O3 bonds which is not observed for the 010 plane. This can be attributed to the fact that in case of 010 plane the two oxygens are coordinated to the same Al, whereas for 100 plane the coordination is with two neighboring Al atoms, whose distances is such as to require unfavorably large O_P -P- O_P angles for strong binding. Further stabilization of the GPs **B** motif in the 010 plane case comes from two additional proton transfers observed from GP to the diaspore surface.

Regarding the total interaction energies, the dominant binding motifs for the diaspore-IHP complexes are also different for 010 (**3M**) and 100 (**2M**). In case of 100 the total interaction energy is about two times smaller than for 010. Comparing the two motifs we note in particular that the interaction with the two surfaces is different. This is nicely illustrated by the fact that no stable **4M** motif could be observed for the 100 case. One reason for the transformation of the **4M** motif to **2M** motif is that the Al- O_P bonds (regions R1 and R2, see **Figures S5A–C**) at the 100 diaspore surface are inclined due to O_P and surface hydroxyl oxygen repulsion. Hence the movement of oxygens in the Al- O_P bonds (regions R1 and R2) is restricted to the space between consecutive surface hydroxyl oxygens or to move away from surface (see **Figures S5A–C**). Consequently, upon equilibration the oxygens in the Al- O_P bonds could dissociate from diaspore as they are confined between consecutive surface hydroxyl oxygens (see **Figures S5A–C**). In contrast for the 010 diaspore-IHP case, the oxygens in the Al- O_P bonds (regions R3 and R4, **Figures S5E–G**) are not restricted and they are free to move. Hence a stable **3M** motif is observed over the course of production trajectory (see **Figures S5E–G**). Looking at it from a geometric point of view, Al-Al distances on the 010 surface are about 4.4–5.4 Å which is much larger than the 2.4 Å for the 100 surface where the **2M** motif forms (see **Figures S5D,H**). Given the typical distances between the phosphate groups in IHP, bonding to the 100 surface plane yields a higher strain and thus it becomes weaker as compared with the 010 surface plane.

In case of the 100 surface the diaspore-water interaction energy is 3.4 times smaller compared to the 010 case. In fact less than half of surface Al atoms formed **M** motifs with water compared to the 010 diaspore surface. Also the radial distribution function of diaspore surface oxygens with water hydrogens in **Figure S4** shows higher water accumulation near the 010 diaspore surface compared to the 100 diaspore surface which suggests stronger interaction for the 010 diaspore surface with water.

4. SUMMARY AND CONCLUSIONS

In our previous study (Ganta et al., 2019), a strong and spontaneous binding of IHP and GP with the 010 diaspore surface has been described, which provided the motivation for studying the effect of surface saturation on these interactions. Therefore, the more saturated 100 diaspore surface has been investigated here using periodic boundary QM/MM based MD simulations. The analysis of the MD trajectories showed the importance of inter- and intramolecular HBs in the formation

of final motifs and also shed light on effects that lead to disassociation and association of P-O-Al bonds in the diaspore-IHP/GP-water complexes.

In case of the diaspore-GP-water complexes, the **B** motif's interaction energy per bond is 1.5 times smaller than the **M** motif. But considering the total average interaction energy, GP is more likely to form a **B** motif with the 100 diaspore surface.

Regarding the diaspore-IHP-water complexes, the interaction energy per bond follows the order **2M** > **M(1)** > **M(2)**. Here, the **M(2)** motif's interaction energy is 1.8 times smaller than the **M(1)** motif due to longer Al- O_P bond length, i.e., due to movement of IHP away from the diaspore surface. Thus the **2M** motif will be also dominating considering the total interaction energy. This is due to the additional covalent bond and a proton transfer to the diaspore surface. Hence IHP is likely to form a **2M** motif with the 100 diaspore surface.

Regarding the water interaction with 100 diaspore and IHP/GP, it can be concluded that the average IHP-water interaction energy is about 2.3 times larger than the GP-water one due to IHP's higher water accessible surface area. Both IHP and GP show proton transfer events to water and formation of strong to moderately strong HBs with water. The diaspore-water interaction energy is only 1.1 times that of the GP-water case, but 2.8 times smaller than IHP-water one. Thus, water has a stronger interaction with IHP than with the 100 diaspore surface.

Of course, studying a particular perfect surface plane can at best give qualitative trends if compared to real surfaces of mineral particles in soil. Studying two abundant surface planes, however, it is possible to pinpoint important factors which influence the behavior of P-compounds at the mineral/water interface. The present investigation focused on the effects of surface saturation and thus electrostatic potential on IHP/GP adsorption. The soil minerals exhibit a positive charge with an unsaturated surface and active sites for pH < PZC. For a pH far below PZC a higher positive charge, i.e., more unsaturated surface is observed (Cornell and Schwertmann, 2003; Tan, 2011). The IHP and GP adsorption onto goethite (with PZC around 9–10) is decreased with increasing pH and reached near zero values for pH around 10 (Celi et al., 1999; Li et al., 2017). This shows that the mineral surface saturation varies with pH and thus the ability of a mineral to adsorb phosphates. Higher surface saturation leads to more negative charges on the 100 surface as compared to the 010 case. Phosphates in water are partially deprotonated and thus have an effective negative charge. Thus the phosphate groups will be attracted stronger to the 010 diaspore surface plane. The denser distribution of water around the 010 surface compared to the 100 surface and transformation of IHP's **M** and **B** motifs to **2M** motif highlight the stronger electrostatic potential of 010 surface than 100.

Comparing our previous study (Ganta et al., 2019) with the present one, it can be concluded that the diaspore surfaces with different degrees of saturation exhibit different interaction energies with phosphates. Moreover, both surface planes form multiple bonds with IHP while the **B** binding motif dominates for GP. The overall interaction energies show that IHP is bound to diaspore stronger than GP and this confirms the prevailing view that the number of phosphate groups is a decisive parameter

determining the adsorption strength (Anderson and Arlidge, 1962). This could also explain why higher percentages of IHP are found in the forest soil colloid samples than GP as revealed by liquid-state NMR measurements (Missong et al., 2016). However, not all available phosphate groups will contribute to the binding, with details depending on the surface saturation. The present study also stresses the importance of inter- and intra-molecular HBs and the observation that IHP is less protonated than solution counterparts when $\text{pH} < \text{PZC}$ as shown by Johnson et al. (2012). For both modeled diaspore surfaces, there is no observed dissociation for the bonds involved in C-O, C-H, and C-O-P as suggested by Celi et al. (1999) and Li et al. (2017). In the present case of IHP we cannot confirm the suggestion of a 4M motif made by Ognalaga et al. (1994).

DATA AVAILABILITY STATEMENT

All datasets generated for this study are included in the article/Supplementary Material.

AUTHOR CONTRIBUTIONS

PG has performed the present work and analyzed the results. AA and OK have suggested, designed,

and supervised the scientific approach for the present study. All authors have discussed and interpreted the present results and contributed to writing the submitted manuscript.

ACKNOWLEDGMENTS

All authors gratefully acknowledge the financial support by the German Research Foundation (DFG) as a part of the SPP 1685 Priority program Ecosystem Nutrition: Forest strategies for limited phosphorus resources. AA would like to thank the financial support by the InnoSoilPhos-project, funded by the German Federal Ministry of Education and Research (BMBF) in the frame of the BonaRes-program (No. 031A558). This research was performed within the scope of the Leibniz Science Campus Phosphorus Research Rostock. The authors thank the North German Supercomputing Alliance for providing HPC resources (project mvpp00016).

SUPPLEMENTARY MATERIAL

The Supplementary Material for this article can be found online at: <https://www.frontiersin.org/articles/10.3389/ffgc.2020.00071/full#supplementary-material>

REFERENCES

- Ahmed, A. A., Gros, P., Kühn, O., and Leinweber, P. (2018a). Molecular level investigation of the role of peptide interactions in the glyphosate analytics. *Chemosphere* 196, 129–134. doi: 10.1016/j.chemosphere.2017.12.162
- Ahmed, A. A., Gypser, S., Leinweber, P., Freese, D., and Kühn, O. (2019). Infrared spectroscopic characterization of phosphate binding at the goethite-water interface. *Phys. Chem. Chem. Phys.* 21, 4421–4434. doi: 10.1039/C8CP07168C
- Ahmed, A. A., Leinweber, P., and Kühn, O. (2018b). Unravelling the nature of glyphosate binding to goethite surfaces by ab initio molecular dynamics simulations. *Phys. Chem. Chem. Phys.* 20, 1531–1539. doi: 10.1039/C7CP06245A
- Anderson, G., and Arlidge, E. Z. (1962). The adsorption of inositol phosphates and glycerophosphate by soil clays, clay minerals, and hydrated sesquioxides in acid media. *J. Soil Sci.* 13, 216–224. doi: 10.1111/j.1365-2389.1962.tb00699.x
- Bol, R., Gruau, G., Mellander, P.-E., Dupas, R., Bechmann, M., Skarbøvik, E., et al. (2018). Challenges of reducing phosphorus based water eutrophication in the agricultural landscapes of Northwest Europe. *Front. Mar. Sci.* 5:276. doi: 10.3389/fmars.2018.00276
- Bol, R., Julich, D., Brödlén, D., Siemens, J., Kaiser, K., Dippold, M. A., et al. (2016). Dissolved and colloidal phosphorus fluxes in forest ecosystems—an almost blind spot in ecosystem research. *J. Soil Sci. Plant Nutr.* 179, 425–438. doi: 10.1002/jpln.201600079
- Boy, J., Valarezo, C., and Wilcke, W. (2008). Water flow paths in soil control element exports in an andean tropical montane forest. *Eur. J. Soil Sci.* 59, 1209–1227. doi: 10.1111/j.1365-2389.2008.01063.x
- Bussi, G., Donadio, D., and Parrinello, M. (2007). Canonical sampling through velocity rescaling. *J. Chem. Phys.* 126, 014101:1–014101:6. doi: 10.1063/1.2408420
- Celi, L., Lamacchia, S., Marsan, F. A., and Barberis, E. (1999). Interaction of inositol hexaphosphate on clays: adsorption and charging phenomena. *Soil Sci.* 164, 574–585. doi: 10.1097/00010694-199908000-00005
- Chitrakar, R., Tezuka, S., Sonoda, A., Sakane, K., Ooi, K., and Hirotsu, T. (2006). Phosphate adsorption on synthetic goethite and akaganeite. *J. Colloid Interface Sci.* 298, 602–608. doi: 10.1016/j.jcis.2005.12.054
- Cordell, D., and Neset, T.-S. (2014). Phosphorus vulnerability: a qualitative framework for assessing the vulnerability of national and regional food systems to the multi-dimensional stressors of phosphorus scarcity. *Glob. Environ. Chang.* 24, 108–122. doi: 10.1016/j.gloenvcha.2013.11.005
- Cornell, R. M., and Schwertmann, U. (2003). *The Iron Oxides: Structure, Properties Reactions Occurrence and Uses*. Weinheim: Wiley-VCH Verlag GmbH and Co. KGaA.
- Doolette, A., Smernik, R., and Dougherty, W. (2009). Spiking improved solution phosphorus³¹ nuclear magnetic resonance identification of soil phosphorus compounds. *Soil Sci. Soc. Am. J.* 73, 919–927. doi: 10.2136/sssaj2008.0192
- Ganta, P. B., Kühn, O., and Ahmed, A. A. (2019). QM/MM simulations of organic phosphorus adsorption at the diaspore–water interface. *Phys. Chem. Chem. Phys.* 21, 24316–24325. doi: 10.1039/C9CP04032C
- Gerke, J. (2015). Phytate (inositol hexakisphosphate) in soil and phosphate acquisition from inositol phosphates by higher plants: a review. *Plants* 4, 253–266. doi: 10.3390/plants4020253
- González, M. A. (2011). Force fields and molecular dynamics simulations. *Collect. SFN* 2011 12, 169–200. doi: 10.1051/sfn/201112009
- Gros, P., Ahmed, A., Kühn, O., and Leinweber, P. (2017). Glyphosate binding in soil as revealed by sorption experiments and quantum-chemical modeling. *Sci. Tot. Environ.* 586, 527–535. doi: 10.1016/j.scitotenv.2017.02.007
- Gros, P., Ahmed, A. A., Kühn, O., and Leinweber, P. (2019). Influence of metal ions on glyphosate detection by FMOC-Cl. *Environ. Model. Assess.* 191:244. doi: 10.1007/s10661-019-7387-2
- Guan, X.-H., Shang, C., Zhu, J., and Chen, G.-H. (2006). ATR-FTIR investigation on the complexation of myo-inositol hexaphosphate with aluminum hydroxide. *J. Colloid Interface Sci.* 293, 296–302. doi: 10.1016/j.jcis.2005.06.070
- Guo, H., and Barnard, A. S. (2011). Thermodynamic modelling of nanomorphologies of hematite and goethite. *J. Mater. Chem.* 21, 11566–11577. doi: 10.1039/c1jm10381d
- Gypser, S., Hirsch, F., Schleicher, A. M., and Freese, D. (2018). Impact of crystalline and amorphous iron- and aluminum hydroxides on mechanisms of phosphate adsorption and desorption. *J. Environ. Sci.* 70, 175–189. doi: 10.1016/j.jes.2017.12.001

- Hens, M., and Merckx, R. (2001). Functional characterization of colloidal phosphorus species in the soil solution of sandy soils. *Environ. Sci. Technol.* 35, 493–500. doi: 10.1021/es0013576
- Holzmann, S., Missong, A., Puhlmann, H., Siemens, J., Bol, R., Klumpp, E., et al. (2015). Impact of anthropogenic induced nitrogen input and liming on phosphorus leaching in forest soils. *J. Soil Sci. Plant Nutr.* 179, 443–453. doi: 10.1002/jpln.201500552
- Humphrey, W., Dalke, A., and Schulten, K. (1996). VMD – visual molecular dynamics. *J. Mol. Graph.* 14, 33–38. doi: 10.1016/0263-7855(96)00018-5
- Jiang, X., Bol, R., Nischwitz, V., Siebers, N., Willbold, S., Vereecken, H., et al. (2015). Phosphorus containing water dispersible nanoparticles in arable soil. *J. Environ. Qual.* 44, 1772–1781. doi: 10.2134/jeq2015.02.0085
- Johnson, B. B., Quill, E., and Angove, M. J. (2012). An investigation of the mode of sorption of inositol hexaphosphate to goethite. *J. Colloid Interface Sci.* 367, 436–442. doi: 10.1016/j.jcis.2011.09.066
- Kruse, J., Abraham, M., Amelung, W., Baum, C., Bol, R., Kühn, O., et al. (2015). Innovative methods in soil phosphorus research: a review. *J. Soil Sci. Plant Nutr.* 178, 43–88. doi: 10.1002/jpln.201400327
- Kubicki, J. D. (ed.). (2016). *Molecular Modeling of Geochemical Reactions*. Chichester: Wiley and Sons.
- Kubicki, J. D., Paul, K. W., Kabalan, L., Zhu, Q., Mrozik, M. K., Aryanpour, M., et al. (2012). ATR-FTIR and Density Functional Theory study of the structures, energetics, and vibrational spectra of phosphate adsorbed onto goethite. *Langmuir* 28, 14573–14587. doi: 10.1021/la303111a
- Kwon, K. D., and Kubicki, J. D. (2004). Molecular orbital theory study on surface complex structures of phosphates to iron hydroxides-calculation of vibrational frequencies and adsorption energies. *Langmuir* 20, 9249–9254. doi: 10.1021/la0487444
- Li, H., Wan, B., Yan, Y., Zhang, Y., Cheng, W., and Feng, X. (2017). Adsorption of glycerophosphate on goethite: a macroscopic and infrared spectroscopic study. *J. Soil Sci. Plant Nutr.* 181, 557–565. doi: 10.1002/jpln.201700517
- Limbach, H.-H., Tolstoy, P. M., Pérez-Hernández, N., Guo, J., Shenderovich, I. G., and Denisov, G. S. (2009). Oho hydrogen bond geometries and NMR chemical shifts: from equilibrium structures to geometric H/D isotope effects, with applications for water, protonated water, and compressed ice. *Isr. J. Chem.* 49, 199–216. doi: 10.1560/IJC.49.2.199
- Marx, D., and Hutter, J. (2009). *Ab Initio Molecular Dynamics: Basic Theory and Advanced Methods*. Cambridge, UK: Cambridge University Press.
- Missong, A., Bol, R., Willbold, S., Siemens, J., and Klumpp, E. (2016). Phosphorous forms in forest soil colloids as revealed by liquid-state P-NMR. *J. Soil Sci. Plant Nutr.* 179, 159–167. doi: 10.1002/jpln.201500119
- Missong, A., Holzmann, S., Bol, R., Nischwitz, V., Puhlmann, H., Wilpert, K., et al. (2018). Leaching of natural colloids from forest topsoils and their relevance for phosphorus mobility. *Sci. Tot. Environ.* 634, 305–315. doi: 10.1016/j.scitotenv.2018.03.265
- Newman, R. H., and Tate, K. R. (1980). Soil phosphorus characterisation by 31 P Nuclear Magnetic Resonance. *Commun. Soil Sci. Plant Anal.* 11, 835–842. doi: 10.1080/00103628009367083
- Ognalaga, M., Frossard, E., and Thomas, F. (1994). Glucose-1-phosphate and myo-inositol hexaphosphate adsorption mechanisms on goethite. *Soil Sci. Soc. Am. J.* 332–337. doi: 10.2136/sssaj1994.03615995005800020011x
- Ozboyaci, M., Kokh, D. B., Corni, S., and Wade, R. C. (2016). Modeling and simulation of protein-surface interactions: achievements and challenges. *Q. Rev. Biophys.* 49:e4. doi: 10.1017/S0033583515000256
- Pant, H. K., Warman, P. R., and Nowak, J. (1999). Identification of soil organic phosphorus by 31 P Nuclear Magnetic Resonance spectroscopy. *Commun. Soil. Sci. Plant Anal.* 30, 757–772. doi: 10.1080/00103629909370244
- Parfitt, R. L., and Atkinson, R. J. (1976). Phosphate adsorption on goethite (α -FeOOH). *Nature* 264, 740–742. doi: 10.1038/264740a0
- Senn, H. M., and Thiel, W. (2009). QM/MM methods for biomolecular systems. *Angew. Chem.* 48, 1198–1229. doi: 10.1002/anie.200802019
- Strassner, T. (2006). Isotope effects in chemistry and biology. Edited by amnon kohen and hans-heinrich limbach. *Angew. Chem.* 45, 6420–6421. doi: 10.1002/anie.200585384
- Tan, K. (2011). *Principles of Soil Chemistry, Fourth Edition*. Books in Soils, Plants, and the Environment. New York, NY: Taylor & Francis.
- Torrent, J., Schwertmann, U., and Barron, V. (1992). Fast and slow phosphate sorption by goethite-rich natural materials. *Clays Clay Miner.* 40, 14–21. doi: 10.1346/CCMN.1992.0400103
- Tossell, J. A., Vaughan, D. J., and Johnson, K. H. (1973). Electronic structure of ferric iron octahedrally coordinated to oxygen. *Nat. Phys. Sci.* 244, 42–45. doi: 10.1038/physci244042a0
- Turner, B. L., Papházy, M. J., Haygarth, P. M., and Mckelvie, I. D. (2002). Inositol phosphates in the environment. *Philos. Trans. R. Soc. B* 357, 449–469. doi: 10.1098/rstb.2001.0837
- Vincent, A. G., Vestergren, J., Gröbner, G., Persson, P., Schleucher, J., and Giesler, R. (2013). Soil organic phosphorus transformations in a boreal forest chronosequence. *Plant Soil* 367, 149–162. doi: 10.1007/s11104-013-1731-z
- Yan, Y., and Kühn, O. (2010). Geometric correlations and infrared spectrum of adenine-uracil hydrogen bonds in CDCl₃ solution. *Phys. Chem. Chem. Phys.* 12, 15695–15703. doi: 10.1039/c0cp00009d
- Yan, Y. P., Liu, F., Li, W., Liu, F., Feng, X. H., and Sparks, D. L. (2014). Sorption and desorption characteristics of organic phosphates of different structures on aluminium (oxyhydr)oxides. *Eur. J. Soil Sci.* 65, 308–317. doi: 10.1111/ejss.12119
- Zentel, T., and Kühn, O. (2017). Properties of hydrogen bonds in the protic ionic liquid ethylammonium nitrate. *Theor. Chem. Acc.* 136:87. doi: 10.1007/s00214-017-2119-6

Conflict of Interest: The authors declare that the research was conducted in the absence of any commercial or financial relationships that could be construed as a potential conflict of interest.

Copyright © 2020 Ganta, Kühn and Ahmed. This is an open-access article distributed under the terms of the Creative Commons Attribution License (CC BY). The use, distribution or reproduction in other forums is permitted, provided the original author(s) and the copyright owner(s) are credited and that the original publication in this journal is cited, in accordance with accepted academic practice. No use, distribution or reproduction is permitted which does not comply with these terms.

Supplementary Material

1 ADDITIONAL QM/MM TECHNICAL DETAILS

The electrostatic embedding QM/MM method is implemented here using the CP2K package (CP2K, 5.1, 2017) where QM is simulated by the quickstep method (VandeVondele et al., 2005) and MM by FIST (Mundy et al., 2017). For the QM part, density functional theory (DFT) is adopted in which Goedecker-Teter-Hutter (GTH) pseudopotentials (Krack, 2005) and the Perdew-Burke-Ernzerhof (PBE) (Perdew et al., 1996) exchange correlation functional are used together with the D3 empirical dispersion correction (Grimme et al., 2010). The double- ζ valence polarised (DZVP-MOLOPT-SR-GTH), MOLOPT (VandeVondele and Hutter, 2007) basis set has been selected for all QM atoms except water for which single- ζ valence basis was selected to reduce computational costs. The HBs between diaspore-water and between water molecules could be well defined using these basis sets (Kubicki, 2016). The SCF convergence threshold of 10^{-5} hartree was chosen. The counterpoise scheme (Boys and Bernardi, 1970) is used to correct the basis set superposition error (BSSE) for interaction energies.

For the MM part of the modeled system, the bottom three layers of diaspore surface (480 atoms) has been modeled with CLAYFF force fields (Cygan et al., 2004), water with SPC based water model (Berendsen et al., 1987) and IHP/GP using the CHARMM force fields obtained via SwissParam force field generation tool (Zoete et al., 2011). The SPC based water model is compatible with both CLAYFF and CHARMM force fields. More details about force fields used here are given in (Ganta et al., 2019). The QM/MM coupling driver is part of the CP2K package, namely we used the gaussian expansion of the electrostatic potential method (GEEP) (Laino et al., 2006). The QM/MM simulations here are performed within a canonical (NVT) ensemble that means simulation of molecular systems at constant number of atoms (N), volume (V), and temperature (T).

REFERENCES

- Berendsen, H. J. C., Grigera, J. R., and Straatsma, T. P. (1987). The missing term in effective pair potentials. *J. Phys. Chem.* 91, 6269–6271. doi:10.1021/j100308a038
- Boys, S. and Bernardi, F. (1970). The calculation of small molecular interactions by the differences of separate total energies: Some procedures with reduced errors. *Mol. Phys.* 19, 553–566. doi:10.1080/00268977000101561
- Cimas, Á., Tielens, F., Sulpizi, M., Gageot, M.-P., and Costa, D. (2014). The amorphous silica–liquid water interface studied by ab initio molecular dynamics (AIMD): local organization in global disorder. *Journal of Physics: Condensed Matter* 26, 244106. doi:10.1088/0953-8984/26/24/244106
- CP2K (5.1, 2017). *Open source molecular dynamics code* (www.cp2k.org)
- Cygan, R. T., Liang, J. J., and Kalinichev, A. G. (2004). Molecular models of hydroxide, oxyhydroxide, and clay phases and the development of a general force field. *J. Phys. Chem. B* 108, 1255–1266. doi:10.1021/jp0363287
- Gageot, M.-P. (2010). Theoretical spectroscopy of floppy peptides at room temperature. a dftmd perspective: gas and aqueous phase. *Phys. Chem. Chem. Phys.* 12, 3336–3359. doi:10.1039/B924048A
- Ganta, P. B., Kühn, O., and Ahmed, A. A. (2019). QM/MM simulations of organic phosphorus adsorption at the diaspore–water interface. *Phys. Chem. Chem. Phys.* 21, 24316–24325. doi:10.1039/C9CP04032C

- González, M.A. (2011). Force fields and molecular dynamics simulations. *Collect. SFN 2011* 12, 169–200. doi:10.1051/sfn/201112009
- Grimme, S., Antony, J., Ehrlich, S., and Krieg, H. (2010). A consistent and accurate ab initio parametrization of density functional dispersion correction (DFT-D) for the 94 elements H-Pu. *J. Phys. Chem.* 132, 154104:1–154104:15
- Groenhof, G. (2013). *Introduction to QM/MM Simulations* (Totowa, NJ: Humana Press). 43–66. doi:10.1007/978-1-62703-017-5_3
- Huang, P., Pham, T. A., Galli, G., and Schwegler, E. (2014). Alumina(0001)/water interface: Structural properties and infrared spectra from first-principles molecular dynamics simulations. *The Journal of Physical Chemistry C* 118, 8944–8951. doi:10.1021/jp4123002
- Ingólfsson, H. I., Lopez, C. A., Uusitalo, J. J., de Jong, D. H., Gopal, S. M., Periole, X., et al. (2014). The power of coarse graining in biomolecular simulations. *WIREs Computational Molecular Science* 4, 225–248. doi:10.1002/wcms.1169
- Krack, M. (2005). Pseudopotentials for H to Kr optimized for gradient-corrected exchange-correlation functionals. *Theor. Chem. Acc.* 114, 145–152. doi:10.1007/s00214-005-0655-y
- Kubicki, J. D. (ed.) (2016). *Molecular Modeling of Geochemical Reactions* (Chichester: Wiley and Sons)
- Kubicki, J. D. and Watts, H. D. (2019). Quantum mechanical modeling of the vibrational spectra of minerals with a focus on clays. *Minerals* 9, 141. doi:10.3390/min9030141
- Laino, T., Mohamed, F., Laio, A., and Parrinello, M. (2006). An efficient linear-scaling electrostatic coupling for treating periodic boundary conditions in qm/mm simulations. *J. Chem. Theory Comput.* 2, 1370–1378. doi:10.1021/ct6001169. PMID: 26626844
- Marx, D. and Hutter, J. (2009). *Ab Initio Molecular Dynamics: Basic Theory and Advanced Methods* (Cambridge University Press). doi:10.1017/CBO9780511609633
- Mundy, C., Balasubramanian, S., Bagchi, K., Hutter, J., Kuo, A. S. I., Laino, T., et al. (2017). *Frontiers in Simulation Technology (FIST)* (www.cp2k.org)
- Ozboyaci, M., Kokh, D. B., Corni, S., and Wade, R. C. (2016). Modeling and simulation of protein–surface interactions: achievements and challenges. *Q. Rev. Biophys.* 49, e4. doi:10.1017/S0033583515000256
- Perdew, J. P., Burke, K., and Ernzerhof, M. (1996). Generalized gradient approximation made simple. *Phys. Rev. Lett.* 77, 3865–3868. doi:10.1103/PhysRevLett.77.3865
- Senn, H. M. and Thiel, W. (2009). QM/MM methods for biomolecular systems. *Angew. Chem.* 48, 1198–1229
- VandeVondele, J. and Hutter, J. (2007). Gaussian basis sets for accurate calculations on molecular systems in gas and condensed phases. *J. Chem. Phys.* 127, 114105:1–114105:8. doi:10.1063/1.2770708
- VandeVondele, J., Krack, M., Mohamed, F., Parrinello, M., Chassaing, T., and Hutter, J. (2005). Quickstep: Fast and accurate density functional calculations using a mixed gaussian and plane waves approach. *Comput. Phys. Commun.* 167, 103–128. doi:https://doi.org/10.1016/j.cpc.2004.12.014
- Zoete, V., Cuendet, M. A., Grosdidier, A., and Michielin, O. (2011). Swissparam: A fast force field generation tool for small organic molecules. *J. Comput. Chem.* 32, 2359–2368. doi:10.1002/jcc.21816

2 FIGURES

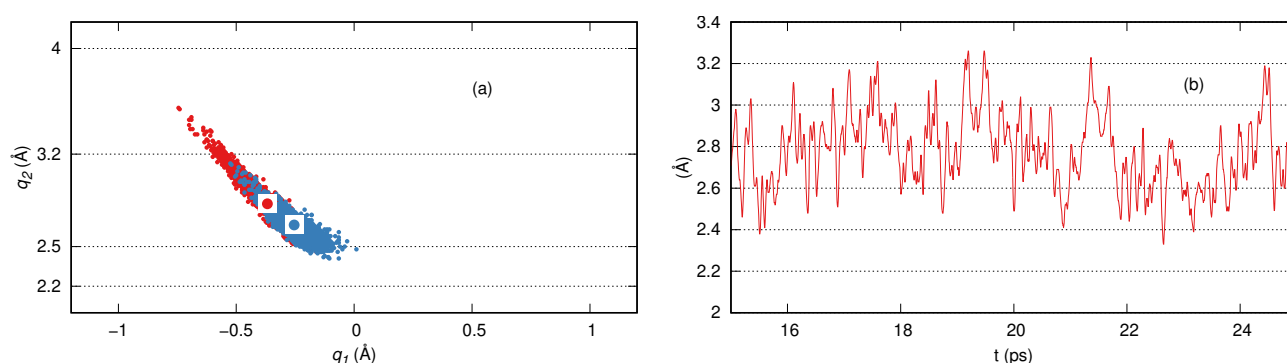


Figure S1: Correlation plot of hydrogen bond (HB) length (q_2) and deviation of the H atom from the HB center (q_1) of two HBs formed between the diaspor surface and water for the diaspor-GP-water **M** motif (a) Al1-O11 bond length for the diaspor-IHP-water **M(2)** motif (b).

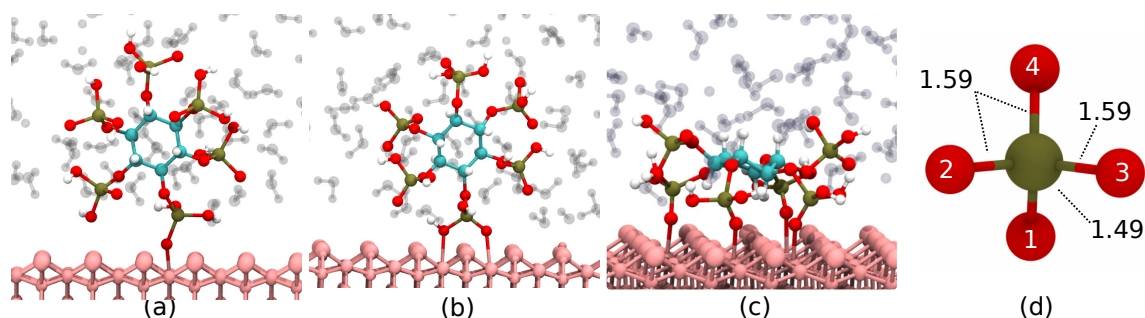


Figure S2: Diaspor-IHP-water initial binding motifs, **M(1)** case initial motif: **M** (a), **M(2)** case initial motif: **B** (b), **2M** case initial motif: **4M** (c), free tetrahedral PO_4^{3-} (d).

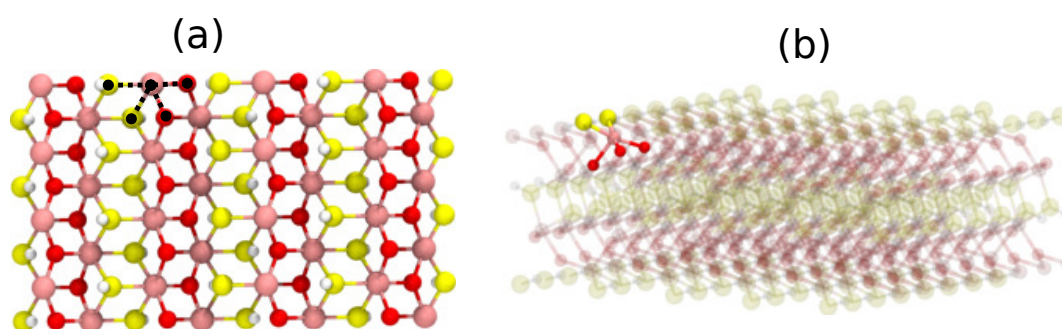


Figure S3: Side view of the neutral and pure 010 and 100 diaspor surface planes. Surface Al atoms of the diaspor 010 surface plane are coordinated by four oxygen atoms (a) and 100 diaspor surface plane are coordinated by five oxygen atoms (b). Pink, red, yellow and white colors correspond to Al, bridging oxygen, hydroxyl oxygen and hydrogen respectively.

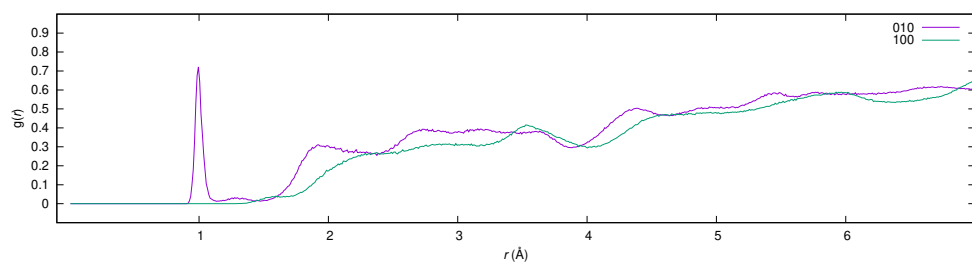


Figure S4: Comparison of radial distribution functions calculated for the 010 and 100 diaspore surface oxygen atoms and water hydrogen atoms.

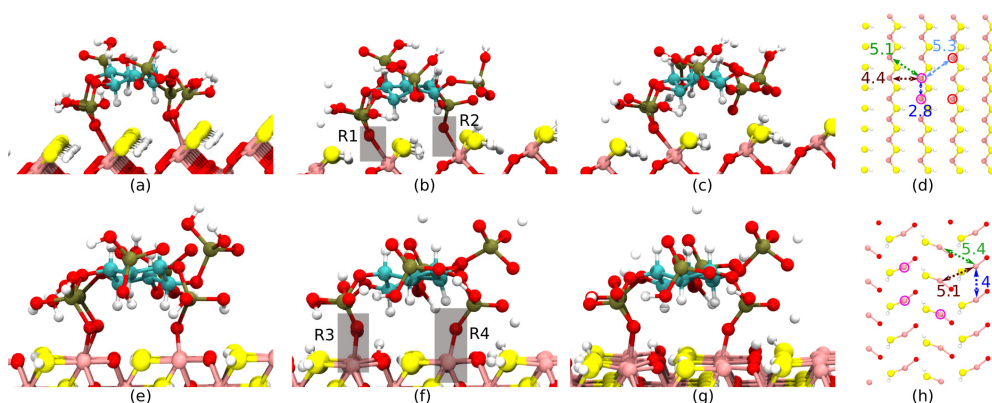


Figure S5: Snapshots along the MD trajectory for the 100 diaspore-IHP-water **2M** motif (a-c) and the top view of surface atoms showing interatomic Al-Al distances (d). Similarly, the snapshots of **3M** motif (e-g) and top view of surface atoms showing interatomic Al-Al distances (h). The circle around Al atom denote the site of Al-O_P bonds in **2M** and **3M** motif, respectively wherein the red circle denotes the site where Al-O_P bond dissociated. Note that water is ignored in this image for better view.

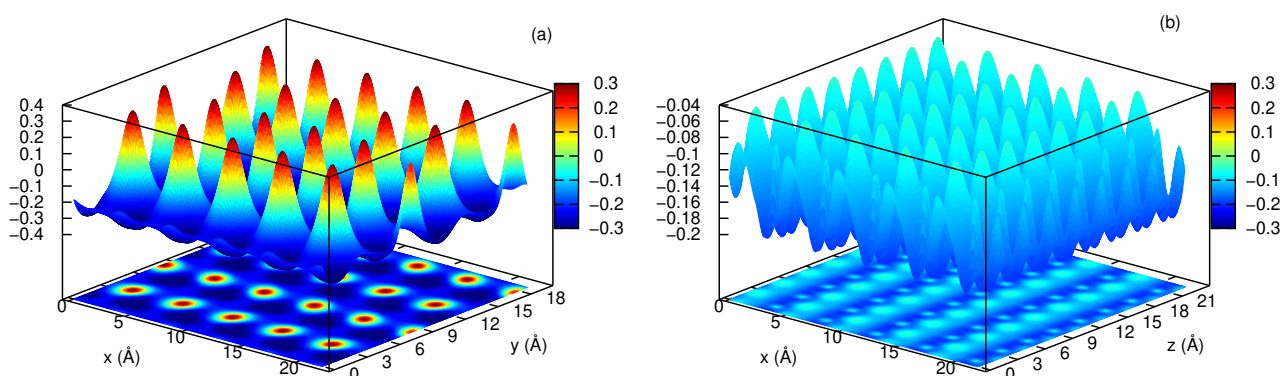


Figure S6: Electrostatic potential (a.u.) at 1 Å (perpendicular to surface) for the bare 010 diaspore surface plane (a) as well as for the bare 100 diaspore surface plane (b). These have been calculated for bare surfaces without involving phosphates and water.

Article

Ab Initio Molecular Dynamics Simulations of the Interaction between Organic Phosphates and Goethite

Prasanth B. Ganta ¹ , Oliver Kühn ^{1,2}  and Ashour A. Ahmed ^{1,2,*} 
¹ Institute of Physics, University of Rostock, Albert-Einstein-Str. 23-24, D-18059 Rostock, Germany; prasanth.ganta@uni-rostock.de (P.B.G.); oliver.kuehn@uni-rostock.de (O.K.)

² Department of Life, Light, and Matter (LLM), University of Rostock, Albert-Einstein-Str. 25, D-18059 Rostock, Germany

* Correspondence: ashour.ahmed@uni-rostock.de; Tel.: +49-381-498-6943

Abstract: Today's fertilizers rely heavily on mining phosphorus (P) rocks. These rocks are known to become exhausted in near future, and therefore effective P use is crucial to avoid food shortage. A substantial amount of P from fertilizers gets adsorbed onto soil minerals to become unavailable to plants. Understanding P interaction with these minerals would help efforts that improve P efficiency. To this end, we performed a molecular level analysis of the interaction of common organic P compounds (glycerolphosphate (GP) and inositol hexaphosphate (IHP)) with the abundant soil mineral (goethite) in presence of water. Molecular dynamics simulations are performed for goethite–IHP/GP–water complexes using the multiscale quantum mechanics/molecular mechanics method. Results show that GP forms monodentate (**M**) and bidentate mononuclear (**B**) motifs with **B** being more stable than **M**. IHP interacts through multiple phosphate groups with the **3M** motif being most stable. The order of goethite–IHP/GP interaction energies is GP **M** < GP **B** < IHP **M** < IHP **3M**. Water is important in these interactions as multiple proton transfers occur and hydrogen bonds are formed between goethite–IHP/GP complexes and water. We also present theoretically calculated infrared spectra which match reasonably well with frequencies reported in literature.

Keywords: P-inefficiency; goethite; glycerolphosphate; inositol hexaphosphate; MD simulations; QMMM; binding energies; infrared spectra



Citation: Ganta, P.B.; Kühn, O.; Ahmed, A.A. Ab Initio Molecular Dynamics Simulations of the Interaction between Organic Phosphates and Goethite. *Molecules* **2021**, *26*, 160. <https://doi.org/10.3390/molecules26010160>

Received: 12 November 2020

Accepted: 23 December 2020

Published: 31 December 2020

Publisher's Note: MDPI stays neutral with regard to jurisdictional claims in published maps and institutional affiliations.



Copyright: © 2020 by the authors. Licensee MDPI, Basel, Switzerland. This article is an open access article distributed under the terms and conditions of the Creative Commons Attribution (CC BY) license (<https://creativecommons.org/licenses/by/4.0/>).

1. Introduction

Phosphorus (P) scarcity is becoming one of the major global environmental challenges, which needs attention on par with climate change because of the foreseen P peak scenario [1–3]. The P in today's fertilizer is mostly from mined P rocks, and given the current mining rate they are predicted to be exhausted within next 50–100 years [4,5]. Complicating the situation further, the P rock reserves are available only in few countries and a P peak scenario could affect regions like UK, Western Europe, and India who obtain these resources mainly through imports [2,6,7]. As P rock reserves dwindle with time, the food security of P-importing countries is in question, which, in the long-term, might flip oil based economies to P based economies. The oil crisis in the 1970s emphasized the need for renewable energy sources, but unfortunately for the peak P crisis there is no alternative but to develop ways to increase, reuse, and secure the domestic P production [1,6–8].

The P input to soil (P fertilizers or from nature) is not fully available to plants as most of it is bound to soil organic matter [9–11] or soil minerals [12–16]. To overcome this, fertilizers are often applied in the agriculture industry to maintain and boost the agricultural production. As a side effect, P bound to minerals runs off along water paths during heavy rains and in the long-term causes eutrophication of waterways [17]. Recent studies show that the soil minerals in rain water retain about 50% of P in the soil solution [18,19]. In addition, heavy rains further decrease P efficiency as P-bound soil minerals, i.e., P colloid complexes, disperse with rain water and accumulate in specific regions unavailable

to plants [20]. Methods that support effective extraction of P from these colloids would increase domestic P sources which in turn would improve the food security of global population.

Orthophosphate (OP) is one of the most abundant inorganic phosphate, which exists mainly in the form of phosphate ions ($\text{H}_2\text{PO}_4^{1-}$, HPO_4^{2-} , PO_4^{3-}) [21,22]. Regarding organic phosphates, inositol hexaphosphate (IHP) [23–25] and glycerolphosphate (GP) [26–28] are some of the abundant and most common organic phosphates in soil. Often they are present in soil as oxyanions with deprotonated phosphate groups [29–31]. Therefore, the negatively charged phosphates bind to positively charged soil mineral surfaces to form P colloids. The most common P-fixing minerals are Fe and Al(oxyhydr)oxides [32–34] and Ca-oxides [33]. Goethite ($\alpha\text{-FeOOH}$) is one of the most reactive and abundant mineral that interacts with phosphates [35]. Strong interactions have been reported for OP [15,36–39] as well as for IHP [30,31,40,41] and GP [29], especially at low to medium pH. The interaction of phosphates with goethite or most minerals is through bonded and non-bonded interactions, for instance, covalent bonds, hydrogen bonds (HBs), van der Waals (vdW) interactions, and electrostatic attraction to form surface complexes [33,42,43]. Numerous studies show that P compounds with a single phosphate group form one to two covalent bonds between the phosphate group's oxygens and surface iron atoms [15,36,44] within inner-sphere complexes. IHP may bind through one to four of its six phosphate groups [31,40,41,45] to form covalent bonds with surface iron atoms. In contrast, Johnson et al. [30] suggested that IHP forms outer-sphere complexes. In addition to the covalent bonds and electrostatic interaction between phosphates and goethite, water also plays an important role for the stability of these complexes. In fact, the P colloids often exist in a solvated state in both arable and forest soils. The study by Ahmed et al. [46] showed the importance of water in surface complexation reactions and highlighted how water maneuvers the phosphate interaction with mineral by forming strong to moderately strong HBs with phosphates [47,48].

A molecular level study of solvated P colloids could provide additional insight into these interactions and improve our understanding of P availability to plants [13]. Molecular simulations are efficient tools to achieve this with proven track record [42,49]. For instance, Kwon and Kubicki [50] resolved controversies in experimental studies related to phosphate surface complexes on iron hydroxides. They correlated different types of phosphate binding motifs with goethite to pH and suggested that binding motifs change with pH. Aquino et al. [51] estimated goethite's point of zero charge (PZC) to 9.1 which fits well with experimental values of 6.4–9.7 [22,52,53]. Kubicki et al. [44] explored phosphate and goethite binding motifs and their corresponding stability at different surface planes to find dominant motifs that contribute significantly to infrared (IR) spectra. Ahmed et al. [15] showed that an analysis of theoretical spectra for different motifs could provide an estimate of their ratio of abundance at the goethite surface.

The main objective of the current study is to unravel the interactions of IHP/GP at the 010 goethite–water interface. This is achieved by analyzing binding motifs, interaction energies, and IR spectra obtained using periodic boundary quantum mechanics/molecular mechanics (QM/MM) [54] molecular dynamics simulations.

2. Modeling and Computations

2.1. Goethite Surface

Goethite is an orthorhombic crystal containing ferric (Fe^{3+}) iron which is coordinated by six oxygen atoms [35]. The bulk oxygens are triply coordinated and they are of two distinct types: (1) bridging oxygen coordinated by three iron atoms plus a HB and (2) hydroxyl oxygens coordinated by three iron atoms and one proton, see Figure 1c. Its unit cell contains 16 atoms, i.e., four $\text{FeO}(\text{OH})$ units with lattice constants $a = 9.95$, $b = 3.01$, $c = 4.62$ Å. Some common goethite surface planes are 010, 100, 021, and 110 (as per Pnma space group). The IHP and GP interactions with goethite are studied here by considering the 010 goethite surface which is known for its high stability [55,56], see

Figure 1c. The unsaturated and undercoordinated iron and oxygen atoms at the goethite surface generate an overall positive surface charge that attracts IHP/GP and also water to the surface. Compared to bulk, the surface iron atoms are coordinated by only four oxygens while the bridging and hydroxyl oxygens are coordinated by only two irons instead of three. Modeling an undercoordinated surface supports experimental studies that phosphate (IHP [31] and GP [29]) adsorption occurs mostly at pH lower than the goethite PZC, where its surface is unsaturated and has positive surface charge [29,31].

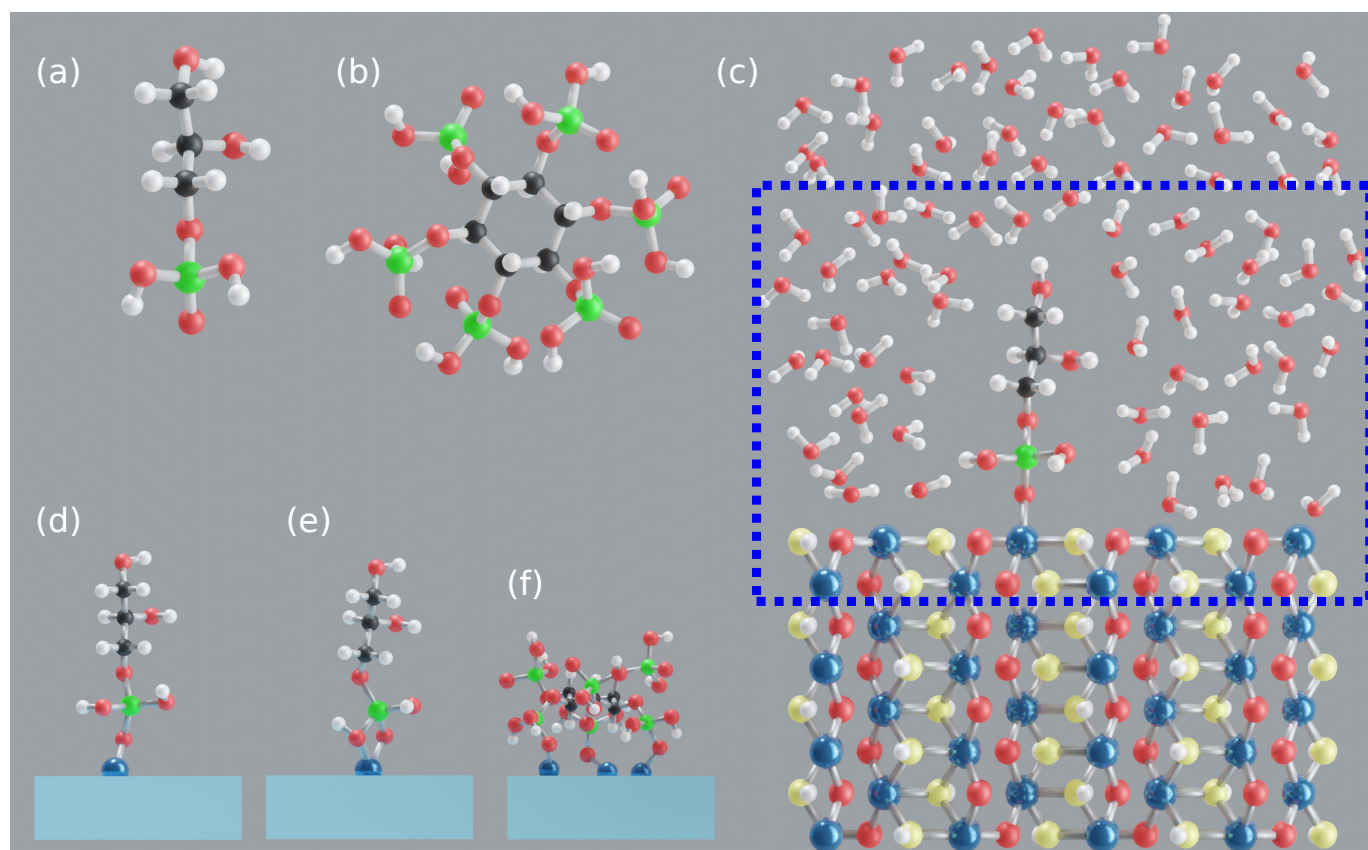


Figure 1. GP [$C_3H_9O_6P$] (a), IHP [$C_6H_{18}O_{24}P_6$] (b), goethite-GP-water complex (c), **M** motif (d), **B** motif (e), and **3M** motif (f). Blue, red, yellow, white, black, and green colors correspond to iron, bridging oxygen, hydroxyl oxygen, hydrogen, carbon, and phosphorus atoms, respectively. The dotted line denotes the QM box.

2.2. Model Systems

First, a surface slab is modeled by repetition of the goethite unit cell as $2a \times 4b \times 5c$. Then, GP (see Figure 1a) is added onto the goethite slab to form covalent bond(s) with a surface iron atom, see Figure 1c. The binding motifs considered for goethite–GP complex are based on experimental studies related to OP [22,57] and organic compounds with monophosphate groups [29,43] interacting with goethite. The study by Li et al. [29] of GP adsorption on goethite suggests that GP predominantly forms monodentate mononuclear motifs (**M**, 1Fe+1O a covalent bond between Fe atom and phosphate free oxygen, see Figure 1d). However, considering OP's [58] interaction with goethite, an additional motif called bidentate mononuclear motif (**B**, 1Fe + 2O two covalent bonds between Fe atom and unprotonated and protonated phosphate O atoms, see Figure 1e) is modeled. The bidentate binuclear motif (**BB**, 2Fe+2O, two covalent bonds between two surface Fe atoms and two oxygens from phosphate, see Figure S4a) which is commonly discussed for OP interaction with goethite [22,36,50] is not considered here as the distance between consecutive Fe atoms does not match the range of distances between oxygen atoms in the phosphate group.

Similarly, IHP (see Figure 1b) is added onto the goethite surface to form goethite–IHP complexes. The IHP interaction with goethite is different compared to GP because of the additional phosphate groups. Guan et al. [45] studied IHP adsorption onto aluminum hydroxide and showed that IHP binds to the surface through two phosphate groups. Moreover, Celi et al. [31] and Ognalaga et al. [40] suggested that IHP interacts with goethite through multiple phosphate groups. Unlike for OP and GP, there is no suggestion for a clear dominant motif for IHP interaction with goethite. Therefore, in addition to the **M** and **B** motifs, a tridentate motif **3M** (**3M**, 3Fe + 3O three covalent bonds between three surface Fe atoms and one protonated, two unprotonated phosphate O atoms, see Figure 1f) is considered. The **3M** motif is considered here based on the goethite surface Fe atom's and IHP O atom's structural flexibility to form bonds.

The complexes discussed so far are solvated to include the effects of water on their interactions. The goethite–IHP/GP complexes are solvated perpendicular to the studied surface plane up to ≈ 18 Å using VMD [59] at a density of ≈ 1 g cm^{−3}, see Figure 1c. To ease the discussion about the interactions, the Fe/Al-bonded oxygens are denoted as O_p. Note that even though the initial motifs considered here may not include all possible surface configurations they should allow us to draw conclusions from common motifs.

2.3. Computational Details

The atoms in the modeled complexes are separated into two regions as required by the QM/MM method [54,60]. The atoms of the reactive region (QM) of goethite–IHP/GP–water complexes include the top goethite layer, phosphate, and water within ≈ 10 Å from goethite surface. The average number of QM atoms in each model is around 350–400 depending on the complex; the total average number of atoms per each model is around 1200–1250. The atoms excluded from the QM region are described at the MM level with classical force fields (FF). Note that simulating the above complexes with 1200+ atoms using pure QM methods is a computational roadblock [42,61], and to overcome this the QM/MM approach is adopted here.

The potential and forces of the QM subsystems are calculated using density functional theory (DFT) as implemented in the Quickstep code [62]. Here, the nucleus and highly localized core electrons of atoms are replaced by Goedecker–Teter–Hutter (GTH) pseudopotentials [63], while the valance electrons are described with the double- ζ valance-polarized MOLOPT (DZVP–MOLOPT–SR–GTH) basis set [64]. For water atoms, the valance electrons are defined with the simpler single- ζ valance (SZV–MOLOPT–SR–GTH) basis set to further reduce computational cost. The exchange correlation interactions and vdW interactions are included with Perdew–Burke–Ernzerhof (PBE) [65] exchange correlation functional and D3 empirical dispersion correction [66], respectively. The MM part is simulated with the FIST module [67], which is an integral part of CP2K [68,69]. The goethite surface is modeled with the CLAYFF FF [70] and the water with the single point charge (SPC) water model [71]. For phosphates IHP and GP, CHARMM FF are obtained from SwissParm, a FF generation tool [72]. Both CLAYFF and CHARMM FFs are compatible with the SPC water model.

The interaction between QM and MM subsections is simulated by Gaussian expansion of the electrostatic potential method (GEEP) [73] which is part of CP2K. This method defines MM charges as smeared out Gaussians and adopts efficient screening techniques to reduce the computational cost in calculating mutual interaction energies between QM and MM subsystems. There is a variety of QM/MM methods available that differ based on the level of theory used to define QM and MM mutual interactions. Here, the electrostatic embedding type of QM/MM method is employed which allows MM atoms to polarize QM atoms and thus to include the effect of surrounding atoms onto the reactive region [60]. For all complexes, the QM box size is $2a \times 22 \times 5c$, i.e., $19.9 \times 22 \times 23.1$ Å, see Figure 1c, and the remaining region is MM.

Molecular Dynamics (MD) simulations are employed to sample the equilibrium dynamics including reactive events. As the phosphate interaction at goethite–water interface

involve proton transfer events and covalent bond changes [46–48], using the QM/MM MD technique is mandatory. Specifically, the electron density cut-off for the auxiliary plane wave basis set is chosen to be 500 Ry with SCF convergence threshold of 10^{-4} Hartree. The MD simulations are performed for 25 ps with a 0.5 fs time step and the temperature is maintained at 300K with canonical sampling through the velocity rescaling thermostat (CSVR) [74].

Each model has been equilibrated for about 10 ps. Interaction energies and information about geometries have been obtained from a subsequent 15 ps production trajectory. Specifically, the interaction energy between the goethite surface and IHP is calculated for every 100 fs (i.e., 150 snapshots) along the production trajectory by using

$$E_{\text{int}} = E_{\text{goe-IHP-complex}} - (E_{\text{goe}} + E_{\text{IHP}}). \quad (1)$$

The terms $E_{\text{goe-IHP-complex}}$, E_{IHP} , and E_{goe} denote total electronic energy of the goethite-IHP-complex, IHP, and goethite surface, respectively. The basis set superposition error (BSSE) in interaction energies is corrected using the counterpoise scheme [75]. The interaction energies that involve water are divided by the total number of water molecules in the simulation box to obtain per water molecule interaction energies for better comparison.

Infrared (IR) spectra for IHP and GP adsorbed onto goethite are calculated using the TRAVIS [76] software. In TRAVIS the IR spectra are obtained by Voronoi tessellation of the electron density yielding molecular dipole moments from bulk phase MD simulations [77,78]. This was done along a 30 ps equilibrium trajectory. The electron density is calculated for each 4 fs, i.e., every 8th snapshot of production trajectory and the massive (≈ 2 TB) electron density files are compressed using the bqb compression tool [79] compatible with TRAVIS. The compressed bqb files are then provided to TRAVIS software to calculate IR spectra. Here, the IR spectra are calculated for the frequency range of 950 to 1250 cm^{-1} , where the characteristic peaks related to phosphate stretching modes are observed.

3. Results and Discussion

3.1. Goethite-GP-Water Interactions

3.1.1. GP M Motif

A stable M motif is observed throughout the production trajectory with an average Fe–O_p bond length of 2.0 Å and average Fe–P distance of 3.2 Å, see Figure 2b. During early stages of equilibration, GP has formed an average of seven HBs with water, of which one is strong enough for a proton transfer to happen from GP to water, see Figure 3a. By the end of the equilibration, GP is twice deprotonated with one proton transfer to water and another to surface, see Figure 3a–b. A proton transfer is observed from GP to water (see Figure 3c) in the production trajectory; therefore, GP is three times deprotonated and its phosphate group completely deprotonated. In Figure 3b, a proton transfer event is observed from goethite surface oxygen to water. On average 8 HBs are observed between GP and water over the course of the production trajectory, see Figure S4b. The HBs are calculated using the VMD [59] plugin with HB donor–acceptor distance selected as 3 Å. Figure 3d shows a stable GP M motif at 25 ps.

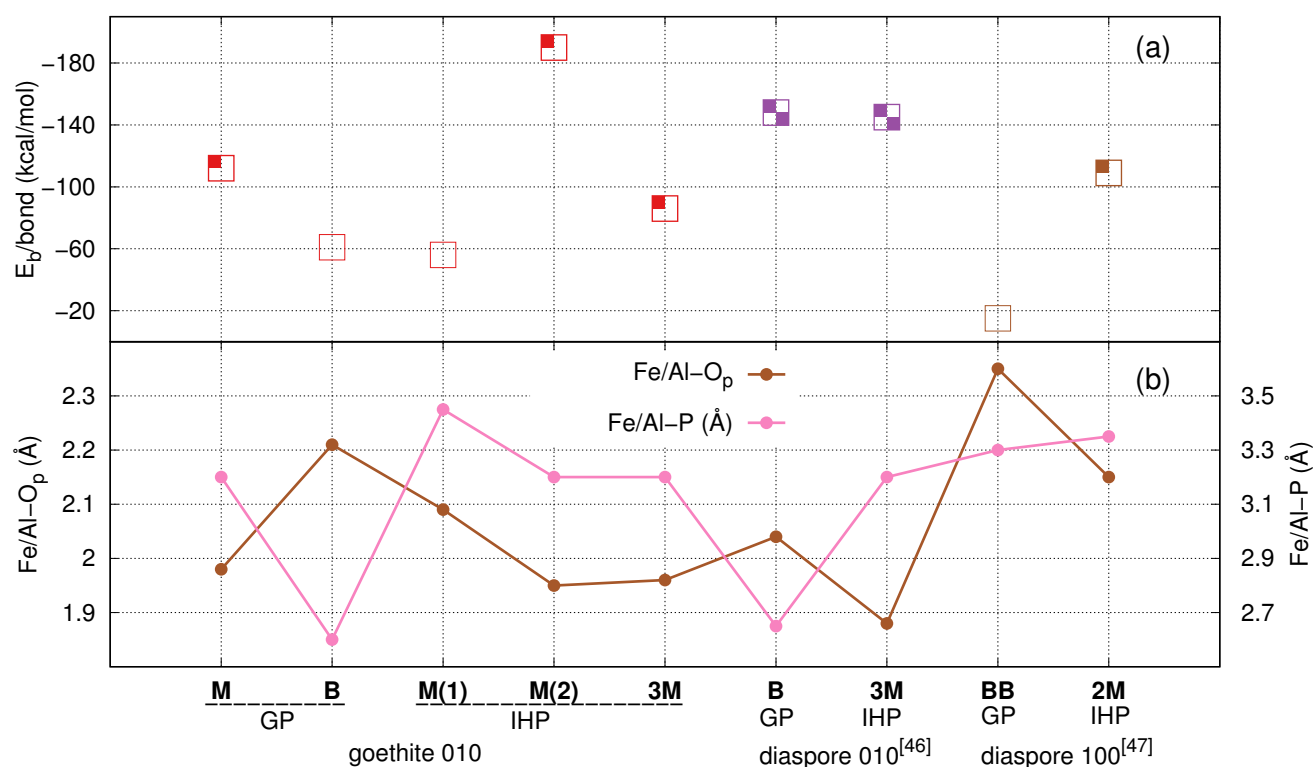


Figure 2. Comparison plot of interaction energies per bond E_b (a) and $Fe-O_p$, $Fe-P$ distances (b). Panels (a,b) also contain data for diaspore–IHP/GP–water complexes [47,48]. In the top figure, the number of filled subsquares denote the total number of proton transfers from IHP/GP to surface and center of box denotes the binding energy. The square with zero filled subsquares denotes zero proton transfers from phosphate to the surface.

The average interaction energy between goethite and GP calculated using Equation (1) is -112 kcal/mol, see Figure 2a. The average GP–water interaction energy per water molecule is -2.3 kcal/mol. The accumulation of water around the goethite surface suggests that water experiences a strong electrostatic pull from goethite surface, see Figure S5. The average goethite–water interaction energy is -6.8 kcal/mol, which is larger than the GP–water interaction energy. The stronger goethite–water interaction is due to multiple $Fe-O_{H_2O}$ covalent bonds (see Figure S4c), proton transfers, and HBs between goethite active sites and water.

3.1.2. GP B Motif

The initial **B** motif was found stable during the production trajectory with a mean average $Fe-O_p$ bond length of 2.21 Å and $Fe-P$ distance of 2.6 Å. The mean average $Fe-O_p$ bond length observed here is longer than in the **M** motif case, probably due to the repulsion between the bonded oxygens, see Figure 2b. In contrast to the **M** motif, proton transfer events are not observed from GP to the goethite surface. GP formed an average of eight HBs with water during equilibration stage and of these two yielded proton transfers from GP to water, see Figure 3e–f. Therefore, GP is deprotonated twice at the end of equilibration and during the production trajectory it formed an average of eight HBs with water. The snapshots in Figure 3g and h show the GP **B** motif at 20 and 25 ps, respectively.

The goethite–GP per bond interaction energy here is -61 kcal/mol per bond which is less than for the GP **M** motif because of the additional proton transfer observed in the latter case. However, the total interaction energy (-122 kcal/mol) here is higher than for the GP **M** motif, see Figure 2a. The GP–water interaction energy is -1.9 kcal/mol, which is smaller than for **M** motif case, probably due to the additional proton transfer from GP to water in the **M** motif.

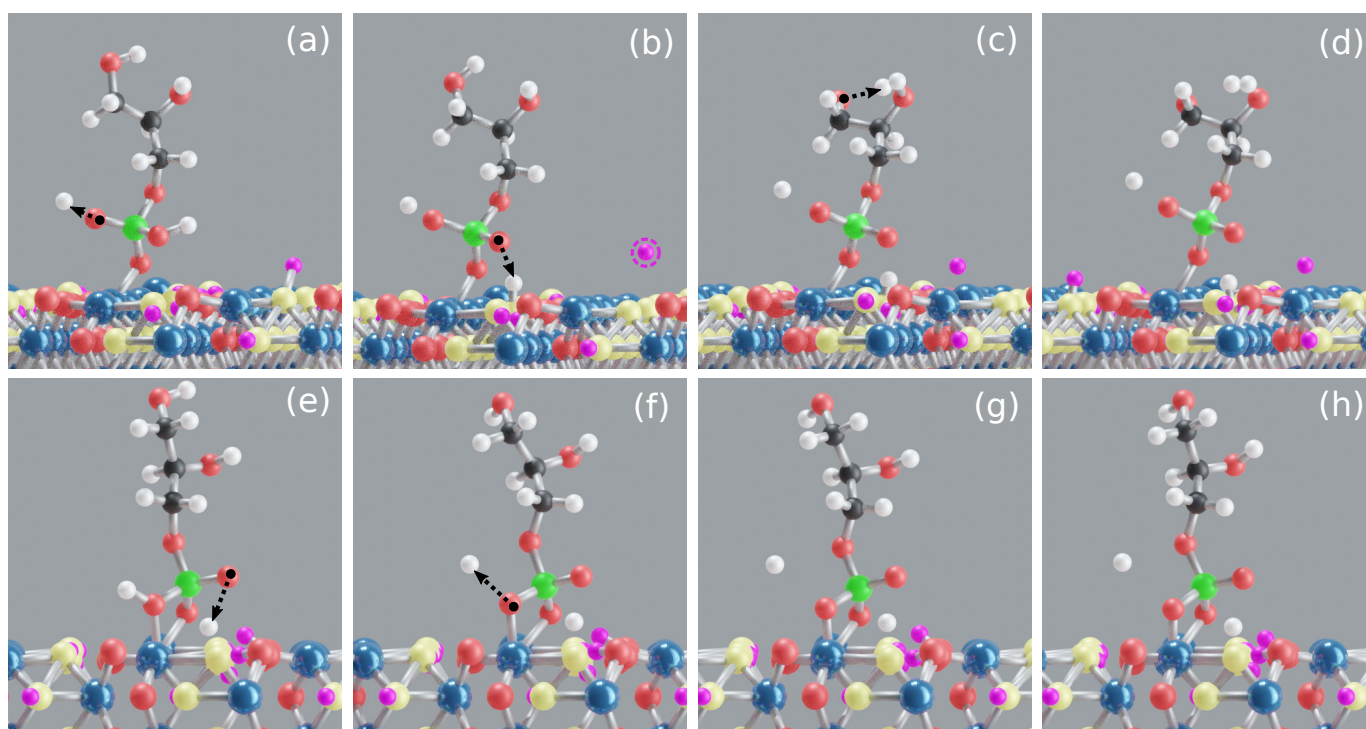


Figure 3. Snapshots of goethite–GP–water models along the simulation trajectory. Proton transfer from GP to water (a), a proton transfer from GP to surface and from surface to water (b), a proton transfer from GP to water (c), a stable **M** motif at 25 ps (d), proton transfers from GP to water (e,f), and **B** motif at 20 ps (g) and 25 ps (h). As proton transfer events are common in these interactions, the goethite surface hydrogen atoms and GP's hydrogen atoms are shown in violet and white colors to avoid confusion. Moreover, the surrounding water is ignored here for better visualization. Snapshots (a,b,e,f) are from equilibration phase.

3.1.3. Discussion of Goethite–GP–Water Interactions

The study by Li et al. [29] of GP on goethite suggested the formation of only the **M** motif and considered that the **B** motif could not be formed due to steric hindrance of the organic moiety in the GP molecule. In addition, Persson et al. [43] suggested a dominant **M** motif for monomethyl phosphate (MMP; $\text{CH}_3\text{--H}_2\text{PO}_4$) adsorption onto goethite. However, similar to our previous studies [47,48], we find that GP forms stable and strong **B** or **BB** motifs, see Figure 2a. In addition, Lü et al. [80] suggested that molecules with similar binding mechanism like GP such as glucose 6-phosphate and adenosine mono/triphosphates form nonprotonated bidentate complexes within first ten minutes after mixing. Furthermore, OP is known to form **M**, **B**, and **BB** motifs when interacting with goethite [33,44,50,58]. This raises the question of why the **M** motif could be the dominant species for GP on goethite, despite the fact that the binding energy for the **B** motif is stronger, see Figure 2a. Note that the interaction energies presented in Figure 2a are per bond. For IHP, we found a transformation of **B** motif to **M** motif on diaspore surface [47,48] because of intermolecular HBs in IHP and its strong interaction with water. Based on this, and on the study by Li et al. [29], one might assume that GP's HBs with water or its steric hindrance might hinder the **B** motif. Nevertheless, Abdala et al. [58] showed that at low ($1.25\ \mu\text{mol m}^{-2}$), medium ($2.5\ \mu\text{mol m}^{-2}$), and high ($10\ \mu\text{mol m}^{-2}$) surface loading of OP onto goethite, the observed motifs are at low **B** (48%), **BB** (47%), and **M** (≈ 0); at medium **B** (77%), **BB** (25%), and **M** (≈ 0); and at high **B** (≈ 0), **BB** (18%), and **M** (77%). This clearly shows that for low surface loading the **B** and **BB** motifs are dominant motifs whereas for high surface loading the **B** motif is not formed in the first place. In addition to surface loading, the surface type is also vital in deciding the dominant motifs of phosphates on surface [15,44]. For the 010 goethite surface, the theoretical study of single phosphate molecule interaction at goethite–water interface by Ahmed et al. [15,46] showed that the

B motif has a stronger binding than **M**. Further, the protonation state of GP's phosphate group here could be understood from the study of Sheals et al. [81] of glyphosate (GLP, $\text{H}_2\text{PO}_3\text{--CH}_2\text{--NH}_2\text{--CH}_2\text{--COO}$) on goethite; the twice deprotonated phosphate species dominate at the low surface adsorption densities and the monoprotonated phosphate species dominate at high surface adsorption densities. Correlating the current study with the above literature, the GP binds through a **B** motif with a twice deprotonated phosphate group dominantly at low surface adsorption density. At high surface adsorption density, GP binds preferentially through a **M** motif with a monoprotonated phosphate group.

The Fe–P distance observed here for the GP **M** motif is within the range of Fe–P distances observed in literature for goethite–phosphate complexes: 3.13–3.37 [82], 3.17–3.32 [83], 3.38 [44], 3.20 [46], and 3.41 [15], see Figure 2b. For the **B** motif, even though the calculated phosphate bond in this motif exhibits a strong interaction energy [46–48], it is not often discussed in experimental studies [22,44]. X-ray absorption studies of Abdala et al. [58] showed that the Fe–P distance observed for **B** motif case is around 2.85 Å, which is close to the value observed here, see Figure 2b. Furthermore, similar Fe–P values are observed for **B** motif in theoretical studies, i.e., 2.64 [46] and 2.58 Å [15]. Comparing the present interaction energies with other systems we notice the following. The present **B** motif exhibits stronger binding energy than the **M** motif, similar to the OP [46] and GLP [15] interaction with 010 goethite surface. Moreover, OP and GLP bind more strongly with goethite than with water, as observed for GP and water here. This suggests that phosphates often have the ability to replace water from goethite surface.

3.2. Goethite–IHP–Water Interaction

3.2.1. IHP **M** Motifs

Here, the initial **M** (Fe--O_p) and **B** ($\text{O}_p\text{--Fe--O}_p$) motifs (see Figure S3a,b) resulted in two different **M** motifs. **M**(1) corresponds to the initial **M** configuration, with an average Fe– O_p bond length and Fe–P distance of 2.09 and 3.45 Å, respectively, see Figure 2b. Two proton transfer events are observed from IHP to water in the equilibration stage, see Figure 4a,b. Moreover, a proton transfer is observed from goethite to water, see Figure 4a. During the production trajectory, IHP is twice deprotonated and the protonation state of IHP has not altered. It has formed an average of 22 HBs with water. In addition, intramolecular HBs are observed between adjacent phosphate groups along the whole MD trajectory, see Figure 4b–d. Similar to our previous studies [47,48], the HBs formed between IHP and water and the intramolecular HBs in IHP are mostly strong to moderately strong HBs. Figure 4d shows the **M**(1) motif at 25 ps. The average goethite–IHP and IHP–water interaction energies observed here are –56 and –5.5 kcal/mol, respectively. The goethite–water interaction energy here is –5.7 kcal/mol which is less than in the GP's **M** motif.

In **M**(2) motif case, the initial configuration was the **B** motif (see Figure S3b), which transformed to form **M**(2). Here, one of the Fe– O_p bonds is dissociated, and for the other bond the average Fe– O_p bond length and Fe–P distance is found to be 1.95 and 3.2 Å, respectively, see Figure 2b. In the equilibration phase, a proton transfer event is observed from IHP's oxygen to the surface (see Figure 4a), followed by formation of an intramolecular HB between the same oxygen and an adjacent phosphate group, see Figure 4b. IHP has formed around 20 HBs with water and two of them are apparently strong enough such that proton transfer events are observed from IHP to water. In addition, IHP has formed multiple intramolecular HBs between phosphate groups, see Figure 4f–h. During the production trajectory, IHP is three times deprotonated with one proton transfer to surface and two to water. One of the protons transferred from IHP to water formed an HB with the goethite surface, see Figure 4g–h. The time averaged goethite–IHP interaction energy observed here is –190 kcal/mol which is higher than the **M**(1) motif case due to additional proton transfers from IHP to goethite surface observed here, see Figure 2e–h.

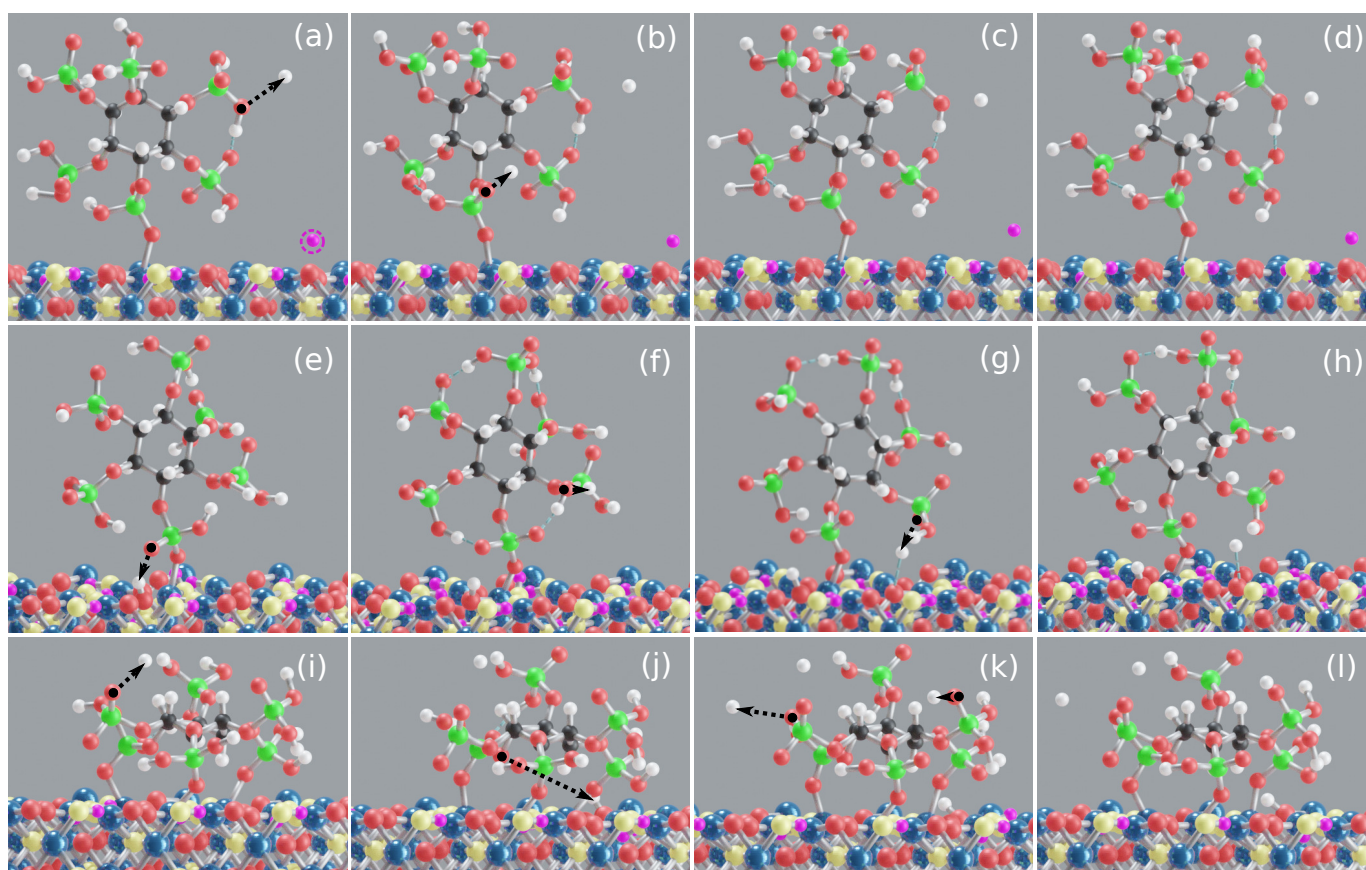


Figure 4. Snapshots of goethite–IHP–water models along the simulation trajectory. In **M(1)** motif, proton transfer from IHP to water and from goethite surface oxygen to water (a), intramolecular HB and a proton transfer from IHP to water (b), and **M(1)** motif at 17 and 25 ps (c,d). In **M(2)** motif, proton transfer from IHP to surface (e), protons transfer from IHP to water (f,g), and **M(2)** motif at 25 ps (h). In **3M** motif, three proton transfers from IHP to water (i,k) and a proton transfer from IHP to surface (j), **3M** motif at 25 ps (l). As proton transfer events are common in these interactions, the goethite surface hydrogen atoms and IHP’s hydrogen atoms are shown in violet and white colors to avoid confusion. Moreover, the surrounding water is ignored here for better visualization. Snapshots that show proton transfers are from the equilibration phase.

3.2.2. IHP 3M Motif

Here, IHP is aligned parallel to the surface to form three Fe–O_p covalent bonds as shown in Figure 1c. A stable **3M** motif is observed during the production trajectory with mean average Fe–O_p bond length of 1.96 Å and the corresponding mean average Fe–P distance of 3.2 Å, see Figure 2b, respectively. During equilibration, IHP has formed an average of 22 HBs with water of which three transformed to proton transfers from IHP to water, see Figure 4i,k. Furthermore, one proton transfer is observed from IHP to the surface, see Figure 4j. The equilibrated IHP is four times deprotonated with three proton transfers to water and one to the surface. The average number of HBs formed between IHP and water in production trajectory is around 23. The Figure 4l shows the IHP **3M** motif at 25 ps.

The time averaged goethite–IHP interaction energy per bond observed here is −86 kcal/mol. The goethite–IHP per bond interaction energy here is small compared to the **M(2)** motif case, but the overall interaction energy is higher than for both **M** motif cases, see Figure 2a. The IHP–water interaction energy is −7.8 kcal/mol which is higher than for the IHP **M** motif cases because of an additional proton transfer from IHP to water.

3.2.3. Discussion of Goethite–IHP–Water Interactions

Evaluating the interaction of the IHP phosphate groups with goethite, the **B** motif is found to be unstable here, similar to our previous studies [47,48] for IHP interaction with diaspore. To our knowledge, studies in literature have not mentioned the existence of **B** or **BB** motifs for IHP interacting with minerals. However, the **M** motif is often observed in theoretical studies [45,47,48] for IHP. Interestingly, for the number of phosphate groups which will bind to the surface different suggestions exist, ranging from four [40], three [45,47], two [47,48], one [47,48], and 0 [30]. The present **M** and **3M** stable motifs add to the list. The goethite–water interaction energy observed here is less than in the GP case. The weaker interaction of water in the latter case is in line with the study by Celi et al. [31] who showed that IHP adsorption on goethite makes the surface more negative than in case of OP.

Numerous studies show that IHP has the ability to compete with OP for the same binding sites and it could release and replace OP on goethite [23]. Comparing IHP and GP interaction energies, IHP exhibits stronger adsorption onto goethite than GP (see Figure 2a) which is in line with experiment [84] and our previous studies [47,48] for diaspore. Therefore, IHP has the ability to replace GP and the order of adsorption energies is IHP > GP > water. The Fe–P distances observed here are in close match to the values observed in experimental [58,82] and theoretical studies [15,44,46,83] of OP adsorption onto goethite. This is in line with Celi et al. [85] suggestion that IHP phosphate groups react with goethite in the same way as OP. Compared to GP, one could also infer that the changes in the phosphate group's geometry observed upon binding to goethite is similar for IHP and GP.

3.3. Theoretical IR Spectra of GP and IHP Adsorbed onto Goethite

The IR spectra of IHP/GP adsorbed onto goethite are calculated only for the stable motifs observed above, i.e., **M** and **B** of GP and **M** and **3M** of IHP. These motifs remained stable also during the extended trajectory used to calculate spectra, see Figures S6 and S7. The theoretical spectra calculated for these motifs are normalized and illustrated in Figure 5. The spectral analysis here is confined to 950–1250 cm^{−1} mainly to focus on the [P–O] stretching modes which are dominant in this range [22,86,87]. Therefore, the discussion below is mainly focused on phosphate ion bondings observed in the production trajectory and the corresponding IR spectra from literature. However, the peak positions of the IR spectra are known to shift differently with environmental factors such as water content and pH [50]. Especially nonprotonated oxygens of phosphate group are more sensitive to water hydrogens and hydroxyl groups and form HBs which might influence the spectra [50,88,89]. Both IHP and GP form strong to moderately strong HBs with surrounding water [47,48] and also contain nonprotonated oxygens, see Figures 3 and 4. Therefore, the calculated spectra here should reflect these interactions. The charge superscript is ignored when representing the phosphate ion bondings, e.g., FeH₂PO₄ or FeHPO₄, as these complexes are part of GP or IHP but not a molecule on their own.

Arai and Sparks [90] predicted the type of aqueous phosphate species based on the number of bands in IR spectra and the corresponding symmetry. According to their study, the aqueous phosphate species and their corresponding symmetry with number of bands (in parentheses) are PO₄–T_d(1), HPO₄–C_{3v}(3), H₂PO₄–C_{2v}(4), and H₃PO₄–C_{3v}(3). The study also showed that after OP binds to goethite the symmetry is reduced and the aqueous phosphate IR bands further split to form additional bands. Here, the symmetry of the phosphate group/s of IHP and GP is further reduced compared to OP bonded to goethite because of the P–O–C connection. Therefore, in the current study the spectrum assignment is performed based on the phosphate group moiety and its binding motif with goethite rather than symmetry.

Before we start the analysis some limitations about this approach should be mentioned. In an experimental set-up the IR spectra are obtained for an ensemble of molecules interacting with different goethite surface types. In contrast, here the analysis is performed for a single IHP/GP molecule interacting with only one goethite surface type. Furthermore,

the IR bands and their corresponding assignments may vary based on pH, experimental conditions, and surface crystallinity [44]. Ahmed et al. [15] provided a novel approach to this problem by calculating weighted averages of theoretical IR spectra involving simultaneously the most common and abundant motifs and surface planes. This study also emphasized the idea that an abundant motif's characteristics dominate the overall spectra which is in line with experimental studies [22,57].

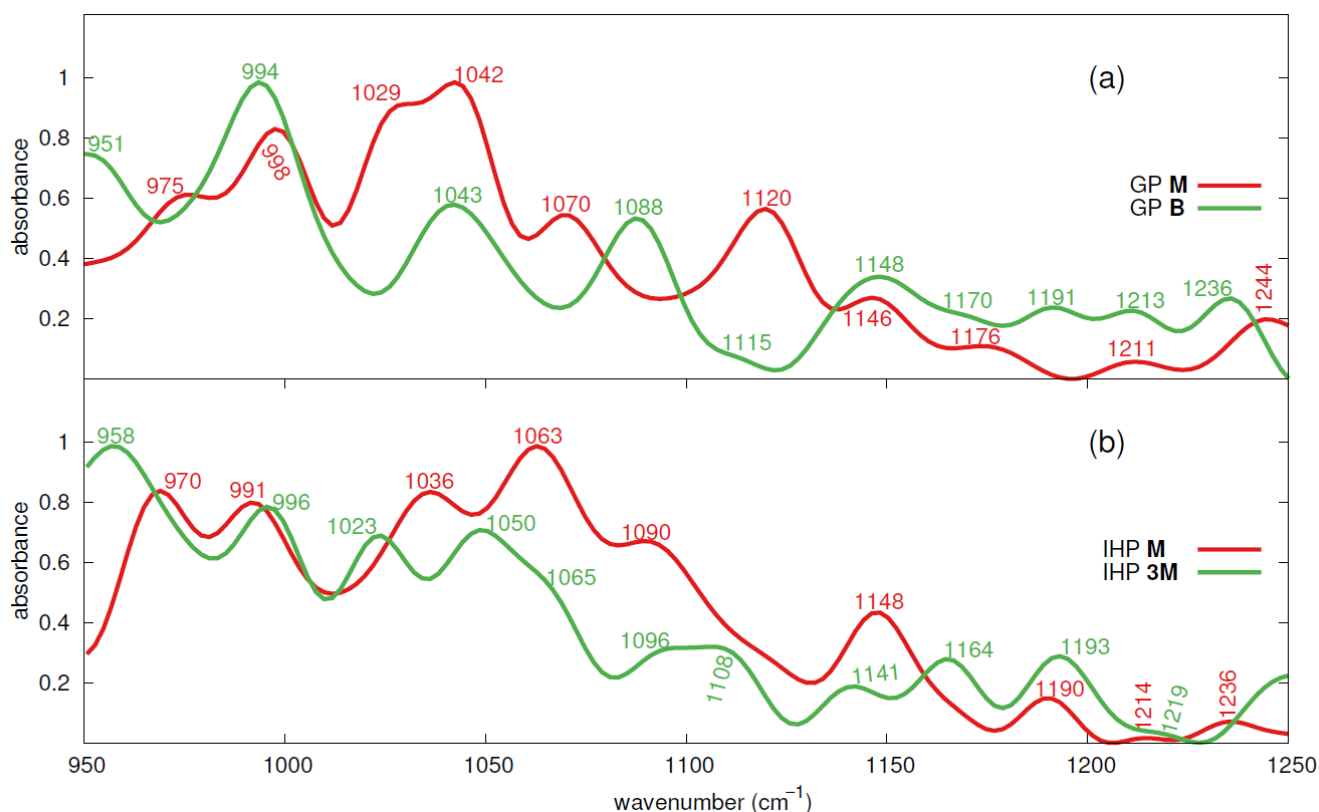


Figure 5. Calculated IR spectra of GP M and B motifs (a) and IHP M and 3M motifs (b).

3.3.1. GP IR Spectra

In the GP M motif case, a deprotonated phosphate species is observed throughout the production trajectory. Therefore, the phosphate species observed here is FePO_4 . The IR spectrum for GP exhibits ten bands at 975, 998, 1029, 1042, 1070, 1120, 1146, 1176, 1211, and 1244 cm^{-1} in the frequency range 950–1250 cm^{-1} , see Figure 5a. The first six peaks are of high to moderately high intense, whereas the remaining ones are less intense. The peaks at 1176 and 1211 cm^{-1} are less intense and wide ranged peaks distributed in frequency range of 1165 to 1187 cm^{-1} and 1200 to 1224 cm^{-1} . In the GP B motif case also a deprotonated phosphate species is also observed throughout the simulation trajectory. Here, the GP exhibits ten bands at 951, 994, 1043, 1088, 1115, 1148, 1170, 1191, 1213, and 1236 cm^{-1} . Here, only the first four bands are of high to moderately high intense and the remaining ones are less intense, see Figure 5a. The bands at 1115 cm^{-1} and 1170 cm^{-1} are shoulder bands distributed in the range of 1109 to 1119 cm^{-1} and 1164 to 1175 cm^{-1} , respectively. The GP M and B motif cases have matching bands within $\pm 6 \text{ cm}^{-1}$ of frequencies at 996, 1041, 1117, 1147, 1173, 1212, and 1240 cm^{-1} . In the following we compare these findings with previous studies.

GP M motif case: Lincoln and Stranks [91] studied phosphate binding to Co in the $\text{Co}(\text{NH}_3)_5\text{PO}_4$ complex and assigned bands at 980 and 1030 cm^{-1} to [P–OCo] and [P–O] modes of monodentate deprotonated phosphate group (CoPO_4), respectively. Tribe et al. [83] assigned bands at 979 and 1032 cm^{-1} to [P–O] modes of FePO_4 phosphate

species for glyphosate adsorption onto goethite. Therefore, the bands at 975 and 1029 cm^{-1} here are assigned to [P–OFe] and [P–O] modes. Compared to the study by Li et al. [29] of GP adsorption onto goethite, the bands at 998, 1042, 1120, and 1146 cm^{-1} could be assigned to [P–O] stretching mode, see Table 1 and Figure 5. The band at 998 cm^{-1} could also be assigned to [P–OFe] stretching mode as multiple studies [15,22,57,83] assigned bands around this frequency to the same stretching mode. Tribe et al. [83] assigned a band at 1063 cm^{-1} to [P–O] stretching mode for the FeHPO_4 complex, and therefore the band at 1070 cm^{-1} here could be assigned to a [P–O] stretching mode. The less intense band at 1176 cm^{-1} might correspond to [P–O] asymmetric stretching mode as Li et al. [29] assigned a band at 1180 cm^{-1} to [P–O] or [P–OH] for HPO_4 phosphate species of aqueous GP. Moreover, Persson et al. [57] assigned a band at 1178 cm^{-1} to [P–O] stretching mode for FeH_2PO_4 and Kubicki et al. [44] listed a band at 1176 cm^{-1} for the FeHPO_4 phosphate species. The band at 1211 cm^{-1} could be assigned to stretching modes of [C–C–C] and [C–O–C] of glycerol group based on the assignment by Nakagawa and Oyama [92] of 1210 cm^{-1} frequency observed in glycerol–water interactions [93]. Regarding the next band at 1244 cm^{-1} , Kubicki et al. [44] assigned the band at 1250 cm^{-1} to [P–O–H] bending vibrations and in addition, Ahmed et al. [15] assigned the band at 1227 cm^{-1} to [P–O–H] bending vibrations for OP on 010 goethite surface. Therefore, the band at 1244 cm^{-1} here could be assigned to GP's unprotonated phosphate oxygens interaction with water hydrogens.

GP **B** motif case: Ahmed et al. [15] study of OP on 010 goethite surface assigned bands at 957 and 964 cm^{-1} to [O–P–2OFe] and [2O–P–OFe] symmetric stretching modes and Persson et al. [57] assigned the band at 966 cm^{-1} to [P–O] stretching mode. Therefore, the band at 951 cm^{-1} could be assigned to [P–O] or [P–OFe] stretching modes. The band at 994 cm^{-1} frequency is close to 998 cm^{-1} frequency found in GP **M** motif case, and therefore it is assigned the same modes, [P–O] or [P–OFe] stretching modes, as the latter frequency. The bands at 1043, 1115, and 1148 cm^{-1} could be assigned to [P–O] stretching mode as per Li et al. [29] study while the band at 1088 cm^{-1} could be assigned to [P=O] [29] or [P–O] [83] stretching modes, see Table 1. The band at 1170 cm^{-1} is assigned [P–O] mode which is the same mode assigned for the band at 1176 cm^{-1} in GP **M** motif case. The band at 1191 and 1213 cm^{-1} could be assigned to [C–C–C] and [C–O–C] stretching modes of glycerol group as assigned for 1211 cm^{-1} frequency observed in GP **M** motif case. The band at 1236 cm^{-1} is assigned the same mode as 1244 cm^{-1} in GP **M** motif case.

Comparing IR spectra of GP **M** and **B** motifs, we conclude that several common band assignments are observed between both cases. The bands between 951 and 998 cm^{-1} are assigned to [P–O] or [P–OFe] stretching modes, and the ones between 1029 and 1176 cm^{-1} are assigned to [P–O] stretching mode except for 1088 cm^{-1} frequency which could be assigned to [P=O] stretching mode as well. The bands between 1191 and 1213 cm^{-1} are assigned to [C–C–C] and [C–O–C] stretching modes of glycerol group, respectively, while the bands between 1236 and 1244 cm^{-1} are assigned to unprotonated phosphate oxygens interaction with water hydrogens. The comparison of spectra calculated here with spectra from the experimental study by Li et al. [29] is shown in Figure S2a. Moreover, spectral peaks characteristic to water are analyzed in light of peaks from literature, see Figure S8.

Table 1. Experimental and theoretical IR frequencies from selected studies related to phosphates OP, GP, IHP, and others on goethite are listed below. The IR frequencies calculated here for GP and IHP on goethite are also presented here. The symbols †, ‡, •, ◦, ▲, ⋯, and ★ denote [P–O], [P=O], [P–OFe], [P–OH], [P–O–C], [P–O ⋯ H], and [C–C–C] plus [C–O–C] modes, respectively. The symbols are assigned to frequencies only when specifically mentioned in reference experimental study. The frequency assigned to multiple modes is denoted as •/◦ represent [P–OFe] or [P–OH] modes while •&/◦ represent [P–OFe] and/or [P–OH] mode.

Study and Description			Wavenumber [cm ^{−1}]										
goethite–OP													
Ref. Tejedor and Anderson [22] pH 6.0, 190 μmol P/g of Gt Fe ₂ HPO ₄ Fe ₂ PO ₄ FePO ₄	982 ^{•/◦}	1004	1030	1045		1099		1128					
		1006 [•]						1123 [‡]					
				1044 [†]		1096 [†]							
		1001 ^{•&/†}	1025 [†]										
Ref. Persson et al. [57] pH 4.2–5.7 [FeH ₂ PO ₄] pH 7.9 [FeHPO ₄] pH 13 [FePO ₄]	966 [†]							1122 [†]		1178 [†]			
		1001 ^{•/◦}		1049 [◦]				1122 [†]					
		1001 ^{•/◦}		1049 [◦]									
				1057 [†]									
Ref. Kubicki et al. [44] pH 4.22 [FeH ₂ PO ₄] pH 7.51 [FeHPO ₄]	982	1009		1044		1091	1122	1157		1195			
			1022	1043	1084		1124		1177				
Ref. Ahmed et al. [15] pH 6.3 M@010 [FeHPO ₄] B@010 [FeHPO ₄] M@100 [FePO ₄] B@100 [Fe ₂ HPO ₄]		1000					1110		1165				
		964	1021	1049								1207	
		957	992	1007	1035	1071						1227	
		957	999		1044	1058							
		953	974		1048								
goethite–[organic P-compounds]													
Ref. Persson et al. [43] (MMP) pH 2.6 FeHPO ₄ pH 9.9 FePO ₄		1003 [†]		1051 [†]				1140 [†]		1185			
		990 [†]		1051 [†]				1120 [†]		1185			
Ref. Tribe et al. [83] (GLP) FeHPO ₃ FePO ₃	973 [†]	1001 [•]	1020 [•]	1030 [†]	1063 [◦]		1118 [†]						
		979 [†]		1032 [†]	1068 [†]	1084 [†]	1095 [†]	1102 [†]					
Ref. Li et al. [29] (GP) pH 3 pH 9		1008 [†]		1052 [†]		1098 [‡]		1139 [†]					
		998 [†]		1044 [†]		1092 [‡]		1126 [†]					
current work M [FePO ₄] B [FePO ₄]	975 ^{†/•} 951 ^{†/•}	998 ^{†/•}	1029 [†]	1042 [†]	1070 [†]		1120 [†]	1146 [†]	1176 [†]		1211 [*]	1244 [◦]	
		994 ^{†/•}		1043 [†]		1088 ^{†/‡}	1115 [†]	1148 [†]	1170 [†]	1191 [*]	1213 [*]	1236 [◦]	
goethite–IHP													
Ref. Yan et al. [41] pH 5		998 [†]				1075 [†]		1135 [†]	1166 [•]				
Ref. Yan et al. [94] pH 5 pH 6		1010				1071		1134	1164				
		998				1068		1131					
Ref. Johnson et al. [30] fitted band centers	974 [†]	991 [▲]	1011 [▲]	1043 [⋯]	1074 [†]	1099 [†]		1128	1160 [†]	1187 [†]	1220 [‡]		
current work M 3M	970 ^{†/▲} 958 ^{†/▲}	991 ^{†/▲}		1036 [⋯]	1063 [†]	1090 [†]			1148 ^{†/•}	1190 [†]	1214 [‡]	1236 [◦]	
		996 ^{†/▲}	1023 [▲]	1050 [⋯]	1065 [†]	1096 [†]	1108 [†]	1141 ^{†/•}	1164 ^{†/•}	1193 [†]	1219 [‡]		

3.3.2. IHP IR Spectra

IHP has six phosphate groups and hence the theoretical spectra calculated here would include the characteristics of different types of phosphate species originating from the six phosphate groups. In addition, intermolecular HBs are also common between adjacent phosphate groups which shift or alter intensity of the IR spectra [88,89]. In the IHP M case, the six phosphate groups transformed to two types of phosphate species, HPO₄ (2) and H₂PO₄ (4), in the production trajectory. The IR spectra for IHP M case exhibited bands at 970, 991, 1036, 1063, 1090, 1148, 1190, 1214, and 1236 cm^{−1}, see Figure 5b. The first five bands are high intense bands while the latter ones are moderately intense to often less

intense. The band at 1090 cm^{-1} is a shoulder band distributed in the frequency range of 1084 to 1099 cm^{-1} while the band at 1214 is a least intense flat band distributed in the frequency range of 1205 to 1222 cm^{-1} . In IHP **3M** motif case all possible phosphate species, PO_4 (1), HPO_4 (2), H_2PO_4 (3), are observed in the production trajectory. The IR spectra have bands at 958 , 996 , 1023 , 1050 , 1065 , 1096 , 1108 , 1141 , 1164 , 1193 , and 1219 cm^{-1} . The bands at 1065 and 1219 cm^{-1} are shoulder bands distributed in the frequency range of 1059 to 1071 cm^{-1} and 1212 – 1225 cm^{-1} , respectively. The bands at 1096 and 1108 cm^{-1} are maxima of a bimodal peak which is distributed in the frequency range of 1084 to 1116 cm^{-1} . The IHP **M** and IHP **3M** motif cases have matching bands within $\pm 6\text{ cm}^{-1}$ of frequencies at 964 , 993 , 1064 , 1093 , 1144 , 1191 , and 1217 cm^{-1} . The IHP spectra obtained here are deconvoluted into Gaussian functions using the PeakFit v4 software [95] to compare current results with Johnson et al. [30] study. PeakFit v4 is the same software used by Johnson et al. [30] for deconvolution of IHP spectra. The deconvoluted spectra and the corresponding fitted band centers are presented in Figure S1.

IHP **M** case: Guan et al. [45] assigned bands between 970 – 985 cm^{-1} and 970 cm^{-1} frequency to $[\text{P}-\text{O}-\text{C}]$ stretching mode for IHP adsorbed onto aluminum hydroxide and for IHP in water, respectively. In contrast, Johnson et al. [30] assigned a fitted band center at 974 cm^{-1} to $[\text{P}-\text{O}]$ mode but he assigned fitted band center at 991 and 1011 cm^{-1} to $[\text{P}-\text{O}-\text{C}]$ stretching mode. Therefore, the peaks at 970 and 991 cm^{-1} (fitted band centers at 967 and 992 cm^{-1} , respectively, see Figure S1a) could be assigned to $[\text{P}-\text{O}]$ or $[\text{P}-\text{O}-\text{C}]$ stretching modes. The band at 1036 cm^{-1} (fitted band center 1036 cm^{-1}) might correspond to the intermolecular HBs between adjacent phosphate groups or between a phosphate group and water adsorbed to goethite surface. This assignment is based on the study of Johnson et al. [30], where the fitted band center at 1043 cm^{-1} is assigned to $\text{P}-\text{O}\cdots\text{H}$ (H from the phosphate group or water adsorbed to goethite surface). The high intense peak at 1063 cm^{-1} with fitted band center at peak center could be assigned to $[\text{P}-\text{O}]$ stretching mode of HPO_4 as per Johnson et al. [30] and Yan et al. [41] studies, see Table 1. The next peak is at 1090 cm^{-1} (fitted band center at 1091 cm^{-1}) and it could be assigned to $[\text{P}-\text{O}]$ mode as Johnson et al. [30] assigned a fitted band at 1099 to such a mode. The fitted band center at 1120 cm^{-1} which does not have a specific assigned peak (see Figure S1a) might correspond to $[\text{P}-\text{O}]$ stretching mode as Johnson et al. [30] assigned fitted band center at 1128 cm^{-1} to $[\text{P}-\text{O}]$ stretching mode. The peak at 1148 cm^{-1} (fitted band centers at 1147 and 1165 cm^{-1}) might correspond to $[\text{P}-\text{OFe}]$ stretching mode as Guan et al. [45] and Yan et al. [41] assigned bands 1148 cm^{-1} , 1157 cm^{-1} , and 1166 cm^{-1} to $[\text{P}-\text{OAl}]$ and $[\text{P}-\text{OFe}]$ stretching modes, respectively. It could also be assigned to $[\text{P}-\text{O}]$ mode as Johnson et al. [30] assigned 1160 cm^{-1} band center to such a mode. The peak at 1190 cm^{-1} the fitted band center is at peak center and it is assigned to $[\text{P}-\text{O}]$ mode as per Johnson et al. [30]. The band at 1214 cm^{-1} (fitted band center at 1213 cm^{-1}) could be assigned to $[\text{P}=\text{O}]$ stretching mode. This is because, Celi et al. [31] suggested that after IHP adsorption onto goethite the $[\text{P}=\text{O}]$ stretching band observed for aqueous IHP at 1223 cm^{-1} frequency might shift to lower frequencies. In addition, Johnson et al. [30] assigned the fitted band center at 1220 cm^{-1} to $[\text{P}=\text{O}]$ stretching mode. Bands within 1230 and 1250 cm^{-1} are not common in goethite–IHP-related studies, see Table 1, and therefore the band at 1239 cm^{-1} is assigned to $[\text{P}-\text{O}-\text{H}]$ bending vibrations based on Ahmed et al. [15]’s study.

IHP **3M** motif case: The first band at 958 cm^{-1} could be assigned to $[\text{P}-\text{O}]$ or $[\text{P}-\text{O}-\text{C}]$ stretching modes based on reasons for assignment of 970 cm^{-1} band in IHP **M** motif case. The next band at 996 cm^{-1} is assigned to $[\text{P}-\text{O}]$ or $[\text{P}-\text{O}-\text{C}]$ stretching modes for the same reasons as given for the assignment of the 977 cm^{-1} band in IHP **M** motif case. The band at 1023 cm^{-1} (fitted band center at 1022 cm^{-1}) could be assigned to $[\text{P}-\text{O}-\text{C}]$ stretching mode, as Johnson et al. [30] assigned the fitted band center at 1011 cm^{-1} to such a mode. Similar to the band at 1036 cm^{-1} for IHP **M** motif case, the band at 1050 cm^{-1} (fitted band center at 1048 cm^{-1}) here could be assigned to inter- and intramolecular HBs among adjacent phosphate groups and a phosphate group with water bound to goethite, respectively. The next bands at 1065 and 1096 cm^{-1} (corresponding fitted band centers at

1068 and 1092 cm^{-1}) are assigned to [P–O] stretching modes similar to peaks at 1063 and 1090 cm^{-1} of IHP **M** motif case, see Table 1. The peak at 1108 cm^{-1} with fitted band center at 1113 cm^{-1} could be assigned to [P–O] stretching mode based on Johnson et al. [30] assignment of fitted band center at 1127 cm^{-1} to [P–O] stretching mode. The band at 1141 cm^{-1} (fitted band center at 1140 cm^{-1}) is assigned to [P–OFe] stretching mode as Guan et al. [45] assigned the band at 1048 cm^{-1} to [P–OAl] stretching mode. It could also be assigned to [P–O] mode since Yan et al. [41] assigned the band at 1135 cm^{-1} to [P–O] mode. The band 1164 cm^{-1} (fitted band center at 1165 cm^{-1}) is assigned to [P–OFe] or [P–O] mode, as Yan et al. [41] assigned the band at 1166 cm^{-1} to [P–OFe] stretching mode and Johnson et al. [30] assigned fixed band center at 1162 to [P–O] mode. The peaks at 1193 and 1219 cm^{-1} are assigned to [P–O] and [P=O] modes for the same reasons given the assignment of peaks at 1190 and 1214 cm^{-1} in IHP **M** motif case.

Summarizing the IHP **M** and **3M** motifs' IR spectra, and their assignments based on literature (see Table 1), we conclude the following. The bands in the frequency range of 958 to 996 cm^{-1} could be mainly assigned to [P–O] or [P–O–C] stretching modes. The bands around 1043 cm^{-1} are assigned to intermolecular HBs between IHPs phosphate groups and intramolecular HBs between IHP phosphate groups and water adsorbed to goethite. The bands observed in the range of 1063 to 1108 cm^{-1} are assigned to [P–O] stretching modes and the ones in 1141–1164 cm^{-1} frequency range are assigned to [P–OFe] or [P–O] modes. The peaks around 1191 cm^{-1} are assigned to [P–O] modes and the ones around 1217 cm^{-1} are assigned to [P=O] modes. The comparison of IHP spectra with spectra from the experimental study of Yan et al. [41] is shown in Figure S2b. A few selected frequency ranges where the IR spectra of water could be characterized are analyzed, see Figure S8.

4. Summary and Conclusions

The world population is expected to increase 34% by 2050 and will reach 9.1 billion [96], challenging the agricultural industry to meet the nutritional needs. Unfortunately, agricultural production is heavily dependent on the soon to be exhausted P rocks. Therefore, there is a need to find ways to recycle and secure P resources to support the raising global population. The current study focused on P interaction with soil minerals, a significant factor that causes P inefficiency and P loss in soil. The present results are expected to provide additional insight into organic P interaction at goethite–water interface.

Analysis of binding energies (see Figure 2) show that the GP **B** motif exhibits stronger overall binding energy than the **M** motif. This is in contrast to the suggestion by Li et al. [29] that GP might not form **B** motif due to steric hinderance of organic moiety. However, based on interaction energies calculated here and the study by Abdala et al. [58], we conclude that GP forms a **B** motif at low goethite surface loading, while at high loading the **M** motif dominates.

Regarding IHP, it is found to interact with goethite through multiple phosphate groups and its **3M** motif has a higher interaction energy than the **M** motif. Furthermore, its **B** motif is unstable which transformed to the **M** motif. The transformation of the **B** to the **M** motif has occurred in our previous studies [47,48] as well, confirming that IHP phosphate groups are more likely to form **M** motifs with goethite. The IHP interaction energy with goethite is stronger than for GP which suggests that it could replace GP to bind with goethite. This is in line with the results of De Groot and Golterman [97] which showed that IHP can replace OP and inhibit it from further adsorption.

The energy required for phosphate to replace a OH^- from the surface could not be estimated from that study. However, Ahmed et al. [15] showed that OH^- has a higher interaction energy than OP and water and thus could replace both. However, in contrast, Li et al. [29] showed that GP replaces OH^- at the goethite surface at a high rate. Therefore, understanding the priority of adsorption is important as a non-replaceable hydroxyl group at the surface could restrict the IHP interaction with goethite and also reduce the range of binding motifs. The current study proposes a competitive adsorption study for multiple

instances of IHP/GP in presence of water and OH^- at the goethite surface to understand effect of high surface loading and influence of OH^- on binding motifs.

Finally, we have investigated the IR signatures of the different binding motifs. The IR spectra calculated for GP **M** and **B** motifs match reasonably with phosphates related IR spectra from literature. This suggests that both motifs might exist simultaneously on the goethite surface. However, given the similarity of spectra, the proportion of these motifs could not be estimated as done by Ahmed et al. [15]. The calculated IR spectra for IHP also matches well with the IR spectra from literature. This validates the current modeling approach for simulating the interactions of IHP and GP at goethite–water interface.

Supplementary Materials: The following are available online, Figure S1: Fitted IR spectra of IHP, Figure S2: Comparison of GP and IHP spectra with experimental spectra, Figure S3: Initial motifs of IHP and GP, Figure S4: GP **BB** motif, HBs between GP and surrounding water and water bonded to surface Fe atoms, Figure S5: Pair correlation function for surface Fe atoms and water oxygens, Figure S6: Fe–O_p covalent bond lengths along simulation trajectories between 25 and 55 ps, Figure S7: Binding energy of IHP **M(1)** motif along simulation trajectory between 25 and 55 ps, Figure S8: IR spectra of GP **M** and **B** motif cases and IHP **M** and **3M** motif cases.

Author Contributions: P.B.G. is responsible for formal analysis, investigation, methodology, visualization and writing—original draft. A.A.A. and O.K. are responsible for conceptualization, funding acquisition, methodology, supervision, writing—review and editing. All authors have read and agreed to the published version of the manuscript.

Funding: We gratefully acknowledge the financial support by the German Research Foundation (DFG) as a part of the SPP 1685 Priority program “Ecosystem Nutrition: Forest strategies for limited phosphorus resources” (P.B.G., O.K., A.A.A.) and the InnoSoilPhos-project (A.A.A.), funded by the German Federal Ministry of Education and Research (BMBF) in the frame of the BonaRes-program (No. 031A558). This research was performed within the scope of the Leibniz Science Campus “Phosphorus Research Rostock”. The authors thank the North German Super computing Alliance for providing HPC resources (project mvp00016).

Data Availability Statement: Not applicable.

Conflicts of Interest: The authors declare no conflict of interest. The funders had no role in the design of the study; in the collection, analyses, or interpretation of data; in the writing of the manuscript; or in the decision to publish the results.

References

1. Cordell, D.; Drangert, J.O.; White, S. The Story of Phosphorus: Global Food Security and Food for Thought. *Glob. Environ. Chang.* **2009**, *19*, 292–305. [\[CrossRef\]](#)
2. Cordell, D.; Neset, T.S.S. Phosphorus Vulnerability: A Qualitative Framework for Assessing the Vulnerability of National and Regional Food Systems to the Multi-Dimensional Stressors of Phosphorus Scarcity. *Glob. Environ. Chang.* **2014**, *24*, 108–122. [\[CrossRef\]](#)
3. Reitzel, K.; Bennett, W.W.; Berger, N.; Brownlie, W.J.; Bruun, S.; Christensen, M.L.; Cordell, D.; van Dijk, K.; Egemose, S.; Eigner, H.; et al. New Training to Meet the Global Phosphorus Challenge. *Environ. Sci. Technol.* **2019**, *53*, 8479–8481. [\[CrossRef\]](#)
4. Steen, I. Phosphorus Availability in the 21st Century : Management of a Non-Renewable Resource. *Phosphorus Potassium* **1998**, *217*, 25–31.
5. Smil, V. Phosphorus in the Environment: Natural Flows and Human Interferences. *Annu. Rev. Environ. Resour.* **2000**, *25*, 53–88. [\[CrossRef\]](#)
6. Rosmarin, A. The Precarious Geopolitics of Phosphorous. *Down Earth Sci. Environ. Fortn.* **2004**, *30*, 27–31.
7. Withers, P. Closing the Phosphorus Cycle. *Nat. Sustain.* **2019**, 1001–1002. [\[CrossRef\]](#)
8. Withers, P.; Forber, K.; Lyon, C.; Rothwell, S.; Doody, D.; Jarvie, H.; Martin-Ortega, J.; Jacobs, B.; Cordell, D.; Patton, M.; et al. Towards Resolving the Phosphorus Chaos Created by Food Systems. *Ambio A J. Hum. Environ.* **2019**. [\[CrossRef\]](#)
9. Ahmed, A.A.; Gros, P.; Kühn, O.; Leinweber, P. Molecular Level Investigation of the Role of Peptide Interactions in the Glyphosate Analytics. *Chemosphere* **2018**, *196*, 129–134. [\[CrossRef\]](#)
10. Gros, P.; Ahmed, A.; Kühn, O.; Leinweber, P. Glyphosate Binding in Soil as Revealed by Sorption Experiments and Quantum-Chemical Modeling. *Sci. Total Environ.* **2017**, *586*, 527–535. [\[CrossRef\]](#)
11. Gros, P.; Ahmed, A.A.; Kühn, O.; Leinweber, P. Influence of Metal Ions on Glyphosate Detection by FMOC-Cl. *Environ. Model. Assess.* **2019**, *191*, 244. [\[CrossRef\]](#) [\[PubMed\]](#)

12. Hens, M.; Merckx, R. Functional Characterization of Colloidal Phosphorus Species in the Soil Solution of Sandy Soils. *Environ. Sci. Technol.* **2001**, *35*, 493–500. [\[CrossRef\]](#) [\[PubMed\]](#)
13. Kruse, J.; Abraham, M.; Amelung, W.; Baum, C.; Bol, R.; Kühn, O.; Lewandowski, H.; Niederberger, J.; Oelmann, Y.; Rüger, C.; et al. Innovative Methods in Soil Phosphorus Research: A Review. *J. Soil Sci. Plant Nutr.* **2015**, *178*, 43–88. [\[CrossRef\]](#) [\[PubMed\]](#)
14. Jiang, X.; Bol, R.; Nischwitz, V.; Siebers, N.; Willbold, S.; Vereecken, H.; Amelung, W.; Klumpp, E. Phosphorus Containing Water Dispersible Nanoparticles in Arable Soil. *J. Environ. Qual.* **2015**, *44*, 1772–1781. [\[CrossRef\]](#) [\[PubMed\]](#)
15. Ahmed, A.A.; Gypser, S.; Leinweber, P.; Freese, D.; Kühn, O. Infrared Spectroscopic Characterization of Phosphate Binding at the Goethite-Water Interface. *Phys. Chem. Chem. Phys.* **2019**, *21*, 4421–4434. [\[CrossRef\]](#) [\[PubMed\]](#)
16. Gypser, S.; Hirsch, F.; Schleicher, A.M.; Freese, D. Impact of Crystalline and Amorphous Iron- and Aluminum Hydroxides on Mechanisms of Phosphate Adsorption and Desorption. *J. Environ. Sci.* **2018**, *70*, 175–189. [\[CrossRef\]](#)
17. Sharpley, A.N.; Chapra, S.C.; Wedepohl, R.; Sims, J.T.; Daniel, T.C.; Reddy, K.R. Managing Agricultural Phosphorus for Protection of Surface Waters: Issues and Options. *J. Environ. Qual.* **1994**, *23*, 437–451. [\[CrossRef\]](#)
18. Holzmann, S.; Missong, A.; Puhlmann, H.; Siemens, J.; Bol, R.; Klumpp, E.; von Wilpert, K. Impact of Anthropogenic Induced Nitrogen Input and Liming on Phosphorus Leaching in Forest Soils. *J. Soil Sci. Plant Nutr.* **2015**, *179*, 443–453. [\[CrossRef\]](#)
19. Bol, R.; Julich, D.; Brödlin, D.; Siemens, J.; Kaiser, K.; Dippold, M.A.; Spielvogel, S.; Zilla, T.; Mewes, D.; von Blanckenburg, F.; et al. Dissolved and Colloidal Phosphorus Fluxes in Forest Ecosystems—An Almost Blind Spot in Ecosystem Research. *J. Soil Sci. Plant Nutr.* **2016**, *179*, 425–438. [\[CrossRef\]](#)
20. Boy, J.; Valarezo, C.; Wilcke, W. Water Flow Paths in Soil Control Element Exports in an Andean Tropical Montane Forest. *Eur. J. Soil Sci.* **2008**, *59*, 1209–1227. [\[CrossRef\]](#)
21. Newman, R.H.; Tate, K.R. Soil Phosphorus Characterisation by ³¹P Nuclear Magnetic Resonance. *Commun. Soil Sci. Plant Anal.* **1980**, *11*, 835–842. [\[CrossRef\]](#)
22. Tejedor-Tejedor, M.I.; Anderson, M.A. The Protonation of Phosphate on the Surface of Goethite as Studied by CIR-FTIR and Electrophoretic Mobility. *Langmuir* **1990**, *6*, 602–611. [\[CrossRef\]](#)
23. Turner, B.L.; Papházy, M.J.; Haygarth, P.M.; Mckelvie, I.D. Inositol Phosphates in the Environment. *Philos. Trans. R. Soc. B* **2002**, *357*, 449–469. [\[CrossRef\]](#) [\[PubMed\]](#)
24. Doolette, A.; Smernik, R.; Dougherty, W. Spiking Improved Solution Phosphorus ³¹P Nuclear Magnetic Resonance Identification of Soil Phosphorus Compounds. *Soil Sci. Soc. Am. J.* **2009**, *73*. [\[CrossRef\]](#)
25. Gerke, J. Phytate (Inositol Hexakisphosphate) in Soil and Phosphate Acquisition from Inositol Phosphates by Higher Plants: A Review. *Plants* **2015**, *4*, 253–266. [\[CrossRef\]](#)
26. Pant, H.K.; Warman, P.R.; Nowak, J. Identification of Soil Organic Phosphorus by ³¹P Nuclear Magnetic Resonance Spectroscopy. *Commun. Soil. Sci. Plant Anal.* **1999**, *30*, 757–772. [\[CrossRef\]](#)
27. Vincent, A.G.; Vestergren, J.; Gröbner, G.; Persson, P.; Schleucher, J.; Giesler, R. Soil Organic Phosphorus Transformations in a Boreal Forest Chronosequence. *Plant Soil* **2013**, *367*, 149–162. [\[CrossRef\]](#)
28. Missong, A.; Bol, R.; Willbold, S.; Siemens, J.; Klumpp, E. Phosphorous Forms in Forest Soil Colloids as Revealed by Liquid-State P-NMR. *J. Soil Sci. Plant Nutr.* **2016**, *179*, 159–167. [\[CrossRef\]](#)
29. Li, H.; Wan, B.; Yan, Y.; Zhang, Y.; Cheng, W.; Feng, X. Adsorption of Glycerophosphate on Goethite: A Macroscopic and Infrared Spectroscopic Study. *J. Soil Sci. Plant Nutr.* **2017**, *181*, 557–565. [\[CrossRef\]](#)
30. Johnson, B.B.; Quill, E.; Angove, M.J. An Investigation of the Mode of Sorption of Inositol Hexaphosphate to Goethite. *J. Colloid Interface Sci.* **2012**, *367*, 436–442. [\[CrossRef\]](#)
31. Celi, L.; M, P.; Marsan, F.A.; Barberis, E. Effects of pH and Electrolytes on Inositol Hexaphosphate Interaction with Goethite. *Soil Sci. Soc. Am. J.* **2001**, *65*, 753–760. [\[CrossRef\]](#)
32. Tsao, T.M.; Chen, Y.M.; Wang, M.K. Origin, Separation and Identification of Environmental Nanoparticles: A Review. *J. Environ. Monit.* **2011**, *13*, 1156–1163. [\[CrossRef\]](#)
33. Tan, K. *Principles of Soil Chemistry*, 4th ed.; Books in Soils, Plants, and the Environment; Taylor & Francis: Abingdon, UK, 2011.
34. Brady, N. *The Nature and Properties of Soils*, 15th ed.; Pearson Education Ltd.: Pearson, Harlow, UK, 2017.
35. Cornell, R.M.; Schwertmann, U. *The Iron Oxides: Structure, Properties Reactions Occurrence and Uses*; Wiley-VCH Verlag GmbH and Co. KGaA: Weinheim, Germany, 2003. [\[CrossRef\]](#)
36. Parfitt, R.L.; Atkinson, R.J. Phosphate Adsorption on Goethite (α -FeOOH). *Nature* **1976**, *264*, 740–742. [\[CrossRef\]](#)
37. Torrent, J.; Schwertmann, U.; Barron, V. Fast and Slow Phosphate Sorption by Goethite-Rich Natural Materials. *Clays Clay Miner.* **1992**, *40*, 14–21. [\[CrossRef\]](#)
38. Chitrakar, R.; Tezuka, S.; Sonoda, A.; Sakane, K.; Ooi, K.; Hirotsu, T. Phosphate Adsorption on Synthetic Goethite and Akaganeite. *J. Colloid Interface Sci.* **2006**, *298*, 602–608. [\[CrossRef\]](#)
39. Ahmed, A.A.; Gypser, S.; Freese, D.; Leinweber, P.; Kuehn, O. Molecular Level Picture of the Interplay between pH and Phosphate Binding at the Goethite–Water Interface. *Phys. Chem. Chem. Phys.* **2020**. [\[CrossRef\]](#) [\[PubMed\]](#)
40. Ognalaga, M.; Frossard, E.; Thomas, F. Glucose-1-Phosphate and Myo-Inositol Hexaphosphate Adsorption Mechanisms on Goethite. *Soil Sci. Soc. Am. J.* **1994**, *332*–337. [\[CrossRef\]](#)
41. Yan, Y.; Koopal, L.K.; Liu, F.; Huang, Q.; Feng, X. Desorption of Myo-Inositol Hexakisphosphate and Phosphate from Goethite by Different Reagents. *J. Plant. Nutr. Soil Sci.* **2015**, *178*, 878–887. [\[CrossRef\]](#)
42. Kubicki, J.D. (Ed.) *Molecular Modeling of Geochemical Reactions*; Wiley and Sons: Chichester, UK, 2016.

43. Persson, P.; Andersson, T.; Nelson, H.; Sjöberg, S.; Giesler, R.; Lövgren, L. Surface Complexes of Monomethyl Phosphate Stabilized by Hydrogen Bonding on Goethite (Alpha-FeOOH) Nanoparticles. *J. Colloid Interface Sci.* **2012**, *386*, 350–358. [CrossRef]
44. Kubicki, J.D.; Paul, K.W.; Kabalan, L.; Zhu, Q.; Mroziak, M.K.; Aryanpour, M.; Pierre-Louis, A.M.; Strongin, D.R. ATR-FTIR and Density Functional Theory Study of the Structures, Energetics, and Vibrational Spectra of Phosphate Adsorbed onto Goethite. *Langmuir* **2012**, *28*, 14573–14587. [CrossRef]
45. Guan, X.H.; Shang, C.; Zhu, J.; Chen, G.H. ATR-FTIR Investigation on the Complexation of Myo-Inositol Hexaphosphate with Aluminum Hydroxide. *J. Colloid Interface Sci.* **2006**, *293*, 296–302. [CrossRef] [PubMed]
46. Ahmed, A.A.; Leinweber, P.; Kühn, O. Unravelling the Nature of Glyphosate Binding to Goethite Surfaces by Ab Initio Molecular Dynamics Simulations. *Phys. Chem. Chem. Phys.* **2018**, *20*, 1531–1539. [CrossRef] [PubMed]
47. Ganta, P.B.; Kühn, O.; Ahmed, A.A. QM/MM Simulations of Organic Phosphorus Adsorption at the Diaspore–Water Interface. *Phys. Chem. Chem. Phys.* **2019**, *21*, 24316–24325. [CrossRef] [PubMed]
48. Ganta, P.B.; Kühn, O.; Ahmed, A.A. QM/MM Molecular Dynamics Investigation of the Binding of Organic Phosphates to the 100 Diaspore Surface. *Front. For. Glob. Chang.* **2020**, *3*, 71. [CrossRef]
49. Gerzabek, M.; Aquino, A.; Haberhauer, G.; Tunega, D.; Lischka, H. Molecular Modelling—Opportunities for Soil Research. *Bodenkultur* **2001**, *52*, 133–146.
50. Kwon, K.D.; Kubicki, J.D. Molecular Orbital Theory Study on Surface Complex Structures of Phosphates to Iron Hydroxides: Calculation of Vibrational Frequencies and Adsorption Energies. *Langmuir* **2004**, *20*, 9249–9254. [CrossRef]
51. Aquino, A.J.; Tunega, D.; Haberhauer, G.; Gerzabek, M.H.; Lischka, H. Acid–Base Properties of a Goethite Surface Model: A Theoretical View. *Geochim. Cosmochim. Acta* **2008**, *72*, 3587–3602. [CrossRef]
52. Strauss, R.; Brümmer, G.; BARROW, N. Effects of Crystallinity of Goethite: II. Rates of Sorption and Desorption of Phosphate. *Eur. J. Soil Sci.* **1997**, *48*, 101–114. [CrossRef]
53. Kosmulski, M. pH-Dependent Surface Charging and Points of Zero Charge. IV. Update and New Approach. *J. Colloid Interface Sci.* **2009**, *337*, 439–448. [CrossRef]
54. Senn, H.M.; Thiel, W. QM/MM Methods for Biomolecular Systems. *Angew. Chem.* **2009**, *48*, 1198–1229. [CrossRef]
55. Xiu, F.; Zhou, L.; Xia, S.; Yu, L. Adsorption Mechanism of Water Molecule on Goethite (010) Surface. *J. Ocean Univ. China* **2016**, *15*, 1021–1026. [CrossRef]
56. Guo, H.; Barnard, A.S. Thermodynamic Modelling of Nanomorphologies of Hematite and Goethite. *J. Mater. Chem.* **2011**, *21*, 11566–11577. [CrossRef]
57. Persson, P.; Nilsson, N.; Sjöberg, S. Structure and Bonding of Orthophosphate Ions at the Iron Oxide–Aqueous Interface. *J. Colloid Interface Sci.* **1996**, *177*, 263–275. [CrossRef]
58. Abdala, D.B.; Northrup, P.A.; Arai, Y.; Sparks, D.L. Surface Loading Effects on Orthophosphate Surface Complexation at the Goethite/Water Interface as Examined by Extended X-Ray Absorption Fine Structure (EXAFS) Spectroscopy. *J. Colloid Interface Sci.* **2015**, *437*, 297–303. [CrossRef]
59. Humphrey, W.; Dalke, A.; Schulten, K. VMD—Visual Molecular Dynamics. *J. Mol. Graph.* **1996**, *14*, 33–38. [CrossRef]
60. Groenhof, G. Introduction to QM/MM Simulations. In *Biomolecular Simulations: Methods and Protocols*; Monticelli, L., Salonen, E., Eds.; Humana Press: Totowa, NJ, USA, 2013; pp. 43–66. [CrossRef]
61. Ozboyaci, M.; Kokh, D.B.; Corni, S.; Wade, R.C. Modeling and Simulation of Protein–Surface Interactions: Achievements and Challenges. *Q. Rev. Biophys.* **2016**, *49*, e4. [CrossRef]
62. VandeVondele, J.; Krack, M.; Mohamed, F.; Parrinello, M.; Chassaing, T.; Hutter, J. Quickstep: Fast and Accurate Density Functional Calculations Using a Mixed Gaussian and Plane Waves Approach. *Comput. Phys. Commun.* **2005**, *167*, 103–128. [CrossRef]
63. Krack, M. Pseudopotentials for H to Kr Optimized for Gradient-Corrected Exchange–Correlation Functionals. *Theor. Chem. Acc.* **2005**, *114*, 145–152. [CrossRef]
64. VandeVondele, J.; Hutter, J. Gaussian Basis Sets for Accurate Calculations on Molecular Systems in Gas and Condensed Phases. *J. Chem. Phys.* **2007**, *127*. [CrossRef]
65. Perdew, J.P.; Burke, K.; Ernzerhof, M. Generalized Gradient Approximation Made Simple. *Phys. Rev. Lett.* **1996**, *77*, 3865–3868. [CrossRef]
66. Grimme, S.; Antony, J.; Ehrlich, S.; Krieg, H. A Consistent and Accurate Ab Initio Parametrization of Density Functional Dispersion Correction (DFT-D) for the 94 Elements H–Pu. *J. Phys. Chem.* **2010**, *132*. [CrossRef] [PubMed]
67. Mundy, C.J.; Balasubramanian, S.; Bagchi, K.; Hutter, J.; Kuo, A.S.I.; Laino, T.; VandeVondele, J. Frontiers in Simulation Technology (FIST). (accessed by CP2K, version 5.1). 2017. Available online: www.cp2k.org (accessed on 12 November 2020).
68. CP2K. Open Source Molecular Dynamics Code. version 5.1, Released October 24, 2017 (r18096). Available online: <http://www.cp2k.org> (accessed on 12 November 2020).
69. Kühne, T.D.; Iannuzzi, M.; Del Ben, M.; Rybkin, V.V.; Seewald, P.; Stein, F.; Laino, T.; Khaliullin, R.Z.; Schütt, O.; Schiffmann, F.; et al. CP2K: An electronic structure and molecular dynamics software package—Quickstep: Efficient and accurate electronic structure calculations. *J. Chem. Phys.* **2020**, *152*, 194103. [CrossRef]
70. Cygan, R.T.; Liang, J.J.; Kalinichev, A.G. Molecular Models of Hydroxide, Oxyhydroxide, and Clay Phases and the Development of a General Force Field. *J. Phys. Chem. B* **2004**, *108*, 1255–1266. [CrossRef]

-
71. Berendsen, H.J.C.; Grigera, J.R.; Straatsma, T.P. The Missing Term in Effective Pair Potentials. *J. Phys. Chem.* **1987**, *91*, 6269–6271. [[CrossRef](#)]
 72. Zoete, V.; Cuendet, M.A.; Grosdidier, A.; Michielin, O. SwissParam: A Fast Force Field Generation Tool for Small Organic Molecules. *J. Comput. Chem.* **2011**, *32*, 2359–2368. [[CrossRef](#)] [[PubMed](#)]
 73. Laino, T.; Mohamed, F.; Laio, A.; Parrinello, M. An Efficient Linear-Scaling Electrostatic Coupling for Treating Periodic Boundary Conditions in QM/MM Simulations. *J. Chem. Theory Comput.* **2006**, *2*, 1370–1378. [[CrossRef](#)] [[PubMed](#)]
 74. Bussi, G.; Donadio, D.; Parrinello, M. Canonical Sampling through Velocity Rescaling. *J. Chem. Phys.* **2007**. [[CrossRef](#)]
 75. Boys, S.F.; Bernardi, F. The Calculation of Small Molecular Interactions by the Differences of Separate Total Energies: Some Procedures with Reduced Errors. *Mol. Phys.* **1970**, *19*, 553–566. [[CrossRef](#)]
 76. Brehm, M.; Kirchner, B. TRAVIS—A Free Analyzer and Visualizer for Monte Carlo and Molecular Dynamics Trajectories. *J. Chem. Inf. Model.* **2011**, *51*, 2007–2023. [[CrossRef](#)]
 77. Thomas, M.; Brehm, M.; Fligg, R.; Vöhringer, P.; Kirchner, B. Computing Vibrational Spectra from Ab Initio Molecular Dynamics. *Phys. Chem. Chem. Phys.* **2013**, *15*, 6608–6622. [[CrossRef](#)]
 78. Thomas, M.; Brehm, M.; Kirchner, B. Voronoi Dipole Moments for the Simulation of Bulk Phase Vibrational Spectra. *Phys. Chem. Chem. Phys.* **2015**, *17*, 3207–3213. [[CrossRef](#)] [[PubMed](#)]
 79. Brehm, M.; Thomas, M. An Efficient Lossless Compression Algorithm for Trajectories of Atom Positions and Volumetric Data. *J. Chem. Inf. Model.* **2018**, *58*, 2092–2107. [[CrossRef](#)] [[PubMed](#)]
 80. Lü, C.; Yan, D.; He, J.; Zhou, B.; Li, L.; Zheng, Q. Environmental Geochemistry Significance of Organic Phosphorus: An Insight from Its Adsorption on Iron Oxides. *J. Appl. Geochem.* **2017**, *84*, 52–60. [[CrossRef](#)]
 81. Sheals, J.; Sjöberg, S.; Persson, P. Adsorption of Glyphosate on Goethite: Molecular Characterization of Surface Complexes. *Environ. Sci. Technol.* **2002**, *36*, 3090–3095. [[CrossRef](#)]
 82. Rose, J.; Flank, A.M.; Mason, A.; Bottero, J.Y.; Elmerich, P. Nucleation and Growth Mechanisms of Fe Oxyhydroxide in the Presence of PO₄ Ions. 2. P K-Edge EXAFS Study. *Langmuir* **1997**, *13*, 1827–1834. [[CrossRef](#)]
 83. Tribe, L.; Kwon, K.D.; Trout, C.C.; Kubicki, J.D. Molecular Orbital Theory Study on Surface Complex Structures of Glyphosate on Goethite: Calculation of Vibrational Frequencies. *Environ. Sci. Technol.* **2006**, *40*, 3836–3841. [[CrossRef](#)]
 84. Anderson, G.; Arlidge, E.Z. The Adsorption of Inositol Phosphates and Glycerophosphate by Soil Clays, Clay Minerals, and Hydrated Sesquioxides in Acid Media. *J. Soil Sci.* **1962**, *13*, 216–224. [[CrossRef](#)]
 85. Celi, L.; Lamacchia, S.; Marsan, F.A.; Barberis, E. Interaction of Inositol Hexaphosphate on Clays: Adsorption and Charging Phenomena. *Soil Sci.* **1999**, *164*, 574–585. [[CrossRef](#)]
 86. Colthup, N.B.; Daly, L.H.; Wiberley, S.E. Compounds Containing Boron, Silicon, Phosphorus, Sulfur, or Halogen. In *Introduction to Infrared and Raman Spectroscopy*, 3rd ed.; Colthup, N.B., Daly, L.H., Wiberley, S.E., Eds.; Academic Press: San Diego, CA, USA, 1990; Chapter 12, pp. 355–385. [[CrossRef](#)]
 87. Olsson, R.; Giesler, R.; Loring, J.S.; Persson, P. Adsorption, Desorption, and Surface-Promoted Hydrolysis of Glucose-1-Phosphate in Aqueous Goethite (Alpha-FeO_{OH}) Suspensions. *Langmuir* **2010**, *26*, 18760–18770. [[CrossRef](#)]
 88. Del Bene, J.E.; Jordan, M.J.T. Vibrational Spectroscopy of the Hydrogen Bond: An Ab Initio Quantum-Chemical Perspective. *Null* **1999**, *18*, 119–162. [[CrossRef](#)]
 89. Fornaro, T.; Burini, D.; Biczysko, M.; Barone, V. Hydrogen-Bonding Effects on Infrared Spectra from Anharmonic Computations: Uracil–Water Complexes and Uracil Dimers. *J. Phys. Chem. A* **2015**, *119*, 4224–4236. [[CrossRef](#)]
 90. Arai, Y.; Sparks, D. ATR-FTIR Spectroscopic Investigation on Phosphate Adsorption Mechanisms at the Ferrihydrite–Water Interface. *J. Colloid Interface Sci.* **2001**, *241*, 317–326. [[CrossRef](#)]
 91. Lincoln, S.; Stranks, D. Phosphato Complexes of Cobalt(III). I. General Structural and Hydrolytic Properties. *Aust. J. Chem.* **1968**, *21*, 37–56. [[CrossRef](#)]
 92. Nakagawa, H.; Oyama, T. Molecular Basis of Water Activity in Glycerol–Water Mixtures. *Front. Chem.* **2019**, *7*, 731. [[CrossRef](#)]
 93. Kataoka, Y.; Kitadai, N.; Hisatomi, O.; Nakashima, S. Nature of Hydrogen Bonding of Water Molecules in Aqueous Solutions of Glycerol by Attenuated Total Reflection (ATR) Infrared Spectroscopy. *Appl. Spectrosc.* **2011**, *65*, 436–441. [[CrossRef](#)] [[PubMed](#)]
 94. Yan, Y.; Wan, B.; Zhang, Y.; Zhang, L.; Liu, F.; Feng, X. In Situ ATR-FTIR Spectroscopic Study of the Co-Adsorption of Myo-Inositol Hexakisphosphate and Zn(II) on Goethite. *Soil Res.* **2018**, *56*, 526–534. [[CrossRef](#)]
 95. Peak Fit v4. *Peak Separation and Analysis Software*; SPSS Science, Inc.: Chicago, IL, USA, 2003.
 96. FAO. FAO’s Director-General on How to Feed the World in 2050. *Popul. Dev. Rev.* **2009**, *35*, 837–839. [[CrossRef](#)]
 97. De Groot, C.J.; Golterman, H.L. On the Presence of Organic Phosphate in Some Camargue Sediments: Evidence for the Importance of Phytate. *Hydrobiologia* **1993**, *252*, 117–126. [[CrossRef](#)]

Supplementary Information:
Ab Initio Molecular Dynamics Simulations of the Interaction between Organic Phosphates and Goethite

Prasanth B. Ganta,^a Oliver Kühn,^{a,b} and Ashour A. Ahmed,^{a,b*}

^aUniversity of Rostock, Institute of Physics, Albert-Einstein-Str. 23-24, D-18059 Rostock, Germany

^bUniversity of Rostock, Department of Life, Light, and Matter (LLM), Albert-Einstein-Str. 25, D-18059 Rostock, Germany

* corresponding author

prasanth.ganta@uni-rostock.de

oliver.kuehn@uni-rostock.de

ashour.ahmed@uni-rostock.de

FIGURES

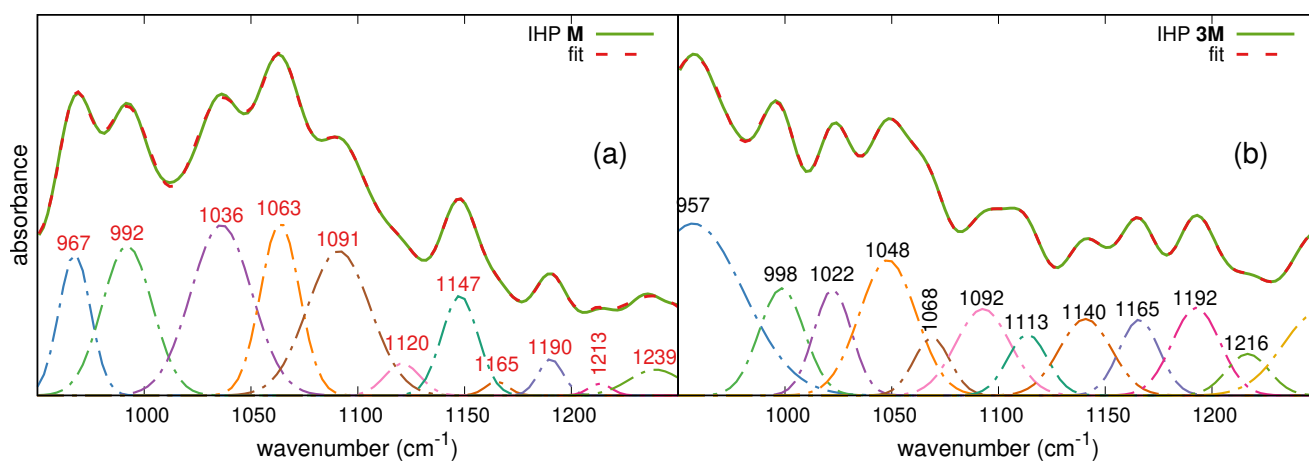


Figure S1: Fitted IR spectra of IHP bonded through **M** (a) and **3M** motifs (b).

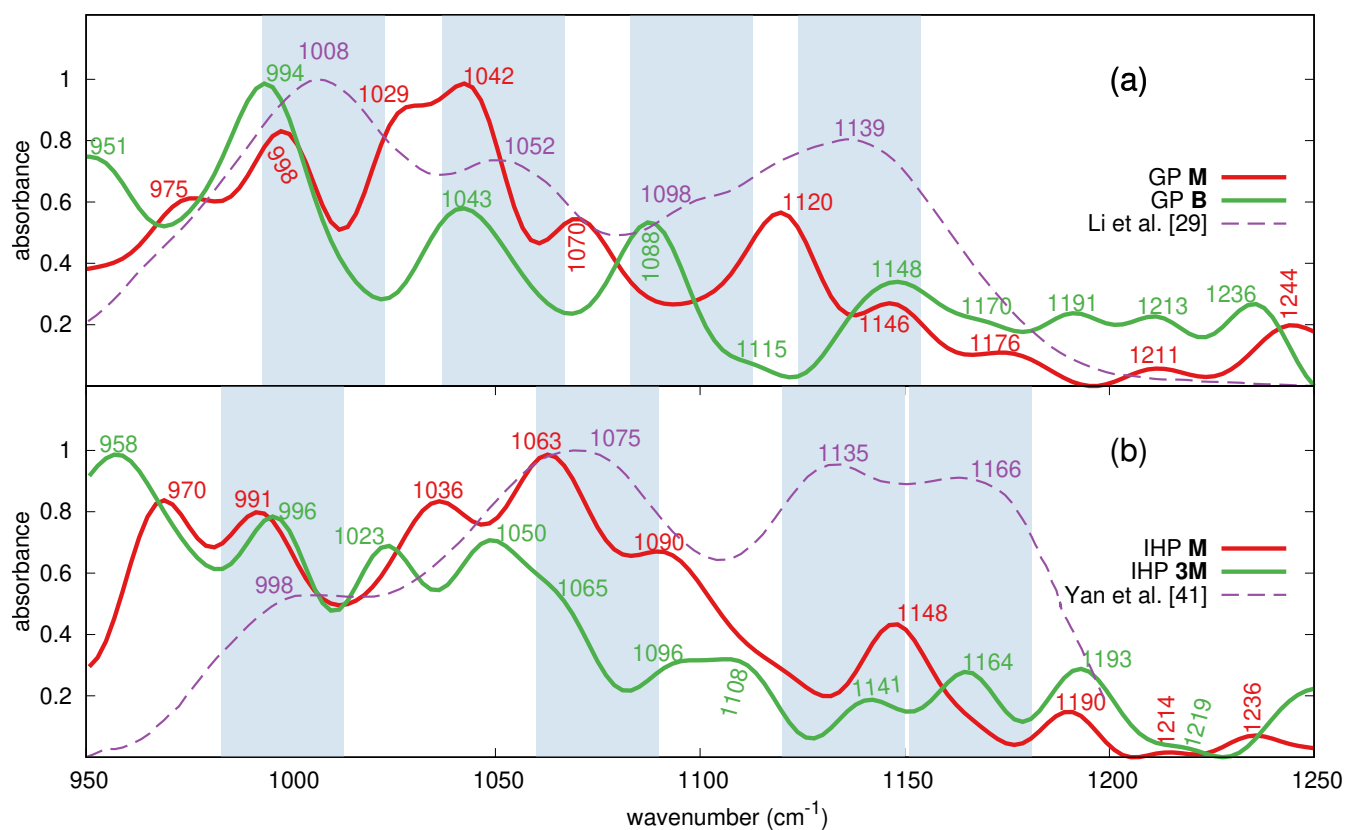


Figure S2: Comparison of GP and IHP spectra with experimental spectra from Li *et al.* [29] and Yan *et al.* [41] studies, respectively. The blue rectangle denotes region within $\pm 15 \text{ cm}^{-1}$ around frequencies observed in experimental studies.

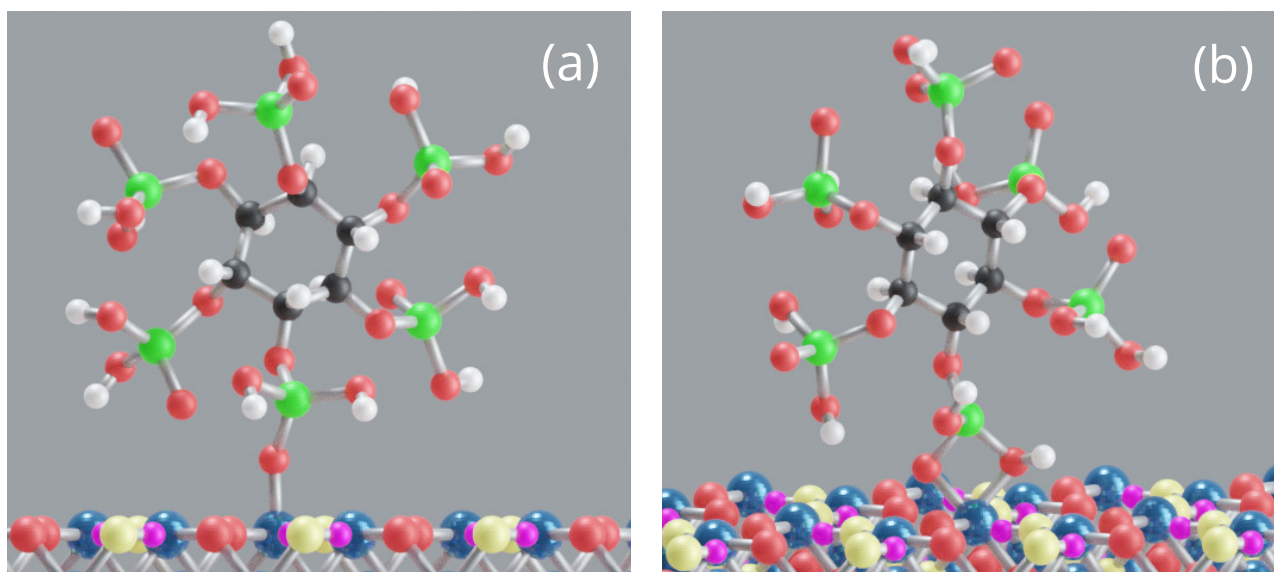


Figure S3: Initial motifs of IHP: **M** motif (a), **B** motif (b).

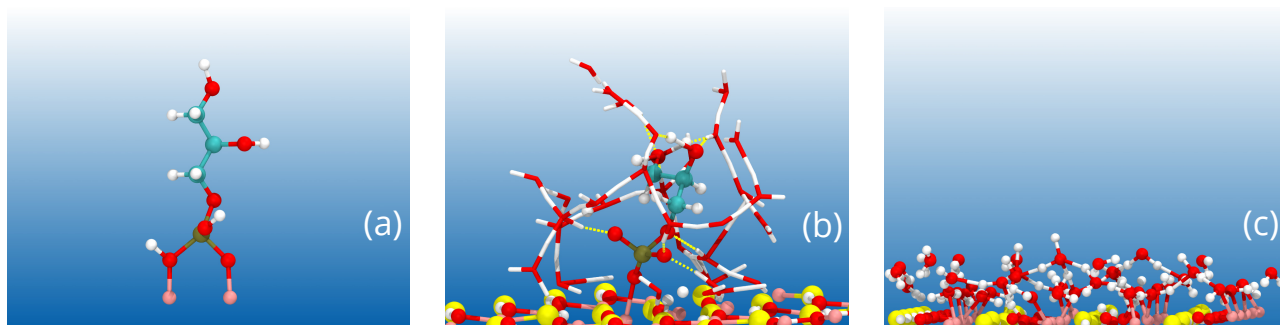


Figure S4: GP **BB** motif (a), HBs (yellow dotted lines) between GP and surrounding water (b), water bonded to surface Fe atoms (c). Pink, red, yellow, white and lime colors correspond to iron, oxygen, hydroxyl oxygen, hydrogen and phosphorus, respectively.

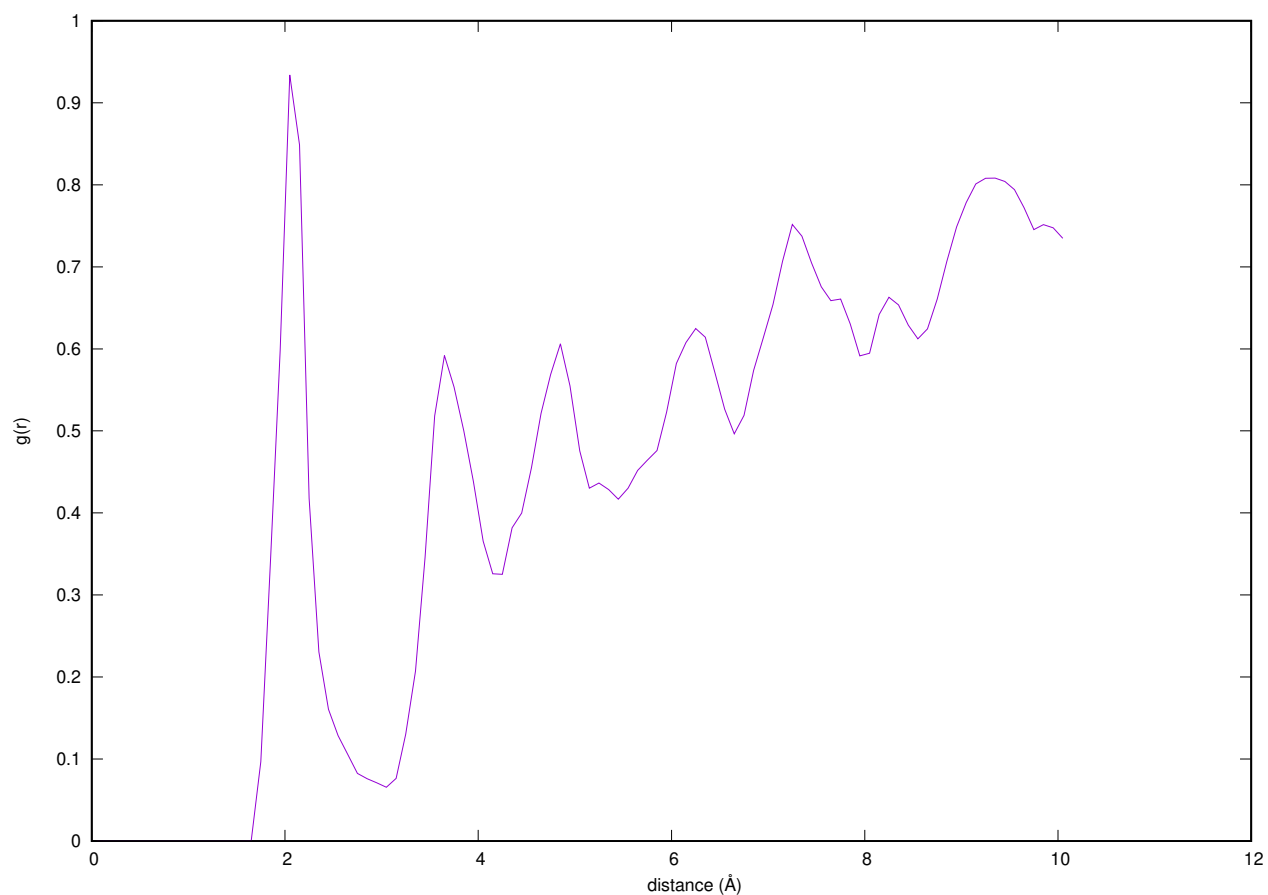


Figure S5: Pair correlation function calculated for surface Fe atoms of goethite and oxygens of water observed for GP **M** motif case.

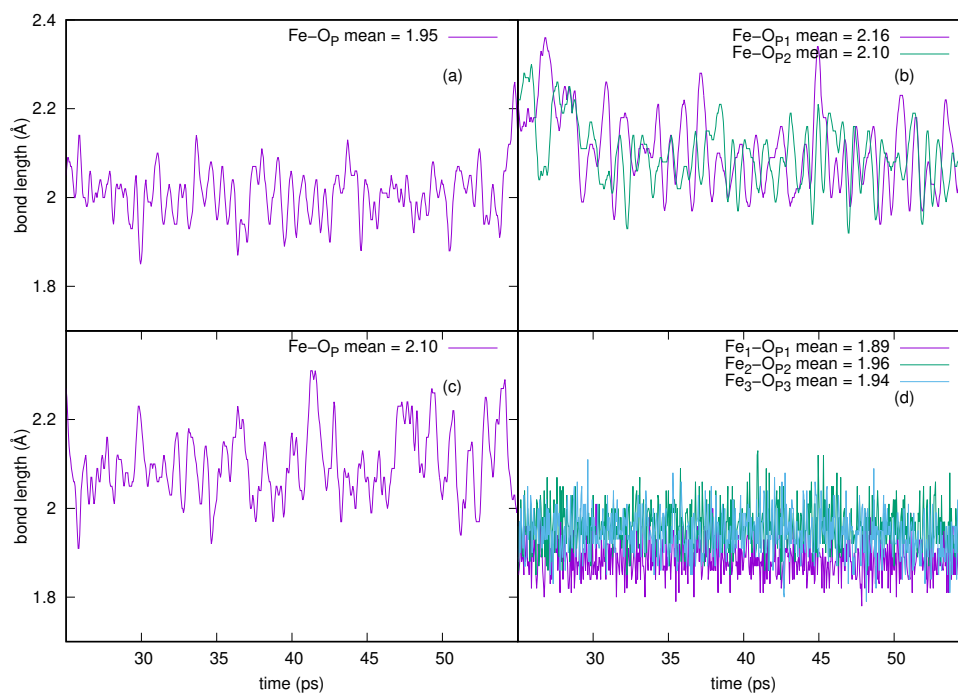


Figure S6: Covalent bond lengths of Fe-OP bonds for GP **M**(Fe-OP) and **B**(Fe-OP₁, Fe-OP₂) motifs (a,b) and IHP **M**(Fe-OP) and **3M**(Fe-OP₁, Fe-OP₂, Fe-OP₃) motifs (c,d) between 25–55 ps.

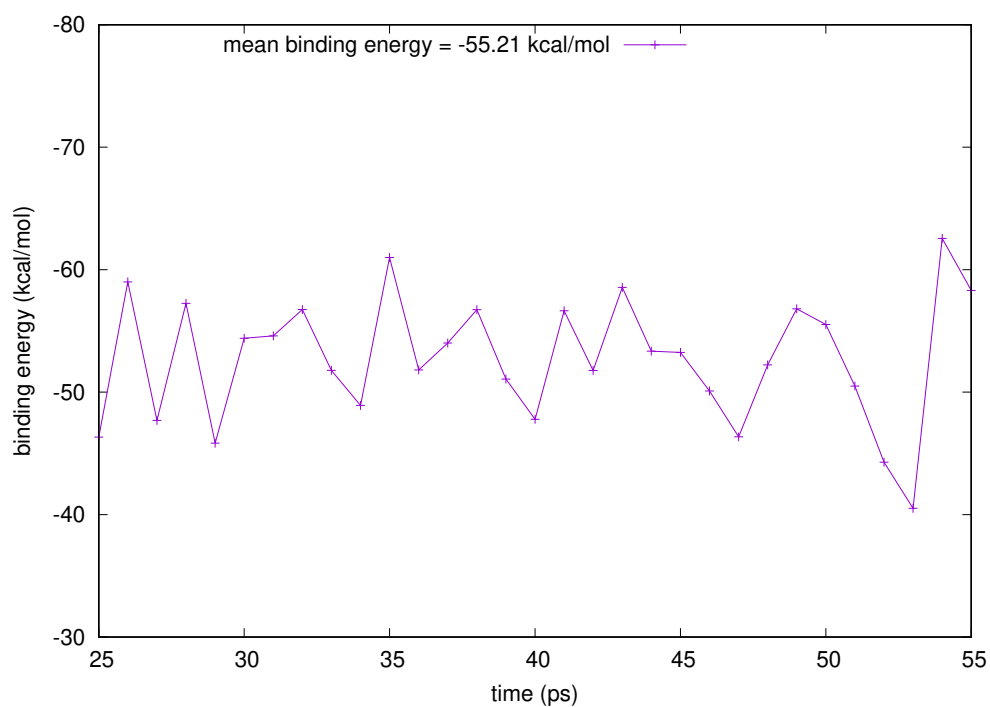


Figure S7: Binding energies along the simulation trajectory of IHP **M** motif in the time range of 25–50 ps.

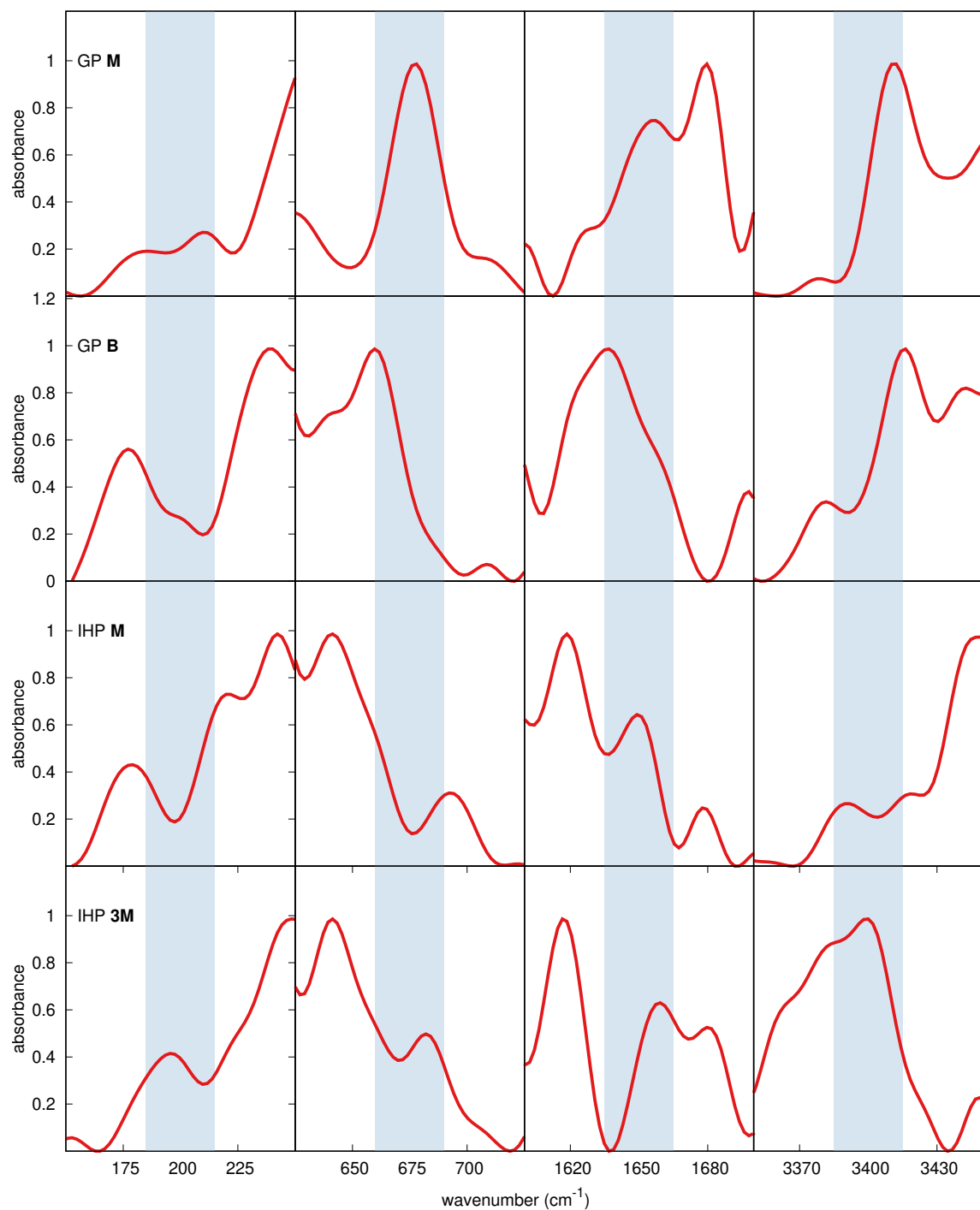


Figure S8: IR spectra of GP **M** and **B** motif cases (first and second rows) and IHP **M** and **3M** motif cases (third and fourth rows) for a selected frequency ranges. Brubach et al. [S1] showed that bands at 200, 675, 1650 and 3400 cm^{-1} are characteristic to water IR spectra and assigned the first two bands to hydrogen movement in intermolecular HBs and the last two to intramolecular [H–O–H] bending and [O–H] stretching modes. A similar assignment for [H–O–H] bending and [O–H] stretching modes is also observed in studies by Libnau et al. [S2] and Maréchal [S3]. The blue rectangle denotes a region within $\pm 15 \text{ cm}^{-1}$ around frequencies 200, 675, 1650 and 3400 cm^{-1} . The overall picture shows that peaks in selected frequency ranges of the calculated IR spectra match mostly with the peaks from the literature [S3, S2, S1].

References

- [S1] J.-B. Brubach, A. Mermet, A. Filabozzi, A. Gerschel, P. Roy, Signatures of the hydrogen bonding in the infrared bands of water, *J. Chem. Phys.* 122 (2005) 184509.
- [S2] F. O. Libnau, O. M. Kvalheim, A. A. Christy, J. Toft, Spectra of water in the near- and mid-infrared region, *Vibrational Spectroscopy* 7 (1994) 243–254.
- [S3] Y. Maréchal, Infrared spectra of water. I. Effect of temperature and of H/D isotopic dilution, *J. Chem. Phys.* 95 (1991) 5565–5573.

Article

The Binding of Phosphorus Species at Goethite: A Joint Experimental and Theoretical Study

Prasanth B. Ganta ¹ , Mohsen Morshedizad ², Oliver Kühn ^{1,3} , Peter Leinweber ^{2,3} and Ashour A. Ahmed ^{1,3,*} 

¹ Institute of Physics, University of Rostock, Albert-Einstein-Str. 23–24, D-18059 Rostock, Germany; prasanth.ganta@uni-rostock.de (P.B.G.); oliver.kuehn@uni-rostock.de (O.K.)

² Chair of Soil Science, University of Rostock, Justus-von-Liebig-Weg 6, D-18059 Rostock, Germany; mohsen.morshedizad3@uni-rostock.de (M.M.); peter.leinweber@uni-rostock.de (P.L.)

³ Department of Life, Light, and Matter (LLM), University of Rostock, Albert-Einstein-Str. 25, D-18059 Rostock, Germany

* Correspondence: ashour.ahmed@uni-rostock.de; Tel.: +49-381-498-6943

Abstract: Knowledge of the interaction between inorganic and organic phosphates with soil minerals is vital for improving soil P-fertility. To achieve an in-depth understanding, we combined adsorption experiments and hybrid ab initio molecular dynamics simulations to analyze the adsorption of common phosphates, i.e., orthophosphate (OP), glycerolphosphate (GP) and inositolhexaphosphate (IHP), onto the 100 surface plane of goethite. Experimental adsorption data per mol P-molecule basis fitted to the Freundlich model show the adsorption strength increases in the order GP < OP < IHP, and IHP adsorption being saturated faster followed by GP and OP. Modeling results show that OP and GP form stable monodentate (**M**) and binuclear bidentate (**B**) motifs, with **B** being more stable than **M**, whereas IHP forms stable **M** and **3M** motifs. Interfacial water plays an important role through hydrogen bonds and proton transfers with OP/GP/IHP and goethite. It also controls the binding motifs of phosphates with goethite. Combining both experimental and modeling results, we propose that the **B** motif dominates for OP, whereas GP forms **M** and IHP forms a combination of **M** and **3M** motifs. The joint approach plausibly explains why IHP is the predominant organically bound P form in soil. This study could be considered as a preliminary step for further studies for understanding the mechanisms of how microbes and plants overcome strong IHP–mineral binding to implement the phosphate groups into their metabolism.

Keywords: P-fertility; orthophosphate; glycerolphosphate; inositolhexaphosphate; goethite; adsorption; surface complexation; MD simulations; QMMM



Citation: Ganta, P.B.; Morshedizad, M.; Kühn, O.; Leinweber, P.; Ahmed, A.A. The Binding of Phosphorus Species at Goethite: A Joint Experimental and Theoretical Study. *Minerals* **2021**, *11*, 323. <https://doi.org/10.3390/min11030323>

Academic Editors: Daniel Tunega, Edgar Galicia-Andrés and Peter Grancic

Received: 4 February 2021

Accepted: 16 March 2021

Published: 20 March 2021

Publisher's Note: MDPI stays neutral with regard to jurisdictional claims in published maps and institutional affiliations.



Copyright: © 2021 by the authors. Licensee MDPI, Basel, Switzerland. This article is an open access article distributed under the terms and conditions of the Creative Commons Attribution (CC BY) license (<https://creativecommons.org/licenses/by/4.0/>).

1. Introduction

The phosphorus (P) adsorption capacity of soil is a crucial factor affecting the P-immobilization process and thus soil fertility, and fate of P in natural environments [1–4]. This adsorption capacity, defined as the amount of adsorbed substance (adsorbate), reached in a saturated solution for a specific adsorbent [5], is fundamentally influenced by the diverse interactions of P with soil constituents, involving free metal ions [6,7], soil minerals [8–11], and soil organic matter [12,13]. In particular, the strong interaction between phosphates and soil mineral surfaces, and especially Fe- and Al-(oxyhydr)oxides, plays a very important role in controlling this process [8,14–18]. The Fe-oxides are widespread in surface environments and constitute a major component of highly weathered soils and sediments. They have attracted considerable attention due to their high P-adsorption capacity [19–21]. Phosphate adsorption on iron oxide surfaces shows a biphasic behavior consisting of a rapid and strong ligand exchange step followed by a slower step [22–25]. The latter phase was described previously by the formation of monodentate (**M**) complexes and conversion into bidentate (**B**) complexes, the competition with other anions, and/or

precipitation events [26]. Alternatively, the slower phase has been assigned to a diffusion process of phosphate ions from an outer-sphere complex to the surface [16,23,27,28].

The extent of P-uptake during these processes depends on reactive surface groups and the degree of crystallinity or porosity of iron oxides [27,29]. In soils, sediments and natural environments, goethite is the most frequent and widespread form of iron oxyhydroxides [30]. It has high crystallinity with a specific surface area varying from 18 to 132 m² g^{−1} [27,31] depending on synthesis conditions which may thus influence the P-adsorption capacity of minerals [32]. Goethite has been studied extensively since it is considered as one of the most reactive surfaces for P compounds in the environment [33]. However, conflicting discussions are still present about the nature of binding motifs of the adsorbed phosphate species and the relative abundance of **M** complexes [34,35] versus **B** ones [36,37]. This could be due to the presence of different surface planes for goethite and several binding motifs for the goethite–phosphate complexes in addition to the different setups and conditions of adsorption experiments reported in literature. Consequently, different opinions have been put forward to assign the goethite–phosphate binding motifs based on infrared (IR) spectroscopy. This involves assignment either by the positions of P–O vibrational bands [36], the number of P–O bands and not their exact position [15], or formation of only an **M** motif with different protonation states depending on pH [38]. Molecular modeling is considered as a powerful tool to resolve such conflicting discussions by providing a molecular level description for the nature of the formed goethite–phosphate complexes.

By using molecular modeling, Kwon and Kubicki [39] studied the binding process of phosphate at goethite and suggested the abundance of the diprotonated **B** complex at pH 4–6 and the deprotonated **B** or monoprotonated **M** complex at pH 7.5–7.9. In a further study [40], they predicted the formation of **M** complexes at the 001, 210, 101, and 100 surface planes and **B** complexes at the 010, 101, and 100 surface planes. Recently, we have simulated the binding mechanism of phosphate at the goethite water interface at about pH 6, considering two different goethite surface planes [10]. The outcome of this study pointed to the abundance of the monoprotonated **B** motif at the goethite–water interface and the importance of water in controlling this binding process via promoting of specific binding motifs, formation of H-bonds (HBs), adsorption and dissociation at the surface, and proton transfer processes. Furthermore, the assignment of calculated IR spectra in this study introduced a new approach for characterizing experimental IR data of adsorbed phosphate species. Investigations at a molecular level for the binding of other P-compounds to soil reactive surfaces have also been reported. For example, the mechanism, nature, strength, and different possible binding motifs of interaction of glyphosate, the most used herbicide, with goethite, as well as with representative models for soil organic matter, have been explored [9]. Moreover, we studied the interaction of organic phosphate such as glycerolphosphate (GP) and inositolphosphate (IHP) at the diaspor(α -AlOOH)–water interface by focusing on two diaspor surface planes [11,41]. The results revealed stronger interactions for both GP and IHP at the 010 diaspor surface plane compared to the 100 surface plane. Further, IHP binds stronger to both surfaces via three phosphate groups compared to GP.

Such a detailed atomistic investigation for the binding mechanisms of both inorganic and organic phosphates at the goethite–water interface is still lacking. Therefore, our objective in the present study is to introduce a molecular level understanding for the binding mechanism of phosphate at the goethite–water interface via a joint experimental/theoretical approach. Specifically, adsorption experiments have been performed for orthophosphate (OP), GP, and IHP on the pure synthetic goethite surface at constant pH and ionic strength. Further, the simulation of these adsorption experiments have been carried out by molecular modeling for the binding processes of OP/GP/IHP at the goethite–water interface, applying hybrid quantum mechanics/molecular mechanics (QM/MM)-based molecular dynamics (MD) simulations.

2. Materials and Methods

2.1. Goethite Preparation and Adsorption Experiments

Goethite was prepared as described by Dultz et al. [42], i.e., a 10 M NaOH solution was added to a 0.5 M FeCl₃ solution (FeCl₃ · 6H₂O, Merck AG) with stirring continuously to bring the pH to 12. The resulting ferrihydrite was aged for 120 h at 55 °C to be converted to goethite. Then, the suspension was subjected to pH adjustment to pH 6 by adding 0.1 M HCl and followed by centrifugation-washing cycles with distilled water until the electrical conductivity was lower than 10 µS cm^{−1}. The so-prepared goethite was freeze-dried and stored as powder for further analysis and experiments.

The results of X-ray diffraction (XRD) analysis confirmed the well-crystallinity of goethite samples; see Figure S1. The measured specific surface area (SAA) of goethite by Brunauer-Emmett-Teller (BET, N₂ adsorption; Nova 4000e, Quantachrome, Boynton Beach, FL, USA) method is 64.5 m² g^{−1}. This value lies in the reported common range values of SSA of goethite in the literature [27,33,43]. It should be noted that different SSA values of goethite were reported in the literature. This could be due to the sensitivity of the BET method to the type of adsorbent, lack of an appropriate linearity criterion (a linear region within the standard pressure range assuming that monolayer adsorption will occur in this pressure range), and presence of micro pores [44]. The mean hydrodynamic diameter of goethite particles is 1.6 ± 0.2 µm as determined by a particle sizer (Zetapals, Brookhaven, Holtsville, NY, USA) on a 100 mgL^{−1} suspension treated with a dispersant agent (0.01 mM Na₄P₂O₇, pH 8) and sonicated for 30 s (Labsonic M, Sartorius Stedim, Göttingen, Germany). The measured point of zero charge (PZC) of goethite particles is 6.3; see Figure S2.

In the present study, the adsorption of three different phosphate compounds involving inorganic orthophosphate (OP, potassium dihydrogen phosphate, CAS number: 7778-77-0) and organic phosphates (α-glycerol phosphate (GP, CAS number: 17603-42-8) and myo-inositol hexakisphosphate (IHP, CAS number: 83-86-3)) on goethite was performed. Here, a stock solution of 10 mM P of each P compound was prepared in 0.01 M CaCl₂ solution. For each experiment, 200 mg sample of goethite was weighed into a 50 mL centrifuge tube and equilibrated with 40 mL of each initial P concentration. Here, twelve different initial P concentrations (0, 0.05, 0.1, 0.15, 0.2, 0.3, 0.5, 1, 2, 3, 5, and 10 mM P) were considered. Each initial concentration was prepared by the dilution of the P stock in 0.01 M CaCl₂ background electrolyte solution, adjusted at pH 5. After an equilibrium period of 24 h at 25 °C under end-over-end shaking at 20 rpm, samples were centrifuged at 4500 g for 15 min. The P content in the filtered supernatant was quantified by inductively coupled plasma-optical emission spectroscopy (ICP-OES) method.

It is noteworthy that all adsorption experiments were performed in triplicate and data were presented as the means of three repeats. Moreover, all used P compounds (myo-inositol hexakisphosphate: C₆H₁₈O₂₄P₆; α-glycerol phosphate: C₃H₉O₆P; potassium dihydrogen phosphate: KH₂PO₄) in the present experiments were of analytical grade chemicals and purchased from Carl Roth GmbH and Sigma-Aldrich. Working solutions were prepared fresh daily by adding accurate quantities of the prepared P stocks into 0.01 M CaCl₂ solution.

To describe the adsorption behaviors of P compounds on goethite, the adsorption data were fitted to the Freundlich [45], Langmuir [46], and Temkin [47] models. The Freundlich model provides a two-parameter equation that describes the relationship between the equilibrium concentration and the adsorbed one onto heterogeneous surfaces through the following equation:

$$Q_{ads} = K_f C_e^{n_f} \quad (1)$$

that is rewritten in a linear form as follows:

$$\ln Q_{ads} = \ln K_f + n_f \ln C_e \quad (2)$$

where Q_{ads} is the amount of adsorbate adsorbed per unit mass (or surface area) of adsorbent, C_e is the adsorbate equilibrium concentration in solution, K_f is Freundlich adsorption

constant (sometimes it is defined as Freundlich unit adsorption capacity), and n_f is the non-linearity exponent (Freundlich exponent) [45]. In the present study, Q_{ads} , C_e , and K_f are expressed in $\mu\text{mol m}^{-2}$, $\mu\text{mol L}^{-1}$ and $\mu\text{mol}^{1-n_f} \text{L}^{n_f} \text{m}^{-2}$, respectively. Notice that the Freundlich model assumes that the adsorption enthalpy depends on the amount of adsorbate. In the limit of small Q_{ads} where the adsorption enthalpy should not depend on Q_{ads} one could describe the isotherm by a Langmuir model as well. The Langmuir adsorption theory assumes that the adsorbate forms a monolayer on a homogeneous adsorbent surface. The following equation expresses the Langmuir isotherm:

$$Q_{ads} = Q_{max} \frac{K_l C_e}{1 + K_l C_e} \quad (3)$$

that is rewritten in a linear form as follows:

$$\frac{C_e}{Q_{ads}} = \frac{C_e}{Q_{max}} + \frac{1}{K_l Q_{max}} \quad (4)$$

where Q_{max} is the maximum amount of the adsorbate which is required to form a monolayer by complete saturation of all binding sites (it is defined also as the maximum monolayer coverage capacity or simply as monolayer capacity [5], $\mu\text{mol m}^{-2}$), K_l is the Langmuir adsorption constant ($\text{L } \mu\text{mol}^{-1}$), which is mainly related to the adsorption energy [46]. The Temkin model exhibits a factor considering the adsorbent–adsorbate interaction with a uniform distribution of binding energies. The model is expressed by the following equation:

$$Q_{ads} = \frac{RT}{b_T} \ln A_T + \frac{RT}{b_T} \ln C_e = B_T \ln A_T + B_T \ln C_e \quad (5)$$

where R is the universal gas constant ($8.314 \text{ J K mol}^{-1}$), T is the absolute temperature (K), b_T is Temkin isotherm constant (J mol^{-1}), A_T is Temkin isotherm equilibrium binding constant ($\text{L } \mu\text{mol}^{-1}$), and B_T is constant related to the heat of adsorption. It is important to mention that our adsorption isotherm data were fitted by two ways. The first way is based on the normal linearization technique while the second way is based on non-linear equations solver function that was described by Bolster and Hornberger [48]. Fitted parameters obtained by both ways were compared to each other and the best fit parameters were selected based on error measures. Non-linear equations solver was found to be more appropriate compared to the linearization technique, and thus the corresponding parameters were selected and presented in the present contribution. For better understanding for the P adsorption behavior, the calculated adsorption coefficients are interpreted on three different bases (per mol P (i.e., per mole of P element), per mol molecule (i.e., per mole of P-containing molecule (OP, GP, and IHP)), and per mass (i.e., per mass (mg) of P-containing molecule)).

2.2. Molecular Modeling and Computational Details

The current molecular modeling approach for the binding process of phosphates at the goethite–water interface is illustrated in Figure 1. Here, three different abundant phosphates are considered, i.e., OP (H_3PO_4), GP ($\text{C}_3\text{H}_9\text{O}_6\text{P}$), and IHP ($\text{C}_6\text{H}_{18}\text{O}_{24}\text{P}_6$), to study the complexation reaction of each phosphate with the goethite surface in the presence of water (see Figure 1a–c). Each constructed goethite–phosphate–water complex model (for example, see Figure 1d), consists of 1– the goethite surface, 2– a phosphate compound with a specific binding motif to the surface, and 3– water molecules surrounding the goethite–phosphate complex. Here, the 100 goethite surface is considered, which is one of the most abundant goethite surface planes in soil systems [33,49]. This goethite surface plane is modeled by the repetition of the goethite unit cell (lattice constants: $a = 9.95$, $b = 3.01$, $c = 4.62 \text{ Å}$) as $1a \times 8b \times 5c$ which consists of 640 atoms (160 Fe, 160 H, and 320 O atoms). The binding motifs formed between these phosphates and the goethite surface are modeled based on previous literature studies [9–11,41,50–52]. The initial motifs of OP and GP with the

goethite surface include monodentate (**M**, 1Fe + 1O one covalent bond between phosphate non-protonated O atom and a surface Fe atom) and bidentate (**B**, 2Fe + 2O i.e., two covalent bonds between two phosphate O atoms, one protonated and other non-protonated and two surface Fe atoms); see Figure 1e,f. For IHP, an additional, **4M** (4Fe + 4O i.e., four covalent bonds between four separate phosphates non-protonated oxygens and four surface Fe atoms) are considered since IHP is known to interact with goethite through multiple phosphate groups, see Figure 1g. To simulate the effect of water on the goethite–OP/GP/IHP complexes, each modeled binding motif is solvated with water molecules at a density of $\approx 1 \text{ g cm}^{-3}$ perpendicular to the studied surface plane with height of $\approx 18 \text{ Å}$ by using the visual molecular dynamics (VMD) package (see Figure 1d) [53]. To ease the discussion about the interactions, oxygen atoms bonded to surface Fe atoms are denoted as O_p .

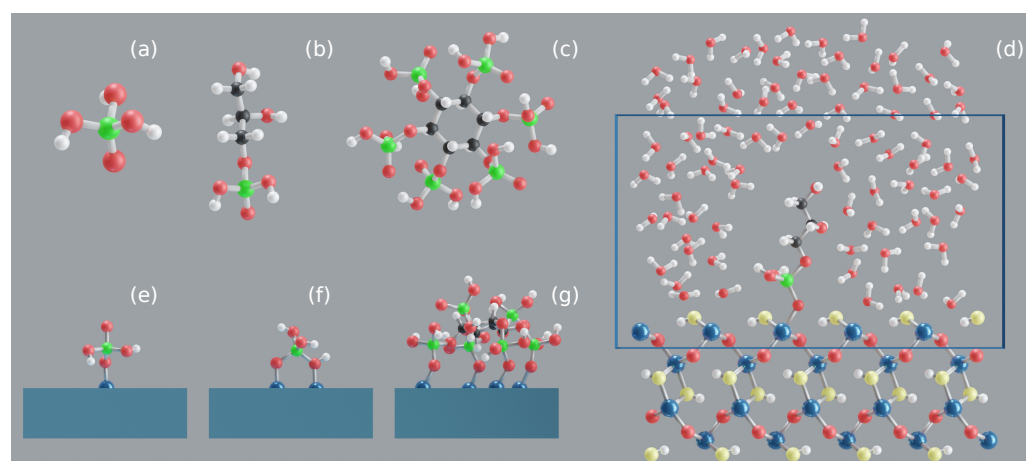


Figure 1. OP (a), GP (b), IHP (c), solvated goethite–GP complex highlighting QM box (d), goethite–OP **M** motif (e) and **B** motif (f), goethite–IHP **4M** motif (g). Blue, red, yellow, white, black and green colors correspond to iron, oxygen, hydroxyl oxygen, hydrogen, carbon and phosphorus atoms, respectively.

Due to the large size for the modeled goethite–OP/GP/IHP–water complexes (each model consists of more than 1200 atoms), the simulation of these systems with pure ab initio methods is computationally expensive and thus not feasible [54,55]. Therefore, the present models will be studied by molecular dynamics (MD) simulations based on the electrostatic embedding QM/MM hybrid approach. It should be noted that the present QM/MM approach has been validated for studying the P binding process at mineral/water interfaces. Specifically, this was achieved in two recent studies by comparing outcome of the QM/MM approach with corresponding results from pure DFT calculations [11] as well as experimental IR spectra [52]. Here, the reactive part (system of interest) is described at a QM level of theory, while the remaining part is described using MM. The QM part includes 1– OP/GP/IHP, 2– the goethite top surface layer (160 atoms), and 3– water molecules within a layer of about 10 perpendicular to the surface (≈ 55 molecules). The total QM box size is $22 \times 8b \times 5c$, i.e., $22 \times 24.08 \times 23.1 \text{ Å}$. The QM part is simulated with density functional theory (DFT) as implemented in the quickstep code in CP2K [56]. A hybrid Gaussian and plane wave (GPW) dual basis method is used with ionic cores described by Goedecker–Teter–Hutter (GTH) pseudopotentials [57] in combination with the Perdew–Burke–Ernzerhof (PBE) [58] exchange correlation functional and the Grimme D3 empirical dispersion correction [59]. The valence electrons of all atoms are defined with the double- ζ valence polarized MOLOPT (DZVP-MOLOPT-SR-GTH) basis set except water for which the single- ζ valence (SZV-MOLOPT-SR-GTH) basis set is used to reduce computational cost [60]. The SCF convergence threshold was chosen to be 10^{-4} hartree. The MM part is described by classical force fields (FF) with FIST module in CP2K [61]. The goethite surface is modeled with the CLAYFF FF [62] while water is modeled with the single point charge (SPC) water model [63] and OP/GP/IHP with CHARMM FF using the SwissParm

tool [64]. Both CLAYFF and CHARMM FFs are compatible with the SPC water model. The interaction between the QM and MM parts in CP2K is implemented using the Gaussian expansion of the electrostatic potential method (GEEP) [65], wherein the MM charge is distributed by defining it using Gaussians instead of point charges to avoid electron spilling. QM/MM-based canonical (NVT, i.e., constant number of atoms N , volume V and temperature T) MD simulations are performed for 25 ps with a 0.5 fs time step while the temperature was maintained at 300 K using velocity rescaling thermostat (CSVR) [66]. The first 10 ps of each trajectory are assigned for the equilibration, and the remaining 15 ps (production trajectory) are used for analysis. The interaction energy between each phosphate and the goethite surface is calculated for every 100 fs (i.e., 150 snapshots) along the production trajectory by using:

$$E_{\text{int}} = E_{\text{G-P complex}} - (E_{\text{G}} + E_{\text{P}}) \quad (6)$$

where, $E_{\text{G-P complex}}$, E_{P} , and E_{G} denote the total electronic energies of the goethite-phosphate complex, the phosphate (OP/GP/IHP), and the goethite surface, respectively. The interaction energies involving water are divided by the number of water molecules in the simulation box for better comparison. The basis set superposition error (BSSE) in interaction energies is corrected using counterpoise scheme [67].

3. Results and Discussion

3.1. Adsorption Isotherms

Despite some data scatter in OP adsorption, Figure 2 shows that almost the maximum adsorption capacities are reached for goethite and the selected range of P concentrations is sufficient to achieve the equilibrium. Here, the sequence of adsorbed P (Q_{ads}) values per mol P is IHP > OP > GP (see Figure 2). For most cases, the coefficients of determination (R^2) values indicated that the Freundlich equation fitted the adsorption data better than the Langmuir and Temkin models; see Table 1. This comes in accord with the study by Tellinghuisen and Bolster [68] that discussed the statistical reasons leading to better fitting for the Freundlich equation case compared to Langmuir and Temkin models for the P adsorption on soils. The Freundlich adsorption constant (capacity) K_f ranged from 0.22 to $4.79 \mu\text{mol}^{1-n_f} \text{L}^{n_f} \text{m}^{-2}$. The order of K_f values suggests that IHP exhibits the strongest adsorption and the highest capacity at the goethite surface, followed by OP and GP (GP < OP < IHP). The magnitude of the Freundlich exponent n_f , that ranged from 0.07 to 0.29 (see Table 1), gives an indication that the sorption mechanism is dominated by adsorption and not absorption [69,70]. Furthermore, the exponent points to the diversity of the energies associated with adsorption of P compounds on the goethite surface. Moreover, $n < 1$ for all cases indicates that upon increasing the P concentration/loading the binding energy between the surfaces and P compounds is reduced. The order of the n_f values (IHP < GP < OP) suggests that the binding energy decreases with increasing the P loading in the order OP < GP < IHP. This means that affinity of the goethite surface to adsorb/bind a P molecule, with increasing the P concentration, increases in the order IHP < GP < OP. According to the Langmuir model, the maximum monolayer adsorption capacities (Q_{max}) are 1.2, 7.64 and $8.35 \mu\text{mol m}^{-2}$, respectively, for GP, OP and IHP (see Table 1). This shows that the order of saturation of the goethite surface with P per mol P is GP < OP < IHP. This trend fits well with that one observed based on the Freundlich K_f values. The Langmuir parameter K_l increased in the order 0.001 (OP) < 0.003 (GP) < 0.06 (IHP) $\text{L} \mu\text{mol}^{-1}$. This constant is mainly related to the adsorption energy and could give information on how strong (i.e., strength) the goethite-P interaction/binding process is. Therefore, based on Langmuir model, one expects that the goethite-P interaction increases in the order OP < GP < IHP. The same order but with different values was obtained from Temkin binding constant A_T which is also related to the binding strength, see Table 1. The Temkin B_T values for OP (0.75), GP (0.13) and IHP (0.52) suggest that the heat of adsorption increases in the order GP < IHP < OP. Regardless the Temkin constant B_T , all other parameters from the

represented isotherm models in the present contribution refer to stronger adsorption and higher capacity for the IHP case compared to OP and GP cases by considering the number of P moles.

Considering the size and chemical structure of IHP (six phosphate groups), GP and OP (only one phosphate group), the adsorption data were presented as well in terms of whole P molecular system. Specifically, both Q_{ads} and C_e concentrations and all related fitted adsorption isotherm parameters are represented per mole and per mass of the whole P-containing molecule (OP, GP, and IHP), see Table 1. It should be noted that n_f and R^2 values for all P compounds do not change upon changing the interpretation/representation of P concentration (Q_{ads} and C_e). In addition, the order of all adsorption parameters (k_f , n_f , k_l , Q_{max} , B_T , A_T) does not change for OP and GP by different interpretations for the P concentration (i.e., per mol P versus per mol molecule and per mass bases). Here, the only change was observed for the IHP case. By considering the number of moles of the P adsorbed molecules (i.e., per mol molecule), the K_f , Q_{max} and B_T values for IHP decreased by a factor of six, while the corresponding K_l and A_T values increased by a factor of six (see Table 1). In principle, this means that the goethite adsorption capacity will decrease to one sixth by considering the whole IHP molecule compared to considering six P moles of each IHP mole. Consequently, the binding/adsorption strength between the goethite surface and each IHP mole will increase by a factor of six compared to the case of considering only one mole of P. In addition, the orders of K_f (GP < OP < IHP), K_l (OP < GP < IHP) and A_T (OP < GP < IHP) do not change compared to the mol P basis. In contrast, the orders of Q_{max} (GP < IHP < OP) and B_T (IHP < GP < OP) changed comparing with considering the mol P cases. Same orders were obtained by considering the P concentration as mass of the adsorbed P molecule. With respect to the K_l order, one can suggest that GP has stronger interaction than OP with the goethite surface. In contrast, the B_T order suggests that OP has stronger interaction than IHP.

In a study evaluating the adsorption properties of goethite, Celi et al. [71] reported the adsorption ratio of 3:2 between IHP and OP at pH 4.5. Later, Martin et al. [72] confirmed the greater affinity of IHP than of OP for goethite, indicating that the maximum amount of adsorbed P were 3.6 and 2.4 $\mu\text{mol P m}^{-2}$ for IHP and OP, respectively. Likewise, Celi and Barberis [73] found that goethite shows a higher affinity for IHP (deduced from Langmuir K_l values) than for other organic and inorganic phosphates. Li et al. [74] reported a maximum GP adsorption of 1.95 $\mu\text{mol P m}^{-2}$ at pH 5 which is close to the value of 1.20 $\mu\text{mol P m}^{-2}$ observed here. However, the lower adsorption of GP as compared to that reported by Li et al. [74] may be due to the differences in experimental conditions. Specifically, Li et al. [74] conducted their adsorption experiment by β -glycerophosphate at a goethite sample with SAA of 46.4 $\text{m}^2 \text{g}^{-1}$ and PZC of 9.2 in 0.1 M KCl as a background electrolyte. Overall, both organic and inorganic phosphates exhibited affinity for goethite. Parfitt [29], compared the adsorption of OP on goethite in CaCl_2 solution, and reported that larger amounts of specifically adsorbed P reflect more reactive and available adsorption sites on the goethite. This was explained by thermal gravimetric analyses that indicated that goethite contains 24% structural OH [74]. Similarly, Guzman et al. [75] showed the affinity for phosphate (exponent coefficient of Freundlich equation) for goethite on a surface area basis. Details of IHP adsorption on goethite have been extensively studied [71,72,76,77]. Ognalaga et al. [50] investigated the adsorption of IHP on synthetic goethite and attributed it solely to the inner-sphere complexation of phosphate groups with reactive OH groups. Celi et al. [71] and Ognalaga et al. [50] suggested that four of the six phosphate groups of each IHP molecule were involved in bonding to goethite while the other two remained free.

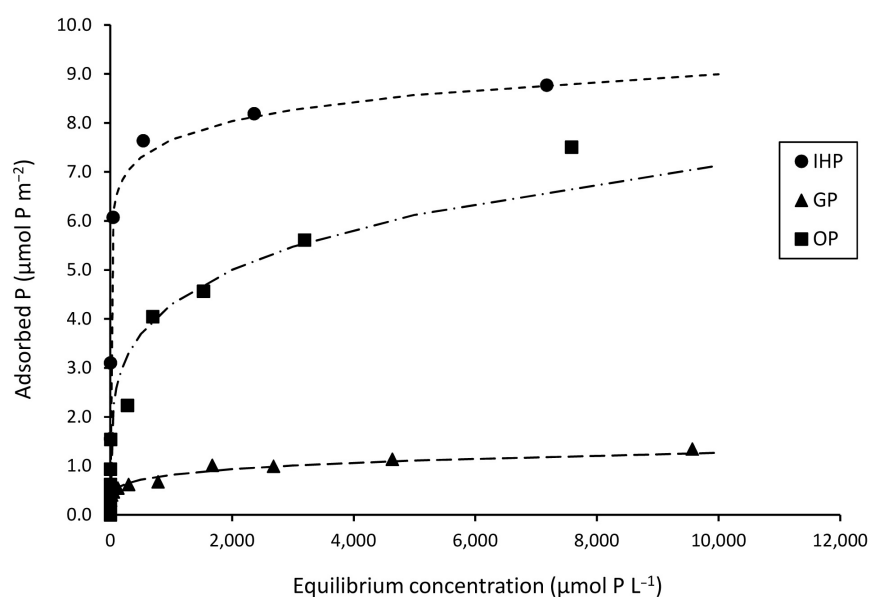


Figure 2. Adsorption isotherms of OP, GP, and IHP on goethite at 0.01 M CaCl_2 electrolyte solution (pH 5). Points represent the original data and dashed lines represent the fitted isotherms according to Freundlich model.

Table 1. Freundlich, Langmuir and Temkin isotherm coefficients (K_f , n_f , K_l , A_T and B_T) of OP, GP and IHP adsorption on goethite at pH 5 in 0.01 M CaCl_2 .

Sorbate	Freundlich			Langmuir				Temkin	
	n_f	K_f	R^2	Q_{max}	K_l	R^2	B	A_T	R^2
OP ($\mu\text{mol P}$)	0.29 ± 0.08	0.57 ± 0.23	0.97	7.64 ± 2.36	0.001 ± 0.001	0.88	0.75 ± 0.16	0.49 ± 0.23	0.83
GP ($\mu\text{mol P}$)	0.19 ± 0.01	0.22 ± 0.02	0.98	1.20 ± 0.06	0.003 ± 0.001	0.81	0.13 ± 0.03	0.89 ± 0.30	0.92
IHP ($\mu\text{mol P}$)	0.07 ± 0.001	4.79 ± 0.02	0.98	8.35 ± 0.04	0.06 ± 0.002	0.92	0.52 ± 0.01	3104.43 ± 467.8	0.99
OP (μmol)	0.29 ± 0.08	0.57 ± 0.23	0.97	7.64 ± 2.36	0.001 ± 0.001	0.88	0.75 ± 0.16	0.49 ± 0.23	0.83
GP (μmol)	0.19 ± 0.01	0.22 ± 0.02	0.98	1.20 ± 0.06	0.003 ± 0.001	0.81	0.13 ± 0.03	0.89 ± 0.30	0.92
IHP (μmol)	0.07 ± 0.001	0.90 ± 0.002	0.98	1.39 ± 0.006	0.36 ± 0.0009	0.92	0.09 ± 0.0004	$18,444.8 \pm 148.6$	0.99
OP (mg)	0.29 ± 0.07	0.14 ± 0.06	0.97	1.04 ± 0.4	0.01 ± 0.01	0.88	0.10 ± 0.02	3.6 ± 1.1	0.83
GP (mg)	0.20 ± 0.01	0.05 ± 0.003	0.98	0.21 ± 0.01	0.02 ± 0.004	0.81	0.02 ± 0.001	5.19 ± 1.53	0.92
IHP (mg)	0.07 ± 0.001	0.61 ± 0.001	0.98	0.92 ± 0.004	0.55 ± 0.01	0.92	0.06 ± 0.0002	7427.1 ± 112.6	0.99

3.2. Molecular Modeling of P Interactions at the Goethite–Water Interface

3.2.1. Orthophosphate

The MD simulations showed that OP maintained the initial motifs (see Figure 1e,f) and formed stable **M** and **B** motifs throughout the simulation trajectory, see Figure 3a–h, respectively. The time averaged Fe–O_p bond length and Fe–P distance observed for the **B** motif are shorter than those for the **M** motif which is probably due to higher stability in the former case, see Table 2. Here, the total interaction energy between OP and the goethite surface of the goethite–OP complex for the **B** and **M** motifs are -82 and -35 kcal mol⁻¹, respectively. The interaction energy per bond of goethite–OP in the **B** motif being higher than in the **M** motif suggests that the alignment of OP with the goethite surface favors the formation of an additional Fe–O_p covalent bond in the **B** motif.

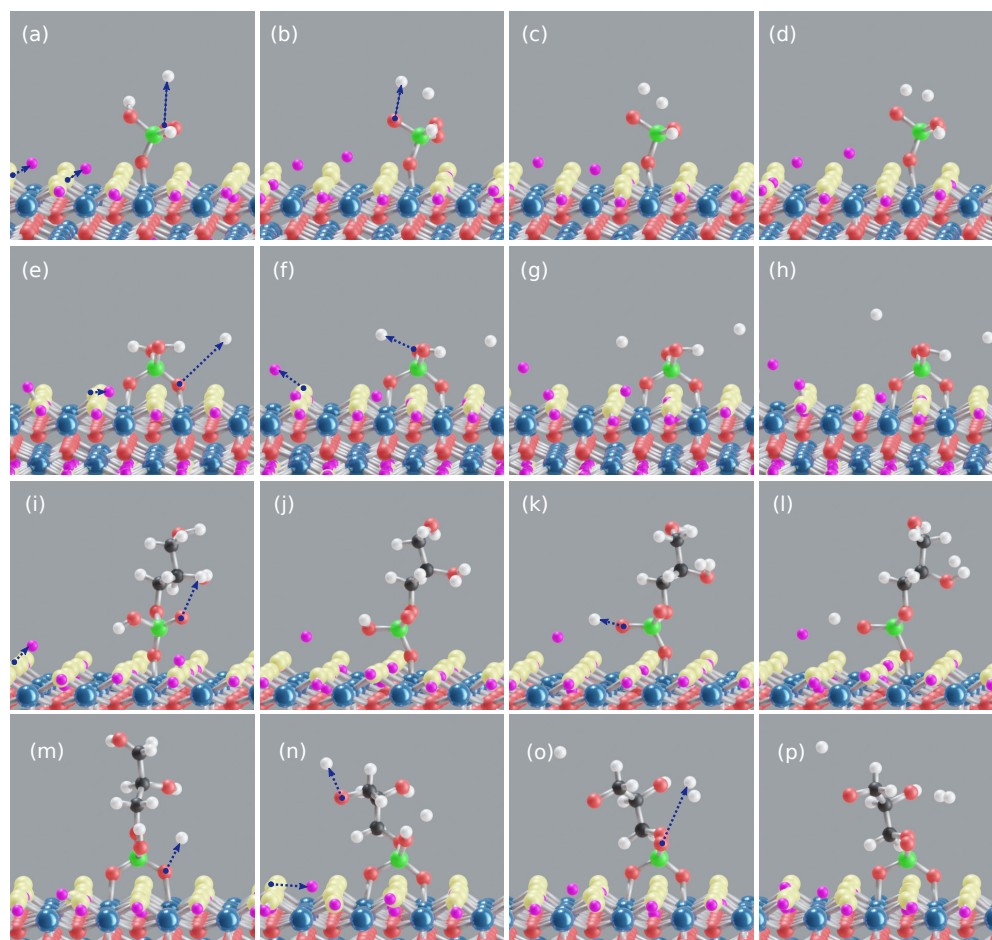


Figure 3. Snapshots along the simulation trajectories of the goethite-OP/GP/IHP-water complexes. OP **M** motif (a–d), OP **B** motif (e–h), GP **M** motif (i–l), GP **B** motif (m–p). Arrows denote proton transfers from phosphates to water and from goethite to water. For all cases, the first two snapshots are from equilibration phase while the last two are from production, except for OP **M** motif case where only (a) is from equilibration phase. The last snapshot for each case is taken at 25 ps. The goethite's hydrogen atoms and OP/GP/IHP's hydrogen atoms are shown in violet and white colors, respectively, for clear visualization of proton transfer events. Blue, red, yellow, black and green colors correspond to iron, bridging oxygen, hydroxyl oxygen, carbon and phosphorus atoms, respectively. The surrounding water is ignored here for better visualization.

Table 2. The interaction energies per number of bonds ($E_{\text{int}}/\text{bond}$) and selected interatomic distances Fe–O_p and Fe–P observed along the trajectories of goethite-OP/GP/IHP-water complexes.

P	Motif	$E_{\text{int}}/\text{bond}$ (kcal mol ^{−1})	Fe–O _p (Å)	Fe–P (Å)
OP	M	−35	2.1	3.5
	B	−41	2.01 & 1.97	3.19 & 3.2
GP	M	−48	1.99	3.19
	B	−38	2.01 & 2.03	3.19 & 3.1
IHP	M(1)	−85	2.0	3.1
	M(2)	−69	2.03	3.2
	3M	−72	2.01 & 1.98 & 1.94	3.1 & 3.2 & 3.4

For both **M** and **B** motifs, two protons are transferred from OP to water (see Figure 3a,b,e,f), forming an average of five HBs each. Consequently, the calculated OP–water interaction energy per water molecule for **M** (−1.7 kcal mol^{−1}) and **B** (−1.6 kcal mol^{−1}) motifs is essentially the same. In addition, proton transfers are observed from goethite to water, see Figure 3a,e,f. The proton transfers observed here occurred only during the

equilibration phase of the complexes and OP remained twice deprotonated in the production trajectory for both cases. The goethite–water interaction energy per single water molecule ($-4.8 \text{ kcal mol}^{-1}$) is lower than the goethite–OP interaction energy for both **M** and **B** motifs. The goethite–water interaction energy is higher than OP–water interaction energies in both motif cases because of goethite’s larger solvent accessible surface area (SASA), proton transfer events from goethite to water (see Figure 3), formation of multiple $\text{Fe-O}_{\text{H}_2\text{O}}$ **M** motifs (on average 15 of 40 surface Fe atoms, see Figure S6) and HBs between goethite and water.

3.2.2. Glycerolphosphate

GP is aligned perpendicular to the goethite surface to form initial **M** and **B** motifs, as shown in Figures 1d and S3c,d. The MD simulations show that these initial motifs are stable during the whole trajectory (see Figure 3i–p, respectively). The time averaged Fe-O_p bond length and Fe-P distance observed for the **M** motif are close to the corresponding values for the **B** motif case; see Table 2. GP forms an average of six and eight HBs with water in the **M** and **B** motifs, respectively. It also exhibits multiple proton transfers to water, two in the **M** motif case and three in the **B** motif. The proton transfer events observed for both cases occurred during the equilibration phase. The total interaction energy between GP and goethite for the **B** motif ($-76 \text{ kcal mol}^{-1}$) is higher than for the **M** motif ($-48 \text{ kcal mol}^{-1}$) due to additional covalent bond in former motif. The higher overall goethite–GP interaction energy of the **B** motif indicates that it is a more favorable motif than the **M** one. However, the goethite–GP interaction energy per bond for the **B** motif is lower than for the **M** motif, suggesting comparatively unfavorable conditions for Fe-O_p bonds in former motif. This is in contrast to the case of OP. The difference comes from the glycerol group in GP. Both OP and GP interact through the phosphate, but through the glycerol group, GP has a higher SASA and exhibits stronger interaction with water than OP (OP/GP–water interaction energies will be discussed below). In the GP **B** motif case, two oxygens of GP’s phosphate group are bound to two individual Fe atoms and when the glycerol group interacts with flexible water atoms, GP fluctuates with water while the surface Fe atoms competitively pull O_p oxygens towards the surface as a counteraction. This may induce strain in the Fe-O_p bonds for the **B** motif and, therefore, the goethite–GP interaction energy per bond for the **B** motif is less compared to the **M** motif. The stretch in the Fe-O_p bonds found in the GP **B** motif is larger than in the OP **B** motif, see Figure S4, which signifies a strain in the Fe-O_p bonds in the former case. In addition, GP is found to oscillate occasionally in a seesaw type of motion over the surface which randomly stretches one of the Fe-O_p bonds to its extreme (maximum Fe-O_p bond length found $\approx 2.4 \text{ \AA}$), see Figure S5. A similar observation was made for GP on 100 diasporite surface [41] which is isomorphous with goethite [33]. The study by Xu et al. [78] showed that GP induces more negative charges onto hematite mineral surface than OP, which might also influence the strength of the Fe-O_p covalent bonds.

Regarding GP–water interaction energies, GP exhibited a slightly stronger interaction with water for the **B** motif ($-2.8 \text{ kcal mol}^{-1}$) case than for the **M** motif one ($-2.5 \text{ kcal mol}^{-1}$). This is due to additional proton transfer observed from GP to water for the **B** motif case (see Figure 3m–o). The GP–water interaction energy here is higher than that of OP–water due to additional glycerol group in GP which contains two polar OH groups that interact strongly with water. Similar to goethite–OP–water complexes, proton transfer is observed from goethite to water in both motifs here; see Figure 3i,n.

3.2.3. Inositolhexaphosphate

IHP was initially aligned perpendicular to the goethite surface to form **M** and **B** motifs (see Figure S3a,b), and parallel to the goethite surface to form the proposed **4M** motif (see Figure 1g). In contrast to goethite–OP–water and goethite–GP–water cases, transformation of initial binding motifs between IHP and the goethite surface with time is observed. The simulation results show that the initial **M** and **B** motifs resulted in two similar con-

formers of **M** motif type; namely, **M(1)** and **M(2)**. On the other hand, the starting **4M** binding motif transformed along the MD trajectory into a **3M** motif. The transformations observed here happened within the equilibration phase of each complex. The corresponding Fe–O_p bond lengths and Fe–P distances of the relatively long-lived binding motifs [**M(1)**, **M(2)**, **3M**] are in close range and lie within half angstrom difference (see Table 2). The **M(1)** motif's goethite–IHP interaction energy is higher than that for the **M(2)** one (see Table 2). This is probably because of the strain in the Fe–O_p bond in the **M(2)** motif due to intramolecular HBs between the phosphate group bound to Fe and its adjacent phosphate groups (see Figure 4h). The **3M** motif has a higher total interaction energy than both **M** motifs due to additional covalent bonds and proton transfer from IHP to the goethite surface. However, the interaction energy per bond between IHP and goethite for the **3M** binding motif is less than for the **M(1)** motif. Thus, in spite of the **3M** motif being the more favorable motif compared to the **M** motifs, the alignment of IHP with goethite as in the **3M** motif weakens the overall strength of the individual Fe–O_p bonds.

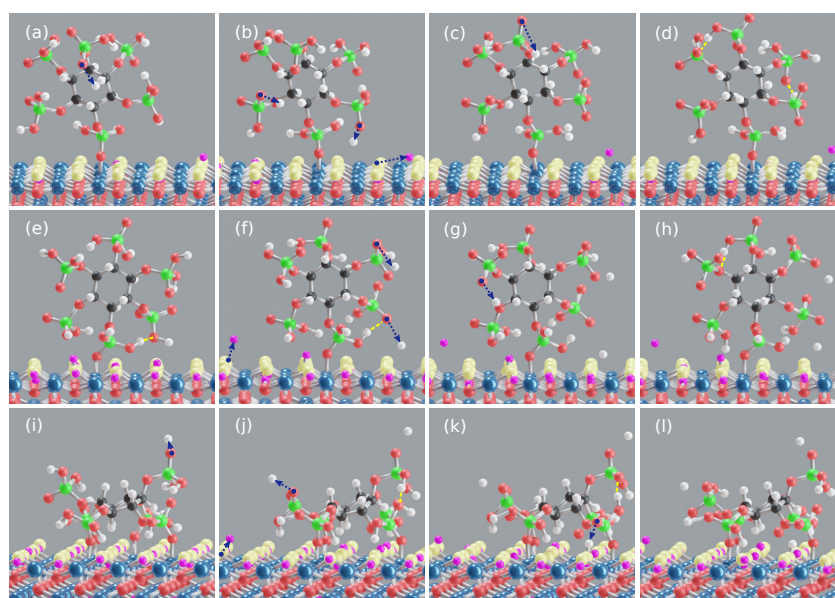


Figure 4. Snapshots along the simulation trajectories of the goethite–IHP–water complexes. IHP **M** motif (a–d), IHP **B** motif (e–h), IHP **3M** motif (i–l). Arrows denote proton transfers from phosphates to water and from goethite to water. The yellow dotted lines denote intramolecular HBs between IHP's phosphate groups. For all cases, the first two snapshots are from equilibration phase while the last two are from production, except for the IHP **3M** motif case where only (i) is from the equilibration phase. The last snapshot for each case is taken at 25 ps. The goethite's hydrogen atoms and IHP's hydrogen atoms are shown in violet and white colors, respectively, for clear visualization of proton transfer events. Blue, red, yellow, black and green colors correspond to iron, oxygen, hydroxyl oxygen, carbon and phosphorus atoms, respectively. The surrounding water is ignored here for better visualization.

Even though an additional proton transfer is observed from IHP to water for the **M(1)** motif, the IHP–water interaction energy ($-7.3 \text{ kcal mol}^{-1}$) is very close to that for the **M(2)** motif case ($-7.2 \text{ kcal mol}^{-1}$). This could be probably due to higher number of time averaged HBs observed for the **M(2)** motif case (25) compared to the **M(1)** case (23). The IHP–water interaction energy observed for the **3M** motif case ($-3.1 \text{ kcal mol}^{-1}$) is lower than those for both **M** cases due to fewer proton transfer processes (2) and HBs (15) observed in the **3M** motif case.

The stronger interaction of IHP with water is vital for understanding the reason for transformation of initial **B** and **4M** motifs to **M(2)** and **3M** final motifs, respectively. For initial **B** motif case, when IHP interacts with flexible water molecules it fluctuates with respect to goethite surface which might induce strain in one of the Fe–O_p covalent bonds

leading to its dissociation. In addition, an intramolecular HB is observed between the Fe bonded phosphate group and its adjacent phosphate group, see Figure 4l. In our previous work on IHP interaction at the diaspore(100)–water interface (diaspore isostructural with goethite), [41] the initial **4M** motif was transformed into a **2M** motif. The reason is that the Al–O_p covalent bonds are inclined and restricted between diaspore’s surface hydroxyl groups. Moreover, when IHP interacts with water and fluctuates during the equilibration phase, the restricted Al–O_p covalent bonds under unfavorable conditions do not have an alternative but to dissociate and move towards water. The same reason holds true here for the transformation process of the initial **4M** motif to a stable **3M** binding motif.

3.3. Discussion of Experimental and Modeling Results

In what follows, we will correlate the present modeling results and the adsorption isotherms as per mole of P-compound. It is important to emphasize that the experimental adsorption results are due to a combination of all different binding motifs at the existing different surface planes (not only the 100 goethite surface plane) in the real goethite sample. Therefore, a direct quantitative comparison is rather difficult and thus we are aiming here to present a qualitative behavior. First, let us recollect that K_f , K_l and B_T relate to the phosphate’s binding energy and that n_f relates to the binding energy of the next incoming P molecule to surface (i.e., binding affinity). Since the Freundlich isotherm provided the best fit to the experimental data for all cases (see Table 1), we will discuss the theoretical results in Table 2 in the context of K_f and n_f . Analyzing the strength of phosphate interaction shows that the K_f values are in line with the order of overall binding energies observed here, i.e., GP **B** < OP **B** < IHP **3M**. The K_f value for OP adsorption is more than twice that of the GP adsorption, suggesting a significant difference between OP and GP interaction with goethite. In light of these results, combined with the theoretical binding energy values (see Table 2), one could suggest that OP might predominantly form **B** motif and GP might form **M** motif as the predominant binding motif. Therefore, the binding strength order could be updated as GP **M** < OP **B** < IHP **3M**. Comparing K_f values for IHP and OP, the K_f for IHP adsorption is about 1.58 times that for OP adsorption, which is very close to the reported adsorption ratio by Celi et al. [71] and Martin et al. [72]. Correlating this ratio to the present calculated binding energies would suggest that one should rather use the average of all three bonding motifs, i.e., both **M** and **3M** binding motifs for the adsorbed IHP molecule are present at the goethite surface. Therefore, based on both experimental and theoretical binding strength values, one could suggest that the overall binding strength increases in the order GP (**M**) < OP (**B**) < IHP (**M** + **3M**).

The order of n_f values (IHP < GP < OP, see Table 1) suggests that IHP adsorption leads to a faster saturation of the goethite surface than GP and OP. Even though IHP binds to goethite through a few phosphate groups, the remaining phosphate groups (often deprotonated) would induce more negative charges to the surface compared to OP and GP cases [71,78]. Moreover, it was found that GP leads to a more negatively charged surface than OP [78]. This explains the reason why the n_f value for GP is lower than for OP.

Let us compare the present modeling results with previous experimental and theoretical studies. In the case of OP, experimental [36,79,80] and theoretical [10,40] results pointed to a formation of both, i.e., **M** and **B**, motifs with goethite. Specifically, for the 100 goethite surface studied here, Kubicki et al. [40] and Ahmed et al. [10] demonstrated that OP often exists in a doubly deprotonated state forming both **M** and **B** binding motifs but with the predominance of the **B** one. This is confirmed by the present MD results, i.e., OP has formed stable **M** and **B** motifs and remained twice as deprotonated in the production trajectory with the **B** motif exhibiting higher interaction energy with the goethite surface compared to the **M** motif. Even though the **B** motif is the more stable motif under the present conditions, it is not always the dominant one, a topic which has been highly debated in the literature [39,40,79,80]. For instance, Persson et al. [80] interpreted their FTIR spectra of the OP adsorption at goethite and hematite by the formation of only **M** binding motifs with different protonation states. This analysis was done as a function of total phosphate concen-

tration, pH, and time. In contrast, Tejedor-Tejedor and Anderson [36] proposed that the **B** motif is the dominant motif, for low surface coverage of OP on goethite over the pH range of 3.6–8.0. Further, they proposed that the **M** motif exists at low surface coverage but as a non-dominant motif. By using DFT calculations, Kwon and Kubicki [39] concluded that the **B** motif is dominant between pH 4–6. Recently, a joint approach by Ahmed et al. [51] involving adsorption experiments and DFT simulations showed that the **M** motif is dominant at both extremely low and high pH values, while the **B** motif is dominant in the intermediate pH range.

Keeping in mind that the present simulations correspond to a low surface coverage scenario and acidic pH, one can conclude that the stable **M** and **B** motifs with abundance of the **B** one here are in line with the studies of Tejedor-Tejedor and Anderson [36], Ahmed et al. [51], and Abdala et al. [79]. Moreover, the time averaged Fe–P distance observed in both motifs (3.5 Å for the **M** motif and 3.19–3.2 Å for the **B** motif) are within the range of values reported in literature, thus giving further support for the present model. For instance, an extended X-ray absorption fine structure study of adsorbed OP on goethite [79] showed that the distances between the surface Fe atoms and the adsorbed phosphate P atoms (i.e., Fe–P distances) for **M** and **B** binding motifs are 3.6 and 3.28 Å, respectively. The Fe–P distances from other studies are in the range of 3.48–3.55 Å for the **M** motif and 3.13–3.37 Å for the **B** motif [10,40,81,82].

Compared to OP, GP adsorption on goethite has not been extensively studied and hence, the information about its binding motifs with goethite is limited. Li et al. [74] showed that GP forms inner-sphere complexes with goethite by replacing water and hydroxyl groups from surface active sites. The study also proposes that GP forms only **M** motifs at the goethite surface based on FTIR spectra analysis. The **B** motif is sterically hindered by the organic moiety. Additionally, Hartree-Fock simulations and FTIR spectra studies by Persson et al. [83] of monomethyl phosphate ($\text{CH}_3\text{--H}_2\text{PO}_4$), an organic P with a single phosphate group like GP, showed that it forms mostly **M** motifs with goethite. Adsorption isotherms and FTIR spectra by Sheals et al. [34] proposed that glyphosate binds predominantly through an **M** motif but **B** motifs might be formed at low P concentration and neutral pH. By using periodic DFT based MD simulations, Ahmed et al. [9] studied the glyphosate binding process at the goethite–water interface by considering three goethite surface planes. The results indicated that the **M** binding motif is the most dominant one at the 100 goethite surface plane, although both **M** and **B** motifs exist at the 100, 010 and 001 surface planes. Summing up these literature data, the **M** motif is the dominant motif for GP like molecules at the 100 goethite surface. This could be supported by our recent study [52] about the P binding at the 010 goethite surface plane. We found that the calculated total interaction energy for the GP **B** motif ($-122 \text{ kcal mol}^{-1}$) is higher than for the **M** motif ($-112 \text{ kcal mol}^{-1}$). However, the goethite–GP interaction energy per bond for the **B** motif is lower than for the **M** motif. This suggests unfavorable conditions for Fe–O_p bonds for the **B** case. This is in accord with outcome of the present contribution. In addition, the calculated interaction energy indicated that the 010 goethite surface plane binds GP stronger than the corresponding 100 surface plane. Regarding the Fe–P distances observed for both GP motifs at both 010 and 100 goethite surface planes, the distances are within the range of Fe–P distances observed for OP on goethite in the literature [10,40,79,81,82]. This suggests that the GP's phosphate group interacts with goethite surface in a similar way to the OP case.

There is no consensus in the literature about the number of IHP's phosphate groups that bind to goethite surface or about dominant binding motifs. The binding motifs observed for goethite–IHP complexes in the current study (**M** and **3M**) have been found in literature before [11,41]. Similarly, we have observed the same binding motifs (i.e., **M** and **3M**) for IHP at the 010 goethite surface plane [52]. Similar to the GP case, the calculated interaction energy referred to stronger interaction for IHP at the 010 goethite surface plane compared to the 100 surface plane. It is important to mention that it is not clear yet in literature which binding motif is the dominant one. For instance, **3M** [11,84], **2M** [11,41]

and **1M** [11] are different binding motifs observed for IHP on minerals. In contrast, Johnson et al. [77] proposed that IHP interacts with goethite by forming outer-sphere complexes. Interestingly, none of the above mentioned studies for IHP suggest that it forms a bidentate binuclear (**B**) motif. Similar to our previous studies [11,41], we found that the initial **B** motif of IHP was not stable due to the strong interaction of IHP with water and intramolecular HBs. Therefore, we propose that IHP phosphate groups form **M** motif with goethite surface.

De Groot and Golterman [85] showed that IHP adsorption onto goethite had an inhibitory effect on OP adsorption and it can release adsorbed OP from the goethite surface. The same could be inferred from binding energies here, where the goethite–IHP binding energies are larger than for goethite–OP complexes. The goethite–GP binding energies are also less than goethite–IHP and one might suggest that IHP might replace GP as well from goethite surface. The same could be inferred from the adsorption strengths order calculated from experiments here. The Fe–P distances observed here show that they are close to the Fe–P distances for OP on goethite [10,40,79,81,82] which suggests that IHP's organic moiety might not influence the individual phosphate groups interaction with goethite but only the conformational flexibility of the overall binding motif [11,41]. This comes in accord with the observation by Celi et al. [71] that phosphate groups of IHP react with a goethite surface similar to OP.

4. Summarizing Discussion

The current study contributes to the efforts in understanding the interaction of phosphates with soil minerals. Here, both experimental and theoretical approaches are adopted to characterize inorganic (OP) and organic (GP, IHP) phosphates interaction with abundant and reactive goethite mineral. The goethite–OP/GP/IHP–water complexes are simulated with the multiscale QM/MM method which provides molecular level insights into adsorption experiments performed for OP/GP/IHP on goethite. The binding energies and interaction mechanisms of phosphates adsorption on goethite from the modeling study are correlated to adsorption data fitted to the Freundlich isotherm, which provided a uniformly better fit than the Langmuir and Temkin models. The model coefficients provided an overview of the pattern of phosphate interactions with goethite and the QM/MM simulations demonstrate, at the molecular level, the attributes that build these pattern.

The modeling results show that OP forms stable **M** and **B** motifs and OP **B** motif has higher interaction energy per bond than OP **M** motif. This suggests that goethite–OP interaction favors the additional covalent bond, which makes the OP **B** motif more stable. For goethite–GP complexes, the order of interaction energies is same as OP case, except that GP **B** motif interaction energy per bond is lower than GP **M** motif. Compared to OP, the GP **B** motif is weaker than OP **B** motif due to a strain in Fe–O_p bonds in former case. The strain is due to GP interaction with water molecules. In addition, Xu et al. [78] study shows that adsorption of GP induces more negative charges on the hematite surface than OP which might strain the Fe–O_p bonds further. Therefore, the literature [34,74] and the calculated binding energies in the present contribution show that GP's dominant motif might be the **M** or **B** motif depending on the GP interaction with environmental molecules. IHP forms **M** and **3M** motifs with multiple intramolecular HBs between adjacent phosphate groups [77]. IHP's **3M** motif exhibits the strongest binding energy with the goethite surface among all goethite–OP/GP complexes here. This comes in accord with our recent study [52] for the binding of GP and IHP at the 010 goethite surface plane. In that study, the **3M** binding motif of IHP showed the strongest interaction with goethite compared to all other existing binding motifs for GP and IHP. Therefore, we propose that the **3M** motif might be the most dominant motif at low surface loading.

The adsorption data from experiment fitted to Freundlich model show that the order of adsorption strength (K_f) is GP < OP < IHP whereas the order of incoming P binding strength with surface (n_f) is IHP < GP < OP. Based on the magnitude and order of experimental K_f values combined with theoretical binding strength values, one could suggest that the overall binding strength increases in the order GP (**M**) < OP (**B**) < IHP (**M**)

+ 3M). This shows that GP might often form **M** motif, whereas OP might form **B**, and IHP might form both **M** and **3M** motifs. The n_f order suggests that IHP adsorption on goethite saturates its surface faster than for the GP and OP cases. The fact that GP adsorption induces more negative charges on goethite than OP supports our suggestions that GP would often form **M** and not **B** motifs and eventually its interaction energy would be less than OP.

Eventually, the present experimental and theoretical results, in agreement with the pertinent literature, plausibly explain why IHP is the predominant organically bound P form in soil. A challenge for further studies and application is to understand and explore the mechanisms by which microbes and plants can overcome the strong IHP–mineral binding and incorporate the phosphate groups into their metabolism.

Supplementary Materials: The following are available online at <https://www.mdpi.com/2075-163X/11/3/323/s1>, Figure S1: XRD pattern for pure goethite sample, Figure S2: Effect of pH on goethite zeta potential, Figure S3: Initial motifs of IHP GP, Figure S4: Sum of covalent bond lengths in OP and GP **B** motifs, Figure S5: Seesaw movement of GP's phosphate group, Figure S6: Multiple covalent bonds between surface iron atoms and water molecules.

Author Contributions: P.B.G. and M.M. performed the modeling and experimental work, respectively, and wrote the manuscript draft. A.A.A., P.L. and O.K. are responsible for conceptualization, funding acquisition, methodology, supervision, writing–review and editing of the present contribution. All authors have read and agreed to the published version of the manuscript.

Funding: We are grateful to S. Dultz, Soil Science, University of Hannover, for preparing and characterizing the goethite. We gratefully acknowledge the financial support by the German Research Foundation (DFG) as a part of the SPP 1685 Priority program “Ecosystem Nutrition: Forest strategies for limited phosphorus resources” (P.B.G., O.K., A.A.A.) and the InnoSoilPhos-project (A.A.A.), funded by the German Federal Ministry of Education and Research (BMBF) in the frame of the BonaRes-program (No. 031A558). This research was performed within the scope of the Leibniz Science Campus “Phosphorus Research Rostock”. The authors thank the North German Super computing Alliance for providing HPC resources (project mvp00016).

Institutional Review Board Statement: Not applicable.

Informed Consent Statement: Not applicable.

Data Availability Statement: Not applicable.

Conflicts of Interest: The authors declare no conflict of interest. The funders had no role in the design of the study; in the collection, analyses, or interpretation of data; in the writing of the manuscript, or in the decision to publish the results.

References

1. Tisdale, S.L. (Ed.) *Soil Fertility and Fertilizers*, 5th ed.; Prentice Hall: Upper Saddle River, NJ, USA, 1993.
2. Andersen, D.S.; Helmers, M.J.; Burns, R.T. Phosphorus Sorption Capacity of Six Iowa Soils before and after Five Years of Use as Vegetative Treatment Areas. *Appl. Eng. Agric.* **2015**, *611*–620. [[CrossRef](#)]
3. Wang, Y.; Zhang, T.; O'Halloran, I.; Tan, C.; Hu, Q. A Phosphorus Sorption Index and Its Use to Estimate Leaching of Dissolved Phosphorus from Agricultural Soils in Ontario. *Geoderma* **2016**, *274*, 79–87. [[CrossRef](#)]
4. Roy, E.D.; Willig, E.; Richards, P.D.; Martinelli, L.A.; Vazquez, F.F.; Pegorini, L.; Spera, S.A.; Porder, S. Soil Phosphorus Sorption Capacity after Three Decades of Intensive Fertilization in Mato Grosso, Brazil. *Agric. Ecosyst. Environ.* **2017**, *249*, 206–214. [[CrossRef](#)]
5. Everett, D.H. Manual of Symbols and Terminology for Physicochemical Quantities and Units, Appendix II: Definitions, Terminology and Symbols in Colloid and Surface Chemistry. *Pure Appl. Chem.* **1972**, *31*, 577–638. [[CrossRef](#)]
6. Urrutia, O.; Guardado, I.; Erro, J.; Mandado, M.; García-Mina, J.M. Theoretical Chemical Characterization of Phosphate-Metal-Humic Complexes and Relationships with Their Effects on Both Phosphorus Soil Fixation and Phosphorus Availability for Plants. *J. Sci. Food Agric.* **2013**, *93*, 293–303. [[CrossRef](#)] [[PubMed](#)]
7. Gros, P.; Ahmed, A.A.; Kühn, O.; Leinweber, P. Influence of Metal Ions on Glyphosate Detection by FMOC-Cl. *Environ. Model. Assess.* **2019**, *191*, 244. [[CrossRef](#)] [[PubMed](#)]
8. Kruse, J.; Abraham, M.; Amelung, W.; Baum, C.; Bol, R.; Kühn, O.; Lewandowski, H.; Niederberger, J.; Oelmann, Y.; Rüger, C.; et al. Innovative Methods in Soil Phosphorus Research: A Review. *J. Soil Sci. Plant Nutr.* **2015**, *178*, 43–88. [[CrossRef](#)] [[PubMed](#)]

9. Ahmed, A.A.; Leinweber, P.; Kühn, O. Unravelling the Nature of Glyphosate Binding to Goethite Surfaces by Ab Initio Molecular Dynamics Simulations. *Phys. Chem. Chem. Phys.* **2018**, *20*, 1531–1539. [\[CrossRef\]](#)
10. Ahmed, A.A.; Gypser, S.; Leinweber, P.; Freese, D.; Kühn, O. Infrared Spectroscopic Characterization of Phosphate Binding at the Goethite–Water Interface. *Phys. Chem. Chem. Phys.* **2019**, *21*, 4421–4434. [\[CrossRef\]](#)
11. Ganta, P.B.; Kühn, O.; Ahmed, A.A. QM/MM Simulations of Organic Phosphorus Adsorption at the Diaspore–Water Interface. *Phys. Chem. Chem. Phys.* **2019**, *21*, 24316–24325. [\[CrossRef\]](#)
12. Gros, P.; Ahmed, A.; Kühn, O.; Leinweber, P. Glyphosate Binding in Soil as Revealed by Sorption Experiments and Quantum-Chemical Modeling. *Sci. Total Environ.* **2017**, *586*, 527–535. [\[CrossRef\]](#) [\[PubMed\]](#)
13. Ahmed, A.A.; Gros, P.; Kühn, O.; Leinweber, P. Molecular Level Investigation of the Role of Peptide Interactions in the Glyphosate Analytics. *Chemosphere* **2018**, *196*, 129–134. [\[CrossRef\]](#)
14. Arai, Y.; Sparks, D. Phosphate Reaction Dynamics in Soils and Soil Components: A Multiscale Approach. In *Advances in Agronomy*; Elsevier: Amsterdam, The Netherlands, 2007; Volume 94, pp. 135–179. [\[CrossRef\]](#)
15. Arai, Y.; Sparks, D. ATR–FTIR Spectroscopic Investigation on Phosphate Adsorption Mechanisms at the Ferrihydrite–Water Interface. *J. Colloid Interface Sci.* **2001**, *241*, 317–326. [\[CrossRef\]](#)
16. Barrow, N.J. A Mechanistic Model for Describing the Sorption and Desorption of Phosphate by Soil. *J. Soil Sci.* **1983**, *34*, 733–750. [\[CrossRef\]](#)
17. Chitrakar, R.; Tezuka, S.; Sonoda, A.; Sakane, K.; Ooi, K.; Hirotsu, T. Phosphate Adsorption on Synthetic Goethite and Akaganeite. *J. Colloid Interface Sci.* **2006**, *298*, 602–608. [\[CrossRef\]](#)
18. Hinsinger, P. Bioavailability of Soil Inorganic P in the Rhizosphere as Affected by Root-Induced Chemical Changes: A Review. *Plant Soil* **2001**, *237*, 173–195. [\[CrossRef\]](#)
19. Ryan, J.; Curtin, D.; Cheema, M. Significance of Iron Oxides and Calcium Carbonate Particle Size in Phosphate Sorption by Calcareous Soils. *Soil Sci. Soc. Am. J.* **1985**, *49*, 74–76. [\[CrossRef\]](#)
20. Baken, S.; Verbeeck, M.; Verheyen, D.; Diels, J.; Smolders, E. Phosphorus Losses from Agricultural Land to Natural Waters Are Reduced by Immobilization in Iron-Rich Sediments of Drainage Ditches. *Water Res.* **2015**, *71*, 160–170. [\[CrossRef\]](#) [\[PubMed\]](#)
21. Bortoluzzi, E.C.; Pérez, C.A.; Ardisson, J.D.; Tiecher, T.; Caner, L. Occurrence of Iron and Aluminum Sesquioxides and Their Implications for the P Sorption in Subtropical Soils. *Appl. Clay Sci.* **2015**, *104*, 196–204. [\[CrossRef\]](#)
22. Torrent, J.; Schwertmann, U.; Barron, V. Fast and Slow Phosphate Sorption by Goethite-Rich Natural Materials. *Clays Clay Miner.* **1992**, *40*, 14–21. [\[CrossRef\]](#)
23. Luengo, C.; Brigante, M.; Antelo, J.; Avena, M. Kinetics of Phosphate Adsorption on Goethite: Comparing Batch Adsorption and ATR–IR Measurements. *J. Colloid Interface Sci.* **2006**, *300*, 511–518. [\[CrossRef\]](#)
24. McLaughlin, J.; Ryden, J.; Syers, J. Development and Evaluation of a Kinetic Model to Describe Phosphate Sorption by Hydrous Ferric Oxide Gel. *Geoderma* **1977**, *18*, 295–307. [\[CrossRef\]](#)
25. Willett, I.R.; Chartres, C.J.; Nguyen, T.T. Migration of Phosphate into Aggregated Particles of Ferrihydrite. *J. Soil Sci.* **1988**, *39*, 275–282. [\[CrossRef\]](#)
26. Torrent, J. Interactions between Phosphate and Iron Oxide. In *Soils and Environment*; Catena Verlag: Reiskirchen, Germany, 1997; Volume 30, pp. 321–344.
27. Strauss, R.; Brummer, G.; Barrow, N. Effects of Crystallinity of Goethite: II. Rates of Sorption and Desorption of Phosphate. *Eur. J. Soil Sci.* **1997**, *48*, 101–114. [\[CrossRef\]](#)
28. Neupane, G.; Donahoe, R.J.; Arai, Y. Kinetics of Competitive Adsorption/Desorption of Arsenate and Phosphate at the Ferrihydrite–Water Interface. *Chem. Geol.* **2014**, *368*, 31–38. [\[CrossRef\]](#)
29. Parfitt, R.L. Phosphate Reactions with Natural Allophane, Ferrihydrite and Goethite. *J. Soil Sci.* **1989**, *40*, 359–369. [\[CrossRef\]](#)
30. Langmuir, D. *Aqueous Environmental Geochemistry*; Prentice Hall: Upper Saddle River, NJ, USA, 1997.
31. Villalobos, M.; Trotz, M.A.; Leckie, J.O. Variability in Goethite Surface Site Density: Evidence from Proton and Carbonate Sorption. *J. Colloid Interface Sci.* **2003**, *268*, 273–287. [\[CrossRef\]](#) [\[PubMed\]](#)
32. Houben, G.; Kaufhold, S. Multi-Method Characterization of the Ferrihydrite to Goethite Transformation. *Clay Miner.* **2011**, *46*, 387–395. [\[CrossRef\]](#)
33. Cornell, R.M.; Schwertmann, U. *The Iron Oxides: Structure, Properties Reactions Occurrence and Uses*; Wiley-VCH Verlag GmbH and Co. KGaA: Weinheim, Germany, 2003. [\[CrossRef\]](#)
34. Sheals, J.; Sjöberg, S.; Persson, P. Adsorption of Glyphosate on Goethite: Molecular Characterization of Surface Complexes. *Environ. Sci. Technol.* **2002**, *36*, 3090–3095. [\[CrossRef\]](#) [\[PubMed\]](#)
35. Olsson, R.; Giesler, R.; Loring, J.S.; Persson, P. Adsorption, Desorption, and Surface-Promoted Hydrolysis of Glucose-1-Phosphate in Aqueous Goethite (Alpha-FeOOH) Suspensions. *Langmuir* **2010**, *26*, 18760–18770. [\[CrossRef\]](#) [\[PubMed\]](#)
36. Tejedor-Tejedor, M.I.; Anderson, M.A. The Protonation of Phosphate on the Surface of Goethite as Studied by CIR–FTIR and Electrophoretic Mobility. *Langmuir* **1990**, *6*, 602–611. [\[CrossRef\]](#)
37. Kim, J.; Li, W.; Philips, B.L.; Grey, C.P. Phosphate Adsorption on the Iron Oxyhydroxides Goethite (Alpha-FeOOH), Akaganeite (Beta-FeOOH), and Lepidocrocite (Gamma-FeOOH): A ³¹P NMR Study. *Energy Environ. Sci.* **2011**, *4*, 4298. [\[CrossRef\]](#)
38. Loring, J.S.; Sandström, M.H.; Norén, K.; Persson, P. Rethinking Arsenate Coordination at the Surface of Goethite. *Chem. Eur. J.* **2009**, *15*, 5063–5072. [\[CrossRef\]](#) [\[PubMed\]](#)

39. Kwon, K.D.; Kubicki, J.D. Molecular Orbital Theory Study on Surface Complex Structures of Phosphates to Iron Hydroxides: Calculation of Vibrational Frequencies and Adsorption Energies. *Langmuir* **2004**, *20*, 9249–9254. [[CrossRef](#)] [[PubMed](#)]
40. Kubicki, J.D.; Paul, K.W.; Kabalan, L.; Zhu, Q.; Mroziak, M.K.; Aryanpour, M.; Pierre-Louis, A.M.; Strongin, D.R. ATR-FTIR and Density Functional Theory Study of the Structures, Energetics, and Vibrational Spectra of Phosphate Adsorbed onto Goethite. *Langmuir* **2012**, *28*, 14573–14587. [[CrossRef](#)] [[PubMed](#)]
41. Ganta, P.B.; Kühn, O.; Ahmed, A.A. QM/MM Molecular Dynamics Investigation of the Binding of Organic Phosphates to the 100 Diaspore Surface. *Front. For. Glob. Chang.* **2020**, *3*, 71. [[CrossRef](#)]
42. Dultz, S.; Steinke, H.; Mikutta, R.; Woche, S.K.; Guggenberger, G. Impact of Organic Matter Types on Surface Charge and Aggregation of Goethite. *Colloid Surf. A* **2018**, *554*, 156–168. [[CrossRef](#)]
43. Antelo, J.; Avena, M.; Fiol, S.; López, R.; Arce, F. Effects of pH and Ionic Strength on the Adsorption of Phosphate and Arsenate at the Goethite–Water Interface. *J. Colloid Interface Sci.* **2005**, *285*, 476–486. [[CrossRef](#)] [[PubMed](#)]
44. Rouquerol, J.; Llewellyn, P.; Rouquerol, F. Is the Bet Equation Applicable to Microporous Adsorbents? In *Studies in Surface Science and Catalysis*; Elsevier: Amsterdam, The Netherlands, 2007; Volume 160, pp. 49–56. [[CrossRef](#)]
45. Freundlich, H. Über Die Adsorption in Lösungen. *Z. Phys. Chem.* **1907**, *57U*. [[CrossRef](#)]
46. Langmuir, I. The Adsorption of Gases on Plane Surfaces of Glass, Mica and Platinum. *J. Am. Chem. Soc.* **1918**, *40*, 1361–1403. [[CrossRef](#)]
47. Tempkin, M.I.; Pyzhev, V. Kinetics of Ammonia Synthesis on Promoted Iron Catalyst. *Acta Phys. Chim. USSR* **1940**, *12*, 327–356.
48. Bolster, C.H.; Hornberger, G.M. On the Use of Linearized Langmuir Equations. *Soil Sci. Soc. Am. J.* **2007**, *71*, 1796–1806. [[CrossRef](#)]
49. Rakovan, J.; Becker, U.; Hochella, M.F. Aspects of Goethite Surface Microtopography, Structure, Chemistry, and Reactivity. *Am. Mineral.* **1999**, *84*, 884–894. [[CrossRef](#)]
50. Ognalaga, M.; Frossard, E.; Thomas, F. Glucose-1-Phosphate and Myo-Inositol Hexaphosphate Adsorption Mechanisms on Goethite. *Soil Sci. Soc. Am. J.* **1994**, *332*–337. [[CrossRef](#)]
51. Ahmed, A.A.; Gypser, S.; Freese, D.; Leinweber, P.; Kuehn, O. Molecular Level Picture of the Interplay between pH and Phosphate Binding at the Goethite–Water Interface. *Phys. Chem. Chem. Phys.* **2020**. [[CrossRef](#)]
52. Ganta, P.B.; Kühn, O.; Ahmed, A.A. Ab Initio Molecular Dynamics Simulations of the Interaction between Organic Phosphates and Goethite. *Molecules* **2021**, *26*, 160. [[CrossRef](#)] [[PubMed](#)]
53. Humphrey, W.; Dalke, A.; Schulten, K. VMD: Visual Molecular Dynamics. *J. Mol. Graph.* **1996**, *14*, 33–38. [[CrossRef](#)]
54. Ozboyaci, M.; Kokh, D.B.; Corni, S.; Wade, R.C. Modeling and Simulation of Protein–Surface Interactions: Achievements and Challenges. *Q. Rev. Biophys.* **2016**, *49*, e4. [[CrossRef](#)] [[PubMed](#)]
55. Kubicki, J.D. (Ed.) *Molecular Modeling of Geochemical Reactions*; Wiley and Sons: Hoboken, NJ, USA, 2016.
56. VandeVondele, J.; Krack, M.; Mohamed, F.; Parrinello, M.; Chassaing, T.; Hutter, J. Quickstep: Fast and Accurate Density Functional Calculations Using a Mixed Gaussian and Plane Waves Approach. *Comput. Phys. Commun.* **2005**, *167*, 103–128. [[CrossRef](#)]
57. Krack, M. Pseudopotentials for H to Kr Optimized for Gradient-Corrected Exchange–Correlation Functionals. *Theor. Chem. Acc.* **2005**, *114*, 145–152. [[CrossRef](#)]
58. Perdew, J.P.; Burke, K.; Ernzerhof, M. Generalized Gradient Approximation Made Simple. *Phys. Rev. Lett.* **1996**, *77*, 3865–3868. [[CrossRef](#)] [[PubMed](#)]
59. Grimme, S.; Antony, J.; Ehrlich, S.; Krieg, H. A Consistent and Accurate Ab Initio Parametrization of Density Functional Dispersion Correction (DFT-D) for the 94 Elements H–Pu. *J. Phys. Chem.* **2010**, *132*, 154104:1–154104:15. [[CrossRef](#)] [[PubMed](#)]
60. VandeVondele, J.; Hutter, J. Gaussian Basis Sets for Accurate Calculations on Molecular Systems in Gas and Condensed Phases. *J. Chem. Phys.* **2007**, *127*, 114105:1–114105:8. [[CrossRef](#)] [[PubMed](#)]
61. Mundy, C.J.; Balasubramanian, S.; Bagchi, K.; Hutter, J.; Kuo, A.S.I.; Laino, T.; VandeVondele, J. Frontiers in Simulation Technology (FIST). 2017. Available online: www.cp2k.org (accessed on 4 February 2021).
62. Cygan, R.T.; Liang, J.J.; Kalinichev, A.G. Molecular Models of Hydroxide, Oxyhydroxide, and Clay Phases and the Development of a General Force Field. *J. Phys. Chem. B* **2004**, *108*, 1255–1266. [[CrossRef](#)]
63. Berendsen, H.J.C.; Grigera, J.R.; Straatsma, T.P. The Missing Term in Effective Pair Potentials. *J. Phys. Chem.* **1987**, *91*, 6269–6271. [[CrossRef](#)]
64. Zoete, V.; Cuendet, M.A.; Grosdidier, A.; Michielin, O. SwissParam: A Fast Force Field Generation Tool for Small Organic Molecules. *J. Comput. Chem.* **2011**, *32*, 2359–2368. [[CrossRef](#)] [[PubMed](#)]
65. Laino, T.; Mohamed, F.; Laio, A.; Parrinello, M. An Efficient Linear-Scaling Electrostatic Coupling for Treating Periodic Boundary Conditions in QM/MM Simulations. *J. Chem. Theory Comput.* **2006**, *2*, 1370–1378. [[CrossRef](#)] [[PubMed](#)]
66. Bussi, G.; Donadio, D.; Parrinello, M. Canonical Sampling through Velocity Rescaling. *J. Chem. Phys.* **2007**, *126*, 014101:1–014101:6. [[CrossRef](#)]
67. Boys, S.F.; Bernardi, F. The Calculation of Small Molecular Interactions by the Differences of Separate Total Energies: Some Procedures with Reduced Errors. *Mol. Phys.* **1970**, *19*, 553–566. [[CrossRef](#)]
68. Tellinghuisen, J.; Bolster, C.H. Least-Squares Analysis of Phosphorus Soil Sorption Data with Weighting from Variance Function Estimation: A Statistical Case for the Freundlich Isotherm. *Environ. Sci. Technol.* **2010**, *44*, 5029–5034. [[CrossRef](#)]

-
69. Ahmed, A.A.; Kühn, O.; Aziz, S.G.; Hilal, R.H.; Leinweber, P. How Soil Organic Matter Composition Controls Hexachlorobenzene-Soil-Interactions: Adsorption Isotherms and Quantum Chemical Modeling. *Sci. Total Environ.* **2014**, *476*, 98–106. [[CrossRef](#)] [[PubMed](#)]
 70. Ahmed, A.A.; Thiele-Bruhn, S.; Aziz, S.G.; Hilal, R.H.; Elroby, S.A.; Al-Youbi, A.O.; Leinweber, P.; Kühn, O. Interaction of Polar and Nonpolar Organic Pollutants with Soil Organic Matter: Sorption Experiments and Molecular Dynamics Simulation. *Sci. Total Environ.* **2015**, *508*, 276–287. [[CrossRef](#)] [[PubMed](#)]
 71. Celi, L.; Lamacchia, S.; Marsan, F.A.; Barberis, E. Interaction of Inositol Hexaphosphate on Clays: Adsorption and Charging Phenomena. *Soil Sci.* **1999**, *164*, 574–585. [[CrossRef](#)]
 72. Martin, M.; Celi, L.; Barberis, E. Desorption and Plant Availability of Myo-Inositol Hexaphosphate Adsorbed on Goethite. *Soil Sci.* **2004**, *169*, 115–124. [[CrossRef](#)]
 73. Celi, L.; Barberis, E. Abiotic Reactions of Inositol Phosphates in Soil. In *Inositol Phosphates: Linking Agriculture and the Environment*; Turner, B.L., Richardson, A., Mullaney, E.J., Eds.; CABI Publishing: Wallingford, UK, 2007.
 74. Li, H.; Wan, B.; Yan, Y.; Zhang, Y.; Cheng, W.; Feng, X. Adsorption of Glycerophosphate on Goethite: A Macroscopic and Infrared Spectroscopic Study. *J. Soil Sci. Plant Nutr.* **2017**, *181*, 557–565. [[CrossRef](#)]
 75. Guzman, G.; Alcantara, E.; Barron, V.; Torrent, J. Phytoavailability of Phosphate Adsorbed on Ferrihydrite, Hematite, and Goethite. *Plant Soil* **1994**, *159*, 219–225. [[CrossRef](#)]
 76. Celi, L.; M, P.; Marsan, F.A.; Barberis, E. Effects of pH and Electrolytes on Inositol Hexaphosphate Interaction with Goethite. *Soil Sci. Soc. Am. J.* **2001**, *65*, 753–760. [[CrossRef](#)]
 77. Johnson, B.B.; Quill, E.; Angove, M.J. An Investigation of the Mode of Sorption of Inositol Hexaphosphate to Goethite. *J. Colloid Interface Sci.* **2012**, *367*, 436–442. [[CrossRef](#)]
 78. Xu, C.Y.; Li, J.Y.; Xu, R.K.; Hong, Z.N. Sorption of Organic Phosphates and Its Effects on Aggregation of Hematite Nanoparticles in Monovalent and Bivalent Solutions. *Environ. Sci. Pollut. Res.* **2017**, *24*, 7197–7207. [[CrossRef](#)]
 79. Abdala, D.B.; Northrup, P.A.; Arai, Y.; Sparks, D.L. Surface Loading Effects on Orthophosphate Surface Complexation at the Goethite/Water Interface as Examined by Extended X-Ray Absorption Fine Structure (EXAFS) Spectroscopy. *J. Colloid Interface Sci.* **2015**, *437*, 297–303. [[CrossRef](#)]
 80. Persson, P.; Nilsson, N.; Sjöberg, S. Structure and Bonding of Orthophosphate Ions at the Iron Oxide–Aqueous Interface. *J. Colloid Interface Sci.* **1996**, *177*, 263–275. [[CrossRef](#)] [[PubMed](#)]
 81. Rose, J.; Flank, A.M.; Masion, A.; Bottero, J.Y.; Elmerich, P. Nucleation and Growth Mechanisms of Fe Oxyhydroxide in the Presence of PO₄ Ions. 2. P K-Edge EXAFS Study. *Langmuir* **1997**, *13*, 1827–1834. [[CrossRef](#)]
 82. Tribe, L.; Kwon, K.D.; Trout, C.C.; Kubicki, J.D. Molecular Orbital Theory Study on Surface Complex Structures of Glyphosate on Goethite: Calculation of Vibrational Frequencies. *Environ. Sci. Technol.* **2006**, *40*, 3836–3841. [[CrossRef](#)] [[PubMed](#)]
 83. Persson, P.; Andersson, T.; Nelson, H.; Sjöberg, S.; Giesler, R.; Lövgren, L. Surface Complexes of Monomethyl Phosphate Stabilized by Hydrogen Bonding on Goethite (Alpha-FeOOH) Nanoparticles. *J. Colloid Interface Sci.* **2012**, *386*, 350–358. [[CrossRef](#)] [[PubMed](#)]
 84. Guan, X.H.; Shang, C.; Zhu, J.; Chen, G.H. ATR-FTIR Investigation on the Complexation of Myo-Inositol Hexaphosphate with Aluminum Hydroxide. *J. Colloid Interface Sci.* **2006**, *293*, 296–302. [[CrossRef](#)] [[PubMed](#)]
 85. De Groot, C.J.; Golterman, H.L. On the Presence of Organic Phosphate in Some Camargue Sediments: Evidence for the Importance of Phytate. *Hydrobiologia* **1993**, *252*, 117–126. [[CrossRef](#)]

Supplementary Materials: The Binding of Phosphorus Species at Goethite: A Joint Experimental and Theoretical Study

Prasanth B. Ganta, Mohsen Morshedizad, Oliver Kühn, Peter Leinweber and Ashour A. Ahmed

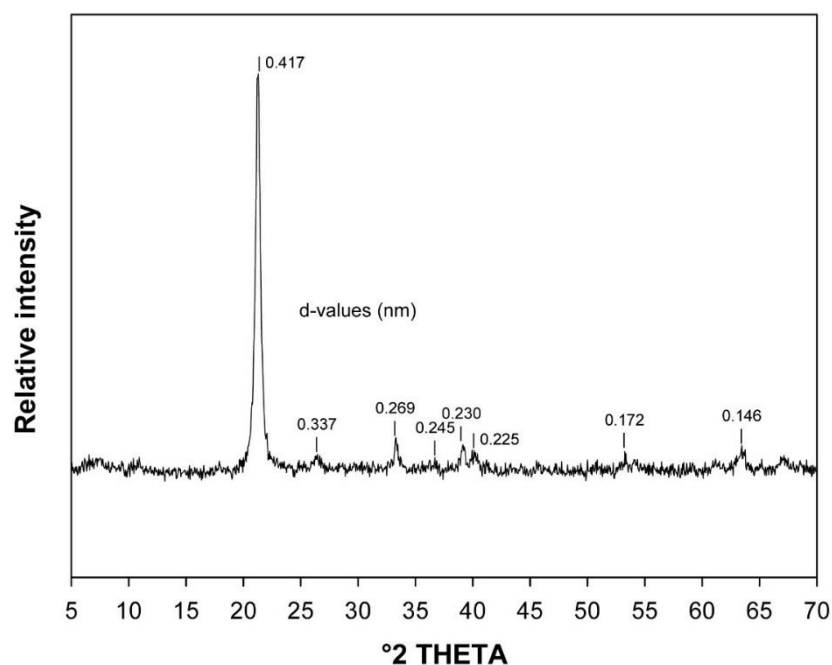


Figure S1. XRD pattern for pure goethite sample.

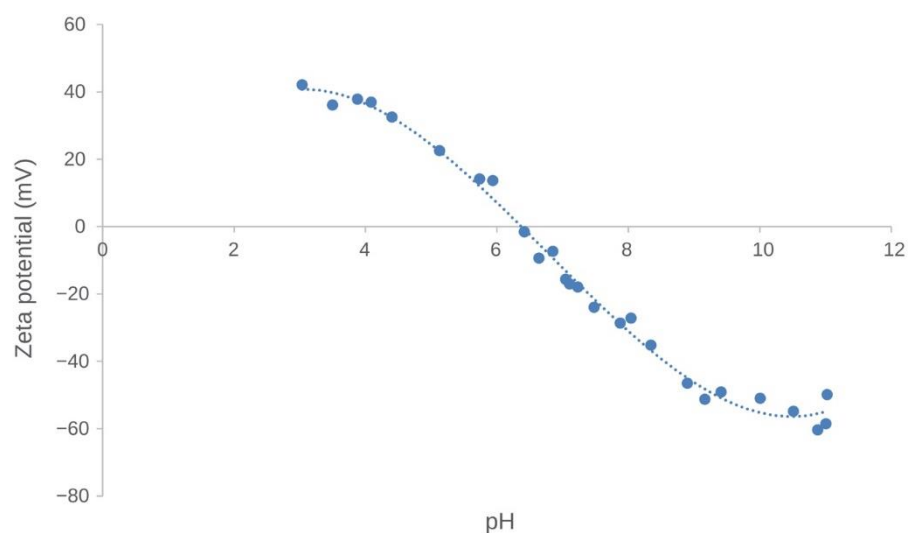


Figure S2. Effect of pH on electrophoretic zeta potential of goethite particles. Dashed line shows polynomial fitting to all data points representing the PZC of 6.3 ($R^2 = 0.99$).

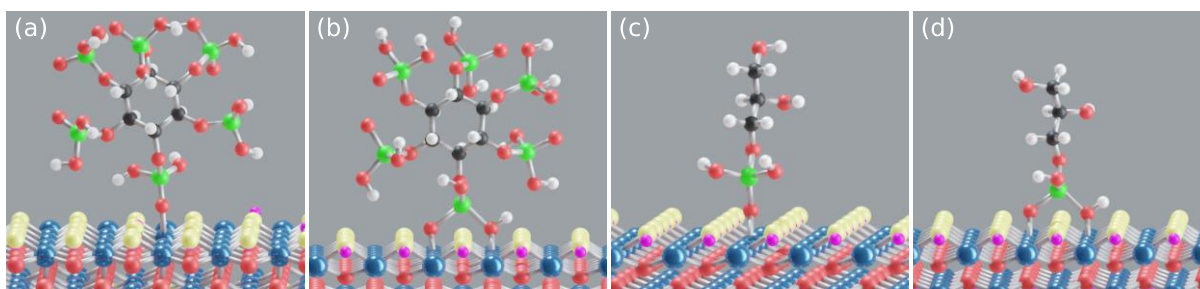


Figure S3. Initial motifs of IHP: **M**, **B** motifs (a,b) and GP **M**, **B** motifs (c,d).

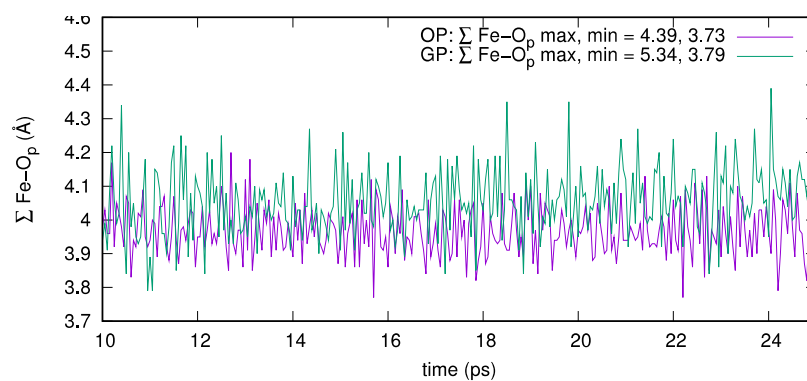


Figure S4. Sum of Fe-O_p bond lengths observed in goethite-OP and goethite-GP **B** motifs.

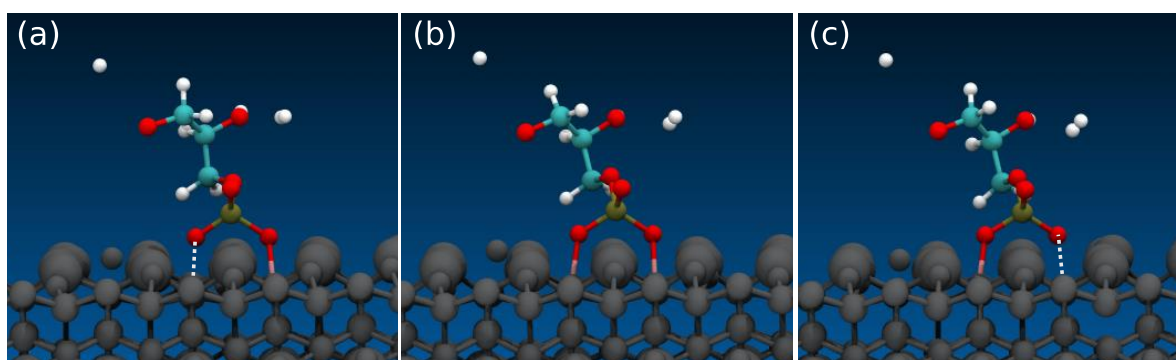


Figure S5. Seesaw movement of the bound GP's phosphate group to the goethite surface for the **B** motif case. (a) and (c) show momentarily elongated Fe-O bonds (left and right bonds, respectively) passing through a more stable **B** motif as shown in (b).

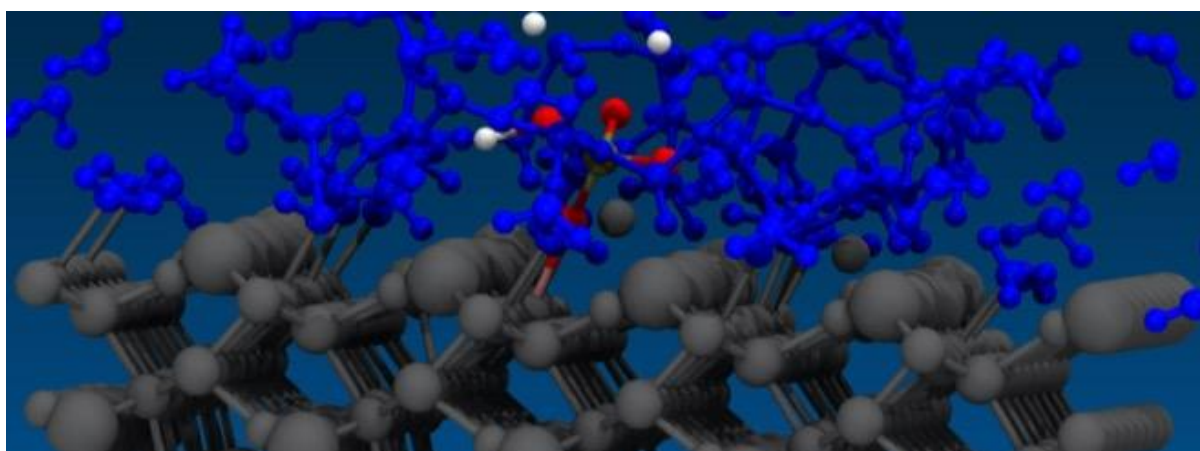


Figure S6. Multiple Fe-O_{water} **M** motifs between water oxygens and surface Fe atoms on goethite.

Acknowledgments

I am grateful to Prof. Oliver Kühn and Dr. Ashour Ahmed for accepting me into this Ph.D. position. Thanks for the scientific discussions, suggestions, corrections on my simulations and manuscripts, and recommendations to attend conferences and courses. Thank you, Prof. Kühn, for your kind support and providing a positive environment to discuss work and share ideas - especially cake meetings. Thank you, Dr. Ahmed, for your invaluable support, patience and guidance in helping me research this unique interdisciplinary topic. Discussions with you have been motivating and tremendously helpful in consolidating the core concepts to set up simulations. I could not have completed this dissertation without your kind support and help.

I thank all our colleagues, especially Tobias, Gilbert and Jan, for their help regarding IT issues, admin training, and pleasant conversations. I enjoyed the work-related and friendly chitchats with Alejandro Ramos, Moyassar Meshhal and Lorenz Dettmann.

Big thanks to the German Research Foundation (DFG)'s financial support as part of the SPP 1685 Priority program and Prof. Peter Leinweber.

Sincere thanks to my parents and brother for their unwavering support and motivation. Heartful gratitude to my incredibly supportive and loving wife.

Finally, I would like to express my gratitude to Germany for providing opportunities to complete my master's degree, start my Ph.D., begin a family and grow professionally. Vielen Dank!



Prasanth Babu Ganta



Nationality: Indian



Born: Andhra Pradesh, India



Email: pbganta@gmail.com



WORK EXPERIENCE

Research Scientist

2021 - 2024



Fraunhofer Institute for Mechanics of Materials IWM, Freiburg

Doctoral Candidate

2017 - 2021



Institute of Physics, University of Rostock

Software Developer

2016 - 2017



Celisca GmbH, Rostock

Research Associate

2015 - 2016



Faculty of Computer Science and Electrical Engineering, University of Rostock

Software Developer & Associate Consultant

2009 - 2012



Capgemini, India



EDUCATION

M.Sc. Computational Engineering

Faculty of Computer Science and Electrical Engineering, University of Rostock, Rostock, Germany

Thesis: Computation of higher order port-signals by means of concatenation methods

B.Eng. Electronics and Communications Engineering

Faculty of Electronics and Communications, Gandhi Institute of Technology and Management, Vizag, India

Thesis: Microcontroller based LCD display and monitoring of external devices



PUBLICATIONS

Ganta, P. B., Morshedizad, M., Kühn, O., Leinweber, P., and Ahmed, A. A. The binding of phosphorus species at goethite: A joint experimental and theoretical study. *Minerals*, 11(3), 323. doi: 10.3390/min11030323

Ganta, P. B., Kühn, O., and Ahmed, A. A. Ab initio molecular dynamics simulations of the interaction between organic phosphates and goethite. *Molecules*, 26, 160. doi: 10.3390/molecules26010160

Ganta, P. B., Kühn, O., and Ahmed, A.A. QM/MM molecular dynamics investigation of the binding of organic phosphates to the 100 diaspore surface. *Front. for. glob. change.*, 3, 71. doi:10.3389/ffgc.2020.00071

Ganta, P. B., Kühn, O., and Ahmed, A. A. QM/MM simulations of organic phosphorus adsorption at the diaspore-water interface. *Phys. Chem. Chem. Phys.* 21, 24316–24325. doi: 10.1039/C9CP04032C